Statistically modelling tennis racket impacts with six degrees of freedom

SPURR, James Christopher

Published version

SPURR, James Christopher (2017). Statistically modelling tennis racket impacts with six degrees of freedom. Doctoral, Sheffield Hallam University.

Statistically modelling tennis racket impacts with six degrees of freedom

James Christopher Spurr

A thesis submitted in partial fulfilment of the requirements of

Sheffield Hallam University

for the degree of Doctor of Philosophy

September 2017

Collaborating organisation: International Tennis Federation

I Abstract

The International Tennis Federation (ITF) is responsible for protecting the nature of tennis. The ITF uses computational models to predict how trends in equipment parameters could affect the games future. The current ball-racket impact model is limited to non-spinning, on-axis, normal ball impact simulations. The aim of this project was to develop a model of oblique, spinning, on- and off-axis ball-racket impacts.

Large scale test data ($n > 1000$) was collected using an impact rig and calibrated high-speed cameras. Impacts for a range of realistic velocities, spin rates and impact locations were collected, measured using automated image processing algorithms to digitise ball centroids. An established spin measurement method was improved to correct for perspective errors associated with the proximity of the cameras to the test volume. The automated algorithms were validated with experimental data and manual methods.

Multi-variate polynomial models to predict the lateral and vertical components of rebound velocities and rebound spin rate were trained and validated using a curve fitting toolbox and ‘n-fold and leave one out cross-validation’ method. Second order models best fit the training data, with the low predictive errors. Root-mean-squared errors were calculated using a test dataset, independent of the training data. These were 0.57 $\mathrm{m \cdot s^{-1}}$ for the lateral rebound velocity model, 0.48 $\mathrm{m \cdot s^{-1}}$ for the vertical rebound velocity model and 30.5 $\mathrm{rad \cdot s^{-1}}$ for the rebound spin rate model. Variance was partially explained by experimentally established inherent variability of the ball and stringbed. Model output confidence was established by simulating small changes in model inputs. The simulated lateral and vertical components of rebound velocity, but not the simulated spin rate, were an order of magnitude greater than the measurement precision.

The new models were combined with ball aerodynamics and ball-to-surface impact models to simulate tennis court trajectories for oblique, spinning, on- and off-axis ball-racket impacts. Increasing stringbed stiffness or the lateral offset of impact location were found to decrease rebound velocity and increase rebound angle – markedly so for a 60 mm lateral offset. Increasing lateral offset also increased the rebound spin rate.

Key words: Statistical model, rackets, impact testing, image processing

II Acknowledgements

I would like to thank Professor Steve Haake, Dr Simon Goodwill, Dr John Kelley and Dr Simon Choppin for their advice and guidance throughout this project. I would also like to thank everyone at the Centre for Sports Engineering Research, who made me feel incredibly welcome and supported during my time working on this project. In particular: Amanda Brothwell, Carole Harris and Terry Senior (a proper northern gent!).

I am also grateful to the International Tennis Federation, for sponsorship of this project. In particular, I'd like to thank Dr Stuart Miller, Jamie Capel-Davies, Janet Page and Nichola Chong, without whose support would not have made this project possible.

I would finally like to thank my amazing wife Jennie and the rest of my family for their support and endless, endless patience!

III Contents

IV List of figures

V List of tables

VI Nomenclature

Abbreviations

ACOR	Apparent coefficient of restitution
COF	Coefficient of friction
COM	Centre of mass
COM_p	Planar centre of mass
COM_{pff}	Front face planar centre of mass
COM_{pbf}	Back face planar centre of mass
COR	Coefficient of restitution
DLT	Direct linear transformation
GSC	Geometric stringbed centre
ITF	International Tennis Federation
MMOI	Mass moment of inertia
RMSE	Root-mean-square error
RoT	Rules of Tennis
SBS	Stringbed stiffness
SEM	Standard error of the mean
SSE	Sum of square errors
XML	Extensible markup language

Roman letters

A	Cross section area (m^2)
$\vec{a}, \vec{b}$	Camera and ball centre vectors
a_b	Ball acceleration ($m \cdot s^{-2}$)
a_d	Acceleration due to drag ($m \cdot s^{-2}$)
a_g	Acceleration due to gravity ($m \cdot s^{-2}$)
a_r	Racket acceleration ($m \cdot s^{-2}$)

b	Transverse distance between racket COM and impact location (m)
c	Lateral distance between racket COM to impact location (m)
$\vec{c}$	Vector between ball centres
C_D	Coefficient of drag
C_L	Coefficient of lift
d	System domain dimensions
D	Diameter (m)
d_{butt}	Racket butt to COM (m)
d_{tip}	Racket tip to COM (m)
d_r	Racket deflection (m)
e	COR
e_A	Apparent coefficient of restitution
e_x	Lateral COR
e_y	Longitudinal COR
e_z	Vertical COR
F_b	Ball force (N)
F_D	Aerodynamic drag force (N)
F_L	Aerodynamic lift force (N)
F_s	Spring force (N)
(L_x, L_y)	Impact location (m)
I_X	Transverse MMOI
I_Y	Polar MMOI
J_b	Ball force impulse (Ns)
J_s	Spring force impulse (Ns)
$\vec{k}$	Apparent spin axis unit vector
k_s	Spring constant ($N \cdot m^{-1}$)
M	System domain dimension division

m_b	Ball mass (kg)
M_{butt}	Racket butt mass (kg)
M_e	Racket effective mass (kg)
m_r	Racket mass (kg)
M_{tip}	Racket tip mass (kg)
n	Data sample size, model order
n_{data}	Data required to describe a system domain
R	Rotation matrix
r	Ball radius (m)
R^2	Coefficient of determination
R_A, R_B, R_C	Racket reaction forces (kg)
R_{GSC}	Universal joint to geometric stringbed centre (m)
R_S	Universal joint to spring attachment (m)
$r\omega$	Instantaneous velocity of ball surface (m·s^{-1})
$RMSE_{ImpX}$,$RMSE_{ImpY}$	RMSE of impact location (m)
$RMSE_{iv}$	RMSE of ball launch velocity (m·s^{-1})
$RMSE_{is}$	RMSE of ball launch spin rate (rad·s^{-1})
$\overline{SBS}$	Mean stringbed stiffness (N)
s_i	Inbound spin rate (rad·s^{-1})
s_o	Outbound spin rate (rad·s^{-1})
t	Time (s)
t_i	Impact duration (s)
t_{impact}	Impact time (s)
T	Translation matrix
T	Stringing tension (lbs)
(u, v)	Image coordinates (p)
$\vec{v}$	Start unit vector
V_o	Normalised outbound ball velocity (m·s^{-1})

V_1	Inbound ball velocity (m·s^{-1})
V_2	Rebound ball velocity (m·s^{-1})
V_b	Ball velocity (m·s^{-1})
$(V_{b_x}, V_{b_y}, V_{b_z})$	Ball velocities (m·s^{-1})
V_i	Mean inbound velocity (m·s^{-1})
V_{iR}	Inbound resultant ball velocity (m·s^{-1})
(V_{ix}, V_{iy}, V_{iz})	Inbound ball velocities (m·s^{-1})
V_{oR}	Outbound resultant ball velocity (m·s^{-1})
(V_{ox}, V_{oy}, V_{oz})	Outbound ball velocities (m·s^{-1})
V_{r_0}	Initial racket velocity (m·s^{-1})
$\vec{v}_{rot}$	Resulting unit vector
$(V_{r_x}, V_{r_y}, V_{r_z})$	Racket velocities (m·s^{-1})
V_{t_R}	Resultant impact test velocity (m·s^{-1})
$(V_{t_x}, V_{t_y}, V_{t_z})$	Impact test velocities (m·s^{-1})
(x, y, z)	Real-world coordinates (m)
$(X_A\ Y_A), (X_B, Y_B), (X_C, Y_C)$	Distances of racket reaction forces to COM$_p$ (m)
$(\hat{X}_C, \hat{Y}_C, \hat{Z}_C)$	Camera origin unit vector
(X_{COM}, Y_{COM})	COM$_p$ (m)
(X_f, Y_f)	Focal length (m)
(X_i, Y_i, Z_i)	Reconstructed ball coordinates to camera origin (m)
(X_j, Y_j, Z_j)	Reconstructed ball coordinates to intermediate origin (m)
(X_k, Y_k, Z_k)	Reconstructed ball coordinates to local racket origin (m)
(X_M, Y_M, Z_M)	Intermediate origin coordinates
$(\hat{X}_M, \hat{Y}_M, \hat{Z}_M)$	Intermediate local origin unit vector
$(\hat{X}_R, \hat{Y}_R, \hat{Z}_R)$	Local racket origin unit vector
x_s	Spring extension (m)

Greek letters

α	Spin ratio
ΔCOM_P	Discrepancy between racket face COM_p (mm)
Δ_{threeU}, Δ_{threeV}, , $\Delta_{throatU}$, $\Delta_{throatV}$, Δ_{tipU}, Δ_{tipV}, Δ_{nineU}, Δ_{nineV}	Discrepancies between stringbed marker centroid components (mm)
ΔV_a	Ball acceleration due to gravity ($m \cdot s^{-2}$)
ΔV_d	Ball acceleration due to drag ($m \cdot s^{-2}$)
σ_A, σ_B, σ_C	Standard deviations of racket location digitisation (p)
σ_{BUTT}	Standard deviation of racket butt digitisation (p)
σ_{LF}, σ_{RF}	Standard deviations of racket frame extremity digitisation (p)
σ_{nineU}, σ_{nineV}, σ_{threeU}, σ_{threeV}, $\sigma_{throatU}$, $\sigma_{throatV}$, σ_{tipU}, σ_{tipV}	Standard deviations of stringbed marker centroid components (p)
σ_{norm}	Standard deviation of normalised outbound velocity ($m \cdot s^{-1}$)
σ_{SBS}	Standard deviation of stringbed stiffness (lbs)
σ_{spin}	Standard deviation of outbound spin rate ($rad \cdot s^{-1}$)
ρ	Air density ($kg \cdot m^3$)
θ	Stringbed plane orientation to vertical (°)
θ_{APP}	Angle of apparent rotation (°)
θ_{min}	Rotation resolution of the *SpinTrack3D* algorithm (°)
θ_{rot}	Racket calibration image rotation (°)
θ_{spin}	Angle of spin (°)
$(\widehat{\omega}_{ix}, \widehat{\omega}_{iy}, \widehat{\omega}_{iz})$	Inbound spin axis
$(\widehat{\omega}_{ox}, \widehat{\omega}_{oy}, \widehat{\omega}_{oz})$	Outbound spin axis
ω_s	Spin rate ($rad \cdot s^{-1}$)
(ω_x, ω_y)	Angular velocity components ($rad \cdot s^{-1}$)

This thesis is dedicated to Jen and Emmy.

Sorry it took so long.

Chapter 1 – Introduction

1.1 Introduction

The following thesis presents the work of a research project to advance the modelling of tennis. The project developed the tools, data collection methods and analysis techniques to create a statistical model of oblique, spinning, on-and off-axis tennis ball impacts with tennis rackets. The project culminates with the generation and assessment of three statistical models.

1.2 Motivation for the research

One of the challenges of governing a global, multi-billion dollar sport, such as tennis, is predicting how the sport will evolve and the influence governance rulings will have on possible future developments. Governing bodies, such as the International Tennis Federation (ITF), are conscious that governance decisions affect multiple stakeholders – including players, fans, sports industry and the media.

There are several examples within tennis where technological developments have significantly altered the trajectory of the sport. For example, the development of graphite composite tennis rackets allowed for bigger, lighter frames which immediately influence the style of play (Miller, 2006). The ITF reacted to this development by introducing new regulations. However, the reactionary style of governance is less desirable than a proactive approach.

One influence of proactive decision making is access to high-quality, quantitative data. Such data can be used to model trends, which in turn can be used to predict future scenarios. The ITF's Science and Technical department conduct research to monitor the state of the game. The culmination of this research was the development of the tennis simulation tool, *TennisGUT* (Dignall et. al., 2004), which uses analytical models of ball-racket impacts, ball aerodynamics and ball-surface impacts. However, the power of this tool is limited by the power of the models to simulate complex scenarios.

The ball-racket model is limited to ball impacts which are normal to the stringbed plane (Goodwill, 2003a). This limits the simulations to relatively simple scenarios. To simulate more sophisticated scenarios, the ball-racket model requires updating. Given the complexity of the ball-racket impact system, previous failed attempts to improve the analytical model suggest an alternative approach should be considered (Choppin, 2008).

The statistical modelling of ball-racket impact data could offer a viable alternative. However, to assess the feasibility of this approach, original research is required to develop the methods and tools to collect and analyse large datasets and generate the models.

1.3 Project aim

This project aims to demonstrate if a statistical modelling approach is capable of improving the ball-racket impact model of *TennisGUT* to simulate more sophisticated scenarios than currently possible. To this end, a statistical model of oblique, spinning on- and off-axis tennis ball impacts with a tennis racket will be created.

1.4 Project structure

The first part of this project will be to thoroughly review relevant literature. From this, a clear set of objectives will be defined. A test rig will be developed to collect ball-to-racket impact data, using high-speed cameras to film the impacts. This will include considerations for ball projection, camera position and test area lighting. Software will be created to automatically analyse the high-speed camera images of the impacts. Several studies will be conducted to validate the implementation of the automated algorithms, which will measure pre- and post-impact ball velocities, spin and impact locations on the racket stringbed. The impact data will be used to create several multivariate statistical models. Each model will be evaluated by fit and estimation error to select the best performing. These will be further evaluated to quantify the predictive power and demonstrate if the statistical modelling approach is capable of improving upon the current ball-racket impact model.

Chapter 2 – Literature review

2.1 Introduction

The International Tennis Federation's (ITF) Science and Technical department's mission statement reads:

"*to protect the nature of tennis by actively preserving the skills traditionally required to play the game, and, to encourage innovation and improvements which maintain the challenge of the game and make it more exciting to play and watch*" (ITF, 2008b)

As guardians of the Rules of Tennis (RoT), the department's research contributes to tennis governance and regulation by monitoring the nature of the game (Miller, 2007). This aims to understand the influence of the properties, and use, of equipment with two outcomes:

1. To ensure the player is the primary determinant of match outcomes.
2. To identify trends that allow prediction of how the game may develop.

The major challenges of protecting the nature of tennis are reliably predicting the evolution of current developments and possible future innovations. Ultimately, the predicted outcomes are assessed against some established desirable criterion, which describe tennis as "challenging" and "exciting", whilst retaining the heritage of the sport. In response to these challenges, the Science and Technical department conducts quantitative research to measure and understand (i) how players use equipment during play (e.g. to generate spin), and (ii) the influence of equipment properties (e.g. on racket power). The results of this research are combined to establish an overall effect, and predict possible futures based on current trends.

For this, the department developed a suite of field-based and laboratory-based research projects, to collect data from both the tennis court and under laboratory conditions (figure 2.1). The field studies provide ongoing quantification of player performance, and ecological validation for the design of laboratory based research.

Figure 2.1 – Measuring spin rate during real-play at the Wimbledon Qualifying event (left) and the ITF *Racket Spin Rig* to measure spin generation of different strings (right).

The result of these on-going efforts to quantify, understand and predict the nature of tennis was the development of the tennis simulation tool, *TennisGUT* (Dignall et. al., 2004). The software uses analytical models to simulate the three components of a tennis shot:

1. Ball-to-racket interactions.
2. Ball flight aerodynamics.
3. Ball-to-surface interactions.

The models describe the behaviour of equipment, representing the latest understanding of the physical principals of the interactions. The output of a simulation is a visualisation of the flight of the ball (figure 2.2) and the three-dimensional coordinate and time data of the trajectory.

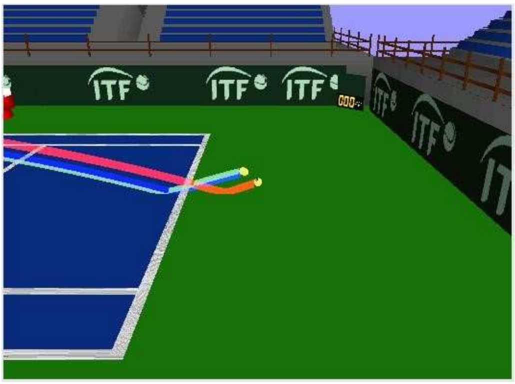

Figure 2.2 – *TennisGUT* simulation showing the flight and bounce of the ball on a virtual tennis court.

The data generated by the Science and Technical department's research agenda and use of Tennis*GUT*, with respect to the overall aim of governing the sport, is shown diagrammatically in figure 2.3.

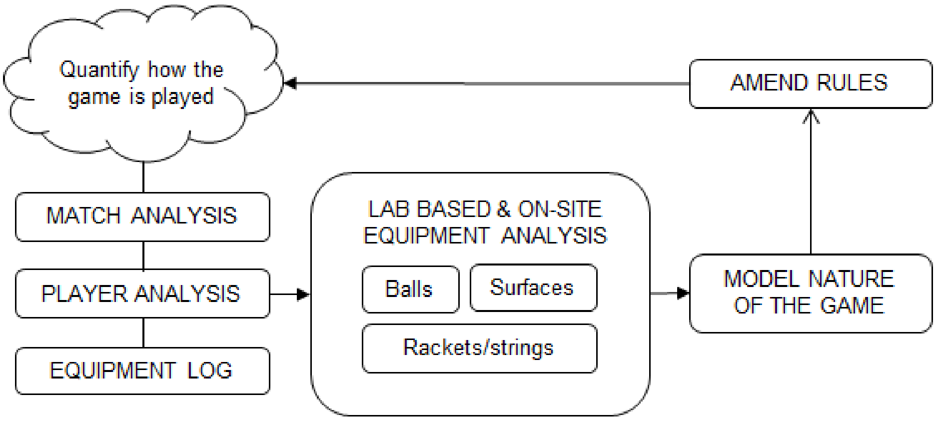

Figure 2.3 – The ITF Science and Technical research agenda.

2.2 Tennis model

The established relationships within each model of *TennisGUT* can be used to calculate the effects of changes to individual equipment parameters. This is particularly advantageous when the system being modelled is complex (i.e. multiple parameters). In addition to this, laboratory data is translated to a tennis court frame of reference. The effects of current developments or possible future developments can be quantified in real terms. However, the predictive power of *TennisGUT* is limited by the complexity of the models. As such, there is a driving force to continually improve the models and enhance the sophistication of the simulations.

This offers an interesting avenue for research. The development of tennis models and, in particular, *TennisGUT* have been described by many previous authors (most relevant examples include: Brody, 1979, Haake et. al., 2000, Goodwill, 2002, Goodwill et. al., 2003a, Dignall et. al., 2004, Goodwill et. al. 2005) and most succinctly by Miller (2007) and Haake et. al. (2007a). The next section describes the current models used in *TennisGUT*.

2.2.1 Ball-racket impact models

The ball-racket impact model was developed by Goodwill et. al. (2003) and summarised by Haake et. al. (2007). The analytical model considers the racket as a one-dimensional flexible beam, split into finite elements (figure 2.4). This allows racket mass and stiffness to be distributed realistically. The ball and stringbed are considered as non-linear springs and dampers in parallel (figure 2.4), to model deformations and speeds.

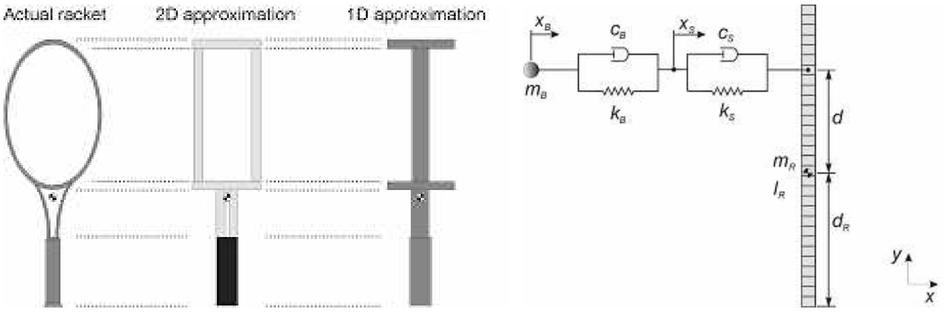

Figure 2.4 – The ball-racket impact model used in *TennisGUT* comprises a racket represented by a one-dimensional flexible bean, split into finite elements (left). The ball and stringbed are represented by an arrangement of parallel non-linear springs and dampers (right).

Real racket and stringbed stiffness values can be obtained from a Babolat RDC (Babolat, 2008), allowing real-world simulation. Modelled ball rebound velocities, over a range of impact positions along the longitudinal axis of the racket, were found to be in good agreement with experimental data, as shown in figure 2.5.

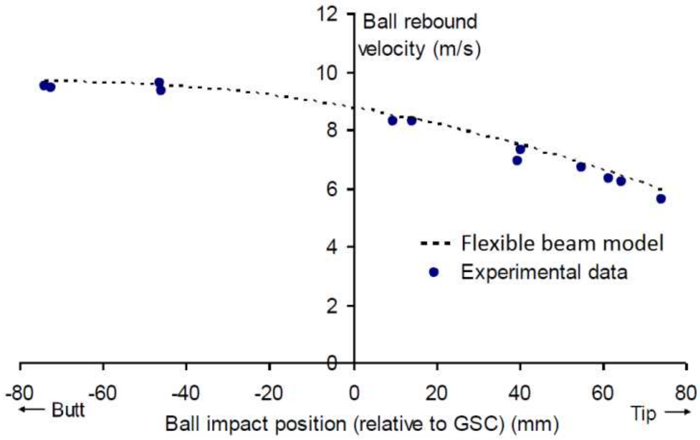

Figure 2.5 – Goodwill et. al. (2003) found good agreement between modelled ball rebound velocities and experimental data for impacts over a range of impact positions.

2.2.2 Aerodynamics model

The aerodynamics model uses aerodynamic equations for a rotating sphere to calculate the drag force, F_D and lift force, F_L acting on the ball throughout a trajectory:

$$F_D = {}^{1}/_{2}\,\rho A C_D V_b^2 \qquad 2.1$$

and,

$$F_L = {}^{1}/_{2}\,\rho A C_L V_b^2 \qquad 2.2$$

where ρ is air density, A is the cross-sectional area of the ball, V_b is ball velocity and C_D and C_L are the coefficients of drag and lift for a spinning tennis ball, respectively. C_D and C_L are dependent on the spin of the ball. For this, the spin ratio, α of the ball is calculated using:

$$\alpha = \frac{\omega_s D}{2V_b} \qquad 2.3$$

where ω_s and D are the spin rate and diameter of the ball, respectively. The final aspect of the aerodynamics model in *TennisGUT* is spin decay. For this, Haake et. al. (2007a) reports the aerodynamics model uses research by Tarnowski (2004), who measured a 14% reduction in spin rate for tennis ball trajectories over the length of a tennis court.

C_D and C_L must be measured experimentally. Chadwick et. al. (2000) used a drop-test methodology, whilst Carrè et. at. (2002) and Greenway (2016) used trajectory measurements. Ball displacement sampling presents a significant source of error for these methods. Goodwill et. al. (2004) and Greenway (2016) used the ITF's wind tunnel (figure 2.6) to directly measure the C_D and C_L for new and used balls at various spin rates and wind speeds. The data generated by the ITF wind tunnel is currently used by the *TennisGUT* aerodynamics model.

Figure 2.6 – The ITF wind tunnel was used to measure the C_D and C_L for non-spinning and spinning tennis balls.

2.2.3 Ball-surface impact models

Dignall et. al. (2004) summarises the ball-surface impact model of *TennisGUT* as the amalgamation of several bodies of research (Daish, 1972, Brody, 1984, Dignall et. al., 2000, Goodwill et. al., 2002b and Haake et. al., 2003). The model combines simple Newtonian mechanics, linear spring-damper models and impulsive reaction forces to describe the interactions between the ball and tennis surface. The components of the model were validated against experimental data. Dignall estimated the error in modelled rebound velocity was 5%. This model accounts for the ball deforming, sliding and rolling through the impact. Surface parameters include the coefficients of friction (COF) and restitution (COR), which are determined experimentally from the ITF's Court Pace Classification Programme (ITF, 2008b).

2.2.4 Model limitations

Ball-racket impact model

Simulated ball-racket impacts are limited to non-spinning, normal impacts along the longitudinal axis of the racket (figure 2.6). This is a significant restriction to the types of tennis strokes that can be simulated. In reality, impacts can be oblique, spinning and off-axis (figure 2.7).

Figure 2.7 – The ball-racket impact model is limited to normal impacts along the longitudinal axis of the racket (left). Real tennis impacts can be oblique, off-axis and include spin (right).

The ball-racket model does not predict the rebound spin of the ball. As such, *TennisGUT* requires rebound spin to be input manually, as this is a necessary input for the ball aerodynamics model. These limitations offer significant scope to improve the functionality of *TennisGUT* and form the basis of the research described in this thesis. Expanding the ball-racket model to cater for a greater variety of tennis strokes requires the model to simulate oblique, spinning, on- and off-axis impacts.

Aerodynamics model

Internal research by the ITF's Science and Technical department (ITF, 2012) showed the wind tunnel's force measurement to be prone to error caused by the process of spinning the ball. The sensitivity of trajectory modelling to the uncertainty in C_D and C_L, is unknown and a possible avenue for future research.

Greenway (2016) used Hawk-Eye data from a controlled experimental set up and real-play to calculate C_D and C_L. The increasing use of Hawk-Eye in tennis (Hawk-Eye, 2008) offers an interesting source of data for continuing this research, given the quantity of data generated. However the accuracy of ball tracking and spin rate measurement using Hawk-Eye has not been measured.

To improve the methods of measuring C_D and C_L would require significant investment

– whether by improving the wind tunnel or gaining access to a tennis court set up with a Hawk-Eye system.

Improving the aerodynamics model is not critical to the research aim of this project. However, the current model may prove a useful tool to assess the development of a new ball-racket model.

Ball-surface impact model

Dignall et. al. (2004) states that the model does not account for surface deformations, as the stiffness of the ground is an order of magnitude greater than that of the ball. This is likely true for the acrylic (hard) surface type, but may not be representative of softer surface types such as clay or grass. Given tennis is played on a variety of surfaces, which are classified into one of 10 types (ITF, 2008b), it is likely that a lack of surface deformation modelling is a limiting factor. However, the agreement to laboratory data suggests this model is representative of real-world scenarios.

As with the aerodynamics model, improving the ball-surface model is not critical to the aim of this project. However, the model may also prove useful in assessing the development of a new ball-racket model.

2.2.5 Tennis models conclusions

This section described the development, validation and limitations of the models used in *TennisGUT* to simulate the ball-racket impact, ball aerodynamics and the ball-surface impact. The ball-racket impact model is the most limited model, as simulations are restricted to non-spinning, normal impacts along the longitudinal axis of the racket. This forms the basis for the research aim of this project, where a new statistical ball-racket impact model will be developed, simulating oblique, spinning, on- and off axis impacts.

2.3 Developing the ball-racket impact model

Several research projects have aimed to improve the sophistication of the ball-racket impact model. Cottey (2002) developed an analytical model of oblique, non-spinning, on-axis impacts. He modelled the ball and strings independently of one another, using spring-dampers to describe deformations. The normal and tangential components of rebound ball velocity were modelled separately, with the tangential component used to calculate spin generation. The model was validated against experimental data, which were collected for ball impacts onto a rigidly held, handle clamped racket. Balls were launched using an air cannon, with ball launch velocity measured using light gates. Planar ball rebound velocity and spin rates were measured through manual digitisation of images collected with a calibrated high-speed camera. In comparing his model's outputs to the experimental data, Cottey calculated a 4.0% error in rebound ball velocity, a 7.0% error in rebound ball angle and a 13.0% error in rebound spin rate. Although these errors were an improvement on previous models (Groppel et. al., 1983 and Cross, 2002), he admitted his model inadequately described the mechanisms of a ball-to-stringbed impact. Interestingly, Cottey used an additional high-speed camera to film the ball-to-stringbed interactions during an impact. He observed and measured several phenomenon, including the ball sliding and rolling across the stringbed and string 'snap-back'. From these observations, he concluded a limitation of his analytical model was the assumption that the ball did not deform appreciably during impact. He went on to describe how a more extensive test programme would help to better understand the mechanism of an impact. However, he conceded the complexity of additional model parameters would make the relationships between parameters difficult to rationalise.

Choppin (2008) attempted to improve the Goodwill et. al. (2003) *TennisGUT* ball-racket impact model with the development of an analytical model of oblique, spinning, on- and off-axis impacts. His model had six degrees of freedom, allowing for appropriate racket rotations for on- and off-axis impacts. The model included a restrictive torque element to simulate a player's grip on the racket handle and limit racket rotations about the longitudinal axis. In balance of this additional complexity, the racket frame was considered a rigid-body. Goodwill (2002) showed this approached was only valid for impacts close to the node point of the racket, but Choppin measured the impact locations of professional players, showing that they tend to hit the ball at, or very close to the node. Choppin used Goodwill’s spring-damper approach to model the ball and stringbed, but improved upon this with an in-plane deformable ball-stringbed spin model to calculate rebound spin rates and axes of the ball.

The model was validated with experimental data. For this, Choppin built an impact rig (figure 2.8) to launch balls onto a realistically supported, stationary racket at multiple impact locations. The racket was handle-clamped and included a torque limiting clutch to replicate a human grip by restricting rotations about the longitudinal axis of the racket (figure 2.8).

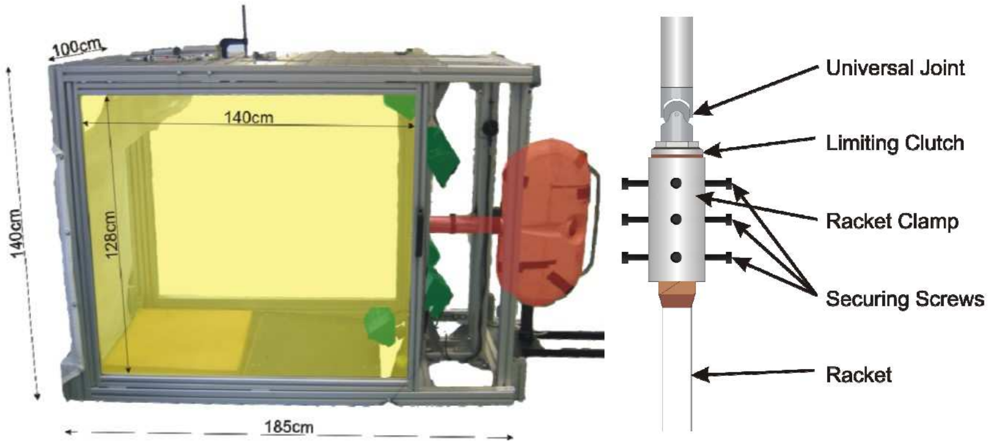

Figure 2.8 – Choppin (2008) validated his model using experimental data from an impact rig (left) with a handle-clamped racket incorporating a torque limiter (right) to replicate a human grip on the racket.

Choppin (2008) found the accuracy and repeatability of the test equipment required the test parameters (e.g. ball velocities) to be measured directly. For this, he filmed impacts with two, synchronised high-speed cameras. The cameras were calibrated to describe a calibrated test volume. The calibration parameters allowed for pairs of digitised two-dimensional image coordinates to be reconstructed to real-world three dimensional positions, relative to a defined origin. To assist with analysis of the large number of test image, he developed automated digitisation algorithms.

Due to the complexity of his analytical model, Choppin used statistical models (multi-variate polynomial regressions) of the experimental impact data as validation. Training the statistical models required a large dataset to map the multiple dimensions of the ball-racket impact system domain (six independent input parameters and two dependent output parameters). Due to project constraints, he limited this validation to rebound ball velocities. Rebound spin rates were partially validated against a sub-sample of the experimental data only.

Choppin found his model showed good agreement for rebound ball velocities close to the node of the racket and off-axis. The rigid-body racket assumption did reduce the agreement for impacts near the throat of the racket, however this was previously justified. Modelled outbound spin measurements were found to agree with experimental data at lower spin rates, but less so as spin rate increased above 2000 rpm. Choppin identified issue with this validation, including measurement error in his experimental data. He concluded that to investigate the causes of spin rate error in his model, the multi-variate regressions could be expanded to include spin rate as an additional parameter. The errors and uncertainty of his validation meant the model did not replace the existing ball-racket impact model in *TennisGUT*.

2.3.1 Developing the ball-racket impact model conclusions

Cottey (2002) and Choppin (2008) developed increasingly sophisticated analytical ball-racket impact models. Cottey's model was limited to oblique, non-spinning impacts onto a handle clamped racket. The model errors (4.0 – 13.0%) were an improvement on previous research. However, he concluded the model parameters inadequately described the ball-racket system and that further research and understanding would benefit future developments. Choppin developed an analytical model of oblique, spinning, on- and off-axis impacts for a racket with six degrees of freedom. The model was validated against a statistical model of experimental data, but the validation was limited by experiment measurement error.

Cottey succinctly described a major limitation of the analytical approach to modelling a ball-racket impact in that the complexity of the system would be difficult to rationalise. Both Cottey and Choppin (2008) simplified their models by assuming the racket was a rigid body, which limits the validity of simulated impact. However, Choppin's research highlighted an alternative approach to model development – the statistical modelling of experimental data. He used experimental data to validate his analytical model, and concluded that trends in his experimental data could be used to inform the design of the analytical model. However, this also proved large-scale data collection and statistical modelling a feasible option outright. The major limitation of his research was due to the accuracy in measuring the experimental data. However, the data and model represented a real system, where compromises such as assuming a rigid-body racket do not apply.

To develop a statistical model, the requirements are those of data collection which must represent the system being modelled (e.g. a player swinging a racket and impacting a moving ball). As the complexity of the system to be modelled increases, so does the data required to describe the system. As such, consideration must be given to effort required to collect the data, as the samples may be very large. The development should also include a detailed validation of the model, to measure model output confidence.

2.4 Modelling complex systems

Statistical modelling of complex systems in tennis research has relatively little representation in the literature. This may be a reflection of the requirements to collect sufficiently large quantities of sample data to represent the system being modelled. Bishop (1995) describes the issue of sampling complex systems as '*the curse of dimensionality*'. He describes how increasing the number of 'features' describing a system can increase the performance of a model, but to a point. As the number of features increases, so does the data required to describe the system. For a system of d dimensions split into M divisions, the data, n_{data} required follows the power law:

$$n_{data} = M^d \qquad 2.4$$

For example, a system split into five dimensions, with five divisions per dimension will require 3,125 data points. Adding an additional dimension increases the data to 15,625.

When considering the collection of data from a laboratory-based impact rig, such as in

Choppin (2008), the task can very quickly scale beyond reasonable expectations. However, this assumes the equal division of each dimension is required. Basheer et. al. (2000) describe how clustering techniques can be used to reduce the divisions of a dimension. Instead of using discrete values for a variable, the values can be clustered into categories (e.g. small, medium or large). Bishop also described how real systems tend to behave in predictable ways. He argued that data is not needed at every division of every dimension. Instead, data can be interpolated to fill in any gaps. This can reduce the precision with which data needs to define the system domain.

2.4.1 System domain dimensions

The parameters that define a ball-racket impact system – the dimensions – can be split by the properties inherent to the equipment being tested (i.e. the physical and geometric properties of racket, ball and string) and impact testing variables (i.e. ball velocities, ball spin, impact locations). To model the system, the parameters are categorised as independent inputs or dependent outputs, the latter of which have traditionally been ball rebound velocity and spin (Cottey, 2002, Choppin, 2008), as these form the inputs for the aerodynamics model of *TennisGUT*. Choppin collected sufficient data to describe a system of six independent input parameters and two dependent output parameters (shown in table 2.1) with careful design of a testing protocol to distribute data within the system domain.

Table 2.1 – Choppin (2008) modelled a system domain comprising six independent input parameters and two dependent output parameters.

Input parameters	Output parameters
Inbound ball velocity components (v_{ix}, v_{iy} v_{iz})	Outbound velocity components (v_{oy}, v_{oz})
Impact location components (i_{px}, i_{py})	
Restrictive handle torque, T	

A statistical model of the ball-racket system needs appropriate data to establish the relationships between the inputs and outputs (model training), facilitating better predictions. Cottey (2002) described how a greater number of input dimensions would be required to better simulate ball-racket impacts. As such, the input dimensions need to be selected carefully. More dimensions could produce a more powerful model, but need more data to adequately describe each dimension (Bishop, 1995).

The aim of this project is to develop a statistical model of oblique, spinning, on- and off-axis impacts, which should simulate rebound ball velocity and spin rate. Therefore, the input dimensions must include inbound ball velocity, spin and impact location on the racket and output dimensions must include rebound ball velocity and spin – the impact testing variables as described at the beginning of this section.

Select physical and geometric properties of the racket, ball and stringbed have been included as model inputs in previous work (Cottey, 2002, Goodwill, 2003 and Choppin, 2008). These models were attempting to simulate the impacts for of a variety of equipment properties. A statistical modelling approach could incorporate these properties if the variables are included as dimensions of the system domain. For example, to establish the relationships between racket mass and ball rebound would require testing several rackets of different mass. However, this primarily requires the necessary test equipment and methods to collect the impact testing variables.

To develop the test equipment and methods and collect a dataset to develop a statistical model, the physical and geometric properties of the racket, ball and strings will be discounted as system dimensions. This will be achieved by collecting data with a single variant of each. This limits the model to restricted simulation of the chosen inputs and outputs. However, if this project is successful, the inclusion of additional dimensions describing physical and geometric properties of the racket, ball and strings can be added by simply collecting more data.

Ultimately, the model could describe a very complex system, if sufficient data is collected. However, this is only possible if the equipment and methods to collect an initial data sample are successful.

2.4.2 Statistical modelling methods

Basheer (2000) describes how neural networks have increased in sophistication and are powerful tools to model complex systems. However, the literature succinctly describes the complexity of such tools. Kirk et. al. (2007) used a neural network to describe the interactions of studded footwear on sports pitches. They concluded the network managed to predict experimental data to within 10%, but the experimental data was limited.

Kirk et. al. described the need for multiple, exclusive datasets to train, validate and test the models. The training and validation data were used to ensure the neural network described the underlying function of the data and not over-fit the noise of the data. In their study, they justified three datasets of equal size. However, Choppin (2008), used a single dataset to train and validate multi-variate polynomial regressions. He justified the use of polynomial regressions, as the methods are relatively simple, but still a powerful tool to model complex data. Choppin used multiple rounds of training and testing to evaluate model fit and estimation error using the '*n-fold and leave one out cross-validation*' method (Kohavi, 1995). This allowed for a comprehensive validation. His models of a complex dataset allowed for the effects of individual inputs on individual outputs to be established.

2.4.3 Modelling summary

Previous research suggests statistical modelling techniques could be a viable alternative to analytical models, to describe the underlying relationships within complex systems. Sufficient data to describe a system is a key requirement, and a possible limitation of the approach, as the amount of data required grows exponentially with increasing system dimensions. Careful design of testing protocols to generate the data is paramount. The parameters of a ball-racket impact include physical and geometric properties of the equipment, as well as impact testing variables. Using single variants of equipment removes the associated dimensions, but these variables should be considered for ongoing testing to increase the sophistication of the models. Neural-networks and multivariate polynomial regression tools have been used to analyse sport equipment performance data. The latter has used to model ball-racket impacts. Analysis of impact data with multi-variate polynomial regression should include ball spin, which had previously been excluded. To train, validate and test the models requires multiple, independent datasets.

2.5 Impact rigs

The objectives of an impact rig are to facilitate data collection on a large scale, whilst replicating realistic conditions, with oblique, spinning, on- and off-axis impacts. This requires consideration of ball launch, racket positioning and racket clamping. Impacts on and off the longitudinal axis of a tennis racket increase the complexity of the test setup, as the racket response will influence the rebound of the ball.

2.5.1 ITF Racket Spin Rig

The ITF's Science and Technical department uses the *Racket Spin Rig* (see figure 2.1) to measure the spin generating properties of strings (Goodwill et. al., 2006). Using a modified BOLA ball launch device (BOLA, 2008), tennis balls are fired at an oblique angle onto a head-clamped tennis racket. The validity of launching a ball onto a stationary racket has been covered by many authors (e.g. Brody, 1997, Brody et. al., 2002, Goodwill, 2002, Choppin, 2008) using a simple frame of reference transformation. The benefit of a stationary racket is the simplification of laboratory based experimentation. The BOLA can launch balls at a range of velocities and spin rates, allowing for several inbound conditions to be tested. The racket is head-clamped to isolate spin generation to the strings only. This set up is a useful starting point to design a new impact rig, as testing is relatively quick. However the racket clamping conditions will need to be modified.

2.5.2 Clamping conditions

Much research has been published to argue the clamping conditions of the racket. On-axis impacts can be simplified to a freely suspended racket; as the transverse mode of vibration generated by the force impulse of ball impact has insufficient time to propagate the full length of the racket and back, before the ball has left the string bed (Hatze, 1976, Watanabe et. al., 1979, Elliot, 1982, Gabiner et. al., 1983, Liu-King, 1983, Missavage et. al., 1984, Cross, 1998, Maeda at. Al., 2002). Ball impact times have been measured from approximately 4 ms to 7.5 ms, depending on the initial ball speed. Cross (1998) measured the propagation time of the force impulse from the centre of the stringbed to the end of the handle as approximately 6.5 ms, meaning a 13 ms period before the force impulse returns to the ball impact location.

Racket clamping conditions will be an important consideration to replicate realistic off-axis impacts. Watanabe et. al., (1979) measured differences in the COR for ball impacts off the longitudinal axis for freely suspended and handle clamped rackets. For an off-axis impact, a torsional mode of vibration is generated by the torque impulse. Kanda et. al. (2002) measured the 1st torsional mode of vibration for a modern tennis racket as 450 Hz, which would be damped by a ball impact of 5 ms. However, this relatively high frequency vibration illustrates the higher torsional stiffness of the racket, when compared to the 1st bending mode of modern rackets (up to 200 Hz). The higher frequency torsional mode suggests the racket will twist about the longitudinal axis during an impact. Therefore, the clamping conditions must allow the racket to twist about this axis, thereby influencing ball rebound.

In real-play, a constraint on the torque impulse is generated by the player's grip, which will need to be replicated by the clamping conditions in the laboratory setup. As previously mentioned, Choppin (2008) developed an impact to measure complex ball-racket interactions using high-speed cameras to track ball and racket (see figure 2.7). The racket was realistically supported using a clutch device to provide a restriction to the generated torque impulse from off-axis impacts.

2.5.3 Impact rig conclusions

The *Racket Spin Rig* and impact rig used by Choppin (2008) present suitable starting points to develop an impact rig. The BOLA ball launch device has sufficient capacity to launch balls at varying velocities and spin rates, however the accuracy and repeatability of this device is unknown. This will influence the process of data collection. The torque-limiting clutch device used by Choppin is a novel method of replicating a human grip, and could be incorporated into a racket clamp that facilitates ball impacts at multiple impact locations. The objectives of the impact rig are to replicate realistic shot conditions and facilitate the collection of large datasets with multiple variable input parameters.

2.6 Impact data collection

To collect data from the impact rig, the ball and racket will need to be tracked over many impacts, with analysis outputting test parameters (i.e. ball velocities, spin rates and impact locations). In general, the literature shows two of methods to accomplish this goal – commercial systems and bespoke high-speed camera solutions.

2.6.1 Commercial tracking systems

Many commercially available motion tracking systems provide image analysis functionality to track objects. The *CODA* (Mitchell et. al., 2000) and *AS200* (Hofmann et. al., 2006), utilise active markers, whilst the *HiRes* system (Wang et. al., 2000; Wang et. al., 2002) and the *MCU240 ProReflex* (Bassement et. al., 2008), use retro-reflective markers to track an object (figure 2.9).

Figure 2.9 – Examples of retro-reflective markers used by commercial tracking systems.

The traditional retro-reflective spheres shown in figure 2.9 may prove problematic for tracking a racket, with concerns for robust attachment through multiple ball impacts. However, Choppin (2008) successfully attached retro-reflective tape directly to the racket frame to measure racket displacements and orientations in real-play. Whilst

Banwell (2013) attached reflective disks to the racket frame and racket stringbed. This allowed him to measure racket frame and stringbed vibrations using a Laser Doppler Vibrometer. Cordingley (2002) found issues with attaching retro-reflective tape to tennis balls, stating the ball cloth did not provide a suitable surface for marker bonding. He went on to remove the cloth from tennis balls, finding the rubber core offered better adhesion. However, alternative methods are presented to track a ball through an impact, which do not require retro-reflective markers. Therefore, the issue is not considered further in this project.

General purpose motion tracking tools are also available (SIMI, 2008), with markerless tracking is increasingly available. However, these tend to limit analysis to human motion for e.g. biomechanical purposes. The limitation of these systems is the measurement of the specific parameters required for ball-racket impact model. For example, the systems reviewed do not offer ball spin measurement. As such, the initial outlay for acquiring such a system is hard to justify, given the requirement for additional measurement methods.

2.6.2 Bespoke analysis solutions

Increasingly, bespoke two- and three-dimensional videogrammetry solutions are being employed for tennis research. The literature reviewed shows videogrammetry a useful tool for collecting data in both the laboratory setting or in the field. For example, Cordingley (2002), Cottey (2002), Goodwill (2002), Choppin (2008) and Sissler (2011) used high-speed video cameras to measure ball velocities and spin rates and ball-stringbed interactions for ball-racket impacts in the laboratory. The data from these experiments was used to validate analytical and finite-element models. Goodwill et. al. (2006) used a high-speed camera, filming at 1,000 frames per second, to measure ball velocities and spin rates, for planar ball impacts onto a head-clamped racket. The laboratory set up meant the camera image resolution could be cropped (typically 512 x 512 pixels) to capture only the necessary field of view containing the ball trajectory. In each of these cases, a single camera measured ball velocities in a single plane. Kelley (2011a) used a high-speed camera to measure ball velocities and spin rates, but for real-play environments (figure 2.10). His method used a frame rate of 1,000 frames per second, using the full resolution of the cameras (typically 1280 x 800 pixels). This maximised the field of view to capture a wide range of ball trajectories. His method included velocity estimation when the ball trajectory was out of plane. Dunn (2014) developed two-dimensional player tracking in tennis from a single, high-definition camera filming at 50 frames per second, while Elliot (2015) used single camera racket silhouettes to estimate three-dimensional positions.

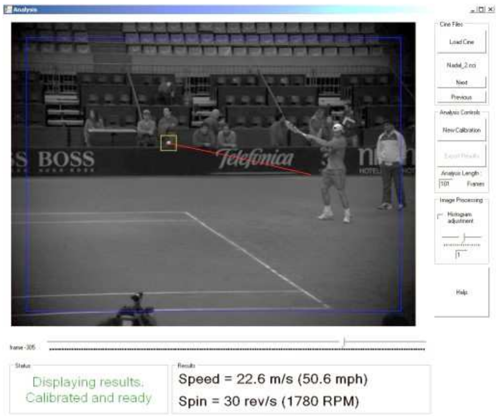

Displaying results.
Calibrated and ready

Speed = 22.6 m/s (50.6 mph)
Spin = 30 rev/s (1780 RPM)

Figure 2.10 – Kelley (2011a) developed a methodology to measure ball velocities and spin rates from single high-speed videogrammetry of real-play in tennis.

Two, synchronised cameras allows for three-dimensional analysis. As mentioned previously, Choppin (2008) used two high-speed cameras and set up a calibrated volume, in which three-dimensional ball and racket motions could be captured (figure 2.11).

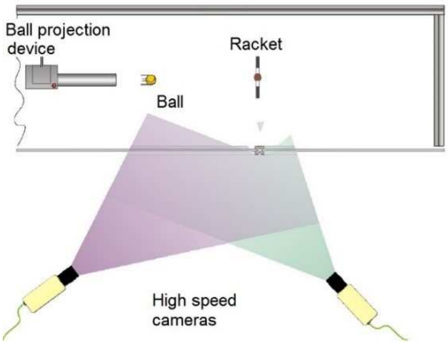

Figure 2.11 – Two, synchronised high-speed cameras can be used to capture ball and racket motions in three-dimensions.

The benefit of bespoke analysis solutions using high-speed cameras is the analysis tools can be tailored to the specific needs of the project. For the laboratory based experiments (e.g. Goodwill et. al., 2006), the test environment can also be adapted to facilitate image digitisation. However, Kelley (2011a) and Dunn (2014), successfully implemented ball tracking in less controlled, real-play environments.

2.6.3 Number of high-speed cameras

The previous examples show that high-speed cameras can be used in conjunction with an impact rig to capture ball-racket impacts. The number of cameras required is dependent on the motions of the objects to be tracked. In Goodwill et. al. (2006), the experimental setup needed only a single camera, as the ball remained in a single plane pre- and post-impact on the head-clamped racket. Choppin's (2008) research suggests impacts onto a realistically supported racket result in out of plane ball trajectories (figure 2.12). In this situation, a single camera would be insufficient to capture the true motion of the ball.

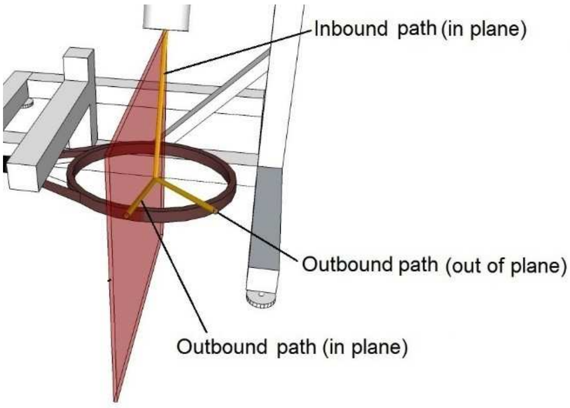

Figure 2.12 – Ball trajectories for impacts onto a realistically supported racket may result in out-of-plane trajectories.

For his research, Choppin used a camera calibration technique to create a test volume in which digitised image coordinates could be reconstructed into real-world three-dimensional coordinates, relative to a defined origin.

2.6.4 Camera calibration

To calibrate two high-speed cameras for three-dimensional measurement, Abdel-Aziz et. al., (1976), Elliot et. al. (1986), Papadopoulos et. al., (2000) and Bray et. al., (2006) used the direct linear transformation (DLT) method. However, Choppin et. al. (2005), Choppin et. al. (2006) and Choppin (2008) used the planar method of camera calibration (Zhang, 1999) using a checkerboard and a MATLAB toolbox (Strobl et. al., 2007). Both methods require a calibration object to provide known points from which a calibration model can be calculated (figure 2.13).

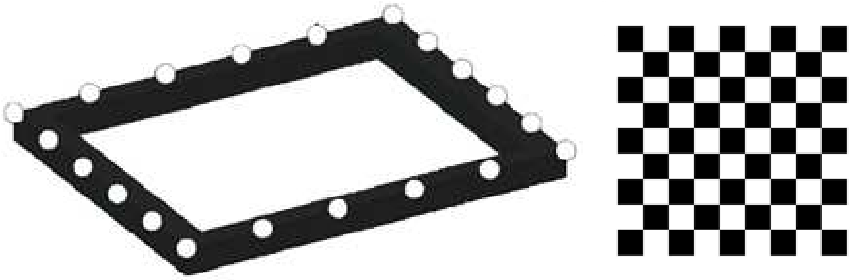

Figure 2.13 – Examples of a calibration frame for DLT method (left) and a checkerboard pattern for planar method (right) of camera calibration

Choppin (2008) evaluated the two-methods by comparing the measurement of reconstructed points of known positions. Figure 2.14 shows the mean and maximum errors for the three-dimensional reconstruction of the known points.

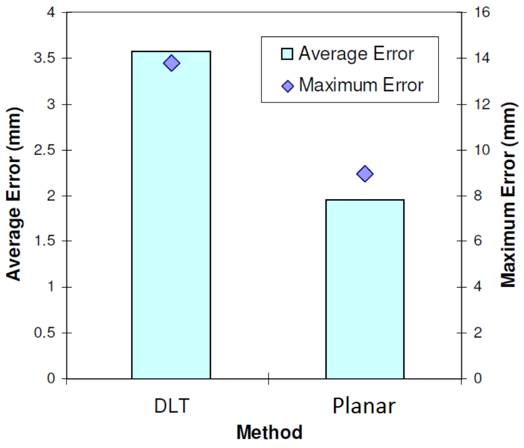

Figure 2.14 – Choppin (2008) measured reconstruction errors with the DLT and planar methods of camera calibration. The planar method had lower mean and maximum errors.

The larger errors of DLT method were attributed to an inaccurate calibration frame, which are innately difficult to manufacture to high-precision. Choppin concluded the planar method was more accurate and more practical. The checkerboard was easier to construct, with a greater number of points to generate camera calibration parameters. The checkerboard was also easier to scale to the size of control volume, which ensured points were collected across the entire control volume.

The planar method produces intrinsic and extrinsic camera parameters. The intrinsic parameters describe, and can be used to correct for, image distortions due to the lens (radial distortions) and camera (tangential distortions). The extrinsic parameters allow for pairs of image coordinates to be reconstructed to three-dimensional real-world coordinates. Reconstructed data can be transformed to a local, defined origin system within the control volume. The calibration parameters are equipment (e.g. camera) and set up (camera position) specific. These must be evaluated prior to use, to ensure the optimum parameters are used.

2.6.5 Impact data collection conclusions

The literature showed commercial and bespoke solutions have been used to collect data. In general, commercial packages offer complete solutions, whilst bespoke solutions, using high-speed cameras, have been successfully implemented in many tennis research projects. The benefit of a bespoke solution is that the final system is tailored to the research.

The use of one and two camera set ups were reviewed. Impacts onto a head-clamped racket required only a single camera to capture planar ball movements. Impacts onto a realistically supported racket required two cameras to capture out-of-plane ball trajectories, in three-dimensions. For this, the cameras can be calibrated using the planar method of camera calibration to define a control volume. Objects within the images can be digitised and the image coordinates reconstructed to a defined origin within the control volume. Given the requirements to collect significant amounts of impact data, emphasis is placed on robust and efficient analysis of the impact test images. The next section looks at literature covering image processing and analysis techniques.

2.7 Image processing and analysis

Digitisation is the measurement of image coordinates and a commonly used tool to extract point information from images. Combined with appropriate calibrations, image coordinates can be reconstructed to real-world measures of position, thus allowing the calculation of displacements, velocities and accelerations. Image calibration requires an object of known length (gauge length) to calculate a calibration factor. Examples of different calibration objects are presented by Cottey (2002), who used a checkerboard with squares of prescribed size, Goodwill et. al. (2006), who used two reflective spheres placed at known separation onto an aluminium bar, and Kelley (2011), who used a tennis ball of estimated diameter.

Manual digitisation has been used by several authors, typically using high-speed imagery to capture ball, racket and stringbed movements. Cottey (2002) used a *Sensicam* to generate a single image of a ball moving towards a racket, using multiple exposures. From this, he manually digitised ball centroids and reference lines added to the ball to calculate ball velocity and spin rate. Cottey used a second high-speed camera to film ball-stringbed interactions, manually digitising the images to measure ball contact lengths and string movements. Cordingley (2002) and Sissler (2011) both digitised high-speed camera images of ball impacts to measure the deformation of ball impacts a rigid plate. In these examples, manual digitisation was a valid process to measure the necessary data, however digitising multiple points through many images is time-consuming and prone to human error. Automated image processing is an efficient means to solve this issue, but automated measurements should be validated for accuracy. For this project, ball and racket digitisation would allow measurement of ball velocity, spin and impact locations. However, the quantity of testing required to collect data and develop the statistical model places emphasis on the development of automated methods.

2.7.1 Automated ball digitisation

There are several examples of automated tennis ball digitisation – the measurement of the ball centroids. Goodwill et. al. (2006), Choppin (2008), Kelley (2011a), Kelley (2011b) used the MATLAB Image Processing toolbox (Mathworks, 2008) to design algorithms which digitised a ball in images taken from real-play and laboratory environments. The final designs of the algorithms were dependent on the images captured, but in all cases key techniques were used:

Image thresholding

Many of the image processing algorithms of the MATLAB Image Processing toolbox require binary (black and white) images. In the literature examples listed above, the ball images were taken using 8-bit monochromatic high-speed cameras, with 255 shades of grey. Greyscale images can be converted to binary with an image threshold algorithm. The simplest threshold function converts pixels of grey levels below a prescribed value (the threshold) to black, and pixels above the threshold to white. Goodwill et. al. (2006) gave considerations for the implementation of image thresholding in the laboratory setup, whereby the relatively bright tennis ball was filmed against a matt-black background.

Image differencing

To remove unwanted information from an image, a useful technique is to subtract a background image from the test image. Kelley (2011a) used this technique to particular effect when processing images taken from the real-world tennis environment. By ensuring an image prior to the test image was captured, he could remove the background (e.g. the tennis court, spectators etc.) leaving the only the ball. Image differencing is of limited use if image background artefacts are moving, however further image processing tools can be used to remove any remaining noise.

Blob detection

The final stage of digitisation is to digitise the ball centroid. Several methods exist for this. Goodwill et. al. (2006) used a *centre of mass* algorithm, which returned the coordinates of the central pixel of a white 'blob'. Other methods include the *bounding box* method, which returns the central coordinate of a box bounding white pixels. Kelley (2011b), used *Hough transform* method, which can be used to identify common shapes within an image, such as a circular tennis ball.

2.7.2 Ball spin measurement

Several examples of ball spin rate measurements are present in the literature. Several authors describe measurement methods using image processing techniques to digitise and compare ball markings across sequential images. The methods are split between spin rate only and those also measuring spin axis.

Spin rate methods

Goodwill et. al. (2006) measured spin rate for tennis balls impacting a head-clamped racket. Using MATLAB (Mathworks, 2008) image processing techniques, ball markings added to the ball (figure 2.15) were identified in sequential images.

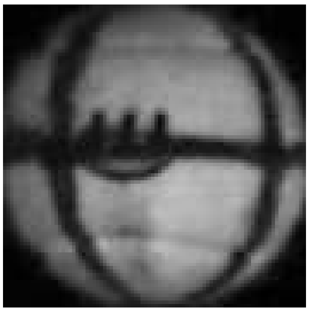

Figure 2.15 – Three mutually perpendicular black lines can be added to a tennis ball to assist spin measurements.

The orientations of the markings were compared for the two images through an iterative process of image rotation. This method assumed the spin axis of the ball remained aligned to the camera axis before and after impact, thereby simplifying the measurement to spin rate only. The method required a large distance between the high-speed camera and impact rig to minimise the camera perspective error on spin rate measurements.

Kelley (2011a) used MATLAB image process techniques to track a tennis ball and identify the ball logo in high-speed camera images of real-play trajectories. As the ball spun, the brightness of the pixels making up the ball dropped when the dark logo faced the camera. Kelley was able to identify the spin rate from a Fourier transform of the brightness measurements. The method was particularly useful for real-play measurements, where the ball cannot be altered. However, the method is reliant on an orientation of spin resulting in the ball logo facing the camera. Research by the ITF (ITF, 2008c) measured a 40% success rate for this method.

Spin rate and spin axis methods

James (2004) used manual digitisation of high-speed camera images to measure the spin rate and spin axis of bowled cricket balls. Reference points added to ball were digitised to determine their three-dimensional position relative to the ball centre (figure 2.16). The spin axis and spin rate were then determined from the direction cosines between the reference points and ball centre (figure 2.16).

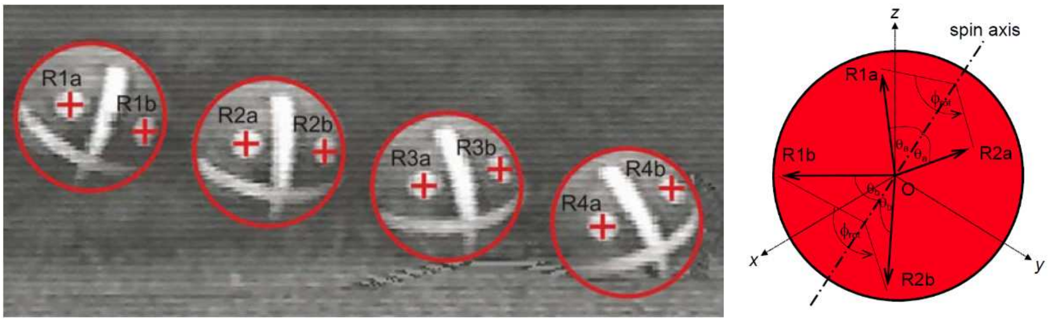

Figure 2.16 – Spin rate and spin axis can be measured from reference points coordinates (left) and directions cosines (right).

Kelley (2011b) developed an automated spin rate and spin axis measurement algorithm, *SpinTrack3D*. The algorithm, based on the methods proposed by Tamaki et. al. (2004), use pattern recognition techniques to compare ball markings in successive image pairs. As with Goodwill et. al. (2006), three mutually perpendicular black lines added to the ball assist measurements. The markings are segmented from the ball and background using image processing. Once segmented, pixel colours (black or white) are inverted to return a binary image as shown in figure 2.17.

Figure 2.17 – The *SpinTrack3D* algorithm inverted the colour of the segmented ball markings resulting in a closely cropped binary image.

The segmented ball marking pixels are then overlaid onto simulated hemispheres of equal radius to the ball. This creates two three-dimensional ball surface models. The *SpinTrack3D* algorithm then applies incremental three-dimensional rotations to the first hemisphere, calculating the axis and angle of rotation to align it with the second hemisphere. Each incremental rotation is scored by counting the ball marking pixels that align. The rotation with the highest score is then output.

Spin axis is reported as a unit vector described by an origin at the ball centroid. The origin is orientated to the camera, as shown in figure 2.18. From the camera perspective, the Y-axis is vertical, X-axis horizontal and Z-axis pointing towards the camera (i.e. a spin axis of [0, 1, 0] is vertical). The angle of rotation for each image pair is measured in radians as a clockwise rotation about the measured spin axis.

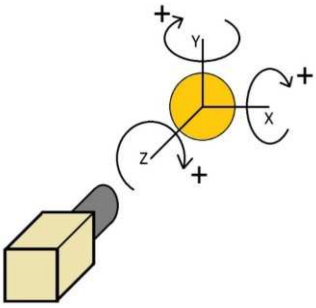

Figure 2.18 – The spin axis was measured to an origin orientated to the camera, with angle of rotation measured clockwise about the spin axis.

As with Goodwill et. al. (2006) method, the distance of the camera relative to ball will influence perspective error. This is an important consideration for implementing a spin measurement method using images from single camera. If the camera to object distance is restricted, causing a meaningful error due to perspective, methods to correct the error will be investigated and implemented.

2.7.3 Impact location measurement

Impact locations are an important measurement for ball-racket impact research. Previous authors have reported the influence of impact location on the rebound characteristics of the ball (e.g. Brody, 1997, Goodwill, 2002, Choppin, 2008). The methods employed generally compare the position of the ball at impact to a reference placed on the racket. However, this requires some consideration for when an impact occurs (e.g. the point of initial contact between the ball and racket, the point of maximum deformation).

Goodwill (2002) used sheets of carbon paper attached to a racket stringbed to measure the accuracy of a ball cannon to impact a defined position. Measuring the impact mark equated to the centre of the ball at maximum deformation. The ITF's *Racket Power Machine* (Kotze, 2005 and Goodwill, 2009) uses a ball dropper and timing gates to accurately drop and time a ball drop onto a rotating racket. The racket motion and position of the ball upon impact replicates a service action. The machine measures the ball drop at two points above the racket, the position of which is continually measured using an encoder. The timing and positional data are used to approximate the initial point of contact between the ball and racket (figure 2.19). Allen (2009) measured impact location measurements with the ITF's *Racket Spin Rig* using ball trajectory data to calculate the ball's position at the instance of contact (figure 2.19).

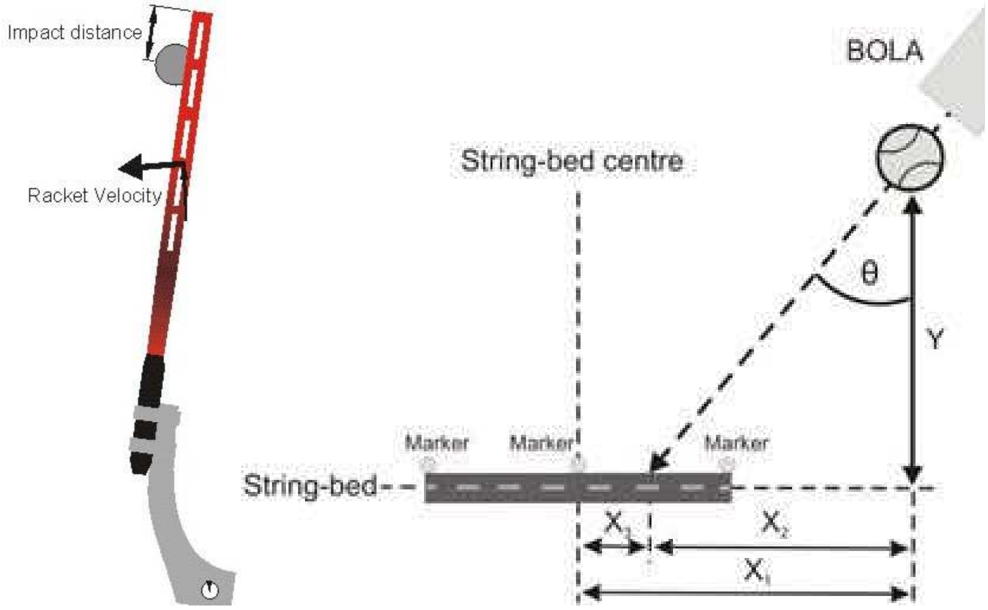

Figure 2.19 – Impact location measurements using the ITF *Racket Power Machine* and ITF *Racket Spin Rig* for the initial point of contact between the ball and stringbed.

The benefit of the latter method – measuring the initial point of contact – is the ball does not need to be digitised through the impact. Accurate digitisation of the ball centroid through the impact would be prone to error, as the ball deforms on the racket stringbed. Therefore, the ball centroid measurements need only be up to the instance of impact.

For reference points to measure the impact location against, Allen (2009) used retro-reflective markers on the racket frame. The markers were relatively secure, as the racket was head-clamped. For real-play measurements and the handled clamped racket test, Choppin (2008) used reflective tape positioned on the racket frame (figure 2.20). The tape was very secure, but required digitisation of non-uniform shapes (i.e. not spherical), which may have introduced some error. The tape was place somewhat arbitrarily on the frame, so Choppin used a racket calibration image to measure the reference points relative to the racket's geometric stringbed centre (figure 2.20).

Figure 2.20 – Choppin (2009) measured impact locations using reflective tape attached to the racket frame as reference points (left). The positions of the reflective tape relatively to the geometric stringbed centre were established from a racket calibration image (right).

2.7.4 Impact testing analysis conclusions

The literature shows that impact testing can be analysed using a variety of image processing methods to digitise high-speed camera images. Several authors have used MATLAB image processing algorithms to automate image digitisation in both the laboratory setting and real-play environments. In the laboratory, considerations can be made to standardise the test environment to assist with designing automated analysis.

Image processing techniques can be used to automatically digitise the ball centroid, which when combined with camera calibration, allow measurement of ball displacements and velocities. Image processing can also be used to measure the spin of the ball. Methods to measure spin rate and spin axis were presented, with the automated method presented by Kelley (2011b) of particular interest.

The literature showed impact locations are either defined at the point of initial contact with the racket or the point of maximum ball deformation. The former requires only ball centroid measurements up to the instance of impact. Measurement during impact requires consideration for ball deformation, which would otherwise reduce the accuracy of digitisation. To act as reference points, reflective markers can be attached to the racket frame. To withstand impacts, non-spherical, reflective tape has been used previously, but the effect on accuracy of digitisation should be considered. To establish the position of reflective markers relative to the racket frame, previous methods used a racket calibration image to establish positions relative to the geometric stringbed centre.

2.8 Literature summary

The ITF's Science and Technical department use a combination of laboratory-based and field-based research to quantify the nature of tennis. The culmination of this research was the development of the tennis simulation software, *TennisGUT.* The software comprises three discrete analytical models, which simulate the three components of a tennis shot: ball-racket interaction, ball flight aerodynamics and ball-surface interactions.

The ball-racket model is the most limited, as simulations are restricted to non-spinning, normal impacts along the longitudinal axis of the racket. Attempts to improve this model have been met with limited success. An analytical model of oblique, spinning, on- and off-axis impacts onto a realistically supported racket showed limited agreement with the statistical analysis of laboratory-based impact data. However, the statistical model offers an alternative approach to model development.

Multivariate polynomial regressions can be used to describe the relationships between multiple input and output parameters. However, multivariate statistical models require large quantities of sample data, to represent the complexities of system being modelled. As the number of dimensions of the system increases, the data required to describe the system increases exponentially. From this, defining the possible parameters and selecting a sub-system of parameters will set an achievable target of data, as well as define a testing protocol to collect the data.

To collect data, laboratory-based impact rigs have been used to replicate realistic conditions under controlled conditions. The ITF's *Racket Spin Rig* is capable of launching balls at varying velocities and spin rates onto head-clamped rackets. However, the accuracy and repeatability of ball launch will influence the design of a testing protocol. To collect impact data for on- and off-axis impacts, the clamp can be replaced with a realistic handle-clamp, including a torque-limiting clutch device to replicate the effect of a human grip in resisting racket rotations for off-axis impacts.

High-speed cameras can be used to film the impacts, with two cameras required to measure three-dimensional, out-of-plane ball trajectories. The cameras can be calibrated using the planar method of camera calibration to define a control volume, correct for image distortions and reconstruct digitised coordinates to a defined origin. Given the requirements to collect significant data, automated image processing algorithms to digitise the images can be employed to create efficient analysis methods. Digitising and reconstructing ball coordinates will allow test velocities and impact locations to be measured. Impact locations have been previously measured at the point of initial contact between the ball and racket stringbed. Reflective markers can be added to the racket to act as reference points for impact locations. These markers need to withstand repeated impacts, and accuracy of digitisation should be considered. The position of the markers relative to the racket (e.g. the geometric stringbed centre) requires prior measurement. The *SpinTrack3D* algorithm can be used to measure test spin rates and spin axes. If the distance between the camera and ball is limited, the effects of perspective error on spin measurement must be accounted for. This will require a method to correct for the perspective error.

2.9 Project aim and objectives

This project aims to develop a statistical model of oblique, spinning, on-and off-axis tennis ball impacts with a tennis racket. To achieve this, the following objectives have been set:

- To facilitate large scale data collection, an impact rig will need to be developed. The impact rig must replicate a range realistic shot conditions and allow measurement of ball velocity and spin and impact locations for each impact test.
- To collect impact test data, high-speed cameras will be used to film and analyse each impact. The analysis of the high-speed camera images must be automated, requiring the development and validation of automated image-processing

algorithms. The automated algorithms must be capable of distinguishing between the inbound and outbound trajectories of the ball.

- The system domain of the ball-racket impact system must be defined with dimensions describing independent input variables (ball velocity, spin and impact location) and dependent output variables (ball velocity and spin). To populate the domain an impact testing protocol must be defined, which maps the domain adequately.
- To develop the statistical model, a two-step process of model training and validation and model testing will be used to establish the relationships between the independent input data and dependent output data. The predictive power of the model will be evaluated to establish the success of the model development.

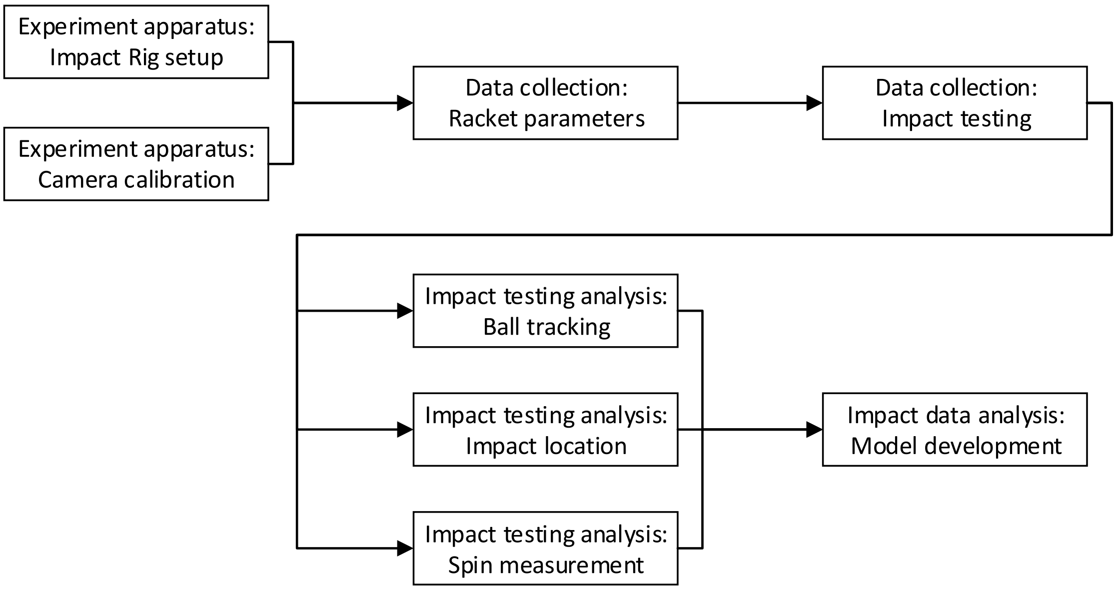

Figure 2.21 – Flowchart outlining the scope of the project.

Chapter 3 - Experiment apparatus

3.1 Introduction

In this chapter, the design of the experimental apparatus are presented. An impact rig was designed to replicate a range of real-play shot characteristics. The impacts were filmed using two high-speed cameras. The flowchart shown in Figure 3.1 identifies the experiment apparatus in relation to the scope of this project.

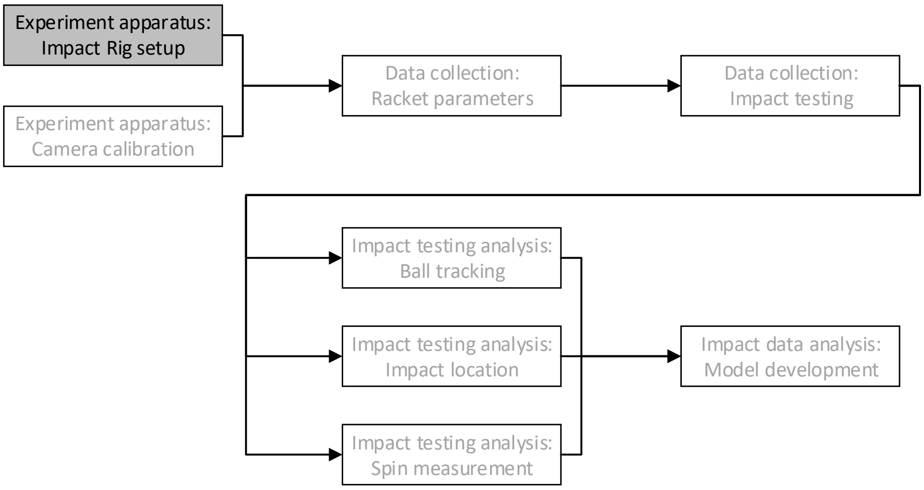

Figure 3.1 – Flowchart outlining the scope of the project. The first part looks at experiment apparatus and the design of an impact rig.

To replicate real-play, mean ground stroke characteristics were calculated from real-play data. From this, the required impact velocities and spin rates and the angle of incidence between the ball and racket were established. The racket was mounted using a racket handle clamp. This clamping condition was shown to have negligible influence on a ball impact (Cross, 1998), as the force impulse generated by an impact has insufficient time to propagate the length of the racket. To replicate a human grip on the racket handle, the clamp included an adjustable torque limiting clutch. This prevented racket rotations about the longitudinal axis when the torque generated by an off-axis impact fell below the set torque limit. This limit was checked using a torque wrench. The mount could be readily moved laterally and longitudinally, to facilitate ball impacts over a range of locations. An extension spring held the racket in place, prior to each ball impact. This design was justified by evaluating the force impulses of a theoretical impact.

A final evaluation was carried out to establish the accuracy and repeatability of the impact rig. This determined the necessary measurements of impact test parameters.

3.2 Objectives

The objectives of this chapter are:

1. To design an impact rig to replicate realistic shot conditions using real-play data.
2. To establish the repeatability of ball launch to determine the required measurements.
3. To determine the number of high-speed cameras required to film the impact tests.

3.3 Impact rig design

The ITF *Spin Rig* (the “Spin Rig”) (figure 3.2) created by Goodwill et. al. (2006) was used as the basis for the impact rig (the “Impact Rig”). The Spin Rig replicated a groundstroke using a BOLA (2008) ball launch device to launch a ball at variable inbound velocities and spins at an oblique angle.

Figure 3.2 – The Spin Rig was the basis for the Impact Rig. The Spin Rig used a BOLA ball launch device to launch a ball with variable inbound velocity and spin onto a head-clamped racket.

3.3.1 Replicating realistic shot conditions

Racket testing in the laboratory is facilitated by transforming the frame of reference of a moving racket and ball, to an initially stationary racket and moving ball (the “laboratory frame of reference"). To replicate realistic shot conditions, real-play data were evaluated to calculate mean ground stroke ball and racket velocities and ball spin rates. The velocities were transformed to the laboratory frame of reference to establish the equivalent impact velocity and the angle of incidence between the ball and racket.

Choppin (2008) measured ground stroke racket and ball velocities during real-play. The mean racket (V_{rX}, V_{rY}, V_{rZ}) and ball (V_{bX}, V_{bY}, V_{bZ}) component velocities for men and women are shown in table 3.1.

Table 3.1 – The mean pre-impact racket and ball component velocities for groundstrokes by men and women, measured at the Wimbledon Qualifying event (Choppin, 2008).

	Mean pre-impact racket velocities (m·s^{-1})			Mean pre-impact ball velocities (m·s^{-1})		
	V_{rX}	V_{rY}	V_{rZ}	V_{bX}	V_{bY}	V_{bZ}
Men	16	6.2	-4.4	-9.3	-0.6	1.1
Women	14.9	5.5	-1.1	-9.3	0.2	0.1

To calculate the relative velocity (V_{tR}) between the ball and racket (the "test velocity"), the component velocities of the racket and ball were combined, as shown in figure 3.3. The resultant velocity was calculated using Pythagoras theorem.

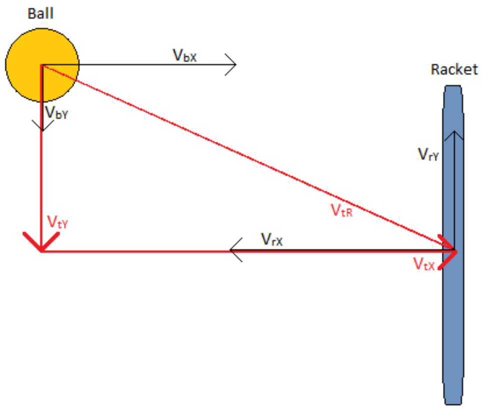

Figure 3.3 – The relative velocities between racket and ball were calculated by combining the pre-impact racket and ball component velocities. The diagram shows a two-dimensional example.

The component (V_{tx}, V_{ty}, V_{tz}) and resultant test velocities calculated from men's and women's mean data are shown in table 3.2.

Table 3.2 – The component and resultant test velocities calculated from the men's and women's data.

	Test velocity (m·s^{-1})			
	V_{tX}	V_{tY}	V_{tZ}	V_{tR}
Men	25.3	6.8	5.5	26.8
Women	24.2	5.7	1.2	24.9

Choppin also measured the angle of incidence (the "playing angle") for ground strokes. The mean and modal playing angles for men and women are shown in table 3.3.

Table 3.3 – The mean and modal playing angles for men's and women's groundstrokes.

	Mean playing angle (°)	
	Mean	Modal
Men	17.8	22.5
Women	18.8	21

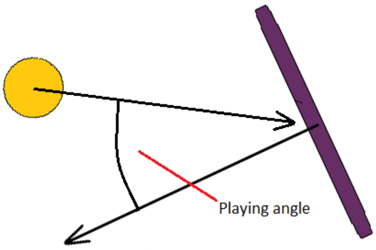

The ITF has collected real-play spin data using Spin Doctor (Kelley, 2011a) since 2007. Table 3.4 shows the mean inbound spin rates for men's and women's topspin ground strokes (the "inbound spin").

Table 3.4 – The mean inbound spin rates for men's and women's ground strokes. The measurements were taken for the ball approaching the racket and filtered to include only topspin shots.

	Mean inbound spin rate (rad·s^{-1})
Men	169.1
Women	209.8

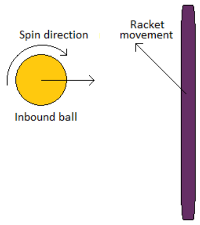

The data in tables 3.2 to 3.4 show that an average ground stroke has a relative inbound ball velocity of 25.0 m·s^{-1}, an angle of incidence of 20° and inbound spin of 200 rad·s^{-1}. The performance of the BOLA was established from research using the Spin Rig (ITF, 2008c) and showed this launch velocity and spin rate to be possible. The BOLA was attached to the Impact Rig with the barrel set to 20° to vertical using a digital spirit level.

3.3.2 Racket mount

The requirements of the racket mount were:

1. Racket support allowing six degrees of freedom – three translational and rotational.
2. Resistance to racket rotation to replicate the effect of a player's grip on the racket handle by restricting racket rotations about the longitudinal axis.

The racket handle clamp used by Choppin (2008) was incorporated into the racket mount. His design used a universal joint and Cross+Morse (2008) M40-3 Torque Limiter to replicate a hand-held condition and allow three degrees of freedom (rotations). A schematic of the handle clamp is shown in figure 3.4.

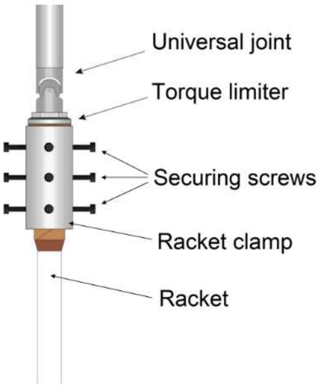

Figure 3.4 – The racket handle clamp used by Choppin (2008). The clamp incorporated a torque limiter to replicate the resistance to racket rotation by the human hand.

The torque limiter restricted rotations about the longitudinal axis of the racket below a specified torque. The torque limit could be set between 3 Nm to 15 Nm by setting a restraining nut. Choppin reported a practical limit for the maximum setting (15 Nm), where rackets failed during his experimental data collection. In light of this, a torque limit of 7.5 Nm was set and tested using a torque wrench. This value was proven to not cause racket failures, whilst being close to the maximum torque limit of 10 Nm for a human grip, reported by Choppin.

The racket handle clamp was mounted to the Impact Rig with an extension spring to hold the racket horizontally (i.e. with the stringbed parallel to the floor). The racket mount can be seen in figure 3.5.

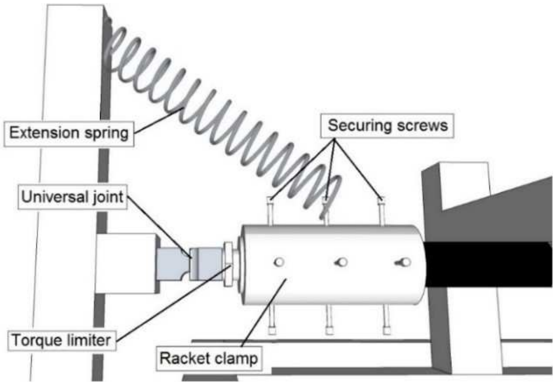

Figure 3.5 – A side view of the racket mount, with the racket handle clamp attached to a vertical post with an extension spring to hold the racket horizontally.

An Ashfield Springs (2008) S.62 extension spring was chosen to provide sufficient lift to hold the racket horizontally. To justify this design choice, the force impulse of a ball impact and the spring were considered. Assuming the racket was a rigid body, the force impulse of ball impact would instantly travel the length of the racket causing a reaction force impulse in the spring, resulting in an external influence on the ball rebound.

The force impulse of the ball, J_b was calculated by:

$$J_b = F_b \cdot t_i \tag{3.1}$$

Where F_b was the force of the ball impacting the stringbed and t_i was the duration of impact of 0.005 s. The resulting force impulse in the spring J_s was calculated by:

$$J_s = F_s \cdot t_i \tag{3.2}$$

where F_s was the reaction force of the spring due to the racket deflecting during the impact.

To calculate J_b the force of the ball impacting the stringbed was calculated using Newton's second law:

$$F_b = m_b \cdot a_b \tag{3.3}$$

where m_b was the mass of the ball (0.06 kg) and a_b was the deceleration of the ball. This deceleration was calculated over half of the duration of impact using:

$$a_b = \frac{v_b}{{t_i}/{2}} \tag{3.4}$$

where v_b was the initial velocity of the ball (25 m·s^{-1}), giving a deceleration of 10,000 m·s^{-2}. Applying this to equation 3.3, the ball impact force, F_b was 600 N. Applying this to equation 3.1, the force impulse of the ball, J_b was 3 N·s.

The reaction force of the spring was calculated using Hooke's law:

$$F_s = k_s \cdot x_s \tag{3.5}$$

where k_s was the spring rate (0.34 N·mm^{-1}, Ashfield Springs, 2008) and x_s was the extension of the spring due to a ball impacting the racket stringbed. To calculate the extension of the spring, the deflection of the racket, d_r was first calculated using:

$$d_r = V_{r_0} t_i + \frac{1}{2} a_r t_i^{\,2} \qquad 3.6$$

where V_{r_0} was the initial velocity of the racket and a_r was the acceleration of the racket. Given the racket was initially at rest, 3.6 simplifies to:

$$d_r = \frac{1}{2} a_r t_i^{\,2} \qquad 3.7$$

The acceleration of the racket was calculated using Newton's second law, rearranged to give:

$$a_r = \frac{F_b}{m_r} \qquad 3.8$$

where m_r was the mass of the ITF *Development* racket (0.330 kg) giving a racket acceleration of 1818.2 m·s^{-2}. Applying this to 3.7 gives a racket deflection of 0.023 m during the 0.005 s ball impact.

Given the racket mounting arrangement (i.e. a pin joint), this deflection would be an arc about the universal joint of the racket mount. As the spring attachment was closer to the universal joint than any point of the racket stringbed, the extension of the spring would be less than the calculated racket deflection. To calculate the spring extension, the racket deflection was assumed for a ball impacting at the geometric stringbed centre. The spring extension, x_s was calculated by considering concentric circles:

$$\frac{d_r}{2 \cdot \pi \cdot R_{GSC}} = \frac{x_s}{2 \cdot \pi \cdot R_S} \qquad 3.9$$

where R_{GSC} was the distance from the universal joint to the geometric stringbed centre and R_S was the distance from the universal joint to the spring attachment. Rearranging 3.9 gives:

$$x_s = \frac{d_r \cdot R_s}{R_{GSC}} \qquad 3.10$$

Figure 3.6 shows the distances R_{GSC} and R_s for an ITF *Development* racket.

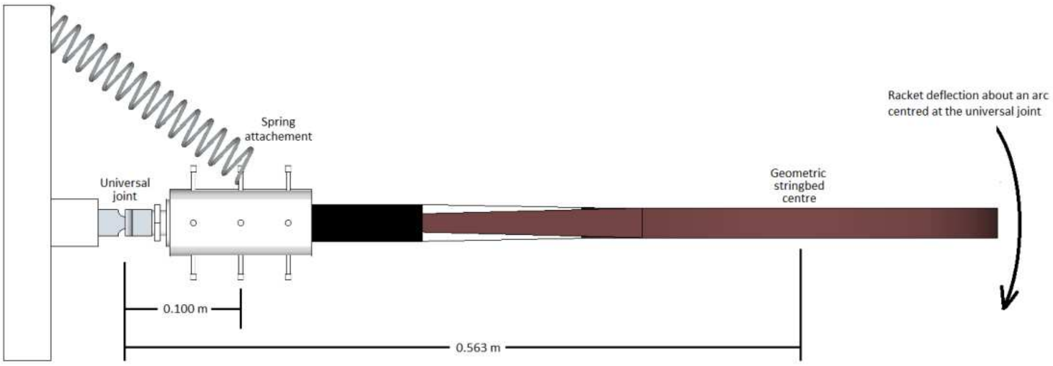

Figure 3.6 – Side view of the racket mount and racket. To calculate the deflection of the spring, the racket deflection was assumed for an impact at the geometric stringbed centre of the racket. The racket deflection was considered as an arc about the universal joint.

The deflection of the spring was calculated at 0.004 m. Applying this to 3.5 gives a spring reaction force, F_s of 1.4 N. Using 3.2 gives a spring reaction force impulse, J_s of 0.007 N·s, or 0.2% of the force impulse of the ball impact. For the rigid body model assumption, this means the spring will have negligible influence on the ball during an impact. For a flexible body racket, the influence of the spring would be even less as the force impulse of the ball impact takes time to travel the length of the racket (Cross, 1998).

The racket mount was positioned under the BOLA as shown in figure 3.7. The mount could be translated by 100 mm longitudinally and laterally. A restraining bar was used to prevent the spring from pulling the racket above horizontal.

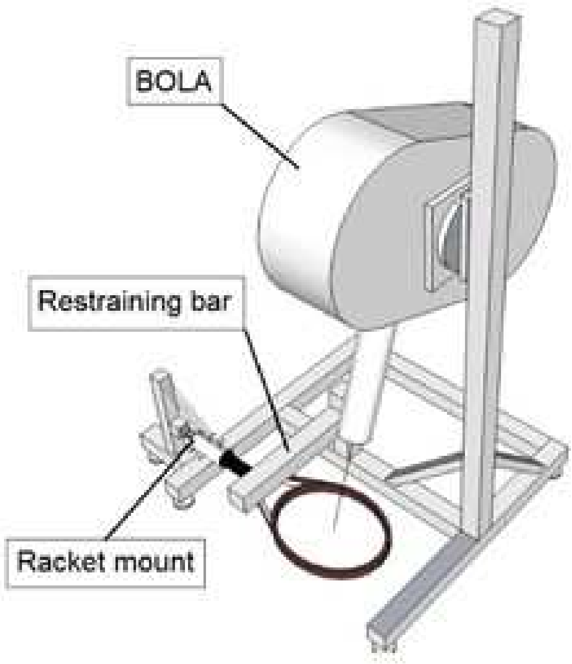

Figure 3.7 – A visualisation of the Impact Rig showing the BOLA, racket mount and restraining bar. The racket mount was attached to position the racket under the BOLA.

3.4 Ball velocity and spin rate repeatability

Previous use of the BOLA had established low repeatability of the launch velocity and spin rate (Goodwill et. al 2006, ITF, 2008c). For testing with the Spin Rig, a high-speed camera was used to film each impact. Automated image processing algorithms measured the inbound and outbound velocity and spin. The algorithms require the spin axis of the ball to be parallel to the longitudinal axis before and after impact in order to measure spin rate. Although spin axis is not measured, given successful use of the software, the spin axis is assumed to have this orientation. As such, the spin is either pure topspin or backspin. However, there is no data to assume this case for impacts onto a realistically supported racket.

Methods were developed to measure the inbound and outbound velocity, spin rate and spin axis of the ball for each impact. This is discussed in Chapter 8. A test protocol was developed using a range of inbound ball velocities and spin rates, including those describing the typical groundstroke, reported in tables 3.3 and 3.4. By using a range of velocities and spin, the system domain was suitably described to model a variety of real-play groundstrokes. This is discussed further in Chapter 9.

3.5 Impact location repeatability

The repeatability of impact location was measured to determine if a direct measurement method was required. Goodwill et. al. (2006) used a barrel to improve the accuracy of the BOLA. However, no data exists to quantify ball launch repeatability.

Two barrel designs were tested, the first, used by Goodwill, contained a straight bore with an internal diameter of 80.0 mm – 11.6 mm greater than the largest allowable ball diameter (ITF, 2008a). The larger diameter prevented the ball from jamming but possibly reduced the consistency of ball launch. The second barrel used a tapered bore, decreasing from an 80.0 mm internal diameter to 69.0 mm (shown in figure 3.8). The repeatability of impact location was measured using a simplified Impact Rig set up.

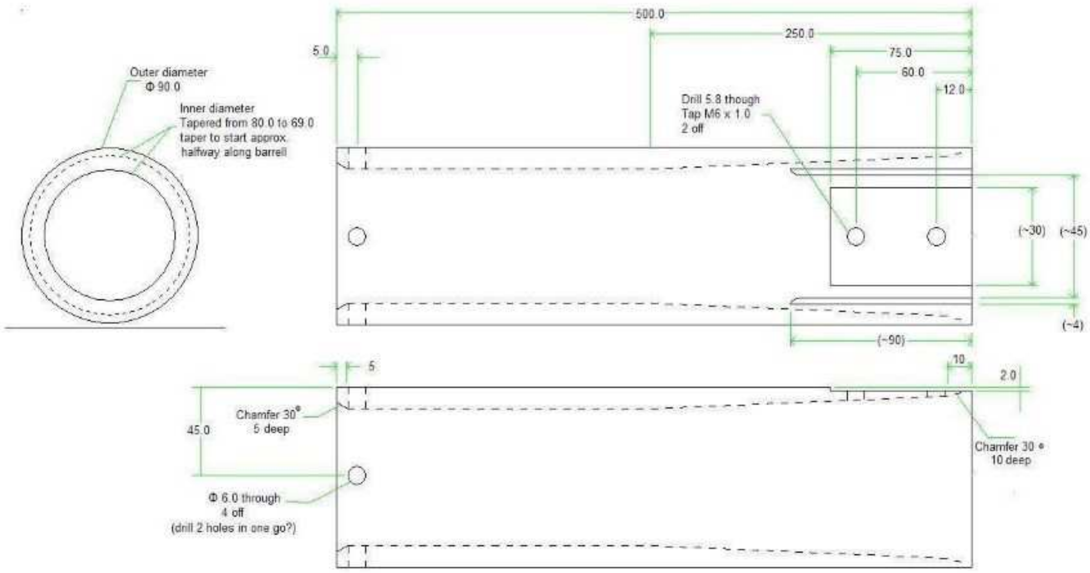

Figure 3.8 – Barrel design: A tapered bore design was tested alongside a straight bore (not shown) to measure the repeatability of impact location. The tapered bore reduced from an 80.0 mm to 69.0 mm internal diameter.

3.5.1 Impact location repeatability method

Impact location repeatability was measured using two synchronised Vision Research Phantom v4.3 high speed cameras. To simplify the experiment, the racket mount was removed from the Impact Rig, with the ball launched directly onto the floor. Figure 3.9 shows the camera positions, with four 500 W halogen lamps used to illuminate the test volume. The cameras were connected to a photodiode trigger mounted to the barrel.

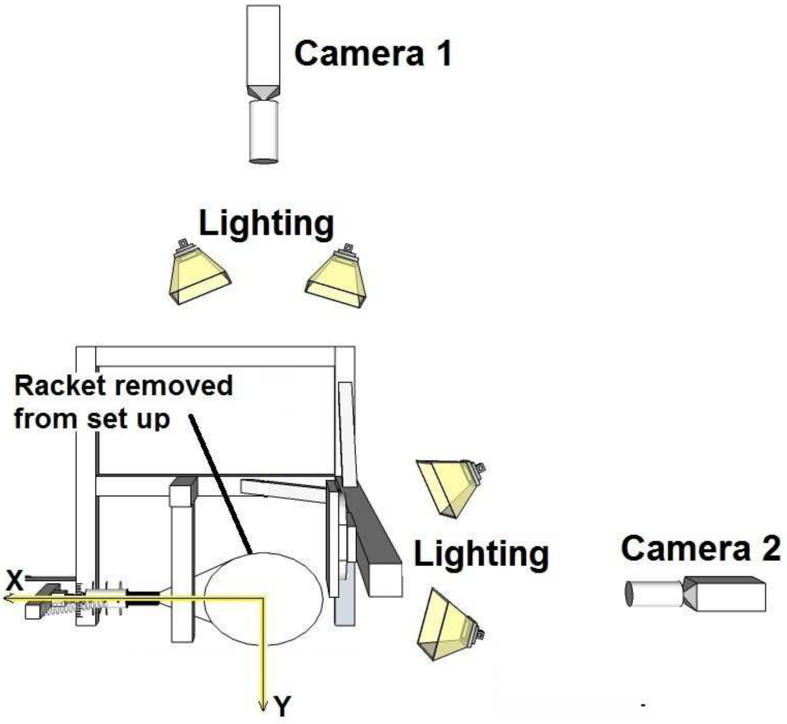

Figure 3.9 – A plan view of the set up used to measure the repeatability of impact location. The racket was removed for the BOLA (not shown) to launch balls directly onto the floor. Impacts were capture with two synchronised high-speed cameras, with lighting to illuminate the test volume. Measurements were made relative to a local coordinate systems.

The planar method of camera calibration (described in the literature review and Chapter 4) was used to create a 0.5 m^3 calibrated test volume. The calibration images were automatically digitised using *Check3D* (2012), which generated the intrinsic and extrinsic camera parameters to reconstruct image (*u,* v) coordinates into three-dimensional real-world (*x, y,* z) coordinates. The (*x, y,* z) coordinates were calculated relative to a defined local coordinate system within the test volume.

To define the local coordinate system, images of a checkerboard placed onto the floor were captured with both cameras. Three checkerboard intersections were manually digitised to define an origin and X- and Y-axes. *Check3D* automatically calculated the mutually perpendicular Z-axis as shown in figure 3.10. The checkerboard was positioned to approximately align the X- and Y-axis with the longitudinal and transverse axis of a racket shown previously in figure 3.9.

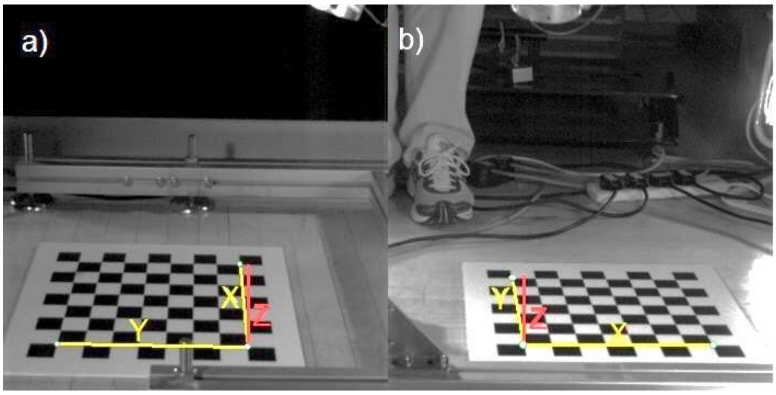

Figure 3.10 – Using *Check3D* to calibrate the left (a) and right (b) high-speed cameras and define a test volume. A local axis system was defined from a checkerboard imaged on the ground. Three manually digitised checkerboard intersections defined the origin and X- and Y-axes (yellow) and Z-axis (red)

In total, 60 impacts were captured with each barrel. The BOLA velocity setting was set to launch the ball at approximately 25 m·s^{-1}. The spin setting was increased in four stages to impart between zero and 400 rad·s^{-1} of backspin onto the ball. The BOLA was assumed to perform as previously used (Goodwill et. al., 2006, ITF, 2008c) with velocity and spin rate ranges of ±2 m·s^{-1} and ±40 rad·s^{-1}, respectively. Vibrations and recoil from launching the ball could have caused the BOLA and barrel to move between ball launches, thereby decreasing repeatability. It was assumed the any such movement would be minimal, given the weight of the Spin Rig frame and BOLA.

Check3D was used to manually digitise the ball and reconstruct the (*u, v*) coordinates relative to the local coordinate system. Impact locations were measured from the frame of initial contact between the ball and ground. An example of the digitisation process is shown in figure 3.11.

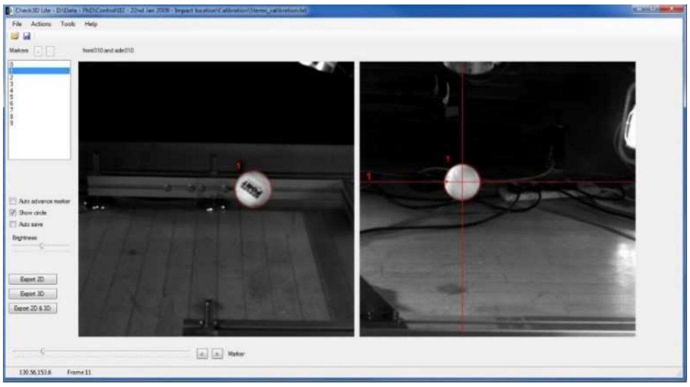

Figure 3.11 – *Check3D* was used to manual digitise the ball locations in each camera image and reconstruct the (*u, v*) coordinates into (*x, y, z*) coordinates relative to the local coordinate system.

3.5.2 Impact location repeatability results

Figure 3.12 shows the impact positions measured from the 60 shots fired through the Spin Rig and tapered barrels.

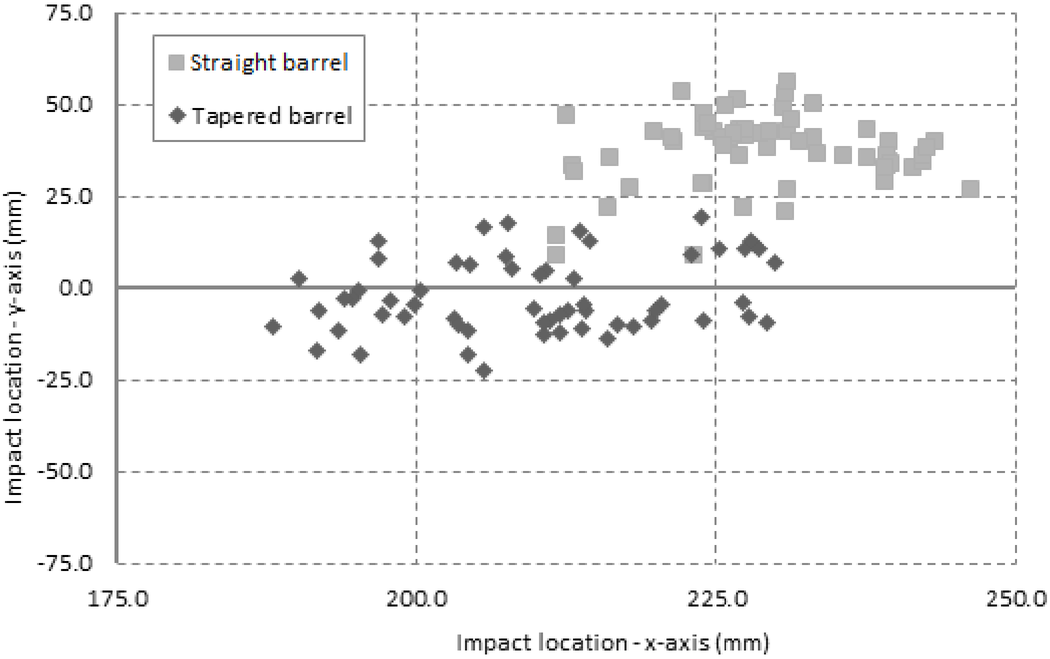

Figure 3.12 – A scatter plot showing the impact locations measured for balls launched with the straight and tapered barrels.

Table 3.5 shows the means and standard deviations for the X and Y components of the impact locations measured with each barrel.

Table 3.5 – The means and standard deviations for the X and Y components of the impact locations measured with the straight and tapered barrels.

	Straight barrel		Tapered barrel	
	X	Y	X	Y
Mean impact position (mm)	229.0	37.0	209.6	-2.2
Standard deviation (mm)	8.5	9.2	11.7	10.2

The data shows that impact locations measured for the straight barrel had a lower standard deviation in both axes compared to the tapered barrel. However, the repeatability for either barrel was low. It was hypothesised that impact location would influence the rebound trajectory from a realistically supported racket. Given the standard deviations for either barrel, a method was developed to measure impact locations for each impact. This is discussed in Chapter 7.

3.6 High-speed camera requirements

The number of cameras to fully capture ball trajectories was determined through experimentation. Goodwill et. al. (2006) required a single high-speed camera, as the inbound and outbound trajectories for impacts onto a head-clamped racket remained in plane. This reduced the component of ball velocity perpendicular to that plain to zero. However, no data exists to assume the same for ball impacts onto a realistically supported racket. If not, two high-speed cameras would be required to measure out-of-plane trajectories.

3.6.1 In-plane trajectories method

Using an ITF *Development* racket mounted to the Impact Rig, ball impacts were filmed using a single Phantom v4.3 high-speed camera to assess the outbound trajectories. Figure 3.13 illustrates the orientation of the camera relative to the Impact Rig, with two 500 W halogen lamps illuminating the test volume. The camera was positioned behind the BOLA with the optical axis aligned with the barrel using a rotating Laserliner (2010) Automatic Level. A frame rate of 1000 frames per second and exposure time of 200 µs were used. The camera was connected to the same photodiode trigger used in section 3.5.

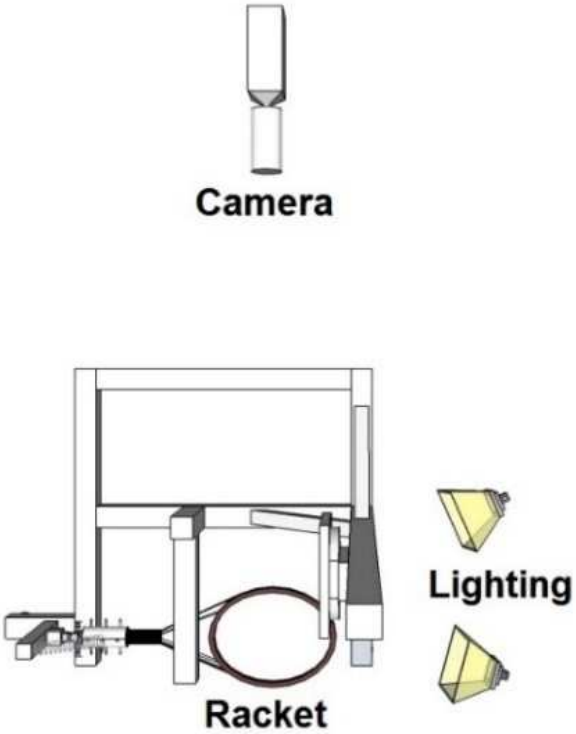

Figure 3.13 – To investigate the planarity of ball trajectories, a single high-speed camera was positioned behind the BOLA (not shown), with lighting to illuminate the test volume.

A plumb-line was attached to the bottom edge of the barrel, with two reflective markers spaced at 550 mm apart to provide a vertical datum and calibration factor (figure 3.14).

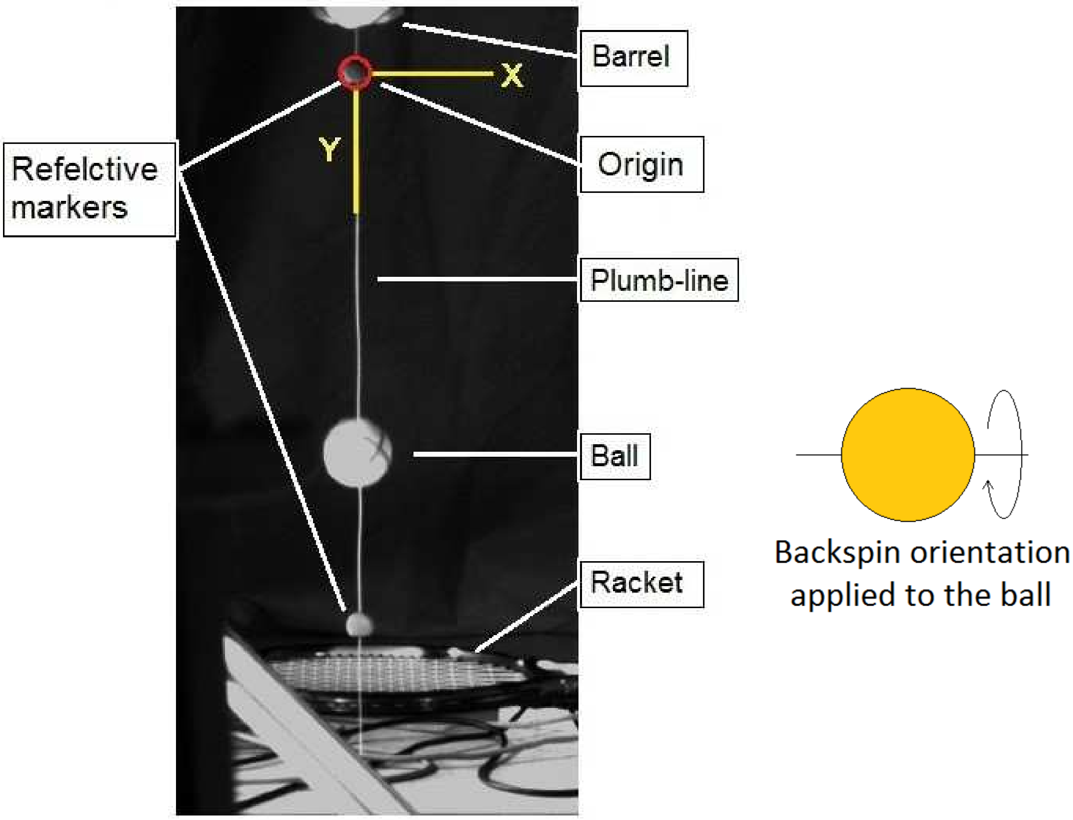

Figure 3.14 – From the cameras view, a plumb-line established a vertical datum and calibration factor for the test images. The ball was launched with increasing backspin.

In total, 20 impacts were captured with each barrel. The BOLA velocity setting was set to launch the ball at approximately 25 m·s^{-1}. The spin setting was increased in four stages to impart between zero and 400 rad·s^{-1} of backspin onto the ball.

Check2D (2008) was used to manually digitise the reflective calibration markers and the ball in each test. The start of an outbound trajectory was defined as the frame in which the ball was observed to move upwards in the image. For each impact, 12 frames of the outbound trajectory were digitised.

3.6.2 In-plane trajectories results

Figure 3.15 shows 1st order regressions fit to the digitised ball data of each outbound trajectory.

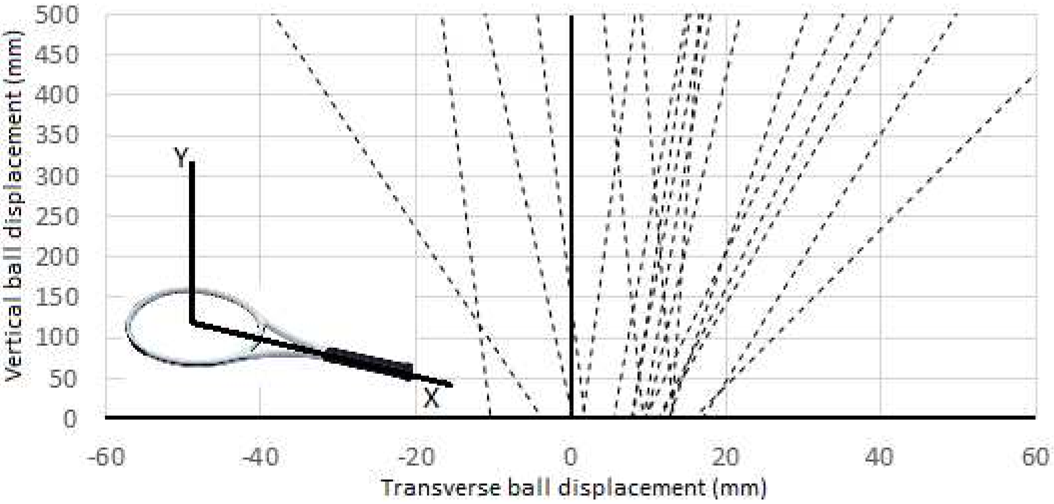

Figure 3.15 – A graph showing 1st order lines of best fit of 20 manually digitised outbound ball trajectories. Each impact had approximately 25 m·s^{-1} inbound velocity and zero to 400 rad·s^{-1} of inbound backspin.

The results show that the outbound trajectories of the ball were not in-plane for impacts onto the realistically supported racket. Simple linear regressions were sufficient to illustrate this point. Therefore, two high-speed cameras were required to film impact testing with the Impact Rig to measure the ball trajectories in three-dimensions.

3.7 Conclusions

This chapter describes the design of the Impact Rig to impact tennis balls onto a realistically supported tennis racket. To replicate real-play, ball velocities and the angle of incidence were determined to be representative of real-play. The racket position could be adjusted to test at multiple impact locations on the racket stringbed. The Impact Rig was based on the ITF Spin Rig, using a BOLA ball machine to launch balls at an oblique angle onto a horizontally mounted racket.

To replicate realistic shot conditions, data from real-play was evaluated to establish average groundstroke characteristics – the relative ball to racket velocity, the inbound ball spin rate and the playing angle. From this evaluation, the BOLA was set to launch balls at 20° to vertical. The mean velocity and spin would be included in the design of a testing protocol, which is discussed in Chapter 9.

The racket mount used a torque limiter to replicate a human grip on the racket handle by restricting rotation about the longitudinal axis. A torque limit of 7.5 Nm was set using a torque wrench. An extension spring was used to hold the racket horizontal (i.e. stringbed parallel to the floor). The reaction force impulse in the spring caused by a ball impact was calculated to be negligible and therefore unlikely to influence the outbound characteristics of the ball. The racket mount was positioned underneath the BOLA and could be adjusted to change impact location.

The BOLA was evaluated to assess the repeatability of the launch velocity, spin and impact location. Low ball velocity and spin repeatability were established from previous use of the BOLA with the Spin Rig (Goodwill et. al 2006, ITF, 2008c). Low impact location repeatability was measured from an investigation using two barrel designs. It was determined that the low repeatability required methods to measure ball velocity, ball spin rate and spin axis and impact location for each test.

A final evaluation measured the planarity of outbound ball trajectories from impacts onto a realistically supported racket. The results showed that two synchronised high-speed cameras would be required to capture the trajectory of the ball in three-dimensions.

The design of the Impact Rig fulfils the first aim of this project, by replicating realistic shot conditions and facilitating the collection of large datasets with multiple variable parameters. The range of measureable test parameters (i.e. ball velocities, spin rates and impact locations) allows for the creation of a broad, multi-dimensional dataset with which to create statistical models. The design and validation of the methods to measure the test parameters are covered in the proceeding chapter. The next chapter describes the camera calibration process.

Chapter 4 – Camera calibration

4.1 Introduction

The experiment apparatus presented in the previous chapter described the design of the Impact Rig. This chapter describes an evaluation of the planar method of camera calibration, shown in context of the project in Figure 4.1. The calibration method produced the necessary parameters to reconstruct image pixel coordinates to real-world three-dimensional measurements. The evaluation established the best image distortion model for the cameras and lenses used with the Impact Rig. A final evaluation established the error of spatio-temporal measurements using the high-speed cameras and chosen calibration model.

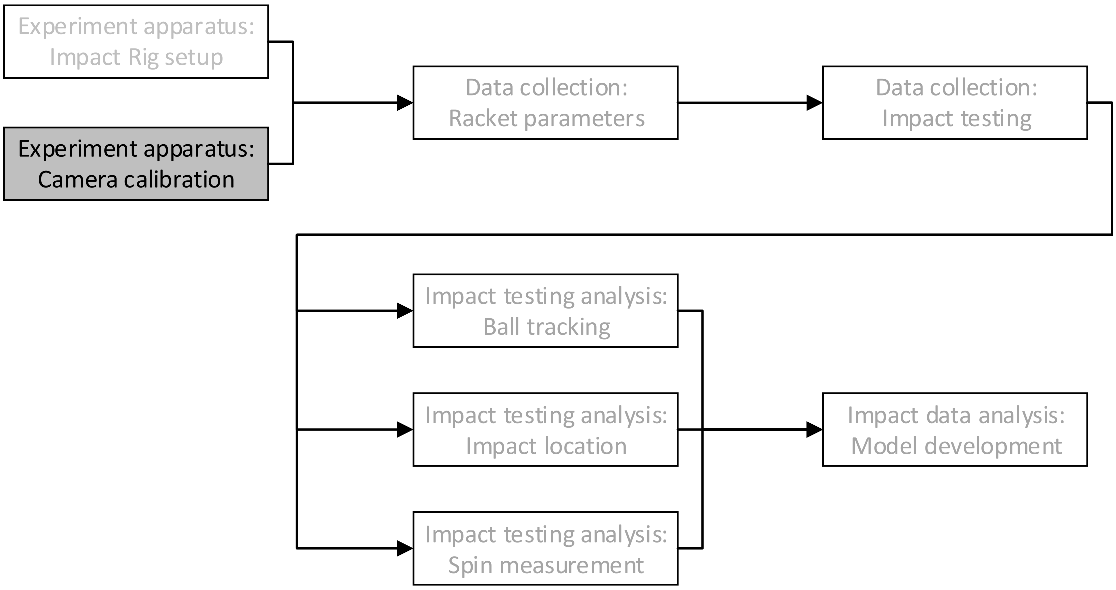

Figure 4.1 – Flowchart outlining the scope of the project. The chapter describes the evaluation of the camera calibration methods used with the Impact Rig.

4.2 Objectives

The objectives of this chapter are:

1. To establish the optimum camera calibration model settings for the equipment and environment specific to the Impact Rig setup.
2. To establish ball velocity measurement error using the camera calibration model.

4.3 Optimum camera calibration model settings

To establish the optimum camera calibration model, the errors in the reconstruction and measurement of a known length were compared for different model settings. The model settings corrected for image distortions caused by the sphericity of the lenses (radial distortions) and the skew of the camera sensor (tangential distortions). Four setting combinations were available:

1. No correction for image distortions.
2. Correction for radial and tangential image distortion.
3. Correction for radial image distortion only.
4. Correction for tangential image distortion only.

To compare the four combinations, a known object was imaged in multiple orientations and positions within a calibrated test volume. The object was manually digitised and the image (*u, v*) coordinates reconstructed to measure the object's length. The mean length calculated using each calibration model was used to compare the four setting combinations. *Check3D* (2012) was used to produce each camera calibration model, manually digitise the images and reconstruct the (*u, v*) coordinate data.

4.3.1 Calibration object

The calibration object comprised two squash balls attached to both ends of a length of a plastic rod. The round shape allowed for accurate digitisation of the squash ball centroids, from any orientation. Each squash ball was coated with white matt paint, to ensure good contrast against the relatively dark background of the test volume (figure 4.2).

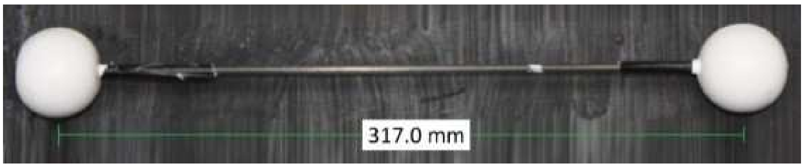

Figure 4.2 – The calibration object comprised two squash balls coated in white paint attached to both end of a plastic rod. The distance between the squash ball centres was 317.0 mm.

The distance between the centres of the squash balls was measured using a high-resolution image taken with a Canon *EOS 450D* digital SLR camera. To calculate a calibration factor, a steel ruler was placed next to the calibration object, parallel with the squash ball centres. To minimise parallax error, the camera was positioned 7 m away. *Check2D* (2012) was used to manually digitise the image, with a circular cursor fit to the perimeter of each squash ball. The mean distance between the squash ball centres and the standard error of the mean was calculated from repeat digitisation across 10 trials (table 4.1).

Table 4.1 – Mean and standard error of the mean of the distance between squash ball centres calculated from repeat manual digitisation of a high-resolution image (n = 10).

	Distance between squash ball centres (mm)
Mean	317.0
Standard error	0.1

4.3.2 Camera set up and checkerboard imaging

Two Vision Research Phantom *v4.3* high-speed cameras were set up to film an approximate 1 m^3 test volume, as shown in figure 4.3. The cameras were set to full resolution (800-by-600 pixels), with an exposure time of 100 µs. The cameras were connected via the *f-sync* output to synchronise the captured frames. A hardware trigger was used to manually trigger both cameras at the required times. Two 500 W halogen lights were set up next to each camera.

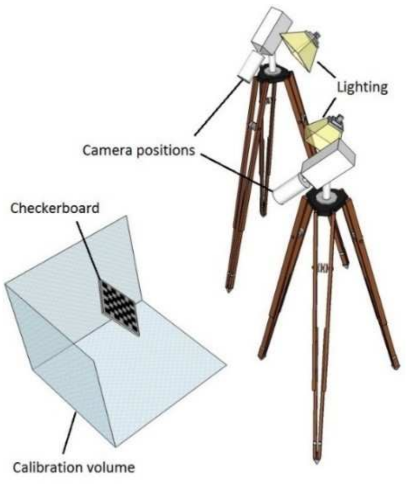

Figure 4.3 – A simulation of the camera calibration analysis experimental set up showing the position of the high-speed cameras, lighting and the calibration volume created from checkerboard images.

For a robust calibration model, 40 images of a seven-by-seven checkerboard with 20 mm-by-20 mm squares were taken throughout the test volume. This number of images ensured the camera sensor area was covered (to best calculate any image distortions) and the test volume adequately defined. Figure 4.4 shows a visualisation of the checkerboard locations relative to the left hand camera. The figure highlights the need to space and orientate the checkboard throughout the test volume in order for a robust calibration model.

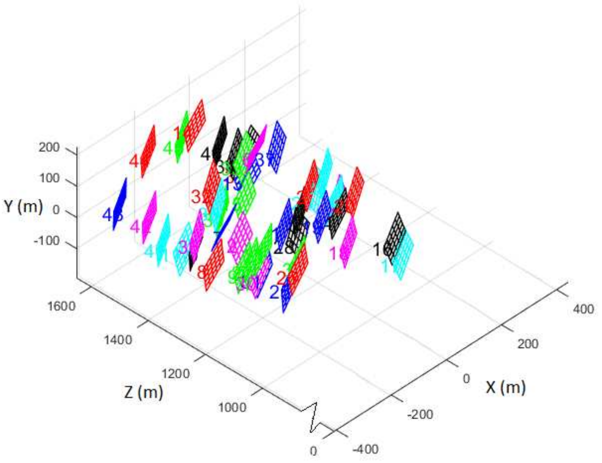

Figure 4.4 – Visualisation of the calibrated test volume with checkboard locations and orientations relative to the left hand camera.

Once the checkerboard images were processed, *Check3D* output details of the intrinsic parameters of the cameras – the calculated focal lengths and principal points. If the principal point differed significantly from the geometric centre of the image, the calibration could be recalculated with the principal point locked to the image centre. Table 4.2 shows the calculated focal lengths and principal points for the two cameras for a camera calibration model. In this case, the principal points were sufficiently close to the image centre to not require recalibration.

Table 4.2 – The calculated focal lengths (X_f, Y_f) and principal points for the two high-speed cameras and radial calibration model.

	X_f	Y_f
Left camera focal length (mm)	1355.2	1362.6
Right camera focal Length (mm)	1264.0	1262.8
Left camera principal point (p)	419.7	290.6
Right camera principal point (p)	361.9	311.8

For each calibration model, the root-mean-squared error (the “reprojection error”) of the discrepancies between the digitised checkerboard intersections and the calibration model were calculated. These reprojection errors can be useful to compare different calibration models. Table 4.3 shows the reprojection errors for the four camera calibration models for both cameras.

Table 4.3 – The root-mean-squared error between the digitised checkerboard intersections and the projected checkerboard intersections for each model for both cameras.

	No distortion model	Tangential & radial model	Radial model	Tangential model
Left camera reprojection error (p)	0.061	0.053	0.058	0.055
Right camera reprojection error (p)	0.055	0.050	0.054	0.054

The checkerboard images were also used to create visualisations for the image distortions caused by the cameras and lenses. Figure 4.5 shows the visualisations for the left and right high-speed cameras and lenses. The visualisations show concentric rings of increasing image distortion towards the periphery of both cameras, with the inner most ring representing one-pixel distortion.

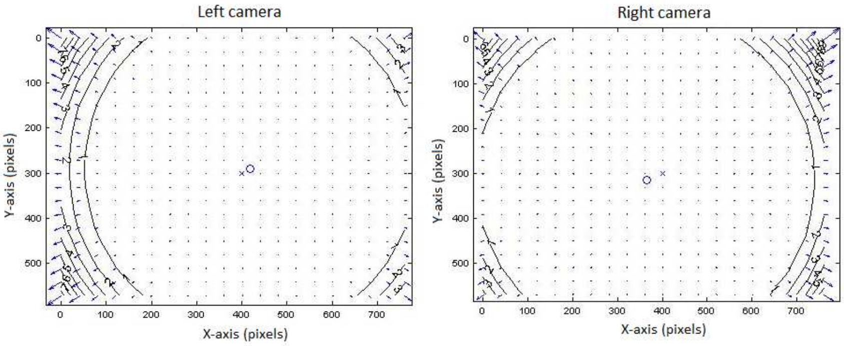

Figure 4.5 – Plots of calculated camera and lens distortions for the left and right high-speed cameras. Concentric rings of increasing whole pixel image distortion are shown (maximum 7 pixels for left camera, 9 pixels for right camera). The cross identifies the geometric centre of the image and the circle identifies the calculated principal point.

Table 4.3 shows very similar reprojection errors from the four models. However, the concentric rings of increasing distortion shown in figure 4.5 suggests a radial distortion model may be most suitable.

4.3.3 Calibration object imaging and digitisation

A total of 16 image pairs were captured of the calibration object in several orientations and positions throughout the test volume. Figure 4.6 shows two image pair examples.

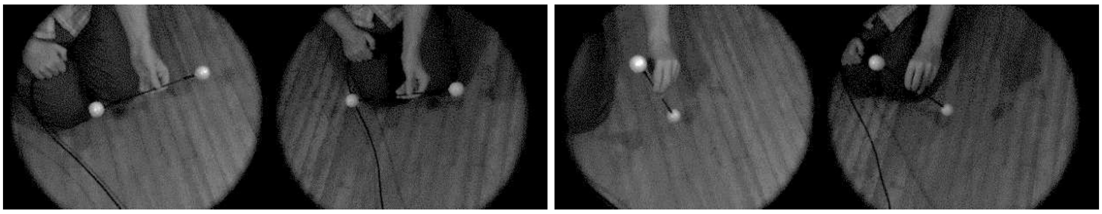

Figure 4.6 – Example images of the calibration object in different orientations and positions within the test volume.

The image pairs were manually digitised using a circular cursor fit to the perimeter of each squash ball (figure 4.7). Once digitised, the (*u, v*) coordinates were reconstructed to real-world (*x, y,* z) coordinates using each calibration model in turn. The distances between the squash ball centres were calculated using Pythagoras' theorem.

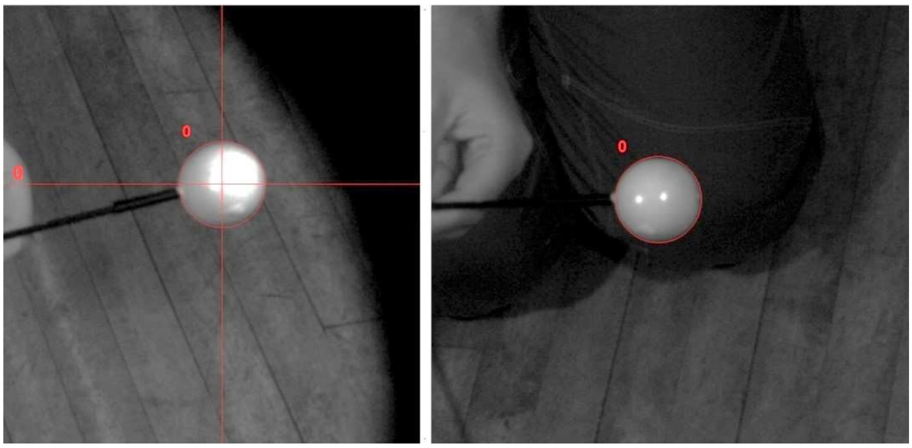

Figure 4.7 – Example images of digitising the calibration object in the image pairs using a circular cursor.

4.3.4 Calibration object results

Table 4.4 shows the mean distances between the squash ball centres and the standard error of the means (SEM) for each calibration model. The percentage differences between the mean values and the high-resolution measurement (table 4.1) are shown.

Table 4.4 – The mean lengths and SEMs for each calibration model with the percentage difference to the high-resolution measurements (n = 16).

Calibration model	Mean distance between squash ball centres (mm)	SEM (mm)	Difference to high-resolution measurement (%)
None	313.9	0.6	-1.0%
Radial & tangential	319.6	0.9	0.8%
Radial only	316.3	0.2	-0.2%
Tangential only	316.0	0.2	-0.3%

The calibration model with no image distortion correction resulted in an under-measurement of the calibration object and the largest error of all the calibration models. Modelling both radial and tangential distortion resulted in an over-measurement of the calibration object, but reduced the error to the high-resolution measurement. This model had the largest SEM, suggesting the model was the least robust over the calibration volume. The radial-only calibration model produced the lowest error, with an average measured length of control object 0.2% smaller than the high-resolution measurement. The low SEM also suggests the calibration model was robust over the full test volume. The tangential-only calibration model produced an equally low SEM, but a higher error for the average length of the control object. Therefore, the radial-only model was used for the camera calibration during impact testing.

4.4 Velocity measurement error

Having established the best calibration model, a second study was carried out to determine the error in spatio-temporal measurements (i.e. velocity measurements). Given the accuracy of the high-speed camera frame rate, the study was simplified to spatial measurements only. This was achieved by measuring the separation of pairs of points, positioned accurately throughout the test volume. For this, the calibration checkerboard was reused to generate additional test images. The checkerboard pattern offered two benefits:

1. The checkerboard intersections were discrete points, which was assumed to maximise the accuracy of manual digitisation.
2. The 36 checkerboard intersections maximised measurement efficiency whilst minimising the number of images required to fill the calibration volume.

An additional benefit was the distance between intersections. Given a ball speed of 20 $\mathrm{m \cdot s^{-1}}$ (a typical ball speed used during impact testing) and a high-speed camera frame rate of 1000 frames per second, the ball would displace 20 mm in the 0.001 s between frames.

4.4.1 Checkerboard imaging and digitisation

In total, 20 additional checkerboard image pairs were captured across the calibrated test volume. The 36 intersections per checkerboard image pair were manually digitised using a cross-hair cursor. The (u, v) coordinates were reconstructed to (x, y, z) coordinates using *Check3D*. The three-dimensional distances between neighbouring intersections were calculated using Pythagoras's theorem. This gave 60 measurements per image pair and a total of 1,200 measurements for the test volume. Table 4.5 shows the mean intersection separation and the pooled standard deviation.

Table 4.5 – The mean and pooled standard deviation for the checkerboard intersection distances across all image pairs (n = 1200).

Mean intersection distance (mm)	Pooled standard deviation (mm)
20.0	0.3

The results show the intersection digitisation and (u, v) coordinate reconstruction were accurate. The mean value had no error, indicating that on average the intersection digitisation and (u, v) coordinate reconstruction were accurate. Assuming the errors were normally distributed, the standard deviation suggests the camera calibration model is robust across the test volume. Given equivalent digitisation accuracy for a tennis ball, the result suggest velocity measurements will also have low error, if averaged across several frames for the inbound and rebound trajectories. The error in digitising a ball is discussed in Chapter 6.

4.5 Conclusion

In this chapter, the planar method of camera calibration was evaluated with a study to compare different image distortion models. The models correct for radial and tangential distortion caused by the high-speed cameras and lenses. The evaluation established the best performing calibration model corrected for radial image distortion only.

A second study established the error of spatio-temporal (velocity) measurements using the radial camera calibration model. The study measured the error in digitising and reconstructing of discrete points of 20 mm separation – the equivalent of an object displacing at 20 $m\cdot s^{-1}$. The study concluded that velocity measurements would have low error, assuming an equivalent digitisation accuracy for a ball.

The output of the camera calibration process was an XML file containing the following parameters:

- Camera intrinsic parameters (e.g. focal length, principal point, distortion model coefficients).
- Camera extrinsic parameters (e.g. translation and rotation matrices describing camera relative positions).

The parameters stored in this XML file were used with ball digitisation data to measure test parameters (see Chapters 6 onwards). In the next chapter, the development of methods to measure key racket parameters is described. The methods were required to measure impact locations during impact testing.

Chapter 5: Racket parameter measurements

5.1 Introduction

The previous chapters established the data to be collected from impact testing and the optimum high-speed camera calibration model to do this. This chapter describes the development of methods to measure key racket parameters, as shown in the project flowchart in figure 5.1.

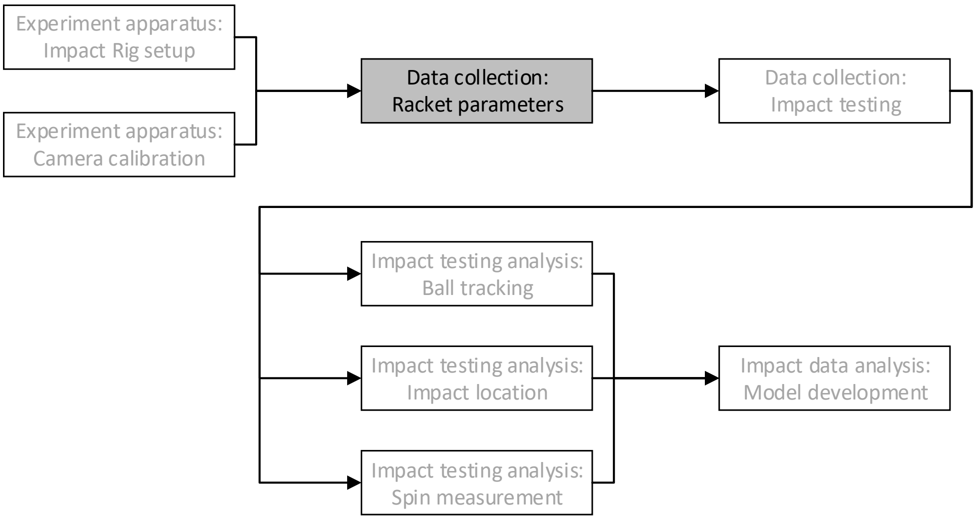

Figure 5.1 - Flowchart outlining the scope of the project. The chapter describes the development of racket parameter measurement methods to measure key test parameters for each racket.

The aim of this chapter is to develop a tool to measure the racket planar centre of mass and the centroids of retroreflective markers attached to the racket stringbed. For these, a local racket origin was defined.

The planar centre of mass method improved upon racket balance point measurements, giving centre of mass in two-dimensions. This established the symmetry of racket physical properties about the longitudinal axis of the racket. The method combined physical and geometric measurements using a semi-automated method.

The stringbed markers provided reference points to establish the stringbed plane and to transform ball velocity, spin axis and impact location measurements to the local racket origin. The marker centroids were automatically digitised from a calibrated image of the racket.

5.2 Objectives

The objectives for this chapter are:

1) To define a local racket origin.
2) Develop and validate the measurement of the racket planar centre of mass.
3) Develop and validate the measurement of stringbed markers centroids.

The third objective includes the development and validation of stringbed marker centroid measurements both prior to and during impact testing.

5.3 Racket parameter definitions

This section provides details of the local racket origin, the racket planar centre of mass and the stringbed markers.

5.3.1 Local racket origin

The racket was considered a plane of length and width (the "racket plane"). The racket was assumed to have uniform thickness, with the racket plane situated at the midpoint. The local origin was placed at the butt of the racket. The Y-axis was aligned to the longitudinal axis through the geometric stringbed centre (GSC) – the midpoint of the racket width. The X-axis was perpendicular to the Y-axis. The local racket origin, GSC, and axes orientations are shown in Figure 5.2.

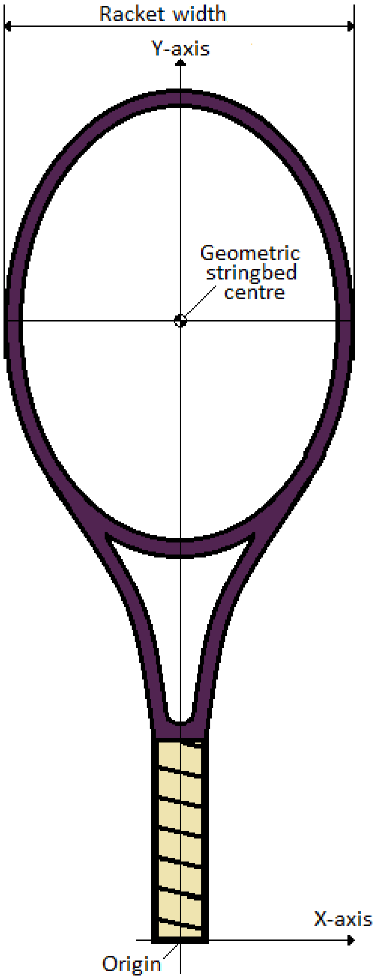

Figure 5.2 – The local racket origin was positioned at the racket butt with the Y-axis aligned to the geometric stringbed centre. The X-axis was perpendicular to the Y-axis.

5.3.2 Planar centre of mass

Traditionally, racket centre of mass (COM) is measured with the racket placed onto a ‘knife-edge’ and balanced to create a state of mechanical equilibrium (Figure 5.3). When the racket is balanced, the moments acting either side of the knife-edge are equal:

$$M_{butt} \cdot d_{butt} = M_{tip} \cdot d_{tip} \tag{5.1}$$

where M_{butt}, M_{tip} are the masses and d_{butt}, d_{tip} are the lengths of the racket, either side of the knife-edge. The COM is measured from the racket butt to the knife-edge (d_{butt} in Figure 5.3 and Equation 5.1).

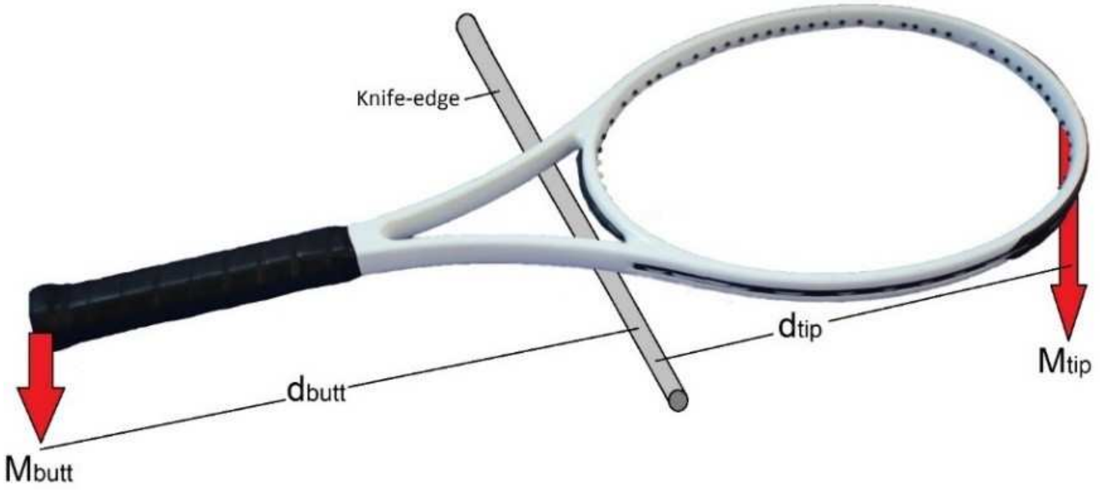

Figure 5.3 – The COM is measured with the racket balanced on a knife edge and in a state of mechanical equilibrium. The measurement is taken from the racket butt.

This method assumes the COM lies on the Y-axis with the physical and geometric properties of the racket symmetrical about this axis. If this is not the case, asymmetric physical properties would cause asymmetric rebound characteristics for impacts either side of the Y-axis. The implications on impact testing require a method to measure the planar centre of mass (COM_P), in the racket plane and relative to the X- and Y-axes.

The COM_P was measured from the moments about the COM_P acting on the frame at three locations. This method required:

1) The reaction forces, R_A, R_B and R_C at three (arbitrary) locations on the racket frame: A, B and C.
2) The component distances of these three locations to the origin (X_A, Y_A), (X_B, Y_B) and (X_C, Y_C).

These are defined further in figure 5.4.

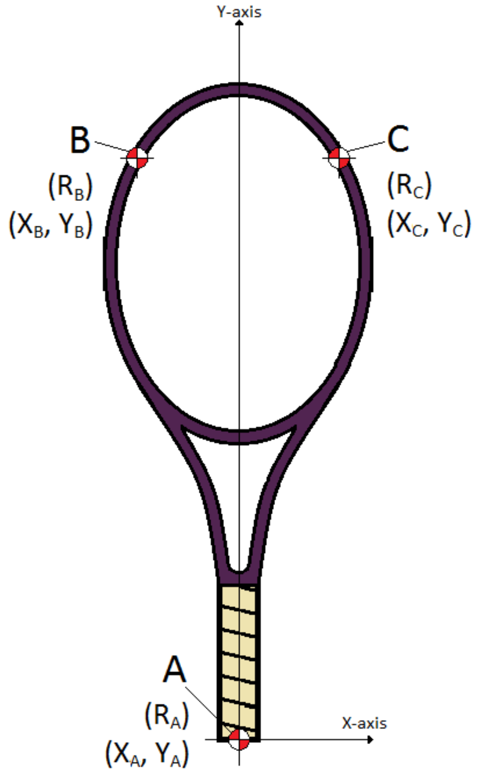

Figure 5.4 – The COM$_P$ was measured from the moments acting at three locations on the racket frame.

The measurements were used to solve the following linear equations:

$$R_A + R_B + R_C = R_{COM} \tag{5.2}$$

$$R_A \cdot X_A + R_B \cdot X_B + R_C \cdot X_C = R_{COM} \cdot X_{COM} \tag{5.3}$$

$$R_A \cdot Y_A + R_B \cdot Y_B + R_C \cdot Y_C = R_{COM} \cdot Y_{COM} \tag{5.4}$$

where R_{COM} is the sum of the three reaction forces and X_{COM} and Y_{COM} are the coordinates of the COM$_P$. As location A coincides with the local racket origin, the moments at location A ($R_A \cdot X_A$ and $R_A \cdot Y_A$) were zero. Substituting Equation 5.2 into Equations 5.3 and 5.4, and rearranging, gives the coordinates of the COM$_P$:

$$\frac{R_B \cdot X_B + R_C \cdot X_C}{R_A + R_B + R_C} = X_{COM_P} \tag{5.5}$$

$$\frac{R_B \cdot Y_B + R_C \cdot Y_C}{R_A + R_B + R_C} = Y_{COM_P} \tag{5.6}$$

5.3.3 Stringbed markers

The stringbed markers were made from 3M reflective tape, cut to approximate 1 cm^2 area, adding negligible mass to the racket. This choice was for two reasons:

1) Repeated impact could compromise traditional spherical markers attached to the racket frame.
2) Markers attached to the stringbed allow direct measurement of the stringbed plane – an important factor for calculating impact locations (see Chapter 7).

The markers were attached at four locations on the stringbed – the tip, throat, three o'clock (the "three" marker) and nine o'clock (the "nine" marker) positions, shown in figure 5.5. Four markers provided assurance that at least three could be digitised in the impact test images – sufficient to define the stringbed plane.

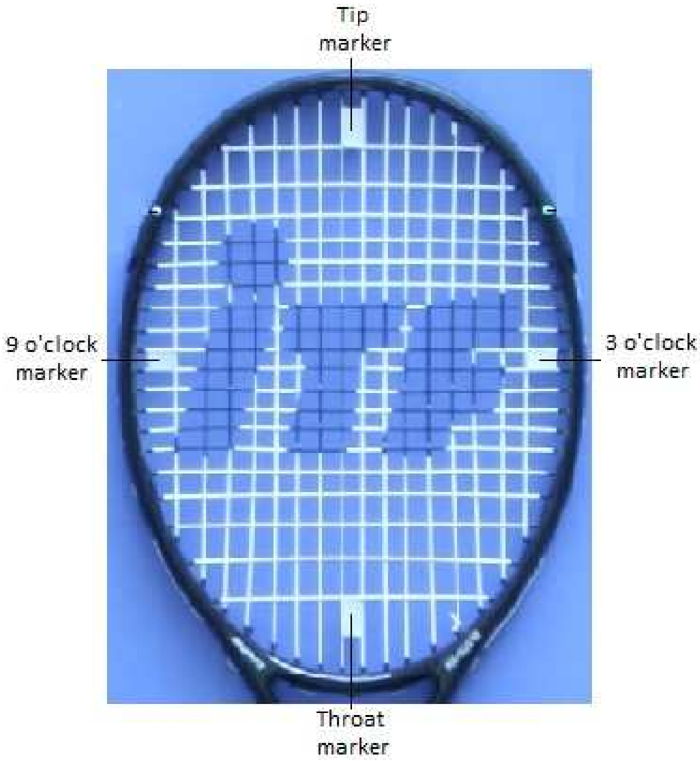

Figure 5.5 – Four stringbed markers were attached to the stringbed at the tip, throat, three and nine positions of the racket face.

5.4 Racket parameter methods – Part 1

Racket parameter measurements required two initial stages:

1) Reaction force measurements to calculate COM_P.
2) Racket imaging to digitise locations A, B and C and the stringbed markers.

5.4.1 Reaction force measurements

To measure reaction forces at locations A, B and C, three round headed pins were attached to the racket, giving discrete contact points. At location A, the pin was pushed into the grip at the racket butt. At locations B and C, the pins were slotted between the racket frame and the bumper guard. The reaction forces were measured using three Newton (2010) *High-Precision Professional Digital Pocket Scales,* shown in Figure 5.6. A Sola (2008) digital spirit level was used to level the racket both longitudinally and laterally. Mean reaction forces were established from 10 repeat trials.

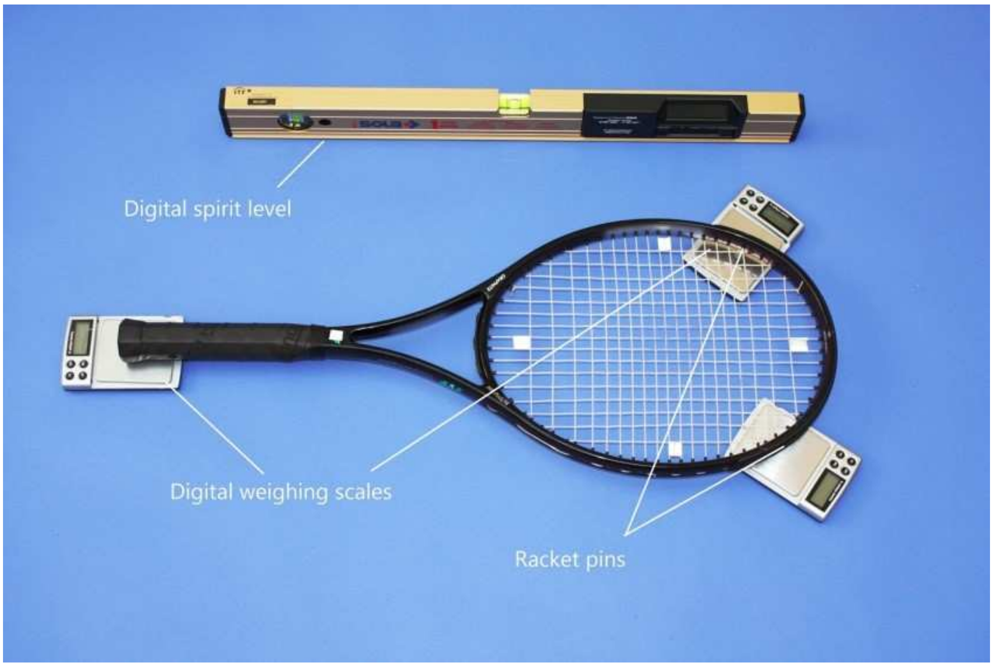

Figure 5.6 – The reaction forces at location A, B and C were measured using digital scales. The racket was levelled using a digital spirit level. Measurements were averaged across 10 trials.

5.4.2 Racket imaging

The centroids of locations A, B and C and the stringbed markers were digitised from a high-resolution image of the racket held against a calibration board. A calibration factor was calculated from two markers separated by 500 mm to provide a gauge length. The racket was held in place using string, as shown in Figure 5.7. Images were taken using a Canon *EOS 450D* digital SLR camera. For validation purposes, images of both faces of the racket were taken. To minimise perspective error due to racket thickness, the camera was positioned 7 m from the calibration board.

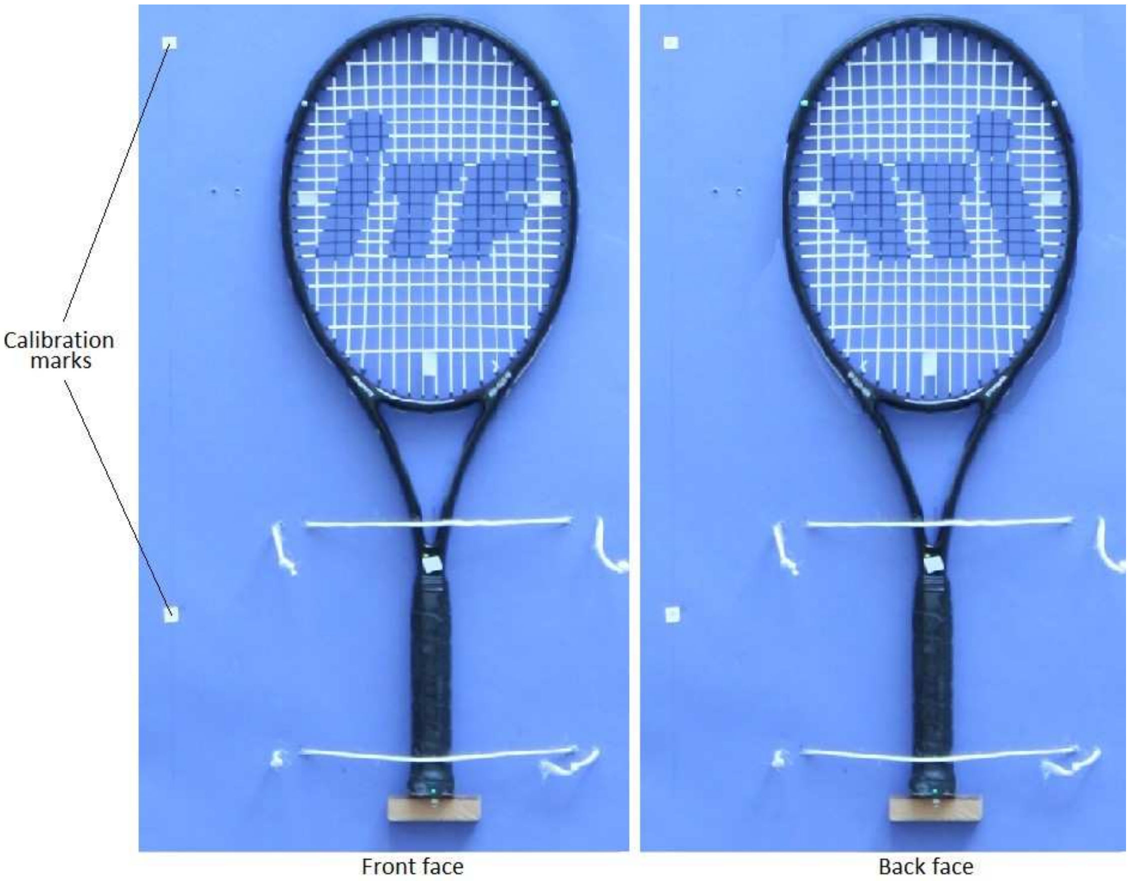

Figure 5.7 – Images were taken for both faces of the racket against a calibration board with calibration marks to calculate a calibration factor.

5.5 Racket parameter methods – Part 2

A semi-automated Racket Calibration tool was developed to process the racket images, calculate the COM$_P$ and digitise the stringbed markers. *MATLAB* image processing algorithms (Mathworks, 2008) were implemented using a Microsoft *Visual Studio* user interface to split the process into four stages:

1. Image crop, manual calibration mark digitisation and calibration factor calculation.
2. Manual image/racket alignment and local racket origin positioning.
3. Manual COM$_P$ measurement.
4. Automated stringbed marker digitisation.

5.5.1 Crop and calibration factor

The images were manually cropped and the calibration factor reference points manually digitised. The Racket Calibration tool included a magnification window to assist with manual digitisation (examples in Figure 5.8).

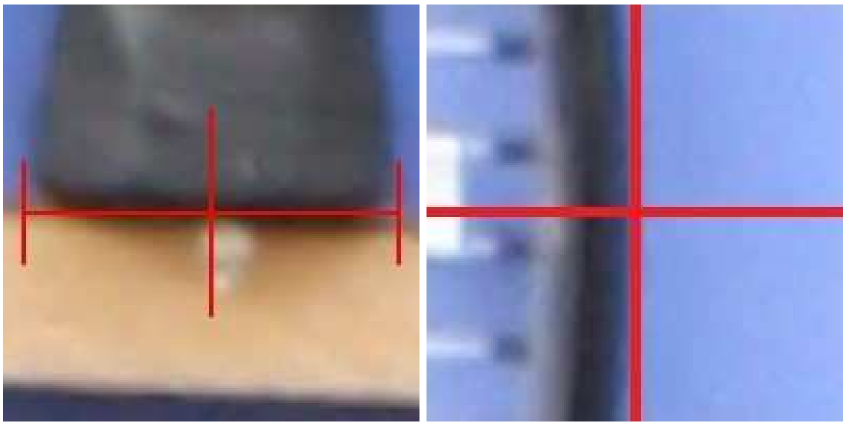

Figure 5.8 – Example images of the magnification window showing the racket butt (left) and racket frame extremity (right). Custom cross-hair designs were used to assist manual digitisation.

5.5.2 Image alignment and local racket origin positioning

The local origin was positioned at the racket butt with the Y-axis aligned to the GSC.

The GSC was calculated by manually digitising the widest points of the racket frame. Manually digitisation used custom crosshair designs within the magnified window, shown in Figure 5.8. To digitise the widest points of the racket frame, the racket had to be vertical within the image. Each time the racket butt and frame extremities were digitised, the image was rotated by an angle, θ_{rot} to vertically align the local origin and the calculated GSC (Figure 5.9).

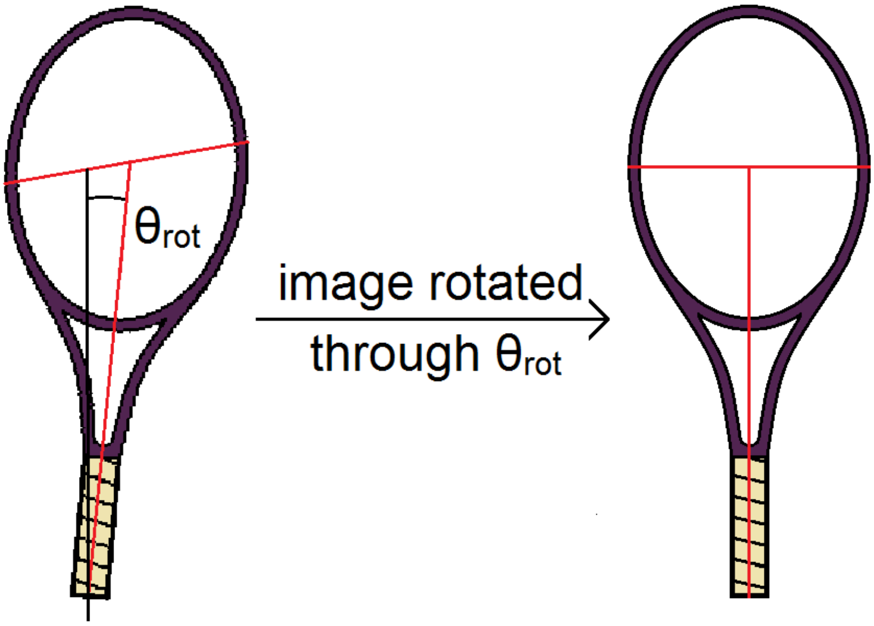

Figure 5.9 – To vertically align the racket, the racket image was rotated by θ_{rot} to align the calculated GSC above the racket butt.

This alignment process was repeated until θ_{rot} fell below a rotation threshold of 0.09°, signifying vertical alignment. The rotation threshold was calculated as a minimum rotation achievable, accounting for the repeatability of manual digitisation.

5.5.3 Image rotation threshold

The rotation threshold was the minimum image rotation achievable for the repeatability of manual digitisation. Below this threshold, the racket was deemed vertical within the image. To establish the repeatability of manual digitisation, *Check2D* (2012) was used to digitise the racket butt and frame extremities from five racket images across 10 trials (n = 50).

Table 5.1 shows the pooled standard deviations of repeat digitisation for the (*u, v*) coordinates of the racket butt (σ_{BUTT}), left frame extremity (σ_{LF}) and right frame extremity (σ_{RF}) of the five rackets.

Table 5.1 – The pooled standard deviations of manually digitising the racket butt and frame extremities from five Racket Calibration images across 10 trials (n = 50).

		u (p)	v (p)
Racket butt	σ_{BUTT}	0.5	0.8
	$2.56\sigma_{BUTT}$	1.3	2.0
Left frame extremity	σ_{LF}	0.3	1.7
	$2.56\sigma_{LF}$	0.8	4.4
Right frame extremity	σ_{RF}	0.3	1.2
	$2.56\sigma_{RF}$	0.8	3.1

Using the mean racket butt and frame extremity (*u, v*) coordinates and 99% confidence limits (2.56σ) for each racket, the maximum image rotations were calculated. This was the largest angle between the possible vectors joining the racket butt to the calculated GSC. This is shown graphically in figure 5.10.

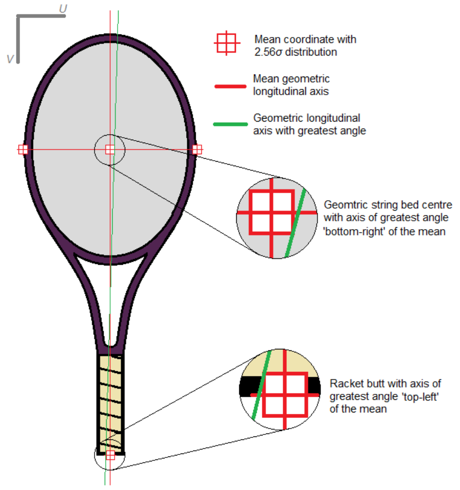

Figure 5.10 – The maximum angle between vectors joining the racket butt to the GSC was used to calculate the image rotation threshold.

The maximum angle between the vectors was 0.09° for each racket. A rotation threshold of ±0.09° was implemented in the Racket Calibration tool.

5.5.4 COM_P method

The COM_P calculations required the centroids of locations A, B and C relative to the local origin. Once the image was aligned, the round headed pins at locations B and C were manually digitised (location A was digitised at the racket butt during the racket alignment process). The three reaction forces measured at locations A, B, and C were entered for the Racket Calibration tool to calculate COM_P using equations 5.5 and 5.6.

5.5.5 Automated stringbed marker digitisation

MATLAB (Mathworks, 2008) image processing algorithms were used to automatically digitise the stringbed markers. The algorithms used were:

- *rgb2gray* – converted the colour image to greyscale by retaining the luminosity of each pixel (figure 5.11 left to middle).
- *im2bw* – converted greyscale image to binary (figure 5.11 middle to right) using a threshold value. The value could be adjusted through the Racket Calibration user interface.

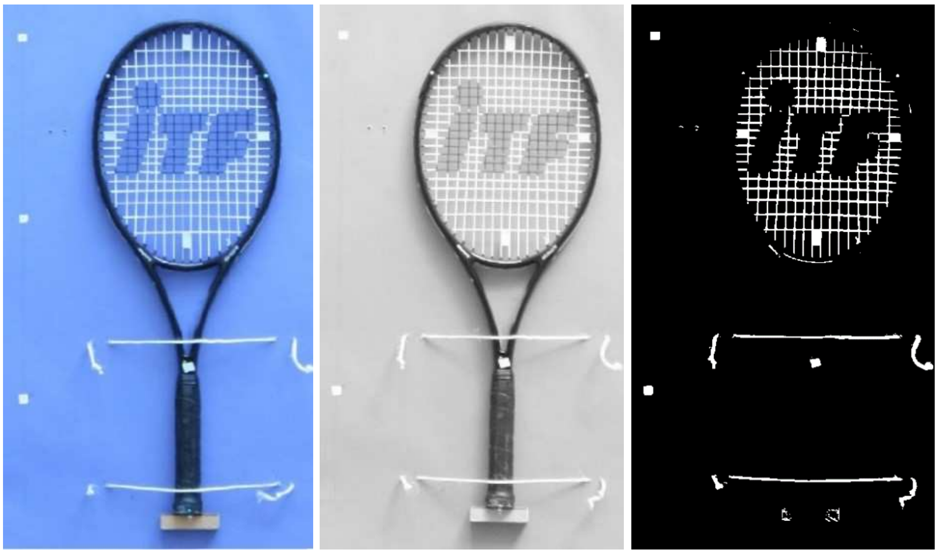

Figure 5.11 – Image processing of Racket Calibration image converted the cropped, colour image (left) to greyscale (middle) and then to a binary, black and white image (right).

- *imerode* – morphological function to '*erode*' white pixel regions (Figure 5.12 left). Specificity and level of erosion defined by a structuring element.
- *imdilate* – morphological function operating in an opposite manner to IMERODE. Used to restore partially eroded stringbed markers (Figure 5.12 right).

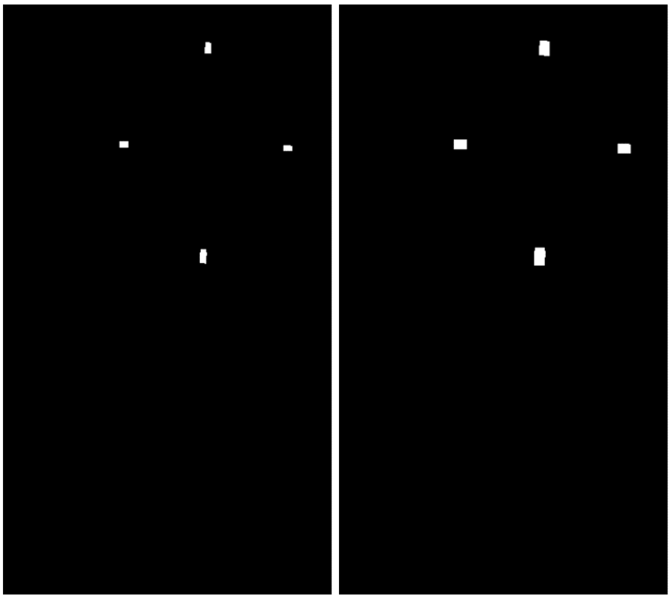

Figure 5.12 – Image processing of the binary image with artefact erosion (left) and dilation (right).

- *bwareaopen* – removed image artefacts of less than a defined number of pixels. Used to remove ‘noise’ missed by the thresholding process.
- *regionprops.centroid* – returned the centroid of each stringbed marker.

The centroids of locations A, B and C, the GSC, the COM$_P$ and the stringbed markers were superimposed onto the racket image, as shown in Figure 5.13.

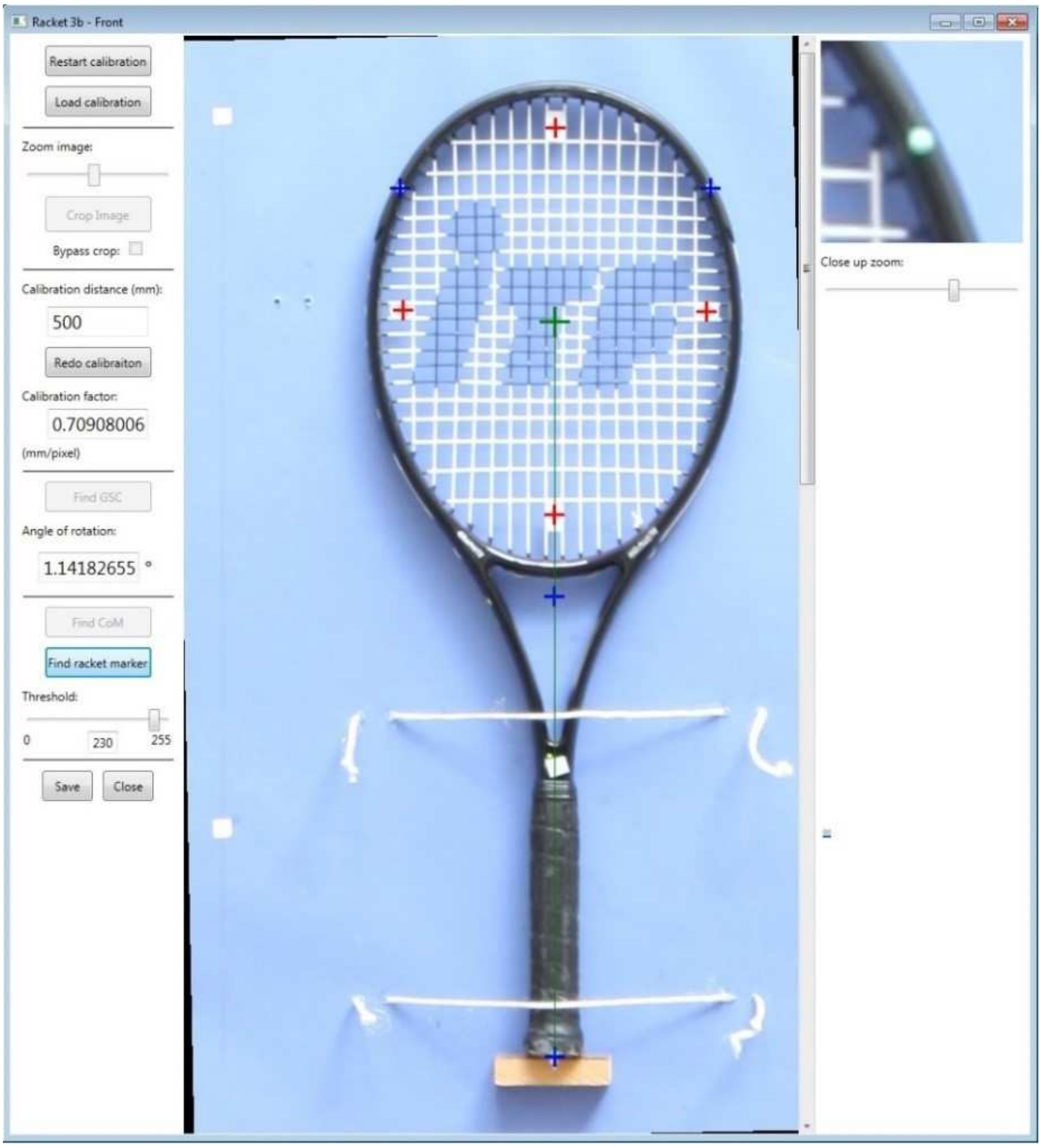

Calibration distance (mm): 500

Calibration factor: 0.70908006 (mm/pixel)

Angle of rotation: 1.14182655 °

Threshold: 0 230 255

Figure 5.13 – The Racket Calibration tool user interface, showing a cropped and rotated racket image. The locations of A, B, C, the COM$_P$ (blue), geometric stringbed centre (green) and stringbed makers (red) were superimposed onto the image.

5.6 Validation study – COM_P

To validate the COM_P method, two stages were required.

1. Establish the uncertainty in each stage of the method (e.g. the repeatability of manual digitisation) and combine to calculate the uncertainty of COM_P.
2. Compare the COM_P for the front and back faces of rackets processed with the Racket Calibration tool.

5.6.1 COM_P uncertainties

Each step of the method was evaluated to quantify sources of uncertainty. Uncertainty at the racket levelling stage (i.e. the effect of spirit level uncertainty propagating to reaction force measurement uncertainty) and the mass measurement stage (i.e. scale uncertainty) were found to be negligible. The repeatability of manually digitising locations A, B and C were established through 10 repeat digitisation trials of five racket images (n = 50), using *Check2D* (2012). Table 5.2 shows the pooled standard deviations of the centroids for locations A (σ_A and $2.56\sigma_A$), B (σ_B and $2.56\sigma_B$) and C (σ_C and $2.56\sigma_C$).

Table 5.2 – The pooled standard deviations of manually digitising locations A, B and C were calculated from five racket images across 10 trials (n = 50).

		u (p)	v (p)
Location A	σ_A	0.5	0.8
	$2.56\sigma_A$	1.3	2.1
Location B	σ_B	0.3	0.2
	$2.56\sigma_B$	0.7	0.5
Location C	σ_C	0.2	0.2
	$2.56\sigma_C$	0.5	0.6

The uncertainty of COM_P was established using the image rotation threshold (±0.09°) and the manual digitisation repeatability (±2.56σ from table 5.2). Using coordinate data from one racket, permutations of image rotation and pixel translations were simulated in Microsoft *Excel*. The maximum variation (COM_P uncertainty) was calculated by propagating uncertainties through the simulated process. The pixel values were converted to real world distances using the calibration factor for the racket image used. The results are shown in table 5.3.

Table 5.3 – The uncertainty in COM_P was calculated from simulations to quantify the effect of the image rotation threshold and manual digitisation repeatability.

	u (p)	*v* (p)	x (mm)	y (mm)
COM_P uncertainty	± 1.1	± 1.5	± 0.8	± 1.1

5.6.2 Comparing racket faces

The COM_P for both faces of three ITF *Development* rackets were measured. Table 5.4 shows the front and back face COM_P measurements (COM_{Pff} and COM_{Pbf} respectively). The X-coordinates for the back faces were inverted, to allow direct comparison between faces (ΔCOM_P).

Table 5.4 – COM_P for the front (COM_{Pff}) and back (COM_{Pbf}) faces of each racket with discrepancies between faces, ΔCOM_P.

	COM_{Pff}		COM_{Pbf}		ΔCOM_P	
	X (mm)	Y (mm)	X (mm)	Y (mm)	X (mm)	Y (mm)
Racket 1	-0.8	329.4	-0.1	329.8	-0.7	-0.4
Racket 2	0.1	322.6	0.0	322.5	0.1	0.1
Racket 3	-0.3	323.5	0.1	323.1	-0.4	0.4

These results show that the maximum discrepancies between faces was 0.7 mm in the X-axis and 0.4 mm in the Y-axis. These values were less than the theoretical uncertainties calculated in table 5.3, at 0.8 mm in the X-axis and 1.1 mm in the Y-axis.

5.7 Validation study – stringbed markers

To validate the measurements of the stringbed markers, four steps were required:

1) Establish the repeatability of manually digitising the markers.
2) Establish the error of automated stringbed marker digitisation by comparison to manual digitisation.
3) Calculate the uncertainty in automated marker digitisation due to the rotation threshold and the manual digitisation repeatability (established in step 1).
4) Compare the marker locations for the front and back faces of rackets processed with the Racket Calibration tool.

5.7.1 Manual stringbed marker digitisation repeatability

The repeatability of manually digitising the stringbed markers was established from 10 repeat trials of five racket images (n = 50), using *Check2D* (2012). Table 5.5 shows the pooled standard deviations of the centroids of the tip (σ_{tipU}, σ_{tipV}), throat ($\sigma_{throatU}$, $\sigma_{throatV}$), three (σ_{threeU}, σ_{threeV}) and nine (σ_{nineU}, σ_{nineV}) markers.

Table 5.5 – The pooled standard deviations of manually digitising each stringbed marker was calculated from digitising five Racket Calibration images across 10 trials (n = 50 for each marker).

Tip marker		Throat marker		Three marker		Nine marker	
σ_{tipU} (p)	σ_{tipV} (p)	$\sigma_{throatU}$ (p)	$\sigma_{throatV}$ (p)	σ_{threeU} (p)	σ_{threeV} (p)	σ_{nineU} (p)	σ_{nineV} (p)
0.4	0.4	0.5	0.3	0.4	0.5	0.4	0.3

5.7.2 Automated stringbed marker digitation validation

Part two of the validation compared the automated digitisation of the stringbed markers to manual digitisation. The automated algorithm was used to digitise the same five racket images used in the previous section. Discrepancies between the automatically digitised centroids and the mean manual centroids were averaged across the five rackets. Table 5.6 shows the mean discrepancies between the (*u, v*) coordinates for the tip (Δ_{tipU}, Δ_{tipV}), throat ($\Delta_{throatU}$, $\Delta_{throatV}$), three (Δ_{threeU}, Δ_{threeV}) and nine (Δ_{nineU}, Δ_{nineV}) markers.

Table 5.6 – The error of automatically digitising the stringbed markers.

Manual digitisation – automated digitisation (p)							
Tip marker		Throat marker		Three marker		Nine marker	
Δ_{tipU}	Δ_{tipV}	$\Delta_{throatU}$	$\Delta_{throatV}$	Δ_{threeU}	Δ_{threeV}	Δ_{nineU}	Δ_{nineV}
-0.3	-0.4	0.3	0.0	0.0	0.4	-0.3	0.1

The sub-pixel errors of automatically digitising each stringbed marker were equal to, or less than, the uncertainty of manual digitisation (table 5.5). Therefore, the accuracy of the automated method was deemed acceptable.

5.7.3 Stringbed marker uncertainty

Part three of the validation calculated stringbed marker centroid uncertainty. This was established using the image rotation threshold (±0.09°) and the uncertainty of manual digitisation (table 5.5). As per the method used in section 5.6.1, permutations of image rotation and pixel translations were simulated in Microsoft *Excel*. The maximum variations of each stringbed marker centroid were calculated by propagating uncertainties through the simulated process. The pixel values were converted to real world distances using the calibration factor for the Racket Calibration image used. The results are shown in table 5.7.

Table 5.7 – The uncertainties in stringbed marker centroids were calculated from simulations to quantify the effect of the image rotation threshold and manual digitisation repeatability.

Stringbed marker	Δx (mm)	Δy (mm)
Tip	± 0.9	± 1.5
Throat	± 0.9	± 1.5
Three	± 0.9	± 1.6
Nine	± 0.9	± 1.6

5.7.4 Comparing racket faces

The final part of this validation compared the stringbed marker centroids digitised for both faces of three ITF *Development* rackets processed using the Racket Calibration tool. Table 5.8 shows the discrepancies between the centroids for the four stringbed markers of each racket. To compare faces, the three and nine marker centroids of the back face were mirrored across the Y-axis. The X-coordinates of the tip and throat markers for the back faces were inverted.

Table 5.8 – The discrepancy between the stringbed marker centroids for the front and back faces of each racket.

	Front face centroids – back face centroids (mm)					
	Racket 1		Racket 2		Racket 3	
	X	Y	X	Y	X	Y
Tip marker	-0.5	0.7	-0.3	-1.1	0.2	0.2
Throat marker	-0.4	-0.2	0.2	-1.0	0.3	-0.1
Three marker	0.2	0.1	-0.9	-0.4	0.6	1.3
Nine marker	-0.6	0.1	0.8	-0.6	-0.1	0.5

The maximum discrepancies between faces was -0.9 mm in the X-axis (three marker for Racket 2) and -1.3 mm in the Y-axis (three marker for Racket 3). The values for all markers were less than or equal to the theoretical uncertainties calculated in table 5.7, at ±0.9 mm in the X-axis (all markers) and ±1.5 mm (tip and throat markers) and ±1.6 mm (three and nine markers) in the Y-axis.

5.8 Impact testing - stringbed marker digitisation

This section described the development of a method to digitise the stringbed markers during impact testing. Described thoroughly in Chapter 6 and 7, the analysis of the high-speed camera impact test images was automated using *MATLAB* image processing algorithms (Mathworks, 2008). Each set of impact test images included an initial frame with the ball out of shot. The stringbed markers were digitised in these initial image pairs (left and right cameras). The image processing functions used were:

- *adaptivethreshold* – this function is described in greater detail in Chapter 6.
- *bwareaopen* – as describe in section 5.5.4.
- *imclearborder* – removed image artefacts connected to the image border.
- *imfill* – using the 'holes' qualifier, filled in image artefacts where black pixels were surrounded by white pixels.
- *imerode* and *imdilate* – as describe in section 5.5.4.
- *regionprops.centroid* – as describe in section 5.5.4.

Figure 5.14 shows examples the image processing. The centroid data were used to qualify each marker (tip, throat, three or nine) using the relative positions within the image.

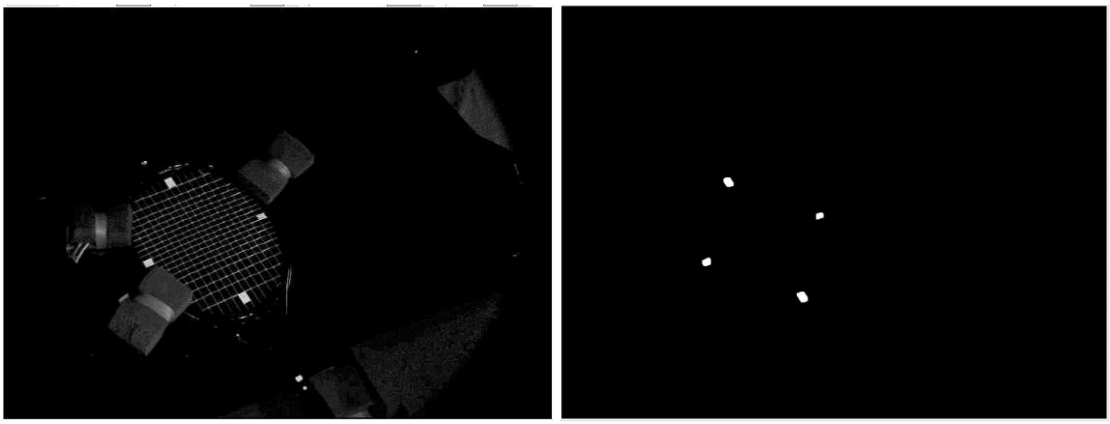

Figure 5.14 – The stringbed markers were automatically digitised from the first frame of each impact test. Shown are the unprocessed (left) and processed (right) images from the left high-speed camera, showing the stringbed markers segmented from the image background.

Three stages were used to validate the automated stringbed marker digitisation:

1) Establish the uncertainty of manually digitising the markers.
2) Establish the error of automated stringbed marker digitisation by comparison to manual digitisation.
3) Compared the orientation of the stringbed plane defined by the stringbed markers to manual measurements using a digital inclinometer.

A calibration volume was set up using the high-speed cameras and camera calibration method described in Chapter 4. Data collection was carried out using rackets placed into the test volume to replicate impact testing conditions.

5.8.1 Manual stringbed marker digitisation repeatability

The uncertainty of manual stringbed marker digitisation was established from repeat digitisation of one pair of racket images (left and right high-speed camera) using *Check3D* (2012) across 10 trials. The stringbed markers in both camera images were considered sufficiently similar to assume equal digitisation variance. As such, the repeatability data were pooled to calculate the uncertainty (n = 80). Cropped images of the stringbed markers are shown in figures 5.15 (left camera) and 5.16 (right camera).

The pooled standard deviation (σ and 2.56σ) of the manual digitisation are shown in table 5.9.

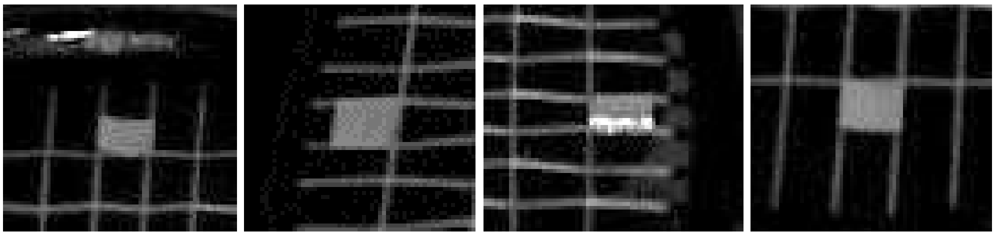

Figure 5.15 – The stringbed markers from left camera, (left to right) showing the tip, nine, three and throat markers.

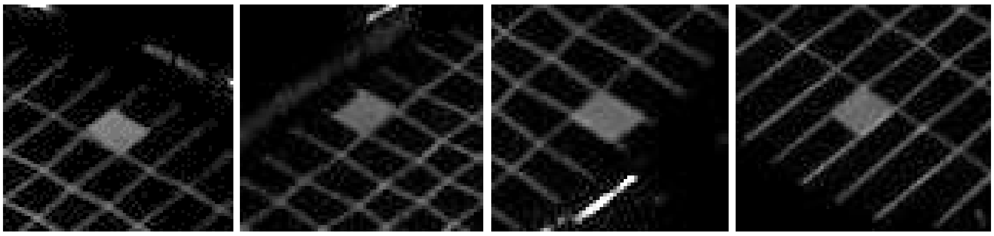

Figure 5.16 – The stringbed markers from right camera, (left to right) showing the tip, nine, three and throat markers.

Table 5.9 – The pooled standard deviation of manually digitising the stringbed markers was calculated from repeat digitisation of one pair of racket images across 10 trials (n = 80).

σ (p)	0.4
2.56σ (p)	0.9

5.8.2 Automated stringbed marker digitation validation

Part two of the validation compared the automated digitisation of the stringbed markers to manual digitisation. The automated algorithm was used to digitise the markers in image pairs for 10 ITF *Development* rackets. Manual digitisation was completed using *Check3D* (2012). The mean error of automated digitisation was calculated by comparing the (*u*, *v*) coordinates for each marker type, in each camera.

The discrepancies for the left camera are shown in table 5.10 and the right camera in table 5.11.

Table 5.10 – (*u, v*) coordinate error in automatically digitising the stringbed markers for the left high-speed camera, by stringbed marker type.

Stringbed marker	Tip	Three	Throat	Nine
u-coordinate error (p)	0.0	-0.6	-0.1	0.4
v-coordinate error (p)	0.5	0.2	-0.7	0.3

Table 5.11 – (*u, v*) coordinate error in automatically digitising the stringbed markers for the right high-speed camera, by stringbed marker type.

Stringbed marker	Tip	Three	Throat	Nine
u-coordinate error (p)	-0.4	0.3	0.2	0.3
v-coordinate error (p)	0.4	0.4	0.1	0.4

The maximum error for the left camera was -0.7 pixels for the *v*-coordinate of the throat marker. The maximum error for the right camera was 0.4 pixels (multiple instances). These were less than the uncertainty of manual digitisation at 0.9 pixels (2.56σ).

5.8.3 Stringbed plane comparison

The final part of the validation used the automated stringbed marker algorithm to calculate the orientations of stringbed planes. The orientations were compared to manual measurements using a digital inclinometer. For this, a racket was clamped to a base plate positioned in the calibrated test volume. The base plate could be rotated about the long axis of the racket, to re-orientate the stringbed plane (figure 5.17).

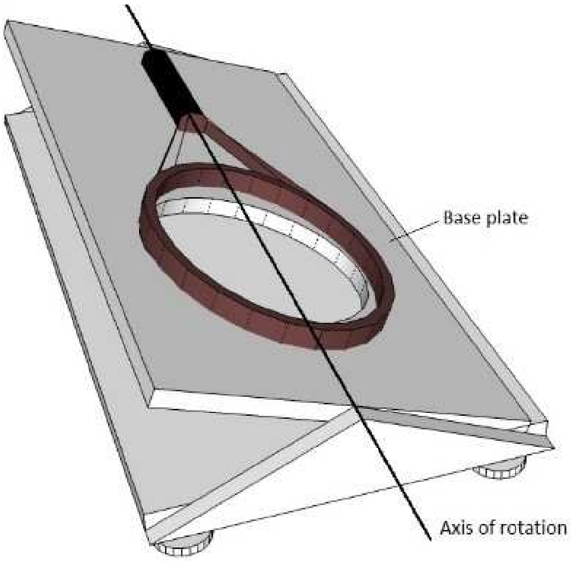

Figure 5.17 – To assess the calculated stringbed plane orientation, a racket was attached to a base plate that could be rotated about the long axis of the racket.

The stringbed plane was measured manually with a Moore & Wright (2010) digital inclinometer placed directly onto the stringbed. High-speed camera image pairs were taken with the racket perfectly level (i.e. 0.0° to horizontal) and then rotated about the long axis to incline the stringbed to 2.0° and 4.0° to horizontal. Between each rotation, the racket was returned to 0.0° to horizontal, giving a total of five image pairs.

To measure the stringbed plane orientations from the stringbed centroids, a reference vector was established. For this, an image pair were taken with the calibration checkerboard placed within the test volume. The checkerboard was set to 0.0° using the digital inclinometer. The left and right checkerboard images were manually digitised using *Check3D* to define a local origin and X- and Y-axes. The unit vector perpendicular to these axes (the "Z-axis") was then assumed vertical and used to measure the angle of the calculated normal of each stringbed plane – the stringbed orientation.

The pairs of centroids for each stringbed marker were reconstructed to three-dimension (*x, y,* z) coordinates relative to local origin, using the intrinsic and extrinsic camera calibration parameters. The *MATLAB* algorithm *fitNormal* (Mathworks, 2008), described in detail in Chapter 7, was used to calculate a stringbed plane of best fit through the four reconstructed stringbed marker centroids. The algorithm output a normal unit vector to this stringbed plane. The angle, θ between the unit vector and the Z-axis were calculated using:

$$\theta = \operatorname{atan}\left(\frac{|a \times b|}{a \cdot b}\right) \qquad 5.7$$

where, a was the Z-axis unit vector, i.e. (0, 0, 1) and b was the stringbed plane normal unit vector. The discrepancies between θ and the stringbed orientations as measured by the digital inclinometer are shown in table 5.12.

Table 5.12 – The discrepancies and mean discrepancy between stringbed plane orientations calculated with centroid data from the automated stringbed marker algorithm and the digital inclinometer for five racket orientations.

Orientation	Manual orientation (°)	Automated orientation (°)	Automated – manual (°)
1	0.0	0.0	0.0
2	2.0	1.9	-0.1
3	0.0	0.1	0.1
4	4.0	4.1	0.1
5	0.0	0.1	0.1
Mean			**0.0**

The results show that the normal to the stringbed plane was measured to within 0.1° of the manual measurements, with a mean discrepancy of 0.0°. These results provide good evidence that the stringbed markers and the automated stringbed marker algorithm accurately define the stringbed plane. This evidence also supports the use of the stringbed markers over traditional markers to define the stringbed plane accurately.

5.9 Conclusion

This chapter described the development of methods to measure key racket parameters and a Racket Calibration tool to measure:

1) The planar centre of mass (COM_P) of a racket.
2) The centroids of four reflective markers attached to the racket stringbed.

The measurements were relative to a local racket origin, situated at the racket butt and orientated to align the Y-axis with the longitudinal axis of the racket.

The COM_P method improved upon existing racket balance point measurements, giving the racket's centre of mass in two dimensions – relative to racket width and length (the racket plane). This allowed assessment of the symmetry of racket physical (inertial) properties. It was assumed inertial symmetry would result in symmetrical ball rebound characteristics for off-axis impacts. This allows either face of the racket to be impact tested. Rackets with asymmetrical properties would be excluded from this project, but would be an interesting route for future research.

The COM_P method required reaction forces and associated moments at three points on the racket frame. The reaction forces were measured for a perfectly level racket using digital scales. The measurement locations were digitised from a high-resolution image of the racket placed against a calibration board. To validate the method, COM_P measurements were compared for both faces of several rackets. These discrepancies were found to be within the established experimental error for the method.

The stringbed marker centroids served two purposes:

1. Reference points for impact locations measurements during testing.
2. Intermediate coordinates to transform impact data to the local racket origin.

Reflective tape was attached directly to the stringbed at the tip, throat, three o'clock and nine o'clock positions on the racket face. The Racket Calibration tool used image processing algorithms to automatically digitise the position of each marker from the high-resolution racket image. The automated process was validated by comparing the discrepancies to manual digitisation against the repeatability of manual digitisation. The method was further validated by comparing the stringbed marker locations for both faces of several rackets. These discrepancies were found to be less than the repeatability of manual digitisation.

This chapter also described and validated the development of an automated algorithm to digitise the stringbed markers from high-speed camera images pairs. This was used to digitise the stringbed markers during impact testing. The validation compared the discrepancies between automated and manual digitisation against the repeatability of manual digitisation.

To justify the use of markers attached directly to the stringbed (over traditional spherical markers) a final investigation measured the stringbed plane orientations from the planes of best of fit through stringbed marker centroids. The orientations were compared to manual measurements with a digital inclinometer. The largest discrepancy was 0.1°, which provided sufficient evidence that the stringbed markers could accurately define the stringbed plane.

The output of the process was an XML file containing the following parameters:

- Racket physical parameters (i.e. the real-world position of the COM_P relative to the local racket origin.).
- Racket geometric parameters (i.e. the real-world positions of the stringbed marker centroids relative to the local racket origin).

The racket geometric parameters stored in this XML file were used with ball digitisation to measure impact locations and transform the ball coordinates to the local racket origin (see Chapters 6 and 7). The next three chapters continue the description of methods used to measure impact testing data. Chapter 6 describes the development of an automated ball tracking algorithm. Chapter 7 describes the development of a method to measure impact location. Chapter 8 describes the implementation and improvement of an existing method to measure spin rate and spin axis.

Chapter 6 – Ball tracking

6.1 Introduction

Having established the pre-testing requirements for impact testing (Impact Rig design, camera calibration, racket parameter measurement), this chapter jumps ahead in the project structure. This chapter describes the development and validation of an automated ball tracking algorithm. The algorithm digitised the ball in the pairs of high-speed camera images from impact testing. This chapter is shown in context of the project in the flowchart in figure 6.1.

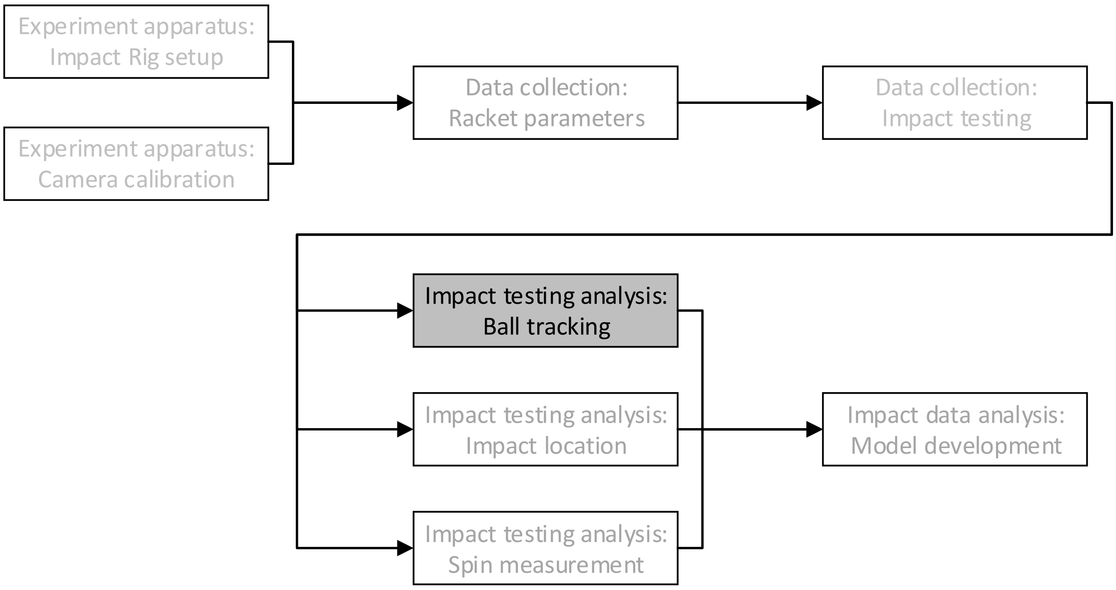

Figure 6.1 - Flowchart outlining the scope of the project. The chapter describes the development of an automated ball tracking algorithm to digitise the ball from impact test images.

The purpose of automating ball tracking was to facilitate data collection on a large scale. The ball was tracked in to and out of the impact, but not whilst in contact with the stringbed (discussed in chapter 7). The ball centroids were reconstructed into three-dimensional real-world coordinates using camera calibration parameters (described in chapter 4).

6.2 Objectives

The objectives of this chapter are:

1. Develop and validate an algorithm to automatically digitise the inbound and outbound ball trajectories for impacts onto a realistically supported racket.
2. Reconstruct the ball centroids into three-dimensional (*x, y, z*) real-world data using camera calibration parameters.
3. Transform the reconstructed coordinates to the local racket origin and calculate inbound and outbound velocities.

6.3 Pre-analysis requirements

In the next sections, the automated ball tracking algorithm and relevant processes are described. Microsoft *Visual Studio* was used to create an Impact Analysis tool. The tool used several Mathworks *MATLAB* image processing algorithms to analyse the high-speed camera images of impact testing. Prior to analysis, the following data were loaded via the user interface:

1. Impact test directory.
   The high-speed camera images of the impact tests were saved in a folder structure organised by a parent directory for the racket tested. The parent directory contained subfolders for the left and right cameras in which sub-subfolders contained images for each impact test.
2. Camera calibration data XML file.
   An XML file containing the intrinsic and extrinsic camera calibration parameters (discussed in Chapter 4). The intrinsic camera parameters were used to correct for image distortions caused by the lenses and high-speed cameras. The extrinsic camera parameters were used to reconstruct the ball centroids into (*x, y, z*) real-world coordinates.
3. Racket Calibration data XML file.
   An XML file containing the racket parameters (discussed in Chapter 5). The racket parameters were required to transform the (*x, y, z*) real-world coordinates to the local racket origin.

The pre-analysis file loading, impact data storage structure and analysis processes are shown diagrammatically in figure 6.2. Following ball digitisation and ball centroid reconstruction, the impact location and ball spin were calculated for each impact test (discussed in Chapters 7 and 8 respectively). The data for each impact were saved as an XML file in the parent directory.

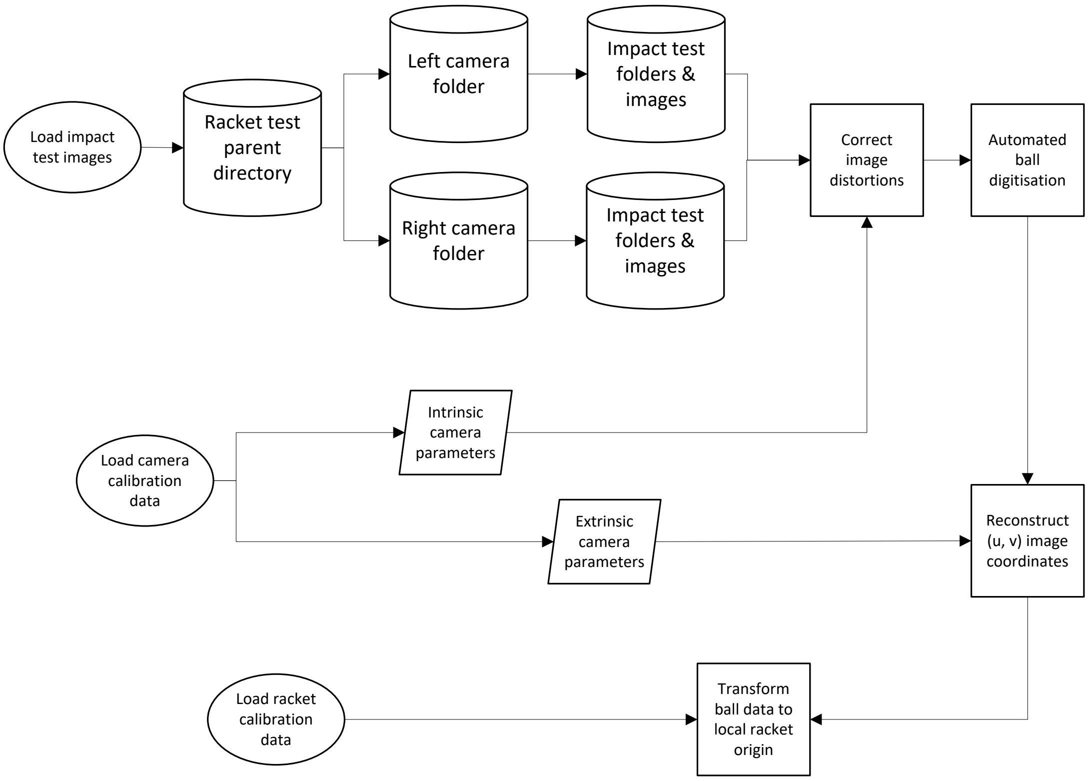

Figure 6.2 – A schematic of impact test data storage structure, calibration file loading and analysis processes for automated ball tracking.

6.4 Image processing definitions

In this section, the *MATLAB* image processes algorithms are described.

6.4.1 Adaptive threshold

To facilitate automated digitisation, images were first converted from greyscale to binary using a threshold function. A threshold function compares individual pixel levels to a static threshold value, converting pixels above the threshold to white and pixels below the threshold to black. However, using a static threshold value required the ball to have uniform brightness. The ball logo, black lines added to measure spin and shadows meant this was not the case. The function *adaptivethreshold* (Mathworks, 2008) filtered the image prior to thresholding by adjusting the brightness of each pixel to the average luminosity within a defined pixel neighbourhood.

The effects of thresholding with and without the *adaptivethreshold* filter are shown in Figure 6.3. The original cropped image shows the ball logo, black lines and shadows (Figure 6.3 - left). Thresholding without filtering converts the ball into four white segments (Figure 6.3 - centre). Thresholding with the filter converts the ball to one single image artefact (Figure 6.3 - right).

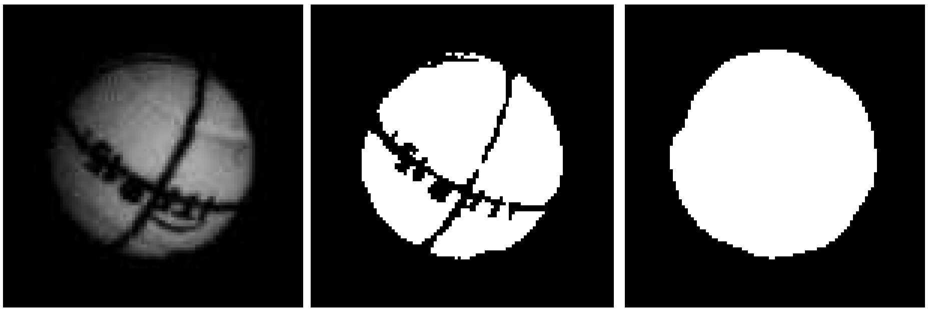

Figure 6.3 – Images of the adaptive threshold process: cropped original image of the ball (left) without *adaptivethreshold* filter (centre) and with *adaptivethreshold* filter (right).

The implementation of *adaptivethreshold* required three parameters:

1) Filter neighbourhood size – the number of pixels around the pixel of interest.
2) Filter average – mean or median averaging of neighbourhood luminosities.
3) Threshold luminosity value – to convert the filtered pixels to a binary value.

A user interface in the Impact Analysis tool was designed to manually fine-tune these parameters. The interface displayed sample images with *adaptivethreshold* applied, updating the images as each parameter was adjusted. The analysis success rate was maximised by setting the optimal function parameters.

6.4.2 Image processing functions

In addition to thresholding the images, *MATLAB* image processing functions were used to segment the ball from the image background. The functions used were:

- *bwareaopen* – removed image artefacts of less than a defined number of pixels. Used to remove ‘noise’ missed by the thresholding process.
- *imclearborder* – removed image artefacts connected to the image border.
- *imfill* – used the ‘holes’ qualifier to fill in image artefacts where black pixels were surrounded by white pixels.
- *imerode* – morphological function to ‘*erode*’ white pixel regions. Specificity and level of erosion defined by a structuring element.
- *imdilate* – morphological function operating in an opposite manner to *imerode*. Used to restore partially eroded image artefacts.
- *regionprops.centroid* – returned the centroid of image artefacts. Used to return the centre pixel coordinates of the ball.
- *imcrop* – cropped the image using the centroid data to centre the cropping rectangle around the ball.
- *edge* – returned the pixels making up the perimeter of the ball.
- *houghcirclemod* – using the Hough Transform to return the centroid of the ball that best fit a circle of defined radius to the edge pixels. This function was a modification of the function *houghcircle* (Mathworks, 2008).

Example original and processed images are shown in Figure 6.4, where the white ball pixels are segmented from the image background.

Figure 6.4 – Example images of an impact test with ball in shot: unprocessed (left) and processed (right) to leave only the ball.

6.5. Ball digitisation and stereo reconstruction

Each impact test comprised images of the ball entering the test volume, impacting the racket and rebounding out of shot. The images were analysed in sequence to digitise the inbound trajectory and then in reverse order to digitise the outbound trajectory. The process was split into four stages:

1) Identify the ball entering the test volume and digitise the first image with the ball fully in shot.
2) Track and digitise the ball forwards until intersection with the stringbed plane.
3) Identify the ball leaving the test volume and digitise the last frame with the ball fully in shot.
4) Track and digitise the ball backwards until intersection with the stringbed plane.

6.5.1 Ball identification

To identify the ball entering the test volume, an algorithm was designed making use of the elevated high-speed cameras, positioned above the racket and looking down into the test volume. From the elevated positions, the ball appeared largest near the start of the trajectory and decreased in size through successive frames. The algorithm processed each test image in turn and counted the white ball pixels. The first image was taken immediately prior to the ball entering the frame, giving an initial white pixel count of zero. As the ball entered frame (figure 6.5a), the white pixel count increased until the ball had fully entered (figure 6.5b). As the ball moved towards the racket, the apparent size of the ball decreased causing the white pixel count to decrease as well (figure 6.5c and d). The maximum white ball pixel count was found to consistently identify the image in which the ball had fully entered frame.

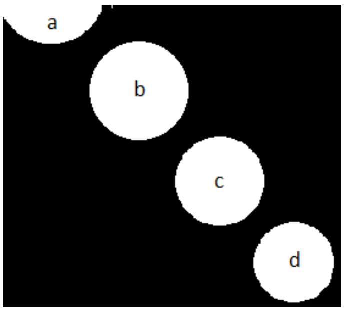

Figure 6.5 – A simulated composite image showing the ball over four sequential images. As the ball entered frame (a), the white pixel count increased. With the ball fully in frame (b), the white pixel count was maximal. As the ball moved towards the racket, away from the cameras (c and d), the white pixel count decreased.

To digitise the ball automatically, the algorithm first estimated the ball centre using *regionprops.centroid* and cropped the image around the ball (figure 6.6).

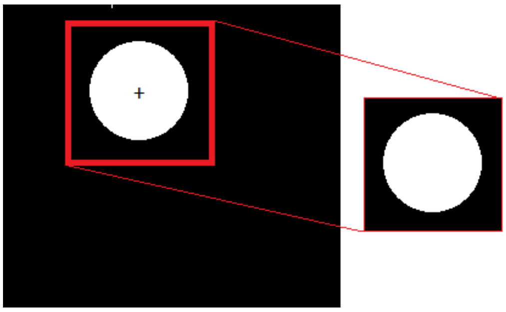

Figure 6.6 – A simulated processed image. The ball centroid, shown by '+', was estimated by *regionprops.centroid*. The image was cropped around the estimated centroid.

The cropped image was processed using *houghcirclemod* to return an accurate ball centroid. The function repeatedly analysed the white pixels, using a range of circle radii as inputs to the Hough Transform (figure 6.7). The radii range allowed for accurate digitisation as the apparent size (and radius) of the ball decreased. The reported ball centroid was taken from the best circle of best fit.

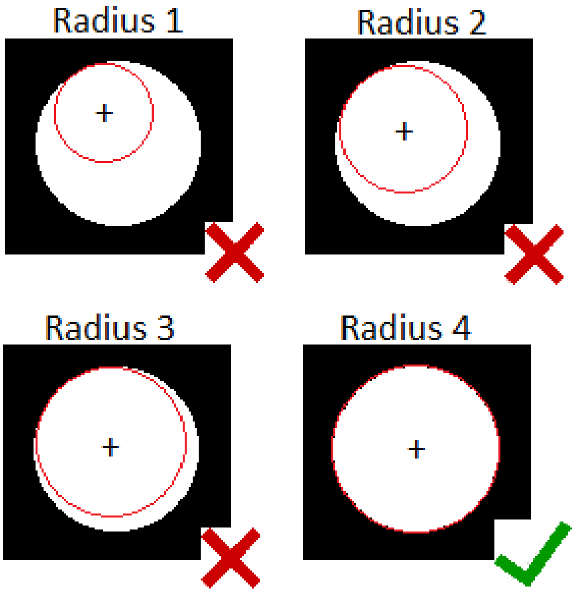

Figure 6.7 – Simulated ball images showing repeated digitisation of the ball using *houghcirclemod* and a range of circle radii to calculate ball centroid ('+'). The final radius best fits the perimeter of the ball.

6.5.2 Ball tracking

Given the initial centroid of the ball, the next image in the sequence was cropped using a large cropping rectangle. This ensured the next ball position was within the cropped region, as shown in figure 6.8. The size of the cropping rectangle was fine-tuned using sample impact test images.

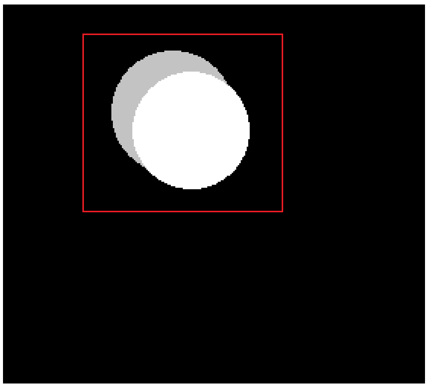

Figure 6.8 – Simulated composite image showing the 2nd ball position (white) overlaid onto the 1st ball position (grey). The cropping rectangle (red) was sufficient to ensure the 2nd ball position was included within the cropped image.

Once two centroids were digitised, a simple linear regression of the data was used to estimate the next ball position (figure 6.9). The method allowed a tight crop, which improved the efficiency of *houghcirclemod*.

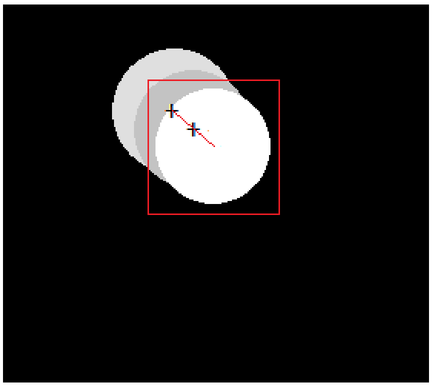

Figure 6.9 – A simulated composite image showing the estimated position of the ball (white) extrapolated from the centroids of the previous two images (red line). The image was cropped around the predicted position of the ball (red square).

6.5.3 Ball centroid reconstruction

The algorithm digitised the synchronised images from each camera simultaneously. The ball centroids were reconstructed to (*x, y, z*) real-world data using the Microsoft *.NET* class library, *Check3Dcore* (Check3D, 2012) and the intrinsic and extrinsic camera parameters. The (*x, y, z*) data were used to calculate the real-world distance between the ball and the stringbed plane. Ball tracking stopped when this distance fell below 33 mm (the mid-point of ball size specification (ITF, 2008a)) and the ball was in contact with the stringbed.

6.6 Ball data transformation

The (*x, y, z*) real-word data were initially relative to the left hand camera origin, described by the axis vectors $\left[\hat{X}_C, \hat{Y}_C, \hat{Z}_C\right]$ in figure 6.10. The data were transformed (rotated and translated) to the local racket origin, described by the axis vectors $\left[\hat{X}_R, \hat{Y}_R, \hat{Z}_R\right]$ in figure 6.10. The transformation used the stringbed markers as reference points within the calibrated test volume. The positions of the stringbed markers relative to the local origin and their digitisation is discussed in Chapter 5.

The stringbed marker (*x, y, z*) data were used to create an intermediate local origin, described by axis vectors $[\hat{X}_M, \hat{Y}_M, \hat{Z}_M]$ in Figure 6.10. The ball (*x, y, z*) data were first transformed to this intermediate origin and then to the local racket origin.

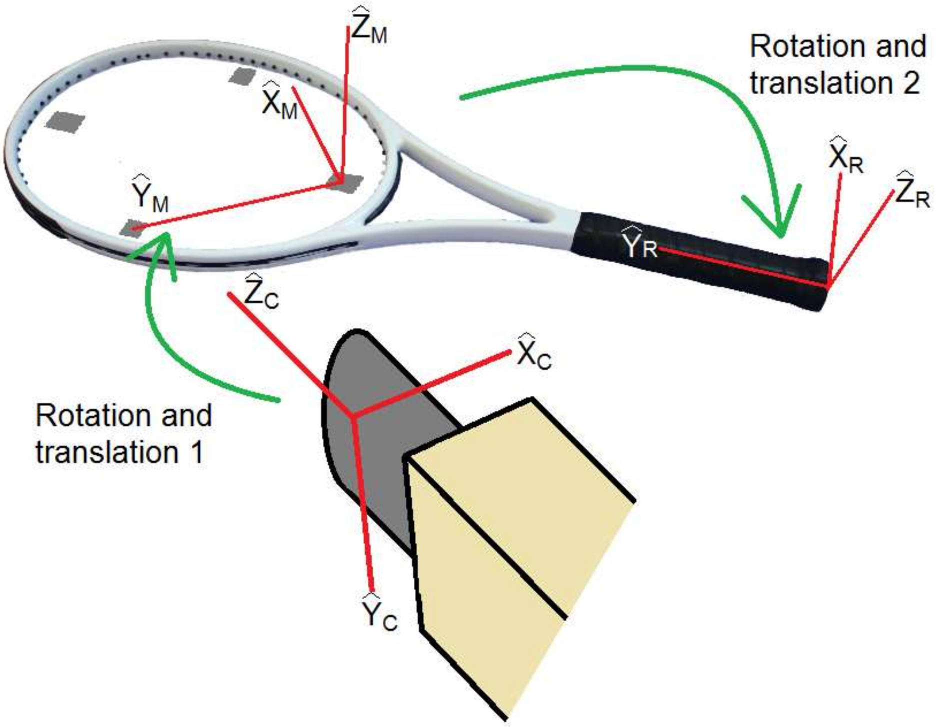

Figure 6.10 –Ball (*x, y, z*) data were transformed from the camera origin $[\hat{X}_C, \hat{Y}_C, \hat{Z}_C]$ to the local racket origin at the butt of the racket$[\hat{X}_R, \hat{Y}_R, \hat{Z}_R]$ using the stringbed markers as reference points within the calibrated test volume.

The two transformations used the same process, with the following example describing the first transformation from the camera origin to the intermediate origin. The translation matrix, **T** was calculated from the coordinates of the camera origin (X_C, Y_C, Z_C) and the intermediate origin (X_M, Y_M, Z_M):

$$\mathbf{T} = \begin{bmatrix} X_M - X_C \\ Y_M - Y_C \\ Z_M - Z_C \end{bmatrix} \quad 6.1$$

Reconstructed ball data (X_i, Y_i, Z_i) were translated to (X_j, Y_j, Z_j) relative to the intermediate origin:

$$\begin{bmatrix} X_j \\ Y_j \\ Z_j \end{bmatrix} = \mathbf{T} \begin{bmatrix} X_i \\ Y_i \\ Z_i \end{bmatrix} \tag{6.2}$$

The rotation matrix, **R** was calculated from the unit vectors describing the orientation of the camera origin $[\hat{X}_C, \hat{Y}_C, \hat{Z}_C]$ and the intermediate origin $[\hat{X}_M, \hat{Y}_M, \hat{Z}_M]$:

$$\mathbf{R} = \begin{bmatrix} \hat{X}_C \cdot \hat{X}_M & \hat{Y}_C \cdot \hat{X}_M & \hat{Z}_C \cdot \hat{X}_M \\ \hat{X}_C \cdot \hat{Y}_M & \hat{Y}_C \cdot \hat{Y}_M & \hat{Z}_C \cdot \hat{Y}_M \\ \hat{X}_C \cdot \hat{Z}_M & \hat{Y}_C \cdot \hat{Z}_M & \hat{Z}_C \cdot \hat{Z}_M \end{bmatrix} \tag{6.3}$$

The translated ball data (X_j, Y_j, Z_j) were rotated to (X_k, Y_k, Z_k) to orientate to the intermediate origin:

$$\begin{bmatrix} X_k \\ Y_k \\ Z_k \end{bmatrix} = \mathbf{R} \cdot \begin{bmatrix} X_j \\ Y_j \\ Z_j \end{bmatrix} \tag{6.4}$$

This process was then repeated using the known position of the local racket origin relative to the stringbed markers.

6.6.1 Intermediate stringbed origin

Prior to data transformation, the intermediate origin was defined from the stringbed markers. The intermediate origin was calculated using a three-step process to define the three axes $[\hat{X}_M, \hat{Y}_M, \hat{Z}_M]$:

1. First, a plane of best fit through the reconstructed stringbed marker coordinates was calculated using the *MATLAB* algorithm *fitNormal* (Mathworks, 2008). The stringbed marker coordinates were then translated onto this plane. The algorithm fit the plane in a least regression sense, outputting a normal unit vector, $\hat{Z}_M$ to the plane.
2. Next, the intermediate origin was placed at one stringbed marker and the second unit vector, $\hat{Y}_M$ calculated in the direction of a second stringbed marker.
3. Third, the unit vector, $\hat{X}_M$ was calculated as the cross product of $\hat{Y}_M$ and $\hat{Z}_M$.

For the second step (origin position and $\hat{Y}_M$ unit vector direction), the four stringbed markers gave six options:

1) Origin at the throat marker, $\hat{Y}_M$ in the direction of the nine o'clock marker (red line in figure 6.11).
2) Origin at the throat marker, $\hat{Y}_M$ in the direction of the three o'clock marker (cyan line in figure 6.11).
3) Origin at the throat marker, $\hat{Y}_M$ in the direction of the tip marker (orange line in figure 6.11)
4) Origin at the nine o'clock marker, $\hat{Y}_M$ in the direction of the three o'clock marker (purple line in figure 6.11).
5) Origin at the nine o'clock marker, $\hat{Y}_M$ in the direction of the tip marker (brown line in figure 6.11).
6) Origin at the tip marker, $\hat{Y}_M$ in the direction of the three o'clock marker (pink line in figure 6.11).

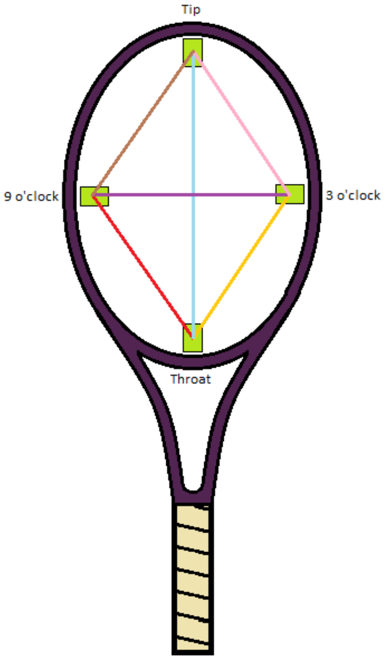

Figure 6.11 – The four racket markers offered six intermediate origins, using combinations of markers define the 2nd unit vector $\hat{Y}_M$. The six possible combinations are shown.

To select the best option, each was used to translate the stringbed marker coordinates to the local racket origin. The final translated centroids were assessed against the measurements made using the Racket Calibration tool (Chapter 5).

To do this, six translation matrices $\mathbf{T1}_{1\text{-}6}$ and rotation matrices, $\mathbf{R1}_{1\text{-}6}$ were calculated to transform the stringbed marker (x, y, z) data using equations 6.2 and 6.4. The racket parameter data was used to calculate a further six translation matrices $\mathbf{T2}_{1\text{-}6}$ and rotation matrices, $\mathbf{R2}_{1\text{-}6}$ to transform the (x, y, z) data from each of the intermediate origins to the local racket origin. For each transformation, the final stringbed marker coordinates relative to the local racket origin were compared to the racket parameter data. The translation and rotation matrices resulting in the smallest average error were used to transform the ball coordinates.

6.6.2 Ball velocity calculation

Ball velocities were calculated from simple linear regression of each velocity component against time. For inbound velocity, all inbound data were used, which was found experimentally to be no more than 20 frames. For outbound velocity, no more than 20 data points immediately post-impact were used. Restricting the data minimised the effects of gravity and drag. As such, the accelerations on the ball due to gravity and drag were assumed to be zero. This simplified the system being modelled, considering only ball velocities in context of the impact with the racket. To justify this assumption, the accelerations were calculated.

6.6.3 Ball accelerations

The accelerations due to gravity and drag acting on the ball were calculated. Figure 6.12 shows the inbound trajectory, V_{iR} was subject to an acceleration due to gravity, ΔV_a and deceleration due to drag forces, ΔV_d. The outbound trajectory, V_{oR} was subject to decelerations from both gravity and drag.

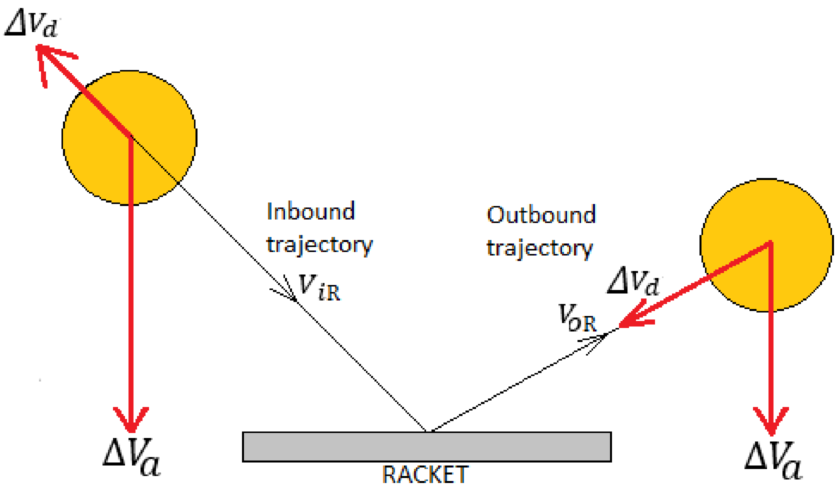

Figure 6.12 – A diagram of the accelerations acting on the ball due to gravity and drag. Gravity acts to accelerate the ball on the inbound trajectory and decelerate the ball on the outbound trajectory. Drag decelerates the ball in both cases.

The velocity calculations were derived from no more than 20 frames of digitised trajectory – a time, t of 0.02 s for a camera frame rate of 1000 frames per second. In that time, the change in the vertical component of velocity, ΔV_v due to gravity, a_g of 9.81 m·s^{-2} was calculated from:

$$\Delta V_v = a_g \cdot t \qquad 6.5$$

As the racket was mounted horizontally and the ball fired downwards, the change in the vertical component of velocity due to gravity over 0.02 s was 0.2 m·s^{-1} for the inbound trajectory and -0.2 m·s^{-1} for the outbound trajectory.

The drag force, D acting on the ball was calculated using:

$$D = C_D \cdot \frac{\rho V^2}{2} \cdot A \qquad 6.6$$

where C_D was the coefficient of drag, ρ was the density of air, V was the velocity of the ball and A was the frontal area of the ball, calculated using:

$$A = \pi r^2 \qquad 6.7$$

where r was the radius of the ball. The acceleration on the ball, a_D due to this drag force was calculated using Newton's second law of motion:

$$a_D = \frac{D}{m_b} \qquad 6.8$$

where m_b was the mass of the ball. Substituting 6.6 into 6.7 and then substituting this into 6.8, the change in velocity due to drag, ΔV_d was calculated using:

$$\Delta V = C_D \cdot \frac{\rho V^2}{2} \cdot \pi r^2 \cdot \frac{1}{m_b} \cdot t \qquad 6.9$$

For a tennis ball C_D of 0.65 (Goodwill et. al., 2004), ρ = 1.225 kg·m^{-3}, a ball velocity of 20 m·s^{-1}, ball radius of 0.033 m, ball mass of 0.057 kg and time 0.02 s, the change in velocity due to drag was 0.02 m·s^{-1}.

The changes in ball velocity were therefore negligible, justifying the use of linear regression to calculate the inbound and outbound velocities. These measurements also justify the design of the test rig, with the racket mounted horizontally and the ball launched downwards.

6.7 Automated ball digitisation validation

To validate the automated ball digitisation algorithm required a standard against which to compare results, such as a pair of light gates. Cottey (2002) used ballistic light gates to measure the launch velocity of tennis ball. He carried out a three-way validation of the light gates, using both an electronic calibration signal (to trigger the light gates) and manual digitisation of high-speed camera images. For a range of 25 to 40 m·s^{-1}, Cottey found the light gates over-measured velocity by 3.9%, whilst the high-speed camera method over-measured by 1.3%. For slower ball velocities, the ITF (2015) validated a pair of Oehler Model 55 light gates (Oehler Research, 2007) and manual digitisation of high-speed camera images against a vertical drop model, which simulated a drop height of 2.54 m. For an instantaneous velocity of 6.4 m·s^{-1}, the light gates under-measured ball velocity by 2.0%, whilst the high-speed camera method under-measured by 0.5%.

Based on these findings, manual digitisation is a sufficiently accurate method to compare the automated ball digitisation algorithm against. Accuracy aside, the advantages of this approach are:

1. Digitisation is limited only by the cameras field of view. Therefore, a ball could be digitised up to the point of contact with a racket. The size and weight of light gates limits their implementation, which is also typically a short gauge length.
2. Once (*u, v*) image coordinates are reconstructed, ball velocities can be measured in any plane. The accuracy of stereo reconstruction was covered in Chapter 4. Light gates, such as the Oehler Model 55, are limited to a single dimension.

Validation of the automated ball digitisation algorithm required three stages:

1. Establish the repeatability of manually digitising the ball.
2. Establish the error of automated ball digitisation by comparison to manual digitisation.
3. Calculate the discrepancy between ball velocities calculated using the automated and manual ball digitisation data.

For this, the Impact Rig was set up to launch balls on to a realistically supported racket. A total of 11 impacts were collected.

6.7.1 Manual ball digitisation repeatability

The repeatability of manually digitising the ball was established through 10 repeat trials of the first impact, using *Check3D* (2012). Example test images are shown in figure 6.13.

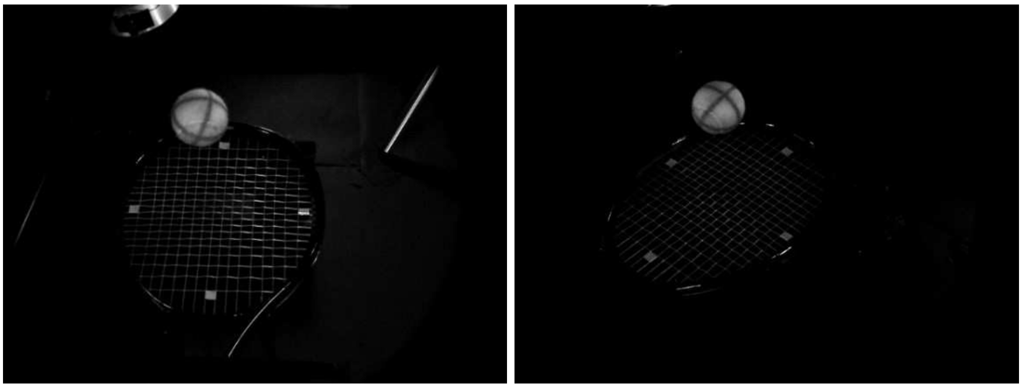

Figure 6.13 – Example images of the ball during an impact test imaged in the left (left) and right (right) cameras.

The impact comprised eight inbound frames and 19 outbound frames. The ball was considered sufficiently similar in all frames from both cameras to calculate a single pooled standard deviation for both components of the ball centroid – a total of 1,080 data points. The pooled standard deviation is shown in table 6.1.

Table 6.1 – The pooled standard deviation for manually digitising the ball was calculated from repeat digitisation of one impact. Ball centroid component data for both cameras were combined (n = 1,080).

Pooled standard deviation (p)	0.4

6.7.2 Comparing automated and manual ball digitisation

Part two of the validation compared the automated ball algorithm to manual digitisation. A further 10 impacts were digitised with both methods, comprising a total of 311 frames for both inbound and outbound trajectories. As with the previous section, the ball was considered sufficiently similar to pool coordinate data from both cameras. This gave a data set of 1,244 points. The mean discrepancy between the automated algorithm and manual digitisation are shown in table 6.2.

Table 6.2 – The error of automated ball digitisation calculated from 10 impact tests (n = 1,244).

Mean discrepancy (p)	-0.5

The error of the automated algorithm (-0.5 pixels) was greater than the repeatability of manual digitisation (0.4 pixels) shown in table 6.1. This suggests the automated algorithm was not as accurate as manual digitisation. However, the effect of the systematic error when automatically digitising absolute ball position measurement does not necessarily effect the calculation of ball velocity. This is discussed in the next section. The effect of the systematic error could influence the calculated impact location of the ball on the stringbed. This is discussed in the next chapter.

6.7.3 Velocity measurement validation

To calculate velocities from manual and automated ball digitisation, the ball centroids from the 10 impacts were reconstructed to (*x, y,* z) real-world data using the camera calibration. The component inbound velocities (V_{ix}, V_{iy}, V_{iz}) and component outbound velocities (V_{ox}, V_{oy}, V_{oz}) were calculated for each impact using a simple linear regression (described in section 6.6.2). The mean discrepancies between the automated and manual data and standard deviations are shown in table 6.3.

Table 6.3 – The error in component ball velocity measurements for automated ball digitisation for inbound and outbound trajectories (n = 10).

	Velocity error ($m \cdot s^{-1}$)	Standard deviation ($m \cdot s^{-1}$)
V_{ix}	0.0	0.1
V_{iy}	-0.1	0.0
V_{iz}	0.1	0.2
V_{ox}	0.0	0.0
V_{oy}	0.0	0.0
V_{oz}	0.0	0.1

The largest mean error was 0.1 m·s^{-1}, with standard deviation of 0.2 m·s^{-1}. This suggests the -0.5 pixel error of automated ball digitisation was systematic and did not result in meaningful ball velocity error.

6.8 Conclusion

This chapter described the development and validation of an automated ball tracking algorithm. The ball was tracked and digitised in high-speed camera image pairs in to and out of impacts with the realistically support racket.

The automated algorithm used several *MATLAB* image processing algorithms. To improve ball segmentation from image backgrounds, a user interface was designed to fine tune the image processing parameters. The algorithm identified the ball using a white pixel count. Thanks to elevated cameras, the white pixel count increased to a maximum when the ball had fully entered frame. As the ball moved towards the racket, the white pixel count decreased. As ball centres were digitised, the algorithm extrapolated the ball trajectory to improve tracking efficiency by estimating successive ball centres.

The ball image (*u, v*) coordinates were reconstructed to three-dimensional (*x, y,* z) real-world coordinates using the high-speed camera calibration parameters. The real-world data was transformed to the local racket origin, using the stringbed markers and racket parameter data. Ball velocities were calculated from no more than 20 frames of reconstructed and transformed data using 1st order regression. This assumed accelerations on the ball due to gravity and drag were small and simplified the system in terms of modelling complexity. The changes in velocity due to gravity and drag over 20 frames (0.02 s) were 0.2 m·s^{-1} and 0.02 m·s^{-1} respectively.

The automated algorithm was validated by comparison to manual digitisation. A systematic error of -0.5 pixels for the automated method was greater than the repeatability of manual digitisation. However, the effect of this error on ball velocity calculations was found to be negligible. The maximum error for component and resultant ball velocities calculated from automated digitisation was 0.1 m·s^{-1}.

In the next chapter, an impact location measurement method is described. The method uses ball data and stringbed marker centroids to calculate the intersection between the ball trajectory and stringbed plane.

Chapter 7 – Impact location

7.1 Introduction

The previous chapter discussed the measurement of ball velocities from digitised ball centroids. The direct measurement was required due the inherent variability of the BOLA ball launch device (discussed in Chapter 3). Further to this, and discussed in this chapter, a method was developed to measure impact locations from the ball trajectory of each test. This analysis of the impacts is shown diagrammatically in the project flowchart in figure 7.1.

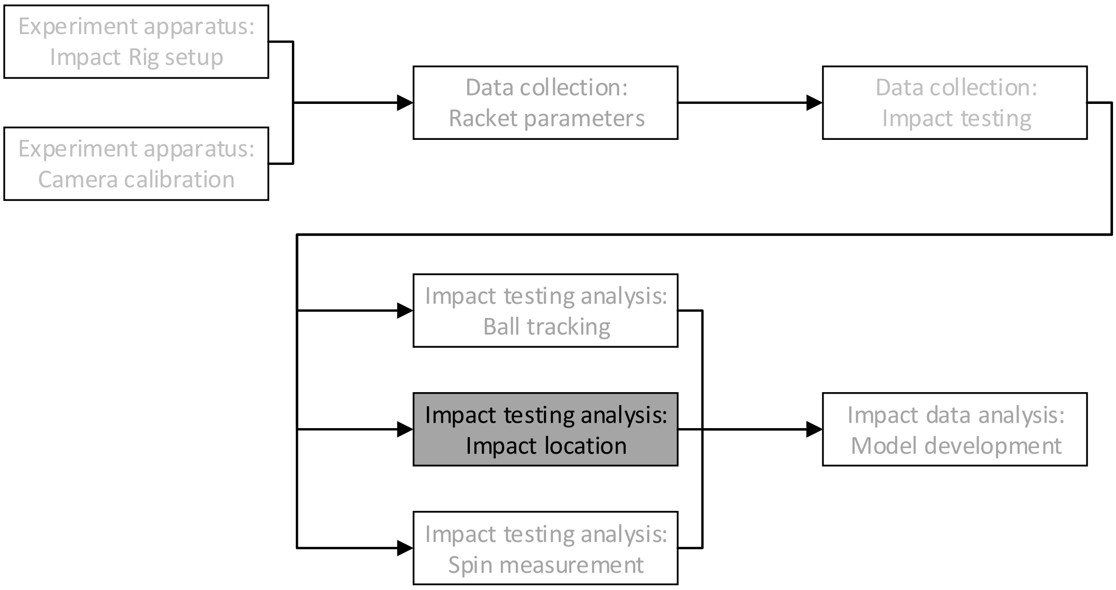

Figure 7.1 - Flowchart outlining the scope of the project. The chapter describes the development of an impact location measurement.

Impact locations were defined as a two-dimensional point measured at the initial contact between the bottom of the ball and the strings. This was calculated from the intersection of the inbound ball trajectory and the stringbed plane, using an assumed nominal ball radius for a Type 2 tennis ball of 33 mm (ITF, 2008a).

The calculated error of the method was used to conduct a sensitivity analysis. This established the effects of small variations in impact locations on outbound ball velocity. For this, a mechanical model was used to simulate ball impacts at two locations on the stringbed.

As the ball was not tracked through the impact, a pilot study was also conducted to quantify ball-to-string interactions. The results provided insight into the inherent variability of an impact.

7.2 Objectives

The objectives of this chapter are:

1. Develop and validate a method to measure impact locations for each impact test.
2. Establish the sensitivity of outbound velocity to small changes in impact location using a simple ball-racket mechanical model.

7.3 Impact location method

Impact location was defined as the initial point of contact between the bottom of the ball and the strings. This definition aligns with ITF racket tests, most notably the ITF *Spin Rig* and ITF MYO racket power machine (Allen, 2009 and Goodwill, 2003b). This also simplifies the required digitisation of the high-speed camera images, as the ball does not need to be tracked through an impact.

Two data were required to calculate impact locations:

1. The inbound trajectory of the ball, using the method described in Chapter 6.
2. The stringbed plane, calculated from the centroids of the stringbed markers digitised in each impact test using the method described in Chapter 5.

Ball trajectories were transformed to the local racket origin, using the stringbed marker centroids as reference points to define a local coordinate system (schematic shown in figure 7.2). In this transformed frame of reference, the z-component of the inbound ball trajectory equated to the vertical distance of the ball centroid above the stringbed plane. Using the known frame rate of the high-speed cameras, a simple linear regression was fit to the z-component data against time. From this, the time, t_{impact} was calculated for a z-component of 33 mm - the midpoint of ball size specification for a Type 2 tennis ball (ITF, 2008a). At t_{impact}, the bottom edge of the ball was intersecting the stringbed plane, thereby defining impact locations as the initial point of contact between the ball and stringbed. The method is shown in figure 7.2.

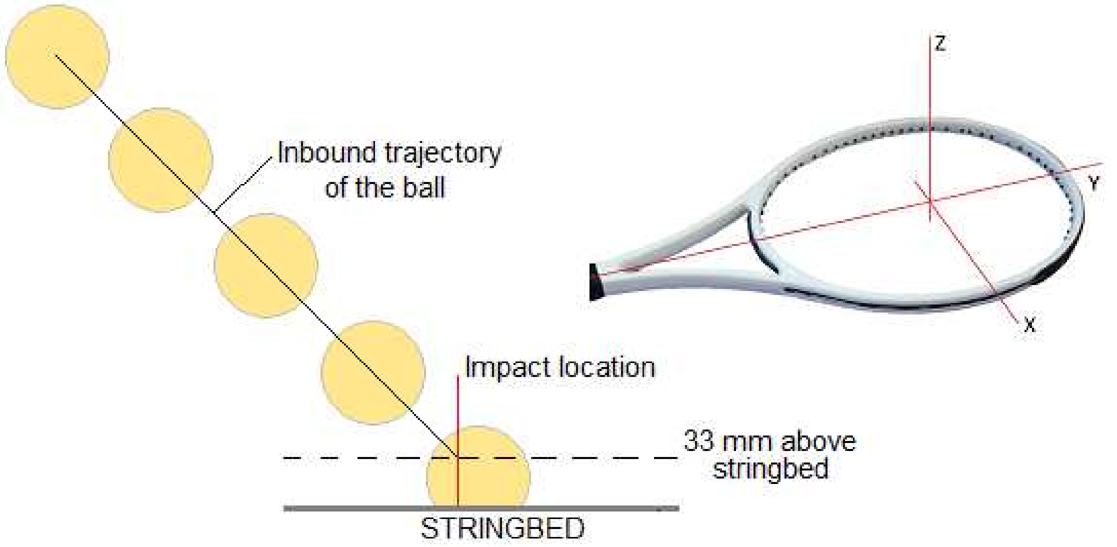

Figure 7.2 –. Using a local coordinate system shown on the racket schematic, impact locations were calculated from simple linear regressions of the ball trajectory components against time. An assumed ball radius of 33 mm was used to calculate the time t_{impact}, at which the ball and stringbed intersected.

Simple linear regressions were then fit to the x- and y-component ball trajectory data against time. Using t_{impact}, the lateral (x-component) and longitudinal (y-component) ball coordinates were calculated, giving impact locations relative to the local origin.

7.4 Impact location error

The error of the impact location method was calculated by comparing the impact locations measured from automated ball digitisation to those measured from manual ball digitisation. For this, data from the ball digitisation validation study (Chapter 6, section 6.7) were used. Ball centroids were digitised manually and automatically for the inbound trajectories of 10 impacts. The data were transformed to the local origin using automatically digitised stringbed marker centroids (see method in Chapter 5). Ball centroid transformation is described Chapter in 6, section 6.6.

Impact location error was defined as the mean of the Euclidean distances between the impact locations calculated from the automated and manual data. The mean and standard error of the mean are shown in table 7.1.

Table 7.1 – The mean error and standard error for impact locations measured from automatic digitisation. (n = 10).

Mean error (mm)	1.5
Standard error of the mean (mm)	0.2

The data shows a systematic error of 1.5 mm for the automatic digitisation data. The error is systematic given the low standard error. This cause of this error was the previously calculated systematic error of the automated ball digitisation algorithm, which was measured as having a 0.5 pixel discrepancy to manual digitisation (see section 6.7.1). Given the benefit of the automated analysis, the impact location error was deemed acceptable. This was justified using a rigid body ball-to-racket impact model to establish the sensitivity of ball rebound velocity for small changes in impact location.

7.5 Impact location sensitivity

The rigid body ball-to-racket impact model described by Brody *et. al.* (2002) calculated ball rebound velocities, V_2 from the apparent coefficient of restitution (ACOR) of a ball to racket impact:

$$V_2 = V_1 \cdot e_A \qquad 7.1$$

where V_1 was the inbound ball velocity and e_A was the ACOR. To calculate the ACOR, Brody used the concept of 'effective mass' to describe the racket mass at the impact location:

$$e_A = \frac{eM_e - m_b}{M_e + m_b} \qquad 7.2$$

where e was the experimentally determined coefficient of restitution (COR) of the ball to racket impact (Brody, 1997), M_e was the effective mass of the racket at the impact point and m_b was the mass of the ball. Effective mass, M_e was calculated using:

$$\frac{1}{M_e} = \frac{1}{m_r} + \frac{b^2}{I_X} + \frac{c^2}{I_Y} \qquad 7.3$$

where m_r was the mass of the racket, b was the transverse distance from the racket centre of mass to impact location, c was lateral distance from the racket centre of mass to impact location, I_X was the transverse mass moment of inertia and I_Y was the polar mass moment of inertia of the racket. These are shown diagrammatically in figure 7.3.

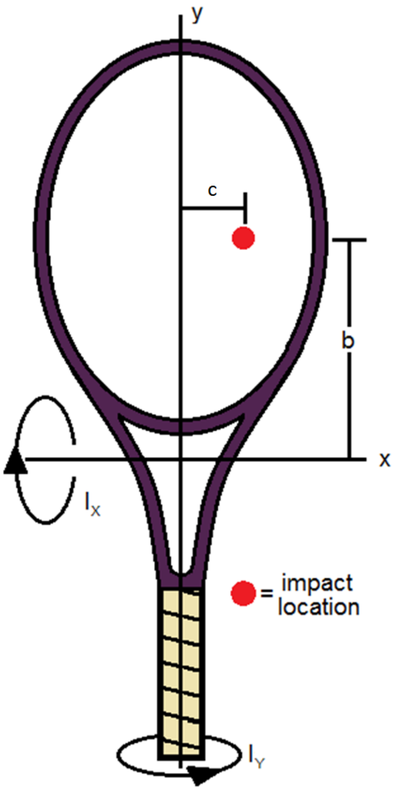

Figure 7.3 – The effective mass of the racket at an impact point on the stringbed calculated from racket properties.

The model parameters used in this study are shown in table 7.2. The COR, e was taken from Brody (1997) and racket mass moments of inertia from Spurr *et. al.* (2014).

Table 7.2 – The rigid body racket model parameters used to model the rebound velocity of a ball impact.

COR, e	0.850
Ball mass, m_b (kg)	0.057
Racket mass, m_r (kg)	0.346
Transverse mass moment of inertia, I_X (kg·m^2)	0.01640
Transverse mass moment of inertia, I_Y (kg·m^2)	0.00142

Impacts were modelled at two points on the stringbed – the first at the geometric stringbed centre (GSC), the second at a 5 cm lateral offset from the GSC. To establish the sensitivity of rebound velocity to small changes in impact location, impacts were simulated for 1 mm and 2 mm offsets from the start locations. Tables 7.3 and 7.4 show the percentage change in rebound velocity at the incremental impact locations, compared to their respective start locations.

Table 7.3 – The percentage differences of modelled outbound velocities for impacts offset by 1 and 2 mm from the start position at the GSC (green cross). The impact locations are shown on the racket schematic (black dots).

		Lateral impact location (m)				
		-0.002	-0.001	0.000	0.001	0.002
Longitudinal impact location (m)	0.002	-0.8%	-0.7%	-0.7%	-0.7%	-0.8%
	0.001	-0.4%	-0.4%	-0.4%	-0.4%	-0.4%
	0.000	-0.0%	-0.0%	-	-0.0%	-0.0%
	-0.001	0.3%	0.4%	0.4%	0.4%	0.3%
	-0.002	0.7%	0.7%	0.7%	0.7%	0.7%

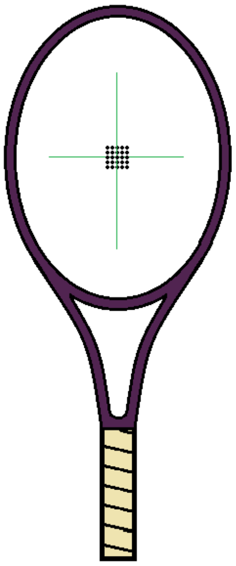

Table 7.4 – The percentage differences of modelled rebound velocities for impacts offset by 1 and 2 mm from the start position with 5 mm lateral offset from the GSC (green cross). The impact locations are shown on the racket schematic (red dots).

		Lateral impact location (m)				
		-0.052	-0.051	-0.050	-0.049	-0.048
Longitudinal impact location (m)	0.002	-3.2%	-2.0%	-0.8%	0.4%	1.5%
	0.001	-2.8%	-1.6%	-0.4%	0.8%	1.9%
	0.000	-2.4%	-1.2%	-	1.2%	2.3%
	-0.001	-2.0%	-0.8%	0.4%	1.6%	2.8%
	-0.002	-1.6%	-0.4%	0.8%	2.0%	3.2%

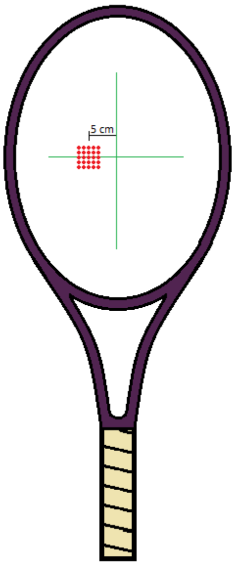

The changes in rebound velocities were less than 1% for impacts up to 2 mm from the start position at the GSC. When that start position was offset from the GSC by 5 cm, the changes were as much as 3.2% for 2 mm offsets.

Brody (1997) determined the COR experimentally, from normal ball impacts onto a head clamped racket. The racket was effectively a rigid body and therefore not subject to energy loses due to racket vibration. For impacts at the racket node, near the GSC, racket vibrations are not excited making and head-clamped racket impacts comparable to a handle clamped racket. For impacts away from the GSC, racket vibrations are increasingly significant, making Brody's COR artificially high. Therefore, the simulated rebound velocities for the start position offset from the GSC were over-estimations, making the measured changes in rebound velocities over-estimates, also. However, the simulated impacts do provide an estimate of the implications a 1.5 mm discrepancy in impact location.

7.6 Ball-to-stringbed interactions

Reducing the measurement of ball-stringbed interactions to the initial contact simplified the development of analysis methods. However, during an impact, the ball can remain in contact with the stringbed for up to 6 ms (Brody, 1979). During this time, the ball will deform and slide or roll across the string-bed. The stringbed will also deform, with individual strings displacing laterally – an important mechanism in spin generation (Haake et. al., 2012). Cottey (2002) measured ball-stringbed contact times and distance travelled by the ball across the stringbed for a range of angles of incidence, inbound velocities and stringing tensions. The variability measured for repeat inbound parameters showed the inherent variability of ball and stringbed. Given how the ball and stringbed interaction (and variability of) will influence rebound ball trajectory, but were not measured during impact testing, a pilot study was conducted in extension of Cottey's testing to measure:

1. Euclidean distance of ball travel.
2. Number of strings contacted.
3. Maximum lateral string displacement.
4. Total number of strings with lateral displacement.

The ball and stringbed are imperfect objects, and any observed variabilities in their interactions will help to inform the later analysis of the main data collection. In particular, this will help in evaluating the predictive power of the models generated.

7.6.1 Ball-to-stringbed interactions method

An ITF *Development* racket was strung with ITF *Development* string at a tension of 60 lbs – the racket and string used for the main data collection undertaken in this project. The racket was left for 24 hours under climate controlled conditions of 20°C ± 2°C and 60% ± 5% relative humidity. Impact testing was carried out using the ITF *Spin Rig* (Goodwill et. al., 2006), with the racket head-clamped to a heavy steel base (approximately 50 kg). Head-clamping isolated the inertial properties of the racket, allowing the stringbed to be investigated. The racket clamp could be rotated about its long axis, with the angle between the racket and inbound ball set to a 20° angle of incidence. This setting served two purposes, the first being to replicate the angle of incidence for the Impact Rig. The second, to make visible the underside of the stringbed. A Vision Research *Phantom v4.2* high-speed camera was positioned to film the underside of the stringbed, using a mirror secured underneath the racket stringbed. The equipment set up is shown in Figure 7.4, with an example of the view of the stringbed.

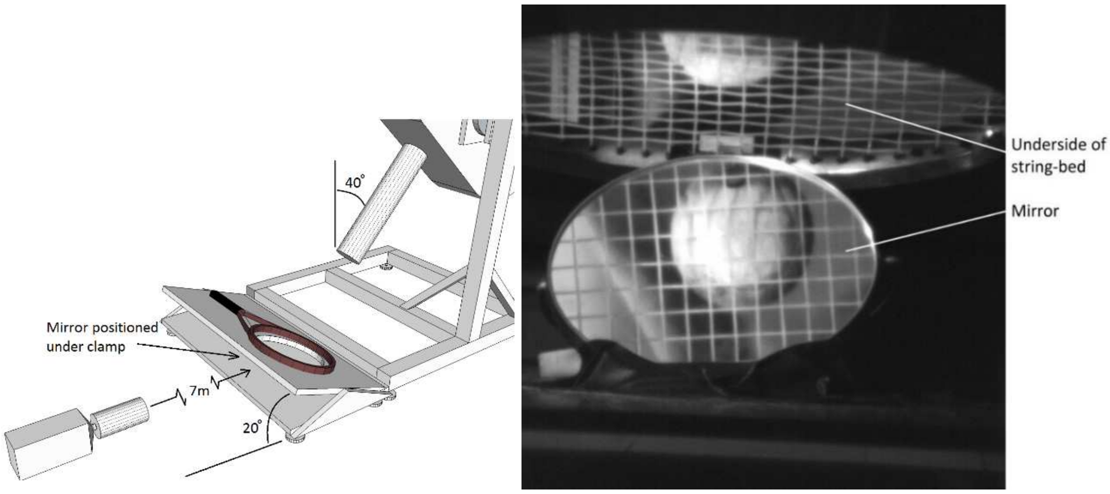

Figure 7.4 –Impact testing set up using the ITF *Spin Rig* (left) allowed the racket to be rotated making the stringbed visible via a mirror placed under the racket (right).

The camera frame rate was set to 1000 frames per second, with an exposure time of 70 µs. Two 500W halogen lamps were positioned to provide sufficient light onto the string-bed, resulting in a well illuminated ball image. A calibration image was recorded, with a 150 mm steel ruler placed onto the stringbed to provide a gauge length in the plane of the stringbed.

In total, 20 impacts were filmed, with nominal inbound ball velocities of 25 $m \cdot s^{-1}$ ± 2 $m \cdot s^{-1}$. The impacts were split into two sets of 10, the first with 0 $rad \cdot s^{-1}$ ± 40 $rad \cdot s^{-1}$ inbound spin, the second with 400 $rad \cdot s^{-1}$ ± 40 $rad \cdot s^{-1}$ of backspin. *Check2D* (2012) was used to manually digitise the high-speed camera images of each impact. The first and last frames with contact between the ball and stringbed were identified. During these frames, the following steps were taken to record the necessary information:

1. *Euclidean distance of ball travel*

Manual digitisation of ball centres to calculate the total Euclidean distance (Deza et. al., 2009) travelled by the ball whilst in contact with the stringbed. Converted to real-world length using the calibration factor calculated from the calibration image of the 150 mm steel ruler. The scatter in ball launch may have resulted in variations in direction travelled relative to the orientation of the strings. Given this was a pilot study, the Euclidean distance travelled was a suitable starting point to measure this interaction between the ball and stringbed.

2. *Number of strings contacted*

Count the number of individual strings with observe contact to the ball during impact.

3. *Maximum lateral string displacement*

Identify the string with maximum lateral displacement. Manually digitise the string at the start of impact and the frame of maximum displacement. Converted to real-world length using the calibration factor calculated from the calibration image of the 150 mm steel ruler. To correct for apparent string displacement due to the stringbed deforming, the apparent displacement of a string near to the impact location was measured for each test and used to correct the maximum string displacement. Figure 7.5 shows an impact sequence with the highlighted string showing maximum displacement.

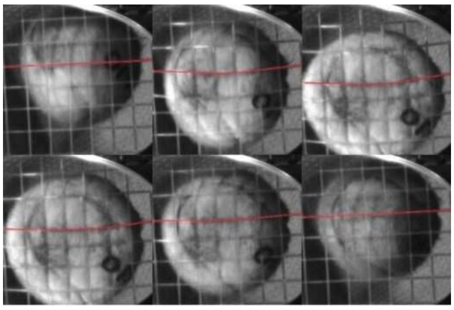

Figure 7.5 – An impact sequence showing the string of maximum lateral displacement (red).

4. *Total number of strings with lateral displacement.*

Count the number of strings observed to displace laterally, beyond any obvious displacement caused by the stringbed deforming.

7.6.2 Ball-to-stringbed interactions results

Figure 7.6 shows the mean Euclidean distance travelled by the ball, for impacts launched with no inbound spin and inbound backspin. The whiskers indicate the range of distances measured.

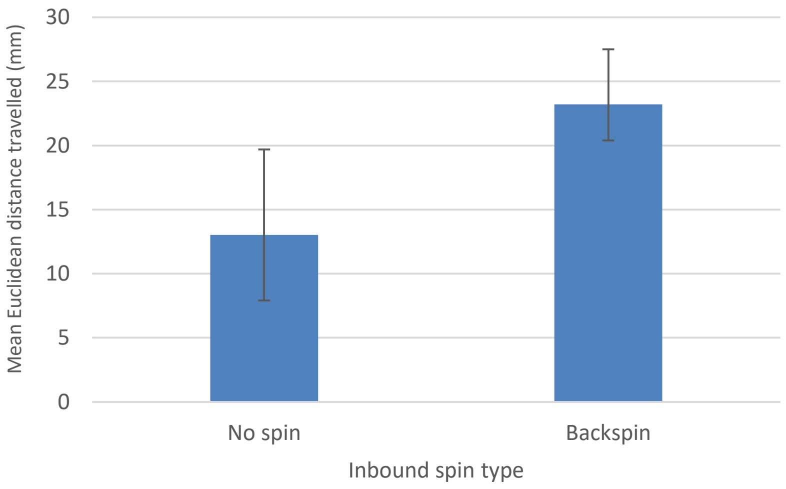

Figure 7.6 – A bar chart showing the mean Euclidean distance travelled by the ball during contact with the stringbed. The results are split by the inbound ball spin direction. The whiskers indicate the range of distances measured (n = 20).

Table 7.5 shows the modal number of strings contacted by the ball and the number of those strings displacing laterally. The data is presented by the inbound ball spin.

Table 7.5 – The modal number of strings contacted by the ball and the number of strings with lateral displacement by inbound ball spin (n = 20).

	No. of strings contacted	No. of strings displacing
No spin	5	3
Backspin	5	2

Figure 7.7 shows the mean maximum lateral string displacement, for impacts launched with no inbound spin and inbound backspin. The whiskers indicate the range of maximum lateral displacements measured.

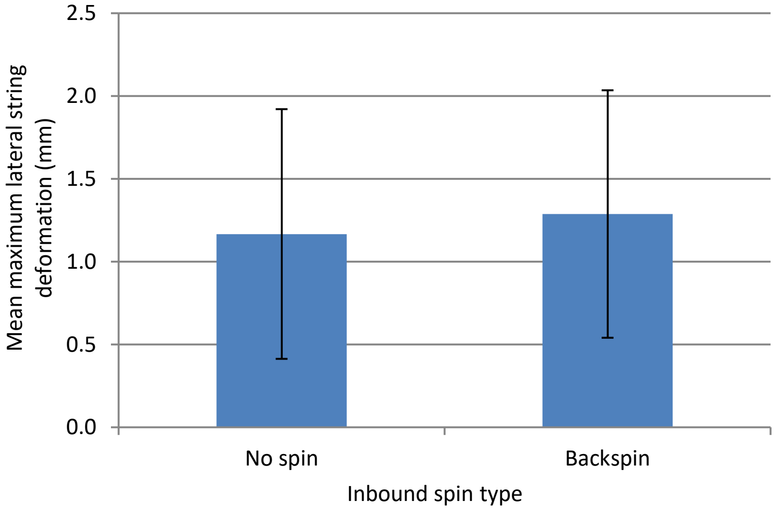

Figure 7.7 – A bar chart showing the mean maximum lateral string displacement by inbound spin type. The whiskers indicate the range of lateral displacements measured (n = 20).

Although the sample sizes were small, some useful observations were made. Moving from the impacts with no inbound spin to inbound backspin, the mean contact length increased from 13.0 mm to 23.2 mm and the mean maximum string displacement increased from 1.2 mm to 1.3 mm. Five strings were contacted by the ball for both spin types, but the total number of string displacing laterally decreased from three to two, as backspin was applied to the ball.

The range of contact lengths and maximum string displacement signifies low repeatability for the interactions. This was expected for two reasons:

1. The variability of ball launch (velocity, spin rate) causing variability in impact location.
2. The imperfect nature of the test objects and the effects of repeated testing on, for example, the initial position of the strings.

Although the effects of the two causes of variability were not isolated, it is highly likely they will influence the rebound trajectory of the ball. Given the difficulty of measuring the ball and stringbed interactions for a handle clamped racket, due to racket displacement during impact, the data presented offers useful insight for later analysis of the main impact testing dataset. The nature of this project requires control of the test apparatus and test objects to collect high-quality data. As such, the effects of the variability of ball launch on rebound trajectory are investigated further in Chapter 9.

7.7 Conclusion

This chapter described the method to measure impact location for each impact test. Using inbound ball trajectory and stringbed marker centroids, the initial intersection between the ball and stringbed plane is calculated for an assumed ball radius of 33 mm.

Impact location error was established by comparing the measurements using manually and automatically digitised ball centroid data. The mean error between impact locations was 1.5 mm. The effect on this error was established using a simple rigid body racket model to quantify the sensitivity of rebound ball velocity to small changes in impact location. The 1.5 mm error equated to a less than 1% difference in the rebound velocities for ball impacts near the geometric stringbed centre. This increased to a 3.2% difference for impacts at a 5 cm lateral offset from the geometric stringbed centre. This value was shown to be an over-estimation due to the rigid body model negating the effects of racket vibrations. These results justified the use of automated digitisation, which vastly decreased analysis time.

The ball was not tracked through the impact, reducing the complexity of analysing the high-speed camera images of impact testing. To justify this simplification, a pilot study was conducted to quantify the interactions between the ball and stringbed. Ball contact length, the number of strings contacted, the number of strings displacing laterally and the maximum lateral displacement were measured for 20 impacts with no inbound spin and inbound backspin. When backspin was applied to the ball, the mean contact length increased by 10.2 mm. The majority of impacts contacted five strings with the number of strings laterally displacing decreased from three to two as backspin was applied to the ball. There was also a small increase of 0.1 mm in the mean maximum string displacement as backspin was applied to the ball. The range of the data suggested small changes at the start of an impact (e.g. impact location, position of the strings etc.) could have measurable effects on the rebound characteristics of the ball. The implications of test apparatus and test object variability are explored further in Chapter 9, with a study to quantify the inherent variability of repeat impacts.

In the next chapter, ball spin measurements are described. The method employed used markings on the ball to measure the spin rate and spin axis of the ball over the inbound and outbound trajectories. A method was developed to correct for perspective error due to the proximity of the cameras to the test volume.

Chapter 8 – Spin measurements

8.1 Introduction

In addition to ball velocities and impact locations, ball spin was a required metric for this study. This chapter describes the implementation of an automated spin measurement algorithm, *SpinTrack3D* (Kelley, 2011a). This measurement step is represented diagrammatically in the project flowchart shown in figure 8.1.

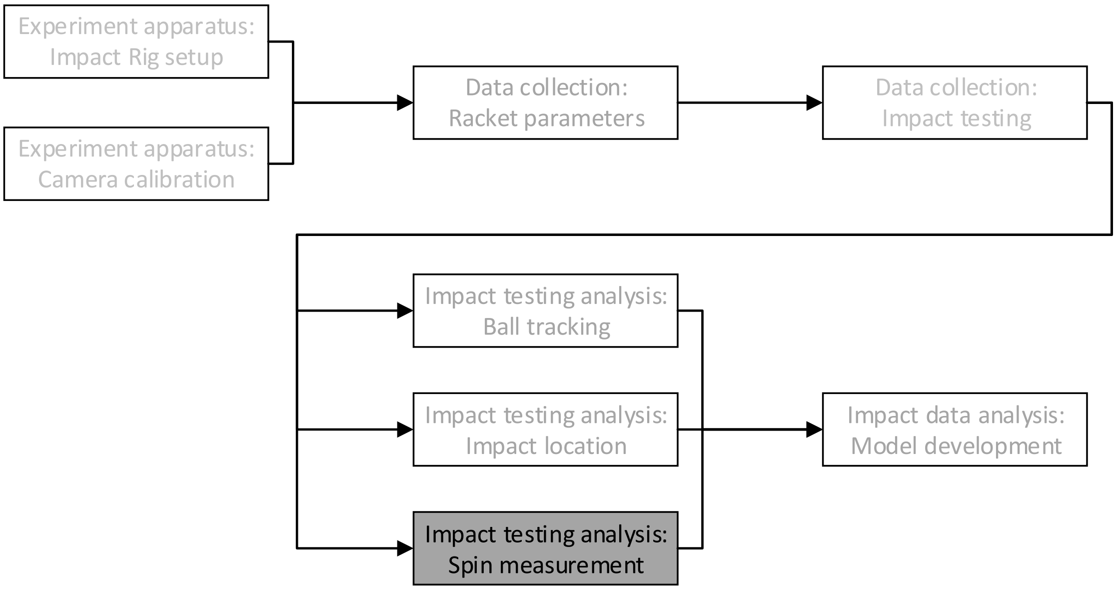

Figure 8.1 - Flowchart outlining the scope of the project. The chapter describes the implementation of an automated spin measurement algorithm.

The *SpinTrack3D* algorithm measured spin by comparing ball markings in consecutive camera images. Additional ball markings were added to the ball to assist this method. The algorithm outputs spin rate as a clockwise angle of rotation about a three-dimensional vector describing the spin axis. Spin was measured for inbound and outbound trajectories.

The *SpinTrack3D* algorithm was modified to correct for perspective error caused by the proximity of the high-speed cameras to the Impact Rig test volume. Measurement error of the algorithm and the modifications were assessed through an experimental set up.

8.2 Objectives

The objective of this chapter is to develop an algorithm to correct for the perspective error when measuring ball spin from images using the *SpinTrack3D* algorithm and validate spin measurement against a theoretical accuracy.

8.3 Ball spin measurement

Ball spin was measured using the *SpinTrack3D* (Kelley, 2011b) algorithm, which was discussed in Chapter 2. This method was chosen to measure both spin rate and spin axis using images from a single high-speed camera already used to film the impacts. Alternative methods (i.e. the back calculation of spin from ball trajectory data) would have been limited by the relatively short ball trajectory of each test, as well as the need for accurate ball aerodynamic properties (i.e. drag and lift coefficients). To aid spin measurements, test balls were marked with three mutually perpendicular black lines (figure 8.2) using a fabric pen to ensure durability through repeated impacts. The lines provided a pattern for the *SpinTrack3D* algorithm to identify, facilitating spin measurement between high-speed camera frames.

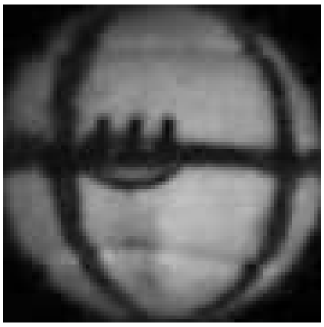

Figure 8.2 – Three mutually perpendicular black lines were added to the ball to assist spin measurements using the *SpinTrack3D* algorithm.

The spin measured between image pairs was described as an angle of rotation about a spin axis. Angles of rotation were measured in radians as clockwise rotations about the spin axis. Spin axis was a unit vector described by an axis system with origin at the ball centroid. Relative to the camera, the axes were orientated with a vertical Y-axis, horizontal X-axis and Z-axis aligned with the camera (figure 8.3). A vertical spin axis has the unit vector [0, 1, 0], for example.

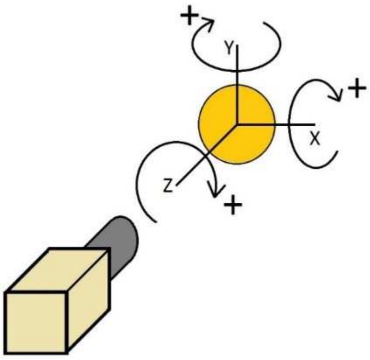

Figure 8.3 – Spin axis was measured with the axis system at the ball centroid and orientated to the camera. Angle of rotation was measured clockwise about the spin axis.

8.3.1 Ball spin measurement implementation

Spin analysis using pattern recognition includes measurement error that, if assumed consistent for all spin rates, would be proportionally larger for lower spin rates. This error could be reduced by skipping images to increase the time base and therefore the ball rotation between images. However, the method is limited to a maximum measureable ball rotation. At higher spin rates, the orientation of the black lines would repeat, giving a false negative measurement. Kelley (2011b) quantified spin measurement confidence using the *SpinTrack3D* algorithm, finding the angle of rotation between image pairs should not exceed 30°. This equates to a spin rate of 524 rad·s^{-1}, If successive images of time base 0.0001 s are used (equivalent to a high-speed camera frame rate of 1000 frames per second). Analysing every other frame limits the measurable angle of rotation between images to 15°, the equivalent of 262 rad·s^{-1}. Using every third frame decreases the angle of rotation to 15°, the equivalent of 175 rad·s^{-1}, and so on.

Skipping images requires some prior knowledge of the spin applied to the ball. This could be achieved by running the *SpinTrack3D* algorithm twice with each analysis – the first pass analysing successive frames, to determine if image skipping is possible, the second pass using the recommended images. However, this decreases the efficiency of an already computationally demanding process, making timely analysis less feasible.

Spin was measured by averaging the measurement from successive frames. This offered three advantages:

1. At low spin rates averaging multiple measurements from a single test reduces the effect of random measurement error.
2. Running the *SpinTrack3D* algorithm once, analysing successive frames, minimises the time of analysis.
3. The probability of pattern repetition is minimised.

Spin analysis was carried out for all frames of an inbound trajectory (maximum of 20 frames) and limited to no more than 20 frames for the outbound trajectory. This minimised the effects of spin decay, which over a long trajectory (e.g. a tennis court) is up to a 14% reduction in spin (Haake et. al., 2007). This limit also matched ball velocity measurements discussed in Chapter 6.

Mean angles of rotation and spin axes for the inbound and outbound trajectories of each impact test were calculated. The mean spin axis was calculated by averaging the vector components of each image pair analysed. The spin axis vector was transformed to the local racket origin using the rotation matrices and method discussed in Chapter 6, section 6.3.5. To further quantify spin measurements, spin rate was categorised as either positive or negative by the direction of the transformed Y-component of spin axis. This axis was parallel to the racket length. If the Y-component was positive, the rotation was the equivalent of a ball travelling towards the racket with backspin. In these cases the spin rate was recorded as a negative value.

8.4 Camera perspective error

The proximity of the cameras to the test volume – approximately 1.2 m – required a correction for the apparent rotation of the ball due to camera perspective error. Apparent rotation only affected ball displacements in the plane perpendicular to the camera axis. Ball displacements parallel to the camera axis (i.e. the ball moving directly away from the camera) do not cause an apparent rotation. The apparent rotation is shown diagrammatically in figure 8.4:

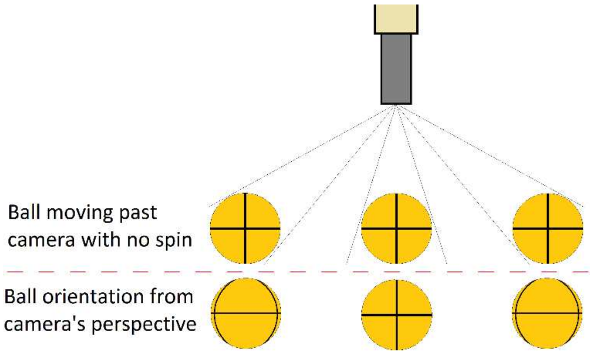

Figure 8.4 – The apparent spin of the ball caused by camera perspective error.

8.4.1 Angle of apparent rotation

The angle of apparent rotation was calculated using the cosine rule:

$$cos(\theta_{APP}) = \frac{\vec{a}^2+\vec{b}^2-\vec{c}^2}{2\vec{a}\vec{b}} \qquad 8.1$$

where θ_{APP} was the angle of apparent rotation, $\vec{a}$ was the vector from camera to ball centroid in the first image, $\vec{b}$ was the vector from camera to ball centroid in the second image and $\vec{c}$ was the vector between the ball centroids. The vectors and angle of apparent rotation are shown diagrammatically in figure 8.5.

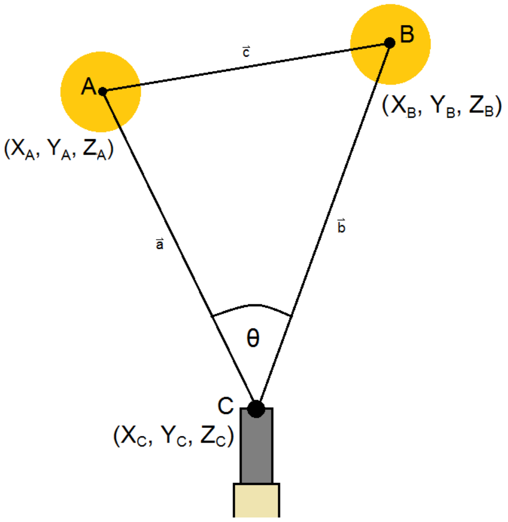

Figure 8.5 – Apparent rotation due to camera perspective error was calculated using the cosine rule, with the vectors $\vec{a}$, $\vec{b}$ and $\vec{c}$ known from reconstructed ball centroid data.

Theoretical apparent rotations were calculated using equation 8.1, for a ball at 1.2 m depth and lateral displacements between 5 mm and 30 mm. Given the frame rate of the high-speed camera (1000 fps), these ball displacements were the equivalent to ball velocities of 5 m·s^{-1} to 30 m·s^{-1} – similar to those used during impact testing. The apparent rotations are shown in figure 8.6.

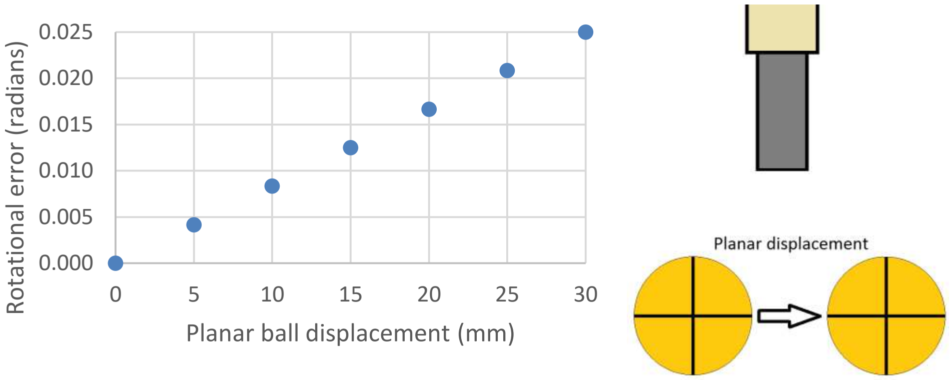

Figure 8.6 – The apparent rotational due to camera perspective error for planar ball displacements between 5 mm and 30 mm.

The apparent rotation for a 25 mm ball displacement was 0.021 radians, the equivalent of a spin rate error of 0.021 rad·s^{-1} (200 rpm) for the camera frame rate used.

8.4.2 Axis of apparent rotation

The spin axis of the apparent rotation was the unit vector perpendicular to the plane made by the vectors $\vec{a}$ and $\vec{b}$ (see figure 8.5). This was calculated using:

$$\vec{k} = \frac{\vec{a} \times \vec{b}}{|\vec{a} \times \vec{b}|} \tag{8.2}$$

where $\vec{k}$ was the apparent spin axis unit vector.

8.4.3 Apparent rotation correction

The *SpinTrack3D* algorithm was modified to calculate the apparent rotation for any image pair analysed. This used equations 8.1 and 8.2, along with the known ball centroid coordinates. The apparent rotation was subtracted from the measured rotation using

Quaternions (Microsoft Developers Network, 2012). *Quaternions* converted the measured and apparent angles and axes of rotation to a four dimension 'axis-angle' vector. A subtraction operator was readily available within the *Quaternion* class of the .*XNA* framework (Microsoft Developers Network, 2012). A validation of this method is discussed.

8.4.4 Quaternion subtraction validation

Rodrigues' rotation formula was used to validate the *Quaternion* subtraction operation. Rodrigues' rotation formula is:

$$\vec{v}_{rot} = \vec{v} cos\theta_{spin} + \left(\vec{k} \times \vec{v}\right) sin\theta + \vec{k}(\vec{k} \cdot \vec{v})(1 - cos\theta_{spin}) \tag{8.3}$$

where $\vec{v}_{rot}$ is the vector resulting from a rotation, θ_{spin} applied about a unit vector rotation axis, $\vec{k}$ to a starting unit vector, $\vec{v}$ (Belongie, 2012).

For this validation, three example angles and axes of rotation were required. The rotations were defined as:

1. The angle of rotation and spin axis measured by the *SpinTrack3D* algorithm (the "measured spin")
2. The calculated apparent angle of rotation and spin axis due to camera perspective error (the "perspective spin")
3. The corrected angle and axis of rotation from subtracting the perspective spin from the measured spin using Quaternion subtraction (the "corrected spin")

Table 8.1 shows the example measured, perspective and corrected spin data from analysing an image pair using the modified *SpinTrack3D* algorithm.

Table 8.1 – The measured, perspective and corrected spin axes and angles of rotation measured by the modified *SpinTrack3D* algorithm.

	Angle of rotation (radians)	Axis of rotation
Measured spin	0.25	[0.010, 0.997, -0.078]
Perspective spin	0.02	[0.000, -0.998, 0.060]
Corrected spin	0.27	[0.009, 0.997, -0.077]

Equation 8.3 was used to apply the measured and perspective spins to a unit vector [0, 1, 0]. The process was then repeated, but applying the corrected spin to the same starting unit vector. Table 8.2 shows the resulting unit vectors.

Table 8.2 – The output vectors resulting from rotating a unit vector using Rodrigues' rotation formula to apply the measured and perspective angles and axes of rotation and the corrected angle and axis of rotation.

	Output vector
Unit vector rotated by the measured and perspective rotations	[0.963, -0.020, -0.267]
Unit vector rotated by the corrected rotation	[0.963, -0.020, -0.267]

The resulting vectors show that applying the measured and perspective spins to the unit vector has the same outcome as applying the corrected spin to the unit vector. This outcome validates the implementation of *Quaternions* to correct the measured spin by the perspective spin.

8.4.5 Ball centroid error

The error in apparent rotation due to manual ball positioning and therefore centroid measurement error were established. Using equation 8.1, 1 mm errors in ball centroid height and lateral positions were simulated. The simulated ball centroids had a depth of

1.2 m. The errors in apparent spin are shown in Table 8.3.

Table 8.3 – The error in apparent rotation for simulated ball centroid errors.

	Simulated error (mm)	Apparent rotation error (radians)
Ball centroid height	1	0.001
Ball centroid lateral position	1	0.001

A 1 mm error in lateral or height measurements resulted in 0.001 radians (0.05°) error in apparent rotation. The results show that realistic ball centroid measurement error does not result in meaningful errors in apparent spin.

8.5 *SpinTrack3D* algorithm accuracy

An experimental set up was used to measure the error of the modified *SpinTrack3D* algorithm. For this, a ball was placed in manually measured positions relative to a high-speed camera and rotated by a known amount. The output of algorithm was compared to the known rotation.

8.5.1 Experimental setup

A ball stand was made comprising a circular base onto which two flats were machined at 0.314 radians (18°) separation, shown in figure 8.7. The flats allowed the base to be accurately rotated about the vertical axis by the equivalent for a ball spinning at 314 rad·s^{-1} (3000 rpm) in 0.001 s. A tennis ball, filled with polyurethane foam and marked with three perpendicular black lines, was attached to the base using a screw secured into the ball centre.

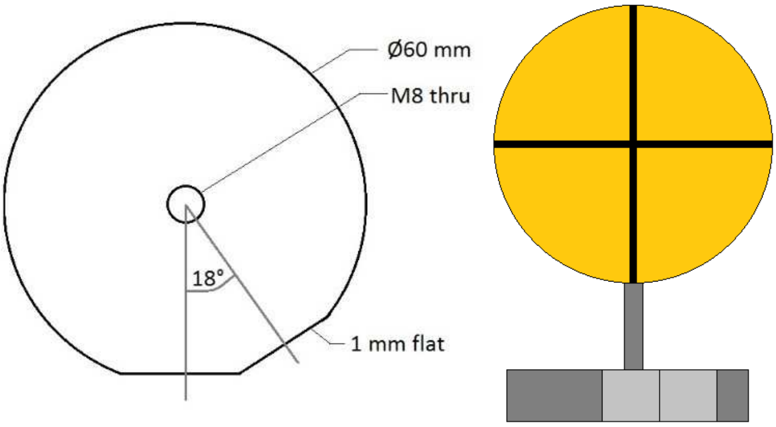

Figure 8.7 – The accuracy of the modified *SpinTrack3D* algorithm was assessed with an experimental setup using a ball stand with two flats at 0.314 radians separation.

The ball stand was placed onto a levelled laboratory-grade granite block (Bowers Group, 2008). Sheets of paper were used to level the block, which was measured using a Sola digital spirit level (SOLA, 2008). The high-speed camera was positioned 1.2 m from the block and manually aligned to the top and side edges using a cross-hair on the live image (figure 8.8). The granite block to camera distance was measured using a Leica laser measure (Leica Geosystems, 2008).

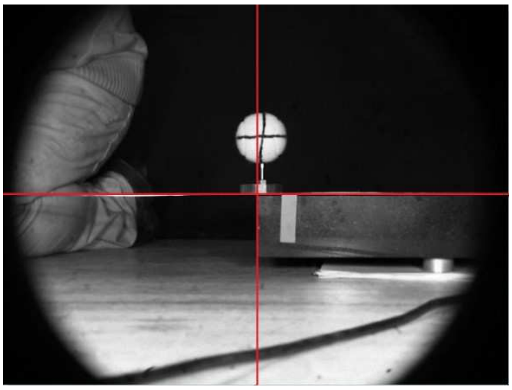

Figure 8.8 – The high-speed camera was aligned to the top and side edges of the granite block using a crosshair on the live image.

The lateral (x-axis) position, height (y-axis) and depth (z-axis) of ball centroids relative to the camera were measured manually. For this, the absolute height of the ball centroid relative to the stand base was measured using a drop gauge (Sylvac, 2008). Calibrated slip gauges were used to increase the height and depth of the stand, by known amounts.

The lateral positions of ball centroids were measured using a steel measure attached to the granite block. The accuracy of the *SpinTrack3D* algorithm was assumed to be symmetrical across the image plane. As such, the ball was placed over a range of positions to cover one quarter of the image plane. The range of ball positions are shown in figure 8.9.

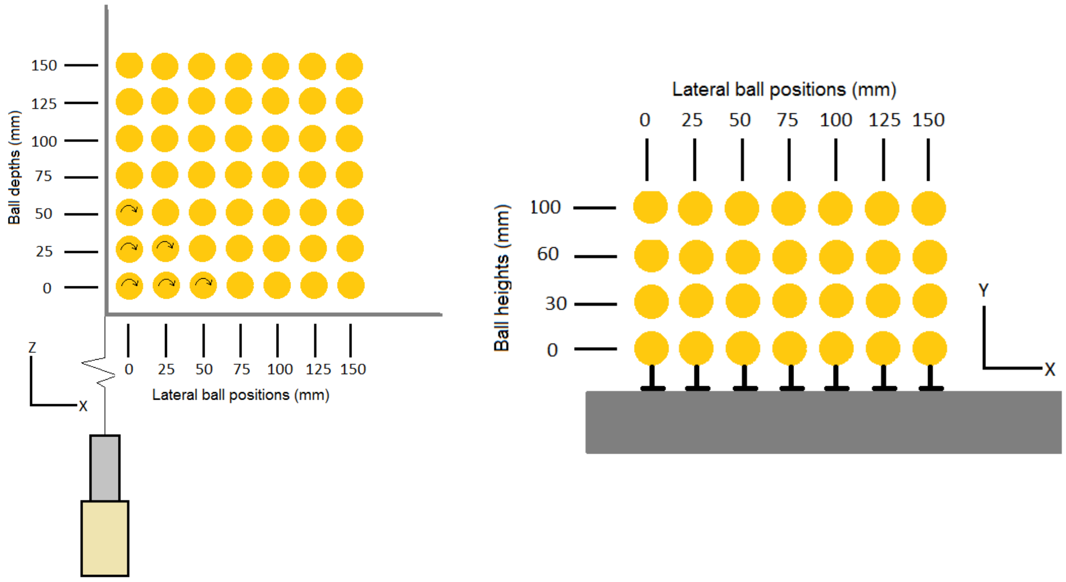

Figure 8.9 – The ball stand was placed at a several lateral positions and depths (left) and heights (right). Ball centroids were measured using a steel measure and calibrated slip gauges.

Two images of the ball were taken in each position, using the ball stand flats to rotate the ball whilst maintaining the absolute position. The image pairs analysed simulated four scenarios combining two spin scenarios:

1. Zero-spin simulation – no ball rotation between images pairs.
2. High-spin simulation – 0.314 radians rotation between images pairs.

with two ball displacement scenarios:

1. Lateral ball displacement between image pairs with ball at one height. Assessment carried out at several incremental depths from the camera.
2. Lateral movement between image pairs with ball at one depth. Assessment carried out several incremental heights above the image centre.

8.5.2 *Zero-spin simulation results*

Table 8.4 shows the mean absolute error and standard deviation for the zero-spin simulations, with the results split by the displacement scenarios listed above. The mean absolute error is the absolute angle of rotation output by the *SpinTrack3D* algorithm minus the expected result of zero radians.

Table 8.4 – Mean absolute error and standard deviation of the *SpinTrack3D* algorithm measurements for the zero-spin simulations, with lateral displacement between image pairs at incremental depths and heights. For reference, the apparent rotation magnitude for the incremental displacement of 25 mm was 0.021 radians.

Ball displacements	Mean absolute error (radians)	Standard deviation (radians)
Lateral, one height, incremental depths	0.024	0.006
Lateral, one depth, incremental heights	0.023	0.006

Figures 8.10 shows a heat map representation of the absolute errors for the zero-spin simulation with lateral ball displacements at several depths from the camera. Spatially, the errors were positioned at the midpoint of the two ball positions for the image pairs. The colour mapping was interpolated between each midpoint. The heat map for the lateral ball displacements at different heights is not shown as the results were similar.

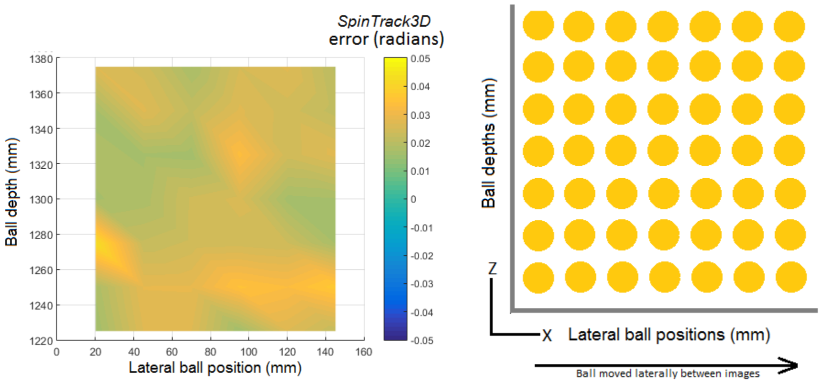

Figure 8.10 – Heat map of absolute error for zero-spin simulation with lateral ball displacements between image pairs at several depths from the camera. Mean error = 0.024 radians.

Figure 8.11 shows the spin axis vectors for all image pairs analysed for the zero-spin simulation with lateral ball displacements at several depths. The equivalent spin axis vectors for the lateral ball displacements at different heights is not shown as the results were similar.

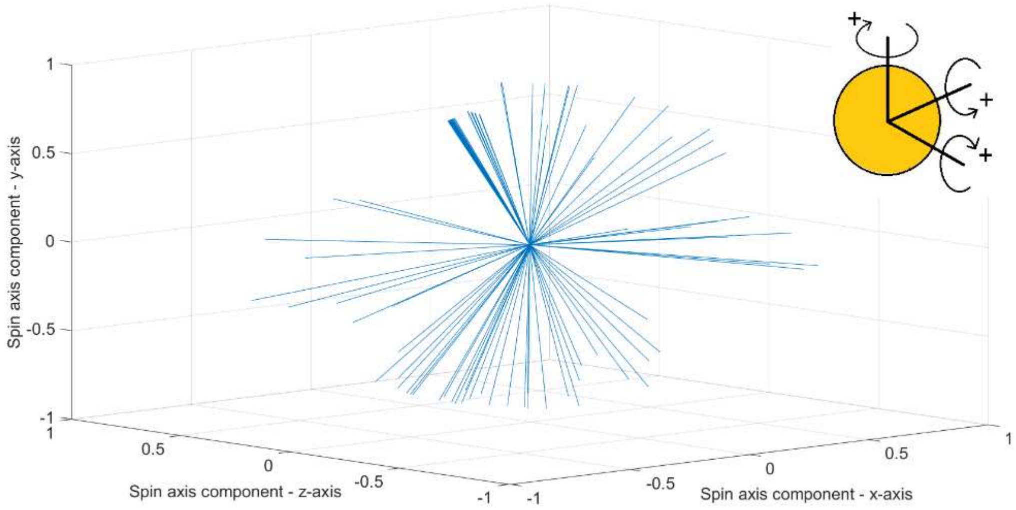

Figure 8.11 – Line plot showing random spin axis vectors for the zero-spin simulation with lateral ball displacements between image pairs at several depths from the camera

8.5.3 High-spin accuracy results

Table 8.5 shows the mean error and standard deviation for the high-spin simulations, with the results split by the displacement scenarios above. Error is the angle of rotation output by the *SpinTrack3D* algorithm minus the expected result of 0.314 radians.

Table 8.5 – Mean error in the *SpinTrack3D* algorithm measurements for the high-spin simulations, with lateral displacement between image pairs at incremental depths and heights. For reference, the apparent rotation magnitude for the incremental displacement of 25 mm was 0.021 radians.

Ball displacements	Mean error (radians)	Standard deviation (radians)
Lateral, one height, incremental depths	-0.017	0.006
Lateral, one depth, incremental heights	-0.025	0.006

Figures 8.12 shows a heat map representation of the absolute errors for the high-spin simulation with lateral ball displacements at several depths from the camera. Spatially, the errors were positioned at the midpoint of the two ball positions for the image pairs. The colour mapping was interpolated between each midpoint. The heat map for the lateral ball displacements at different heights is not shown as the results were similar.

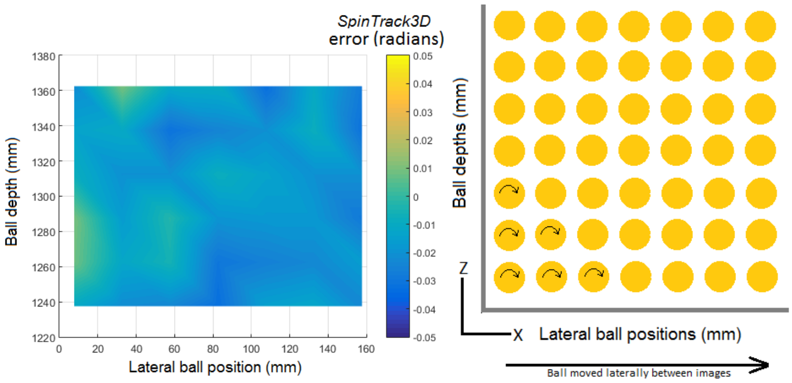

Figure 8.12 – Heat map of absolute error for high-spin simulation with lateral ball displacements between image pairs at several depths from the camera. Mean error = -0.017 radians.

Figure 8.13 shows the spin axis vectors for all image pairs analysed for the high-spin simulation with lateral ball displacements at several depths. The equivalent spin axis vectors for the lateral ball displacements at different heights is not shown as the results were similar.

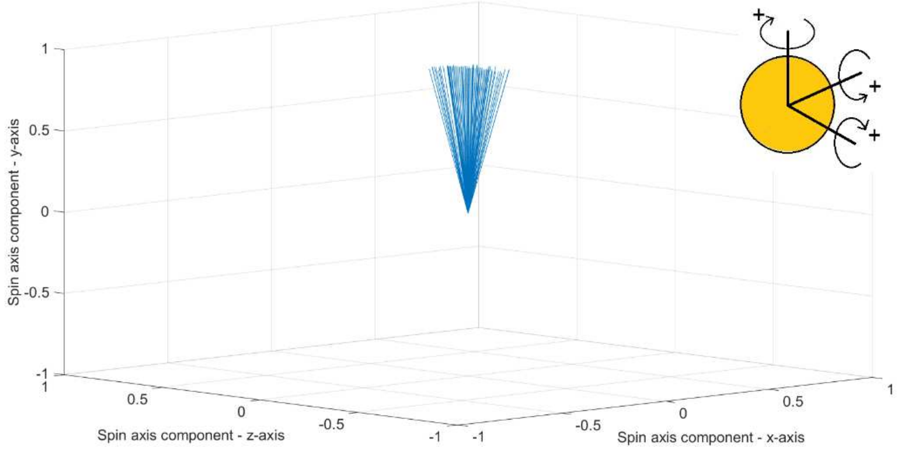

Figure 8.13 – Line plot showing tightly grouped spin axis vectors for high-spin simulation with lateral ball displacements between image pairs at several depths from the camera

8.6 Results discussion

The results from section 8.5.1 and 8.5.2 show the mean error of the modified *SpinTrack3D* algorithm, with the correction for the apparent spin due to camera perspective error. The mean absolute errors for the zero-spin simulations were 0.023 and 0.024 radians. The standard deviations for these measurements were low (0.006 radians). Along with the heat map shown in figure 8.10, the data shows the error is consistent for lateral displacements at different depths from the camera. Figure 8.11 shows the measured axes of rotation for all image pairs are randomly orientated, showing the error to be random. Measuring spin for all frames of the ball trajectories allows the random error to be neutralised, thereby improving the measurement accuracy. The mean errors for the high-spin simulation were under-measurements of 0.017 and 0.025 radians. The standard deviations were low (0.006 radians) and the heat map shown in figure 8.12 suggests the errors are consistent for displacements across the test volume. The tightly grouped vertical orientations of the spin axes (figure 8.13) suggest the error is systematic. The causes of measurement error are discussed next.

The standard deviations measured the uncertainty in measuring spin for multiple instances of single pairs of images. In practice, spin measurements will be averaged across the multiple image pairs for each tests – up to 20 image pairs. As such the expected uncertainty will be the uncertainty multiplied by $\frac{1}{\sqrt{19}}$. This has the effect of reducing the uncertainty from 0.006 radians for each simulated spin scenario, to 0.001 radians.

8.6.1 Theoretical error of the SpinTrack3D algorithm

The error of the *SpinTrack3D* algorithm was the result of a combination of the image resolution and the method used to score the simulated rotations between image pairs (discussed in Chapter 2). The rotations simulated by the *SpinTrack3D* algorithm translate the identified ball marking pixels by some amount. The resulting pixel locations are then compared to the identified ball marking pixels in the second image. The matching pixels are tallied to generate a score quantifying the fit of the simulated rotation to the actual rotation between image pairs. For a known ball radius, r in the high-speed camera images, the minimum rotation, θ_{min} required for a ball marking pixel to move by a whole pixel can be calculated by:

$$\theta_{min} = \arcsin\left(\frac{1}{r}\right) \tag{8.3}$$

This is shown diagrammatically in figure 8.14:

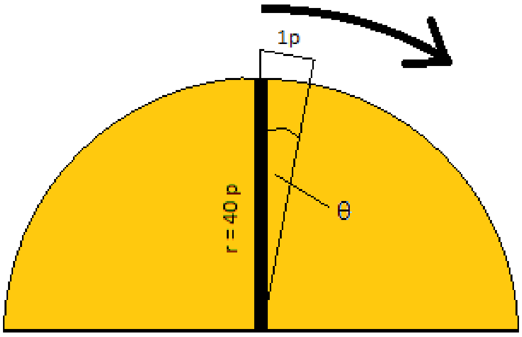

Figure 8.14 – The minimum rotation required to move a pixel by one whole pixel.

For a nominal ball radius of 40 pixels, the minimum rotation is 0.025 radians. This "measurement resolution" is greater than the smallest rotation simulated by the *SpinTrack3D* algorithm. As such, several simulated rotations result in the sub-pixel ball marking translations (see figure 8.15).

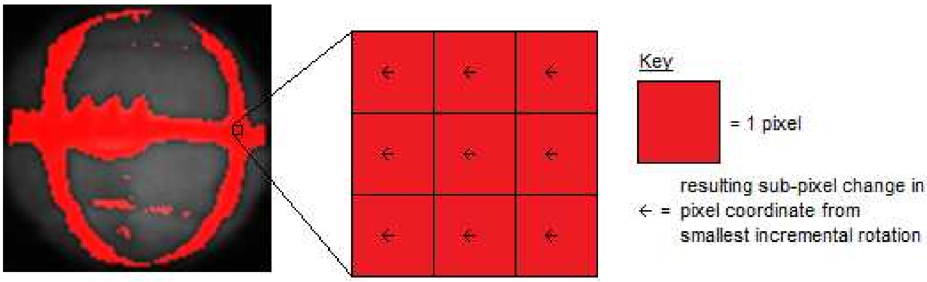

Figure 8.15 – The *SpinTrack3D* algorithm simulated small, incremental rotations of the ball, where the smallest rotations resulted in a sub-pixel repositioning of the pixel centres.

For example, for a ball with zero spin, the algorithm will simulate rotations with sub-pixel translations, which by default align perfectly to the second image. Any rotation with sub-pixel translation will therefore have equally high scores. The *SpinTrack3D* algorithm only reports the first rotation with the highest score, thereby introducing a measurement error. This shows how the measurement resolution of algorithm is greater than the resolution of the image.

The mean results shown in tables 8.4 and 8.5 (range = -0.025 to 0.024 radians), which include the correction for apparent spin, match the theoretical measurement resolution for a nominal ball radius of 40 pixels (0.025 radians). This shows the real-world accuracy of the *SpinTrack3D* algorithm meets the expected accuracy. This validates the implementation and supports the hypothesis that measurement resolution is ball radius (and image resolution) dependent. The magnitudes of the mean results suggest the errors are not spin rate dependent. The mean over-measurement of the zero-spin simulations suggests the *SpinTrack3D* algorithm simulates positive rotations (over-measurement) first, as the reported result is the first simulated rotation with the highest score. The mean under-measurement for the high-spin simulation suggests positive rotations had low scores. Therefore, the negative rotations (under-measurements) are reported.

The random orientations of the zero-spin simulation spin axes (figure 8.11) suggest the errors were the result of the algorithm reporting the first simulated rotation, at the measurement resolution limit (i.e. the smallest rotations within the theoretical accuracy of *SpinTrack3D*). The grouping of vertical spin axes for the high-spin simulation (figure 8.13) suggests the *SpinTrack3D* algorithm is capable of identifying the correct axis of rotation, when rotation is applied to the ball.

8.7 Conclusions

This chapter described the development and validation of an algorithm to correct for perspective error when measuring ball spin from images using the *SpinTrack3D* algorithm. The apparent rotation of a ball at 1.2 m distance from the camera and displacing 25 mm was calculated at 0.021 rad. This was the equivalent of a spin rate error of 21 rad·s^{-1} (200 rpm) for a ball travelling at 25 m·s^{-1}.

For given ball positions, the apparent angle of rotation was calculated using the cosine rule. The axis of rotation was calculated as the vector perpendicular to the plane defined by the camera and ball centroids. The apparent spin was subtracted from the measured spin using *Quaternion* 'axis-angle' vectors. This was validated using Rodrigues' rotation formula. Ball centroid measurement error was found to cause negligible error in the calculation of apparent spin.

The accuracy of the modified *SpinTrack3D* algorithm was measured with an experimental setup to simulate zero-spin and high-spin scenarios. For different combinations of ball displacements, mean absolute error for the zero-spin simulation was between 0.023 and 0.024 radians. Mean error for the high-spin simulation was an under-measurement of between 0.017 and 0.025 radians. The standard deviations for each experiment were consistently low (0.006 radians), suggesting the method is repeatable for the different combinations of ball displacement tested. The measurement errors were explained by the measurement resolution of the *SpinTrack3D* algorithm being greater than the image resolution. For a nominal ball radius of 40 pixels, the measurement resolution was 0.025 radians.

This chapter presented the final developments of the tools required to collect realistic ball-to-racket impact data. In the next chapter, a testing protocol is presented to collect ball-to-racket impact data. The protocol design included considerations for ball degradation caused by ball launch and impact. For this, data was collected to establish the effects of ball degradation on inbound ball velocity and spin. The inherent variability of the ball and stringbed were also investigated. Form this, the variability of outbound ball velocity and spin were calculated.

Chapter 9 - Data collection

9.1 Introduction

The previous chapters focussed on the design, implementation and validation of the tools required to collect ball-to-racket impact test data. This chapter describes the development of the testing protocol, which was used to collect the impact test data. The data collection stage is shown in context of the previous chapters in the project flowchart shown in figure 9.1.

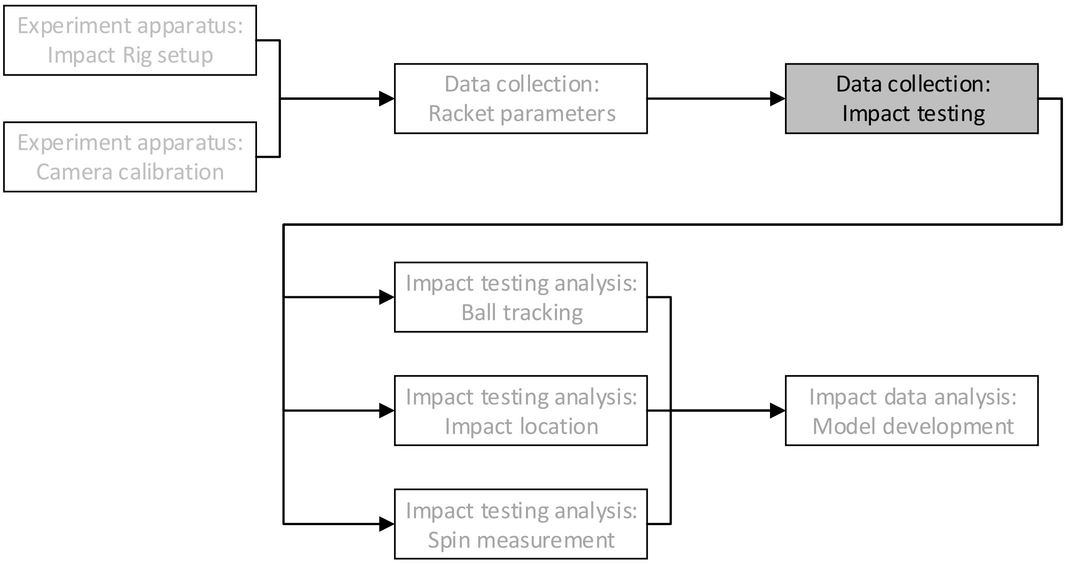

Figure 9.1 - Flowchart outlining the scope of the project. The chapter describes the development of a testing protocol to collect data from ball-to-racket impacts in the Impact Rig.

The protocol used a range of impact test velocities, spin rates and impact locations on the realistically supported racket. Velocities and spin rates replicated realistic conditions by incorporating mean real-play values. The inherent variabilities of the test apparatus and test objects were quantified to ensure an efficient process and that sufficient data would be collected. The effects of ball and stringbed degradation were also quantified, to ensure no detrimental effects on large scale data collection. The effect of inherent variabilities on rebound velocity and spin rate were established. This data was required for evaluating the predictive power of the statistical models trained, tested and validated from the impact test data.

9.2 Objectives

The objectives of this chapter are:

1. Design the test protocol with which to collect realistic ball-to-racket impact data.
2. Quantify the inherent variability of apparatus and test objects.

9.3 Impact testing protocol

The parameters available to define the protocol (“the Protocol”) included:

- Racket physical and geometric properties (e.g. racket mass, racket length).
- String and stringing properties (e.g. string stiffness, stringing tension).
- Ball properties (e.g. ball stiffness).
- Impact testing parameters (e.g. inbound velocity).

The parameters chosen were a balance of the broadness of the dataset and the amount of testing required. A broader dataset, describing a system domain of higher dimensionality, potentially allowed more sophisticated analysis. However, this required more data to fully describe each dimension of the domain. Bishop (1995) described this: ‘The curse of dimensionality’, stating that as dimensionality increased, the data required to describe the domain increased exponentially.

A subset of parameters was chosen to create a viable Protocol which described a useful system domain. The parameters, shown in table 9.1, are grouped by string and impact testing parameters.

Table 9.1 – The parameters chosen to create the Protocol were grouped by string parameters and impact testing parameters.

String parameters	Impact testing parameters
Stringing tension	Inbound ball velocity
	Inbound ball spin rate
	Impact location

Using a single racket, string type and ball brand removed the associated parameters, reducing the dimensionality of the domain and therefore the data needed to describe the system.

9.3.1 Defining the number of impacts

A target number of impacts was established using Bishop's exponential rule:

$$M^d \tag{9.1}$$

Where M was the divisions of each parameter, d. For the four parameters shown in table 9.1, a nominal six divisions per parameter would require 1296 impacts to 'map' the domain. The requirements of machine learning were taken into consideration. The impact data were used to train and validate several models, using estimated predictive errors to select the best performing (Bishop, 1995 and Choppin, 2008). It was assumed the data from 1296 impact tests were sufficient for this. A second, independent dataset was required to test the chosen models and establish predictive errors. It was assumed an additional and equivalent dataset would be required.

Given the inherent variability of the BOLA (2008) measured in Chapter 3, precise division of the impact testing parameters was not feasible. To create a well mapped domain, repeat impacts were collected for nominal test apparatus settings (e.g. specific BOLA settings). The scatter of ball launch over these repeat impacts was treated as pseudo-division of the impact testing parameters. By spacing the nominal test apparatus setting, the scatter should create a well mapped domain. In support of this, Bishop (1995) observed that 'real data' tends not to change arbitrarily between divisions. Instead, the outputs from a 'real' system tend to vary smoothly, as a function of the input parameters. Therefore, gaps in the impact data could be inferred through interpolation. The inherent variability of the test apparatus and the effects on data collection are discussed in the next section.

The nominal test apparatus settings are determined over the course of this chapter. In summary, the Protocol used the following parameter intervals:

- One ITF *Development* racket strung at three nominal string tensions, using ITF *Development* nylon string.

- Impact tests at six nominal impact locations – three on the longitudinal axis of the racket, three offset from this axis. The racket clamp was moved to reposition the racket laterally and lengthwise, moving the impact location relative to the racket width (X-axis) and length (Y-axis) respectively.

- Impact tests at four nominal launch velocities, including the mean real-play velocity of 25 $m \cdot s^{-1}$. The BOLA was set to launch balls with an inbound angle of incidence of 20° to the stringbed normal – the mean real-play playing angle. The orientations of the racket and BOLA meant component velocities parallel to racket length (Y-axis) were close to 0 $m \cdot s^{-1}$. Real-play shot conditions are described in chapter 3.

- Impact tests at three nominal launch spin rates, including the mean real-play spin rate of 200 $rad \cdot s^{-1}$. Balls were launched with the equivalent of backspin to replicate typical groundstroke conditions.

- For each combination of string tension, impact location, ball launch velocity and spin rate, six repeat impacts gave a total of 1296 impacts. For all impact tests, ITF *High-Specification* tennis balls were used.

9.4 Impact test variabilities

Ideally, the system domain would be efficiently mapped by carefully controlling the test parameters. The inherent variabilities of the test apparatus and test objects prevented this. To design an efficient Protocol, these variabilities were quantified through several pilot studies. The aim was to select nominal test apparatus setting which resulted in minimal inadvertent data repetition. Further pilot studies established the effects of test object degradation. From this, a ball impact limit was set to minimise the effects of degradation.

9.4.1 Sources of variability

Test apparatus variability was initially investigated in Chapter 3. Ball launch scatter determined the number of high-speed cameras and impact test analysis methods to measure ball trajectories. Ball launch scatter was not the only source of variability. Table 9.2 summarises the identified sources, split into two groups: '*Apparatus*' and '*Test objects*'. The following sections discuss these identified sources.

Table 9.2 – The identified sources of Apparatus and Test object variabilities affecting data collection using the Impact Rig and Protocol.

Variability type	Source	Effects on
Apparatus	BOLA	Ball launch velocity Ball launch spin rate Impact location
	Racket position	Impact location Ball launch velocity components
	Racket clamp stability	Restrictive torque
Test objects	Ball variability and degradation	Ball launch repeatability Ball marking degradation
	String variability and degradation	Stringbed stiffness

9.4.2 BOLA variability and ball degradation

BOLA variability affected ball launch velocities, spin rates and impact locations. This was assumed to be a random inherent variability of the BOLA ball launching mechanism. However, ball degradation was hypothesised to cause a systematic change in ball launch. The launching mechanism was known to degrade the felt of the ball and repeated impacts known to soften the ball's rubber core. Steele (2006) found no significant differences in COR and rebound spin when a ball was launched onto a clamp racket over 100 impacts. However, her measurements did not assess changes in ball properties between the start and end of here impact testing protocol.

If BOLA variability was random, repeat impacts for nominal apparatus settings would ensure good domain mapping. If ball degradation was systematic, the effects could be minimised by using several balls to complete testing.

The effect of repeat impact testing on ball marking degradation (and spin rate measurement) was also considered. The ITF *Spin Rig* test protocol (Goodwill et. al., 2006), which uses the BOLA, requires only 42 impacts, with 16 repeat impacts per ball. To complete 1296 impacts will require more impacts per ball. The effects of ball marking degradation on spin measurement beyond 16 impacts was unknown.

9.4.2.1 Pilot study 1 – Quantifying BOLA variability and ball degradation

The inherent variability of the BOLA and the effects of ball degradation were quantified. For this, an ITF *Development* racket was head-clamped to a heavy steel base plate (also used in Chapters 5 and 7). The base plate was positioned within the Impact Rig to replicate the location of a handle-clamped racket, with all impacts aimed at the geometric stringbed centre. Ball launch velocities and spin rates of a single ITF *High-Specification* ball were measured over 100 impact test. The BOLA was set to launch the ball with nominal inbound ball velocity and spin rate of 23 m·s^{-1} and 0 rad·s^{-1}, respectively. The ball was marked up with three mutually perpendicular black lines, to facilitate the measurement of, and assess the effects of degradation on spin measurements. Impacts were filmed using two Vision Research *Phantom v4.3* high-speed cameras which were calibrated using the planar method of camera calibration described in Chapter 4. Impacts were analysed using the *Impact Analysis* tool to automatically digitise the test images and measure the ball launch velocities and spin rates.

Figures 9.2 and 9.3 show the ball launch velocities and spin rates over the 100 impacts. To quantify the relationship between the measured variables and ball degradation, a linear relationship was assumed. As such, simple linear regressions were fit to the data. Table 9.3 shows the RMSEs of ball launch velocity (RMSE$_{\text{iv}}$) and spin rate (RMSE$_{\text{is}}$).

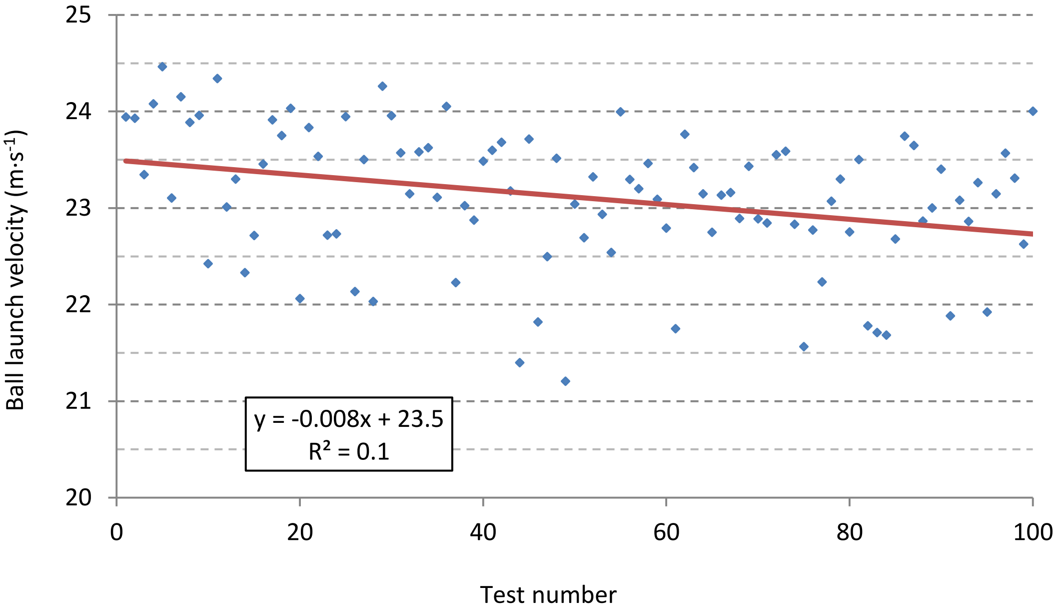

Figure 9.2 – A scatter plot showing ball launch velocities of a single ball over 100 trials using the BOLA ball launch device. A simple linear regression (solid red line) shows a weak, negative correlation between velocity and test number.

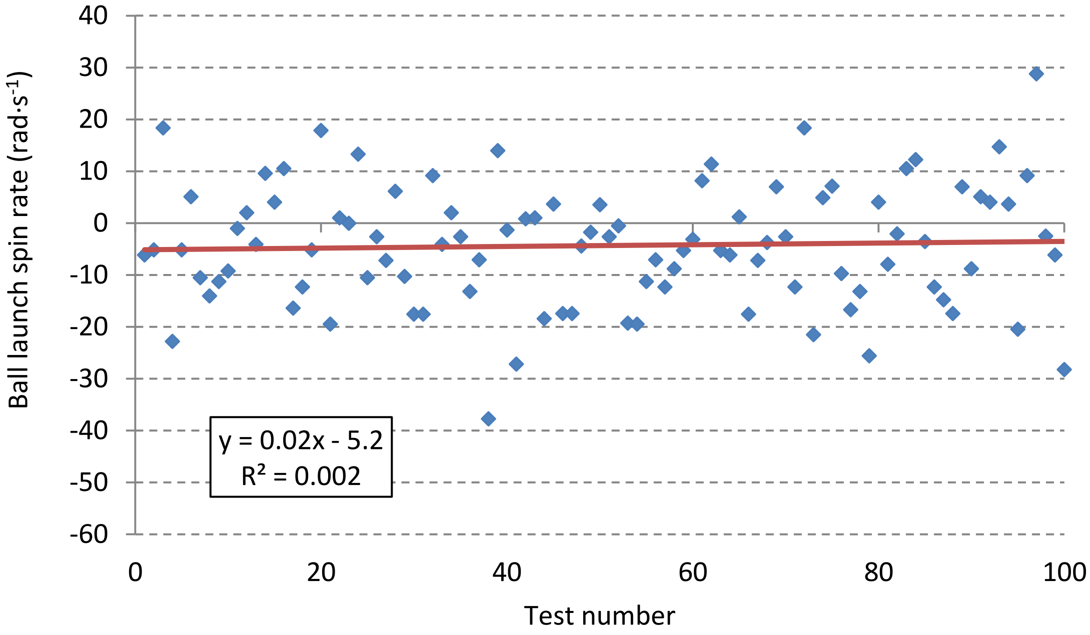

Figure 9.3 – A scatter plot showing ball launch spin rates of a single ball over 100 trials using the BOLA ball launch device. A simple linear regression (solid red line) shows a weak, positive correlation between spin rate and test number.

Table 9.3 – The root-mean-squared error of ball launch velocity ($RMSE_{iv}$) and spin rate ($RMSE_{is}$) for a single ball using the BOLA ball launch device (n = 100).

$RMSE_{iv}$ ($m \cdot s^{-1}$)	$RMSE_{is}$ ($rad \cdot s^{-1}$)
0.7	11.3

Assuming the effects of BOLA variability and ball degradation were independent, the simple linear regressions quantify the effects of ball degradation and the RMSEs quantify BOLA variability. The ball launch velocity regression line indicates a decrease in inbound velocity of 0.8 $m \cdot s^{-1}$ over 100 impacts. The ball launch spin rate regression indicates an increase in inbound spin of 1.6 $rad \cdot s^{-1}$ over 100 impacts. Successful spin measurements over the 100 impacts proved ball marking degradation was not an issue. Quantifying ball degradation was unreliable based on this data, as the R^2 values of both correlations were less than 0.1. However, the observed decrease in ball launch velocity was used to justify a limit of 50 impacts per ball. The data predicted ball launch velocity would decrease by 0.4 $m \cdot s^{-1}$.

The poor correlations were the result of the inherent variability of the BOLA. The RMSEs show ball launch variability was ±0.7 $m \cdot s^{-1}$ and ±11.3 $rad \cdot s^{-1}$. To minimise repetition of data collection using the Protocol, nominal BOLA test settings were set with greater than 0.7 $m \cdot s^{-1}$ and 11.3 $rad \cdot s^{-1}$ between intervals.

9.4.2.2 Pilot study 2 – ball impact limit validation

To validate the ball impact limit of 50 impacts per ball, the first pilot study was repeated using nine balls, an increased launch spin rate and 450 total impacts. Increasing the spin rate was hypothesised to cause greater ball degradation. To establish repeatability, the changes in, and variability of, ball launch velocity and spin rate were compared to the first pilot study.

Figures 9.4 and 9.5 show the ball launch velocities and spin rates of 422 impacts (the *Impact Analysis* tool failed to analyse 28 impacts). Simple linear regressions were fit to the data. Table 9.4 shows the RMSE of the ball launch velocity and spin rate.

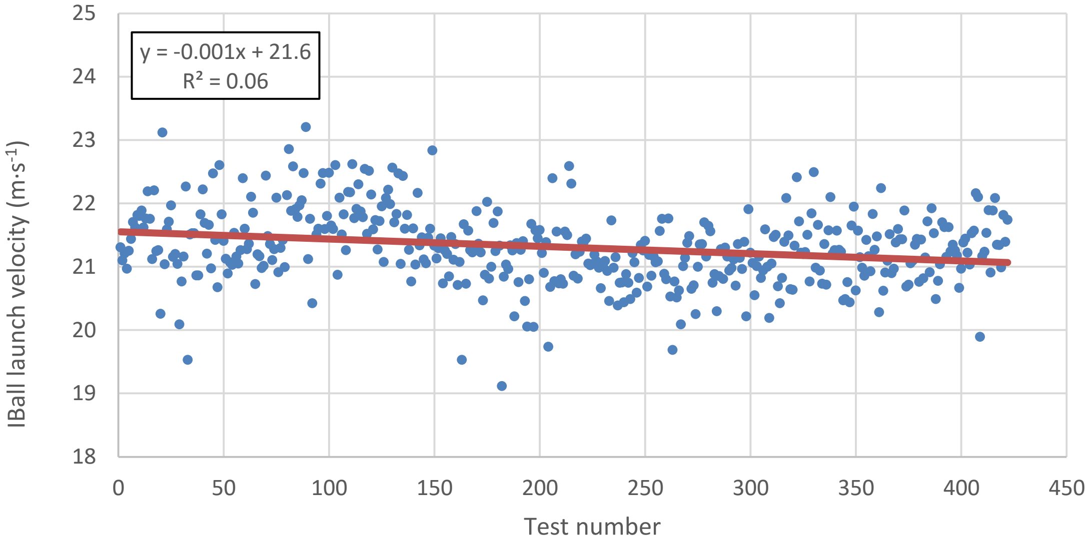

Figure 9.4 – A scatter plot showing ball launch velocities of nine balls over 422 trials using the BOLA ball launch device. A simple linear regression (solid red line) shows a weak, negative correlation between velocity and test number.

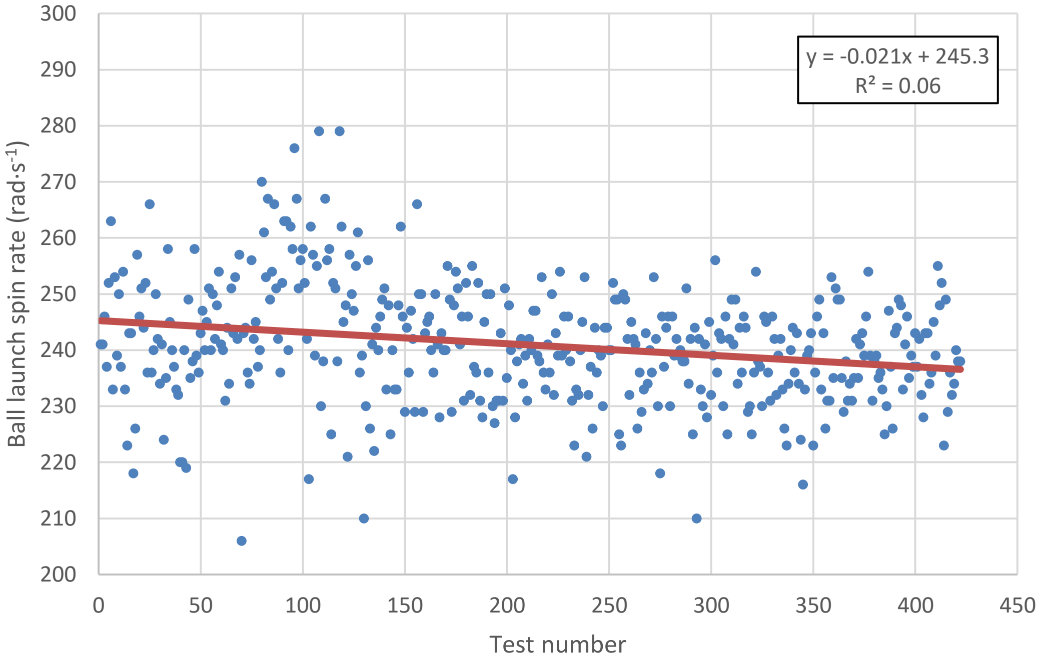

Figure 9.5 – A scatter plot showing ball launch spin rates of nine balls over 422 trials using the BOLA ball launch device. A simple linear regression (solid red line) shows a weak, negative correlation between spin rate and test number.

Table 9.4 – The root-mean-squared error of the ball launch velocity ($RMSE_{iv}$) and spin rate ($RMSE_{is}$) for nine balls using the BOLA ball launch device (n = 422).

$RMSE_{iv}$ ($m \cdot s^{-1}$)	$RMSE_{is}$ ($rad \cdot s^{-1}$)
0.6	10.4

The ball launch velocity regression line shows a weak negative correlation, similar to the first pilot study. Velocity decreased by an average of 0.5 $m \cdot s^{-1}$. This was greater than the 0.4 $m \cdot s^{-1}$ decrease predicted. This may have been the result of the greater ball launch spin rate accelerating ball degradation.

The ball launch spin rate regression line shows a weak negative trend line, which was not observed previously. This may be an effect of accelerated ball degradation from increasing the launch spin rate. The gradient of the line shows spin decreased by 8.9 $rad \cdot s^{-1}$ for nine balls over all impacts, or each ball over 50 impacts.

Both correlations were weak ($R^2 = 0.06$) – a factor of the inherent variability of the BOLA. This variability was repeatable between studies, as the RMSEs were less than, but similar to the first pilot study. The decreases in ball launch velocity and spin rate were deemed acceptable to continue with the ball impact limit for the main data collection exercise.

9.4.2.3 Pilot study 2 - Impact location variability

Impact locations were also measured during the second pilot study, to quantify variability due to the BOLA and ball degradation. Figures 9.6 and 9.7 show the x-axis (lateral) and y-axis (longitudinal) components of 422 impact locations, measured relative to the geometric stringbed centre. Simple linear regression were fit to the data. Table 9.5 shows the RMSEs of each component of impact location ($RMSE_{ImpX}$ and $RMSE_{ImpY}$).

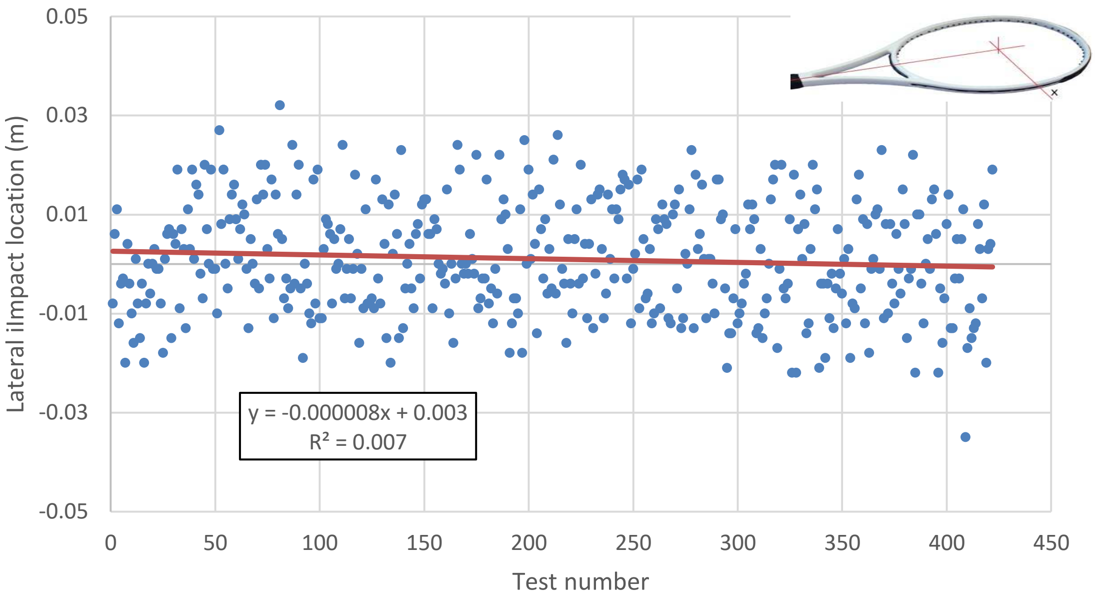

Figure 9.6 – A scatter plot showing the lateral component of impact locations of nine balls over 422 trials. A simple linear regression (red) of the data shows a weak, negative correlation between the lateral component and test number.

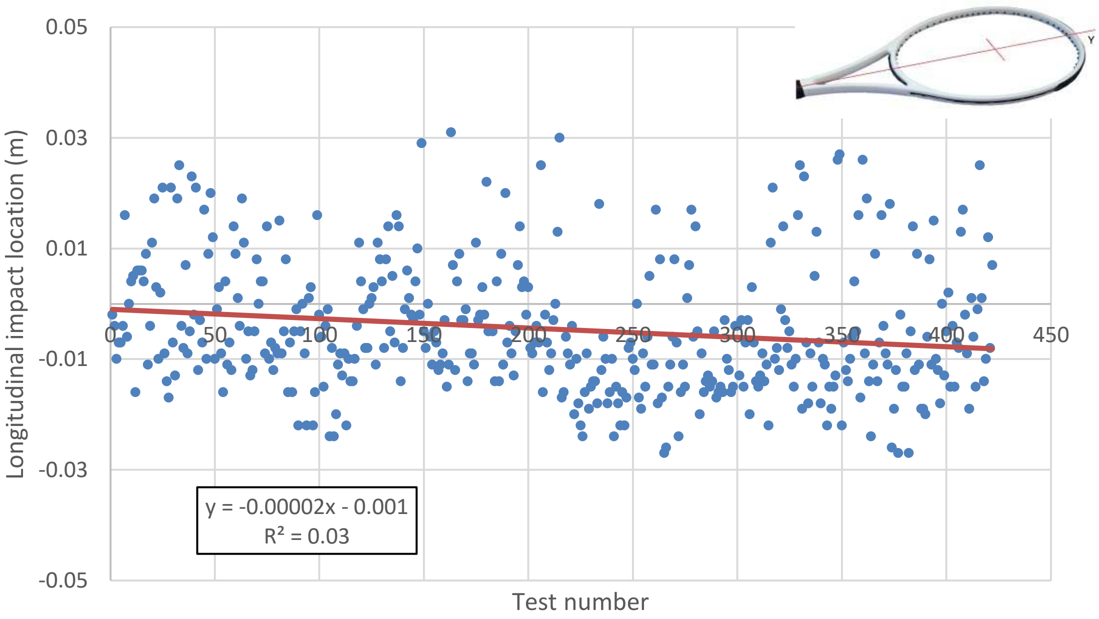

Figure 9.7 – A scatter plot showing the longitudinal component of impact locations of nine balls over 432 trials. A simple linear regression (red) of the data shows a weak, negative correlation between the longitudinal component and test number.

Table 9.5 – The root-mean-squared error of the lateral ($RMSE_{ImpX}$) and longitudinal ($RMSE_{ImpY}$) impact location components for nine ball using the BOLA ball launch device. (n = 422).

$RMSE_{ImpX}$ (m)	$RMSE_{ImpY}$ (m)
0.011	0.031

The trend lines of both components of impact location show weak negative correlations. The lateral component moved by -0.003 m and longitudinal component by -0.008 m. These changes may be correlated to the change in ball launch velocity, discussed previously. However, the influence of ball degradation was minimal. In both cases, the correlations were poor ($R^2 = 0.007$ and 0.03, respectively), due to the inherent variability of the BOLA. The RMSEs of the impact locations indicate the variability of ball launch influenced the variability of the longitudinal component by approximately three times that of the lateral component. These data will be used to set nominal racket locations to minimise impact location repetition and efficiently map the system domain.

9.4.3 Racket position repeatability

The repeatability of racket positioning in the Impact Rig was considered a source of test variability. This affected the location of stringbed markers, which were used to translate inbound and outbound trajectories and impact locations to the local racket origin (Chapters 6 and 7). The design of the Impact Rig racket handle clamp allowed six degrees of freedom – translations and rotations about the lateral (x), longitudinal (y) and vertical (z) axes of the racket. Before each impact, the racket was manually aligned in a start position. Small variations in this manual process were expected.

The repeatability of racket alignment was primarily influenced by racket rotation. Racket translation between impacts was negligible, as the handle clamp was securely fastened to the Impact Rig. Rotations about the lateral axis, pitching the racket up or down, were assumed to cause negligible variations. The racket clamp extension spring provided a constant force, pulling the racket against a securely fastened restraining bar (see figure 9.8). Therefore, the height of the racket at the point of contact with the restraining bar was stable. Racket rotations about the vertical and longitudinal axes (figure 9.8) were susceptible to variation.

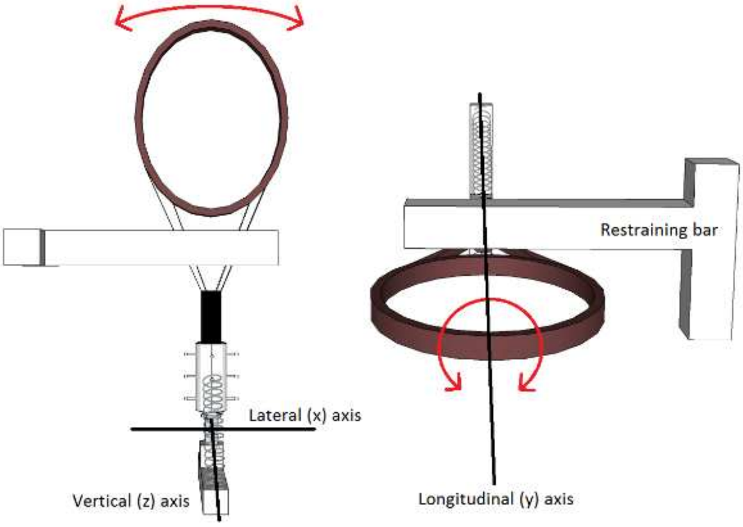

Figure 9.8 – A schematic of manual racket alignment variations. Racket rotation about the vertical axis (left) or longitudinal axis (right) were the causes of variability.

To minimise these variations, racket alignment was inspected prior to each impact. Rotations about the vertical axis were minimised by aligning the racket with marks placed onto the restraining bar. Rotations about the longitudinal axis were minimised by ensuring both sides of the racket throat touched the restraining bar. Ultimately, excessive variations in racket position would affect the distribution of trajectory and impact location data. As such, the distributions will be examined prior to any further analysis, e.g. data modelling. This is discussed in the next chapter.

9.4.4 Racket clamp stability

The torque limiter in the racket clamp was previously used by Choppin (2008) who noted that the simplicity of the device meant the torque limit applied at the racket handle was subject to variability. He supposed the force impulse of a ball impact may have resulted in the effective torque around the handle being different to the value measured by a torque wrench. For this project, a single torque limit was used across all impact tests. The effective torque limit was assumed to be equal for all impacts. To ensure repeatability, and in case the torque limiter loosened during testing, the device was checked at several times using a torque wrench.

9.4.5 String variability and degradation

The following string variabilities were considered:

1. Physical property variability (e.g. string stiffness).
2. Stringing tension variability.
3. Individual string position variability.
4. String degradation.

The physical properties of the string could describe additional domain dimensions. For example, string stiffness has been correlated with spin generation (ITF, 2008c), and can be measured using the method described by Cross (2001). By using a single string type, taken from a single reel, the physical properties were assumed consistent across all tests. As such, the physical string properties were excluded from the system domain.

Stringing tension was included as a test parameter variable. The repeatability of racket stringing was established to ensure no cross over between the nominal stringing tensions used. The measure of racket stringing was s*tringbed stiffness* (SBS), using a Babolat RDC (Babolat, 2008). Table 9.6 shows the mean and standard deviation of stringbed stiffness ($\overline{SBS}$ and σ_{SBS}, respectively) measured from 85 ITF *Development* rackets strung at 60 lbs stringing tensions with a variety of string types – nylon, polyester and natural gut.

Table 9.6 – The mean and standard deviation of stringbed stiffness for ITF *Development* rackets strung at 60 lbs stringing tension using a variety of strings (n = 85).

$\overline{SBS}$ (lbs)	σ_{SBS} (lbs)
62	5

The mean SBS for the ITF *Development* racket was similar to the stringing tension, and was assumed to vary proportionally with stringing tension. The standard deviation of stringbed stiffness was considered the repeatability of stringing. Impact testing stringing tensions, sufficiently space to minimise SBS repetition, were selected using this data.

Ball-to-stringbed impacts are known to cause lateral string displacement within the stringbed. The ball-to-stringbed interactions study in chapter 7 (section 7.6) discussed how small changes in the starting conditions of the strings could have measureable effects on the rebound characteristics of the ball. However, monitoring string positions is difficult. This factor was included in the ITF *Spin Rig* testing protocol; whereby only grossly (noticeably) displaced strings are manually reset between impacts. However, manually resetting strings will result in small variations in the stringbed. These small variations were considered inherent variabilities of the test objects and, along with the inherent variability of the balls, thought to influence the variability of ball rebound characteristics. This is discussed in section 9.6 of this chapter.

String degradation was also considered an inherent variability. Repeat impact testing accelerates the stress relaxation of the strings, measurable as a reduction in stringbed stiffness after testing. The repeated lateral displacement of the strings also causes notches to form at the points of contact between strings. The stringbed stiffness of the 85 ITF *Development* rackets tested previously were measured after 42 impacts of the ITF *Spin Rig* protocol. The mean decrease in stringbed stiffness was 1 lb. This was well within the repeatability of racket stringing, and an acceptable change. However, the *Spin Rig* testing protocol required significantly fewer impacts than proposed in the Protocol.

Due to the difficulties in quantifying string degradation directly, a study was conducted to establish the indirect effects of stringbed and ball degradation. This study, described in section 9.6, quantifies the effects of ball and stringbed degradation on the variability of rebound ball trajectories.

9.5 The Protocol

Having defined the system domain by the test parameters, the nominal test parameters intervals were chosen. These were based on the measured variabilities to create a well mapped domain, by minimising data repetition. The real-play velocities discussed in Chapter 3 were also considered. The nominal test velocities and spin rates were associated with BOLA settings. The Protocol, with nominal values, is shown in table 9.7. The impact locations and inbound ball angle of incidence shown in figure 9.9.

Table 9.7 – The Protocol varied string tension, impact location and ball launch velocity and spin rate. The nominal value of each test interval are shown. For each combination, six repeat impacts were collected, giving a total of 1296 impact tests.

Variable	Intervals	Nominal interval values
String tensions	3	50 lb 60 lbs 70 lbs
Impact locations (see figure 9.2) (relative to geometric stringbed centre)	6	(0.00 m, 0.00 m) (0.08 m, 0.00 m) (-0.08 m, 0.00 m) (0.00 m, 0.06 m) (0.08 m, 0.06 m) (-0.08mm, 0.06 m)
Ball launch velocities	4	23 $m \cdot s^{-1}$ 25 $m \cdot s^{-1}$ 28 $m \cdot s^{-1}$ 30 $m \cdot s^{-1}$
Ball launch spin rates	3	0 200 $rad \cdot s^{-1}$ 400 $rad \cdot s^{-1}$
Repeat impacts	6	
Total impact tests	1296	

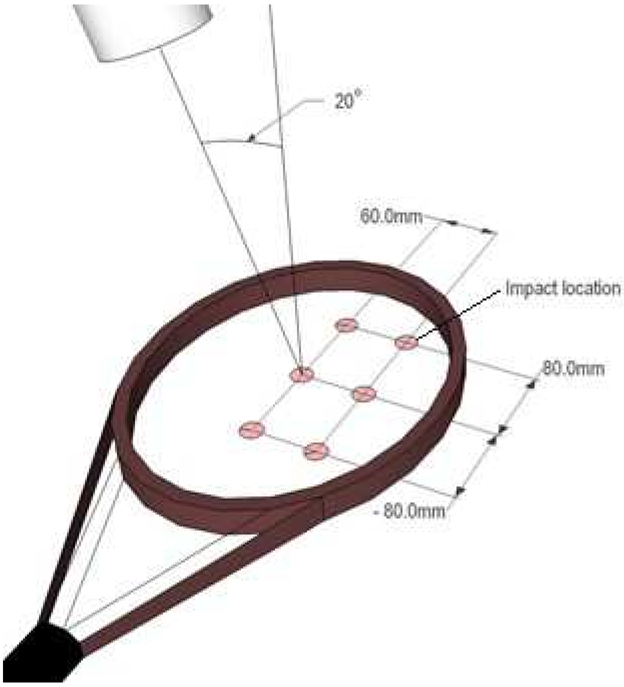

Figure 9.9 – The Protocol tested six nominal impact locations with an angle of incidence of 20°.

In summary of the chosen input test parameter intervals:

- The nominal stringing tensions intervals were twice the standard deviation of SBS from repeated stringing (σ_{SBS} = 5 lbs, table 9.6).
- The nominal impact location intervals were between 2.5 and 5.5 times greater than impact location variability due to the inherent variability of the BOLA. The RMSEs of impact location were 0.011 m in the lateral (x) axis and 0.031 m in the longitudinal (y) axis (table 9.5). The geometry of the racket was also considered, to minimise the risk of the ball impacting the racket frame.
- The nominal ball launch velocity intervals were between three and five times greater than ball launch variability due to the inherent variability of the BOLA ($RMSE_v$ = 0.6 m·s^{-1}, shown in table 9.4). The nominal launch velocities included the real-play mean of 25 m·s^{-1}.
- The angle of incidence of the BOLA barrel to the racket was set to the real-play mean playing angle of 20°.
- The nominal ball launch spin rate intervals were 20 times greater than the inherent variability of the BOLA ($RMSE_s$ of 10.4 rad·s^{-1}, shown in table 9.4). The

nominal spin rate intervals included the real-play mean of 200 rad·s^{-1}.

- To complete the 1296 impacts, 27 balls were used. This resulted in 48 impacts per ball, two less than the ball impact limit of 50.

The effect of racket alignment variability was not quantified in this project. It was assumed six repeat impacts at each nominal test value would ensure the system domain was well mapped. To confirm this, the distributions of the test data were assessed prior to further analyses (see Chapter 10).

9.6 Quantifying rebound trajectory variability

The effects of apparatus and test object variability and test object durability were quantified with analysis of rebound trajectories. Two studies were conducted:

1. Head-clamped racket study:
   To measure the effects of inherent ball and stringbed variability on rebound trajectories. Head-clamping the racket isolated the inertial properties so that measured variabilities could be attributed to the test objects. Ball launch velocities were normalised and impact locations filtered to account for ball launch variability.
2. Handle-clamped racket study:
   To measure the effects of test object degradation on rebound trajectories. The differences in mean rebound velocities and spin rates were measure for impacts at the start and end of the Protocol – after each ball had been used 48 times. Handle-clamping the racket replicated impact testing conditions of the Protocol.

9.6.1 Study 1 – Effect of inherent test object variability on rebound trajectory

A modified Protocol and Impact Rig set were used to quantify the variability of rebound ball velocity and spin rate. The Protocol for one string tension was used (432 impacts) with nominal ball launch velocities and spin rates constant at 23 m·s^{-1} and 200 rad·s^{-1}, respectively. Nine ITF *High-Specification* balls were each used for 48 impacts. An ITF *Development* racket, strung with ITF *Development* string at 60 lbs stringing tension, was clamped to the heavy steel base plate used previously. The racket and base plate were positioned to replicate the location of a handle-clamped racket within the Impact Rig. All impacts were aimed at the geometric stringbed centre. Impacts were analysed using the *Impact Analysis* tool to measure the ball launch and ball rebound velocities and spin rates and impact locations. Post analysis, the data were filtered to exclude any impact locations greater than 20 mm from the geometric stringbed centre. This minimised the assumed effect of impact location on the rebound ball trajectory. The data sample was reduced to 247 impacts.

9.6.1.1 Ball rebound velocity variability

Velocity data were normalised to account for the variability in ball launch. For this, the vertical, lateral and longitudinal components of coefficients of restitution (COR) were calculated for each impact. The components of rebound velocity for each impact were adjusted to the respective mean components of the launch velocities.

Vertical CORs, e_z were calculated for each impact using:

$$e_z = \frac{V_{oz}}{V_{iz}} \qquad 9.2$$

where V_{iz} and V_{oz} were the vertical components of launch and rebound velocities.

The lateral and longitudinal components of horizontal COR were calculated using the method proposed by Cross (2005). For this, he considered the instantaneous velocities, $r\omega$ for a point on the bottom surface of a spinning ball, immediately prior to and after an impact. Lateral CORs, e_x were calculated using:

$$e_x = \frac{v_{ox} - \mathrm{r}\omega_{ox}}{v_{ix} - r\omega_{ix}} \qquad 9.3$$

where v_{ix} and v_{ox} were the lateral (x-axis) components of the launch and rebound velocities. $r\omega_{ix}$ and $r\omega_{ox}$ were the x-axis components of instantaneous velocities prior to and after impact. The longitudinal CORs, e_y were calculated using:

$$e_y = \frac{v_{oy} - r\omega_{oy}}{v_{iy} - \mathrm{r}\omega_{iy}} \qquad 9.4$$

where v_{iy} and v_{oy} were the longitudinal (y-axis) components of the launch and rebound velocities. $r\omega_{iy}$ and $r\omega_{oy}$ were the y-axis components of the instantaneous velocities prior to and after impact.

The instantaneous velocities were calculated using a nominal ball radius, r of 33 mm and the angular velocities of the ball, ω calculated from the ball launch and rebound spin rates. The lateral and longitudinal components, ω_x and ω_y, were calculated using the ball launch and rebound spin axis vectors.

Rebound velocities were normalised using the generalised form of equation 9.2, rearranged to give:

$$V_o = e \cdot V_i \tag{9.5}$$

where V_o was the normalised rebound component velocity, e was the vertical, lateral or longitudinal COR and V_i was the corresponding mean ball launch component velocity.

Figures 9.10 shows the resultant rebound velocities after normalising the data. A simple linear regression has been fit to the data.

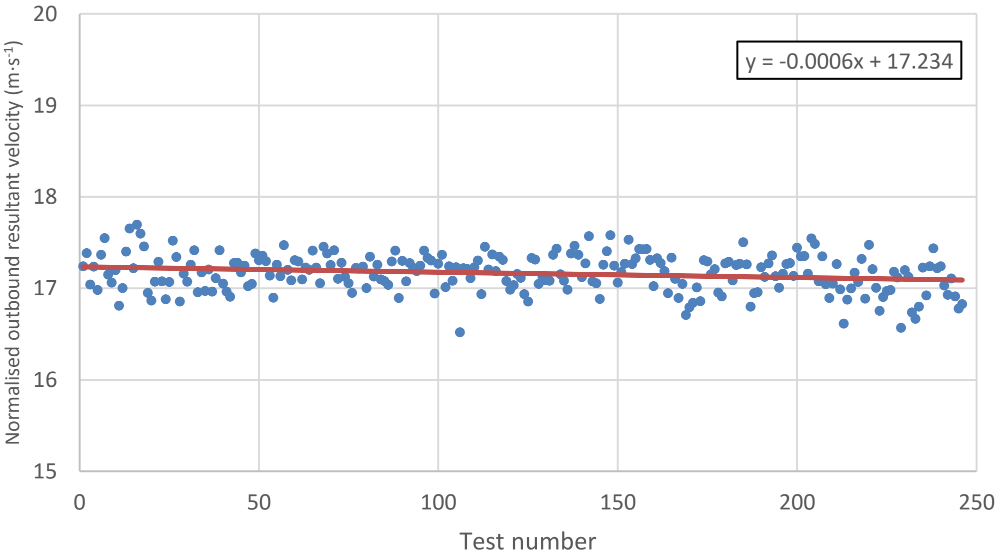

Figure 9.10 – A scatter plot showing the normalised resultant rebound velocities. The simple linear regression shows no overall change in the rebound resultant velocity with test number (n = 247).

The simple linear regression shows a neutral correlation between the resultant rebound velocity and test number. Normalising the data has removed any effects of ball launch variability. The random scatter in rebound velocity, measured post ball launch velocity normalisation, was due to the inherent variability of the balls and stringbed. Figure 9.11 shows the component rebound velocity data plotted as velocity vectors and table 9.8 shows the standard deviations (σ_{norm}) of the component rebound velocities.

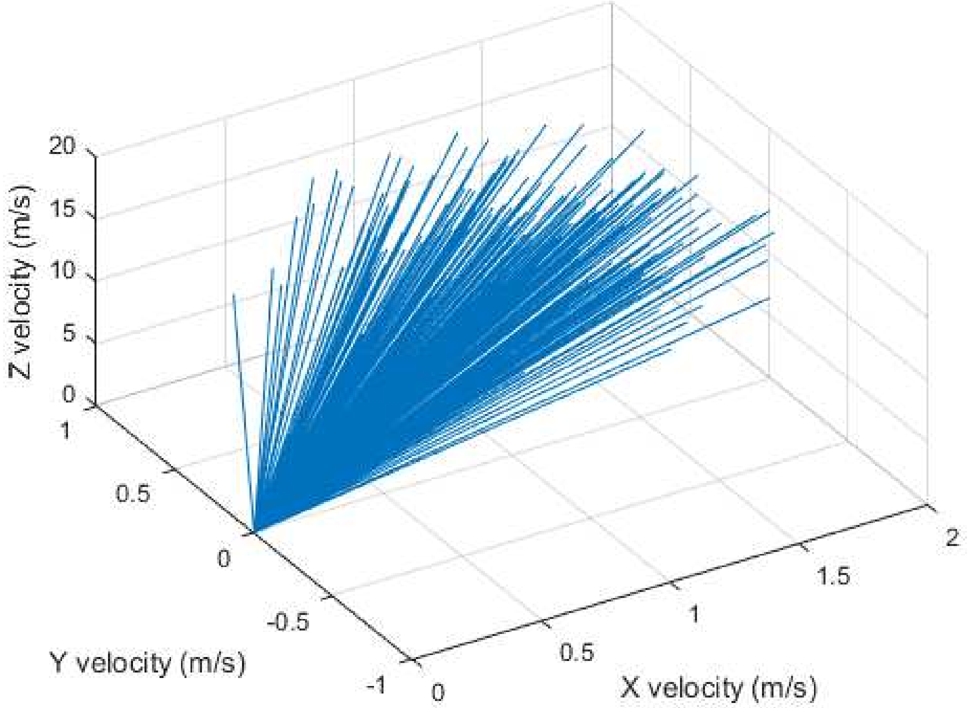

Figure 9.11 – Velocity vectors of the normalised rebound velocities for repeated impacts at the geometric stringbed centre of a head-clamped racket (n = 247).

Table 9.8 – The standard deviations of normalised component and resultant rebound velocities for repeated impacts at the geometric stringbed centre of a head-clamped racket (n = 247).

	Normalised outbound velocity components			
	X-axis	Y-axis	Z-axis	Resultant
σ_{norm} ($m \cdot s^{-1}$)	0.3	0.4	0.2	0.2

The random scatter of the velocity vectors shows the effect of the inherent variability of the ball and stringbed on rebound velocity. The standard deviations of the normalised component and resultant velocities will be used to explain variance in rebound velocity measured by the numerical models trained from the main impact testing dataset.

9.6.1.2 Ball rebound spin rate variability

Rebound spin rate variability was calculated from the impact test data. Spin rate data were not normalised, to account for the variability of ball launch. Figure 9.12 shows a scatter graph of launch and rebound spin rates. A simple linear regression has been fit to the data.

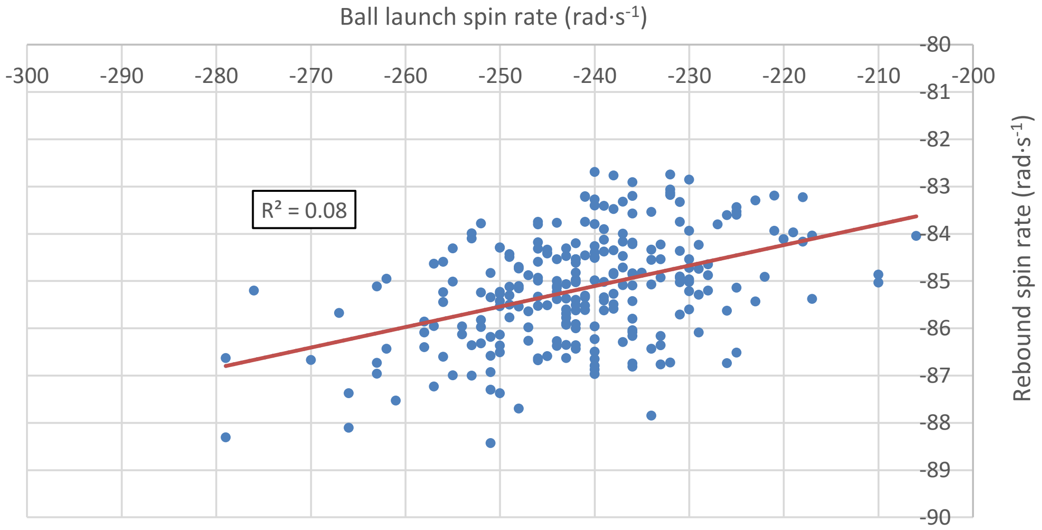

Figure 9.12 – Scatter graph of outbound spin rate plotted against inbound spin rate. A simple linear regression (red) shows a poor correlation, with an R^2 value of 0.08 (n = 247).

The correlation between launch and rebound spin rates is poor (R^2 = 0.08), over the narrow range of launch spin rates. The variability of rebound spin rate is random and attributed to the inherent variability of the ball and stringbed.

Figure 9.13 shows rebound spin rates plotted against test number. A simple linear regression was fit to the data.

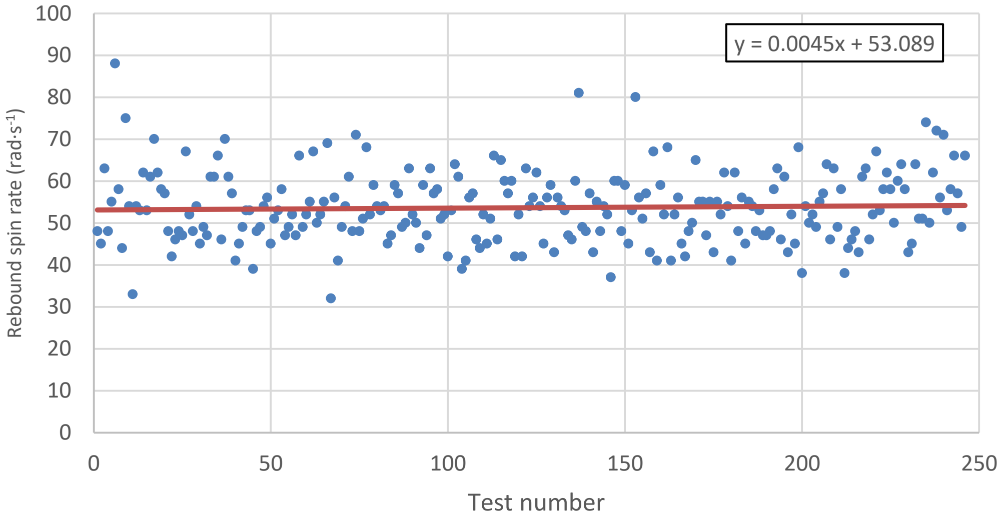

Figure 9.13 – Scatter graph of rebound spin rate against test number for repeated impacts at the geometric stringbed centre of a head-clamped racket. A simple linear regression (red) shows a neutral correlation between spin rate and test number (n = 247).

The simple linear regression shows a neutral correlation between the rebound spin rate and test number. The random scatter of the data shows the effect of the inherent variability of the ball and stringbed on rebound spin rate. Table 9.9 shows the standard deviation, σ_{spin} of the outbound spin rates.

Table 9.9 – The standard deviation of outbound spin rate for repeated impacts at the geometric stringbed centre of a head-clamped racket (n=277).

	Outbound spin rate (rad·s^{-1})
σ_{spin}	8.6

The standard deviations of the rebound spin rate will be used to explain variance in rebound spin rate measured by the numerical models trained from the main impact testing dataset.

9.6.2 Study 2 – Effect of test object durability on rebound trajectory

The effects of test object durability on rebound trajectories for a large number of impacts were assessed. Rebound ball velocities and spin rates were compared for impacts collected at the start and end of the Protocol. The Impact Rig was set up with an ITF *Development* racket, strung with ITF *Development* string to a stringing tension of 60 lbs. The racket was attached to the Impact Rig using the handle clamp. Nine ITF *High-Specification* balls were used. The Protocol was followed (i.e. 432 impacts) with an additional 72 impacts collected by repeating the initial 72 impacts (i.e. racket moved back to initial position, ball launch velocities and spin rates repeated).

Table 9.10 shows the differences in mean resultant rebound velocities for the impacts collected at the start and end of testing. Rebound velocities were grouped and compared by the four nominal launch velocities of the Protocol (n = 18 for each pairing). Statistical significance between pairings was calculated using a Student's t-test ($p = 0.05$).

Table 9.10 –Differences in mean rebound resultant velocities for impacts at the start and end of the Protocol. Rebound data were paired by nominal launch velocities (n = 18 for each group).

Nominal launch velocity	Difference in mean resultant rebound velocities ($m \cdot s^{-1}$)
23 $m \cdot s^{-1}$	0.1
25 $m \cdot s^{-1}$	0.3
28 $m \cdot s^{-1}$	0.1
30 $m \cdot s^{-1}$	-0.1

*results with significant difference between samples ($p = 0.05$).

The differences in mean resultant rebound velocities ranged from 0.3 $m \cdot s^{-1}$ to -0.1 $m \cdot s^{-1}$. No significant differences were found between the paired samples. The differences were within the measured inherent variability of the ball and stringbed, at a 95% confidence level ($1.96\sigma_{norm} = 0.4\ m \cdot s^{-1}$ for resultant rebound velocity, table 9.8).

Tables 9.11 shows the differences in mean rebound spin rates for impacts collected at the start and end of testing. Rebound spin rates were grouped and compared by the three nominal inbound spin rates of the Protocol (n = 24 for each pairing). Statistical significance between pairings was calculated using a Student's t-test (p = 0.05).

Table 9.11 - Differences in mean rebound spin rates for impacts at the start and end of the Protocol. Rebound data were paired by nominal launch spin rates (n = 24 for each group).

Nominal launch spin rate	Difference in mean rebound spin rates (rad·s^{-1})
0 rad·s^{-1}	-17.1*
200 rad·s^{-1}	-18.9*
300 rad·s^{-1}	-8.1*

*results with significant difference between samples (p = 0.05).

The differences in mean rebound spin rates ranged from -8.1 rad·s^{-1} to -18.9 rad·s^{-1}. Significant differences were found between the paired samples. These differences were within the measured inherent variability of the ball and stringbed, at a 99% confidence level ($2.58\sigma_{spin}$ = 22.2 rad·s^{-1} for rebound spin rate, table 9.9). The significant differences may have been a result of the small sample sizes compared in this study (n = 24) and the high inherent variability.

The changes in rebound velocities and spin rates were within the measured inherent variability of the test objects. As such, the effects of ball and stringbed durability on rebound trajectories were within acceptable levels. This validated the Protocol as the method for the main data collection exercise.

9.7 Conclusions

This chapter described the development of a testing protocol (the "Protocol") to collect ball-to-racket impact test data with the Impact Rig. The Protocol was designed to map a defined ball-racket impact system domain. All possible test parameters, or dimensions, of the system were considered. These were reduced to a subset of four. This was influenced by 'the curse of dimensionality', which states that as the dimensionality of the domain increases, the data required to describe the domain increases exponentially. The four test parameters chosen were:

1. Stringing tension.
2. Ball launch velocity.
3. Ball launch spin rate.
4. Impact location.

By constraining the parameters, the data collection method can be proven with a realistic test programme. An exponential rule was used to calculate a target number of impacts to map the system domain. A target of 1296 impacts was set by dividing the four test parameters by six nominal intervals. In reality, the inherent variability of the test apparatus and test objects prevented precise division of the test parameters. The durability of the test objects was also considered a source of variability. To ensure sufficient and efficient mapping of the system domain, the inherent variabilities and effects of durability were quantified. From this, nominal test parameter intervals were set to ensure good domain mapping, whilst minimising data collection repetition. The effects of ball durability on ball launch were used to set a ball impact limit.

In summary of the investigations:

Ball launch variability

A pilot study quantified the changes in and the variability of ball launch velocity, launch spin rate and impact location. These were established from 100 repeat impacts onto a racket. Overall changes in the parameters were attributed to the effects of ball durability. These were measured using simple linear regressions of each parameter against impact test number. The root-mean-square error of each parameter established parameter variability and were attributed to the inherent variability of the BOLA.

The effects of ball durability were:

- Ball launch velocity decreased by 0.8 $m \cdot s^{-1}$.
- Launch spin rate remained unchanged.

- Lateral component of impact location changed by 0.003 m.
- Longitudinal component of impact location changed by 0.008 m.

The RMSE of each parameters were:

- Ball launch velocity = 0.7 m·s^{-1}.
- Launch spin rate = 11.3 rad·s^{-1}.
- Lateral component of impact location = 0.011 m.
- Longitudinal component of impact location = 0.031 m.

The effects of ball durability data were minimised by limiting impacts to 50 per ball. The RMSEs were used to set nominal ball launch velocities intervals of 2 m·s^{-1} and 3 m·s^{-1}, ball launch spin rate intervals of 200 rad·s^{-1} and nominal impact locations with 60 mm lateral spacing and 80 mm longitudinal spacing.

Racket stringing variability

The variability of racket stringing was quantified from stringbed stiffness measurements of 85 ITF *Development* rackets. Stringbed stiffness varied by 5 lbs, for a nominal stringing tension of 60 lbs. A nominal stringing tension interval of 10 lbs was set.

Racket position, racket clamping and string positions

These potential variabilities were considered but not quantified. It was assumed the effects of excessive variation would be apparent in the impact data. The data would be scrutinised prior to any further analyses, which is discussed in the next chapter.

The effects of inherent ball and stringbed variabilities on rebound trajectories were quantified. Ball launch and rebound velocities and spin rates were recorded for 432 impacts onto a head clamped racket. Rebound velocities were normalised to account for ball durability effects. Impact locations were filtered to account for ball launch variability. The standard deviations of the resultant rebound velocity and rebound spin rate were 0.2 m·s^{-1} and 8.6 rad·s^{-1}. These results are used with the development and analysis of numerical models, which are discussed in the next chapter.

The effects of ball and stringbed durability on rebound trajectories were quantified. For this, the Protocol for 432 impacts was applied using a handle-clamped racket. The initial set of 72 impacts were repeated and changes in rebound velocity and spin rate measured. Significant changes in rebound spin rate were observed. The mean changes in rebound velocities and spin rates were within the inherent variabilities calculated previously. This showed impacts onto a handle-clamped racket did not to cause additional degradation or introduce additional variabilities to those already measured. The Protocol was approved for use with the main data collection exercise.

This chapter presented the development of the testing protocol used to collect ball-to-racket impact data. In the next chapter, data collected with the Protocol is used to develop a numerical model describing the ball-to-racket impact system. An initial dataset was used to train and test several multivariate polynomial models of increasing model order. From this, the best model order was selected. A second, independent dataset was used to validate the chosen model and establish the predictive error of model outputs.

Chapter 10 – Model development

10.1 Introduction

Having defined the testing protocol to collect impact data with the Impact Rig, this chapter describes the analysis of the data and development of numerical models. This is shown in context of the project in figure 10.1.

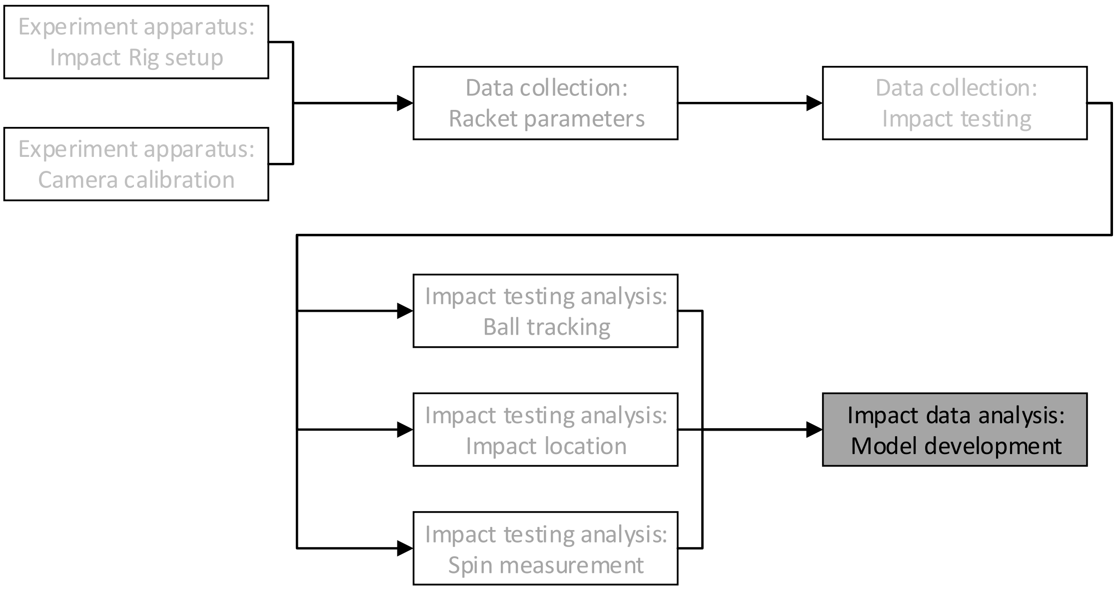

Figure 10.1 - Flowchart outlining the scope of the project. The chapter describes the analysis of impact testing data using the Impact Rig and the generation of a multivariate model.

Models for each dependent impact testing output parameter were developed using two independent datasets. The datasets were cleaned, to remove erroneous data, and reviewed to assess the suitability of each impact test parameter as model inputs. The first dataset was used to train and validate several polynomial regressions of increasing model order. This used the '*n-fold and leave one out cross-validation*' method (Kohavi, 1995) to select the best model orders from fit (mean R^2) and estimation error (mean and standard deviation of the sum of squared errors). The chosen models were tested using the second dataset. The predictive errors of the models (root-mean-squared errors) were calculated. The predictive errors were further quantified with trajectory simulations using *TennisGUT* – the ITF's tennis simulation software.

10.2 Objective

The objective of this chapter is to train, validate and test polynomial regressions of each dependent output parameters and calculate the predictive errors of each model.

10.3 Data summary

Before developing the numerical models, the impact test data were reviewed. A data collection summary is presented, with the steps to clean and filter the data.

10.3.1 Data collection summary

1. The impact testing protocol (the "Protocol" as described in chapter 9) was used to collect impact test data using the Impact Rig (described in chapter 3) and a pair of synchronised high-speed cameras.
2. The Protocol required 1296 impacts with varying ball launch velocities, spin rates and impact locations using one racket strung at three string tensions.
3. The cameras were calibrated using the planar method of camera calibration (described in chapter 4). This calculated intrinsic and extrinsic camera parameters to correct radial image distortions and reconstruct pairs of image coordinates.
4. The high-speed camera images were analysed using the *Impact Analyser* tool. Automated image processing algorithms digitised stringbed markers centroids in the first image pair of each test (described in chapter 5) and ball centroids in the images pairs into and out of each impact (described in chapter 6).
5. Spin rates and spin axes were measured with the *SpinTrack3D* algorithm (described in Chapter 8). Measurement error due to camera perspective was corrected.
6. Stringbed marker and ball centroid image coordinates were reconstructed into three-dimensional, real-world coordinates. Ball velocities and impact locations were calculated (described in chapters 6 and 7).
7. Velocities, spin axes and impact locations were transformed to the local racket origin (see figure 10.2). Transformations were calculated using the stringbed markers as intermediate reference points (described in chapter 6). The stringbed marker centroids were measured relative to the local racket origin using the *Racket*

Calibration tool (described in chapter 5). The longitudinal (y-axis) component of impact locations were translated to the geometric stringbed centre.

Figure 10.2 – Local racket origin for transformed ball velocity, ball spin axis and impact location measurements. The longitudinal component of impact locations were translated to the geometric stringbed centre.

10.3.2 Analysis success rate

The Protocol was used twice, to collect two impact test datasets. The first dataset was used to train and validate first, second and third order multivariate polynomial regressions. The aim was to select the best performing models. The second dataset was used to test the selected models and establish the predictive errors of the models. The *Impact Analyser* was subject to analysis failures. There were two causes:

1. The ball did not rebound out of the calibrated test volume. The automated image processing algorithms relied on a final image pair with the ball out of frame.
2. High-speed camera image brightness. Light in the test volume was influenced by ambient light conditions. Consistent camera settings (exposure times and aperture) were maintained throughout testing, and so were not adjusted to compensate for the lower ambient light levels. The darker images required greater manual refinement of the *Impact Analyser* image processing parameters. This was particularly prevalent for the test dataset, which had a lower analysis success rate.

The analysis success rates for the two datasets are shown in table 10.1. The distribution of the unsuccessful analyses for the training and validation set are shown in figure 10.3.

Table 10.1 – The *Impact Analysis* tool analysis success rate for the training and validation dataset and the test dataset.

Dataset	Impact tests	Impacts successfully analysed	Success rate %
Training and validation	1296	1229	95%
Test	1296	1138	88%

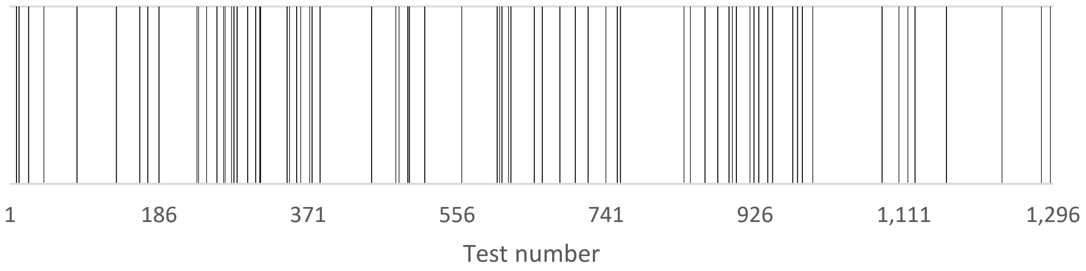

Figure 10.3 – A bar chart showing the distribution of unsuccessfully analysed impacts. Each bar represents a single, unanalysed impact.

The unsuccessful analyses were observed to be randomly distributed. Each combination of test variable was subject to six repeat impacts. For the training and validation dataset, a total of seven combinations of test variable settings resulted in two unsuccessful analyses. This meant these combinations of test variables were represented by four impacts only. In total, 53 combinations of test variable settings resulted in one unsuccessful analyses. This gave no concern for bias in mapping the ball-racket impact system domain, as each combination of settings were well represented. The distribution of data is evaluated in the next section.

10.3.3 Data cleaning

Prior to modelling, the datasets were cleaned by removing erroneous data. Assuming data outliers existed, filters were set at three standard deviations from the mean of each parameter. The velocity intervals were rounded to the nearest integer and spin rates to one decimal place. The filters were:

- Ball launch velocity – x-axis component, v_{ix}: 5 m·s^{-1} to 11 m·s^{-1}.
- Ball launch velocity – y-axis component, v_{iy}: -3 m·s^{-1} to 1 m·s^{-1}.
- Ball launch velocity – z-axis component, v_{iz}: -30 m·s^{-1} to -15 m·s^{-1}.
- Ball launch spin rate, s_i: -600 rad·s^{-1} to 200 rad·s^{-1}.

Two additional filters were created:

- The ball was assumed to always rebound upwards from the racket. Negative values of vertical component of rebound velocity (v_{oz}) were therefore erroneous.
- Figure 10.4 shows a scatter plot of impact locations for the test dataset. One impact was identified as an outlier, highlighted by the red circle. Longitudinal components of impact locations, L_y less than -0.08 m were removed from the datasets.

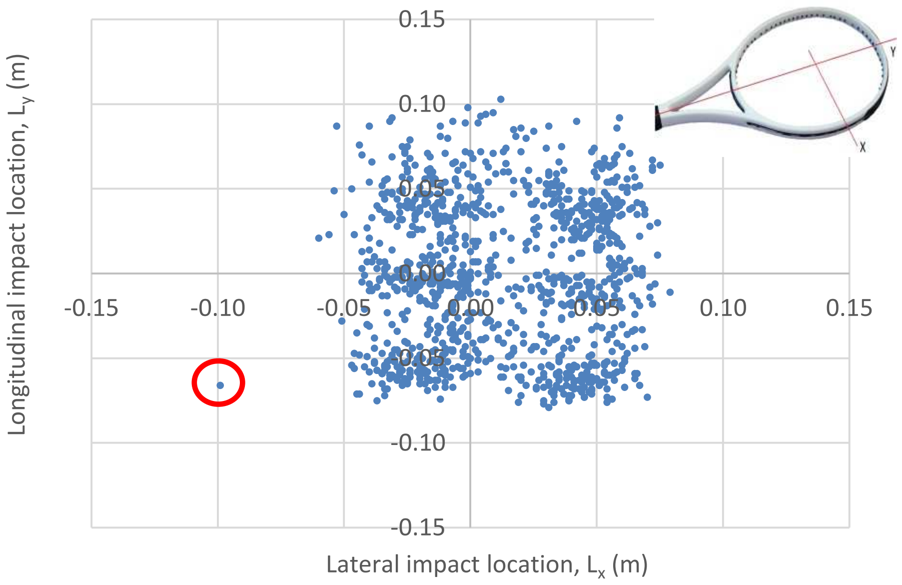

Figure 10.4 – Scatter graph of impact locations. The red circle identifies an outlying impact location.

The filters were applied to both datasets. All data associated with the outliers were removed. Table 10.2 shows the number of impact tests removed from the datasets.

Table 10.2 – Data more than 3 standard deviations from the parameter mean and obvious outlying data were removed. The total impact tests removed from the datasets are shown.

	Impacts successfully analysed	Impact test removed	Impact test removed (%)
Training and validation dataset	1229	49	4%
Test dataset	1138	75	7%

Failed analysis and data cleaning resulted in the training and validation dataset comprising 1180 impacts and the test dataset comprising 1063 impacts. These were 91% and 82% of the original 1296 impacts, respectively.

10.4 Data distributions

Ball-to-racket impacts were described by a system domain of 10 independent input parameters and seven dependent output parameters, shown in table 10.3. Each output parameter was modelled separately, using all input parameters as model inputs.

Table 10.3 – The ball-to-racket impact system domain was described by 10 independent input parameters and seven dependent output parameters.

Input parameters	Output parameters
Stringing tension (T)	Rebound velocity components (v_{ox}, v_{oy}, v_{oz})
Ball launch velocity components (v_{ix}, v_{iy}, v_{iz})	Rebound spin rate, S_o
Ball launch spin rate, S_i	Rebound spin axis components ($\widehat{\omega}_{ox}$, $\widehat{\omega}_{oy}$, $\widehat{\omega}_{oz}$)
Ball launch spin axis components ($\widehat{\omega}_{ix}$, $\widehat{\omega}_{iy}$, $\widehat{\omega}_{iz}$)	
Impact location components (L_x, L_y)	

The distributions of the input parameter data were assessed. Well distributed data ensured well defined models. Figures 10.5 to 10.8 show the distributions of impact locations and ball launch velocities, spin rates and spin axes, for the training and validation dataset. The test dataset was generated from repetition of the Protocol and the data distributions assumed comparable.

Impact locations:

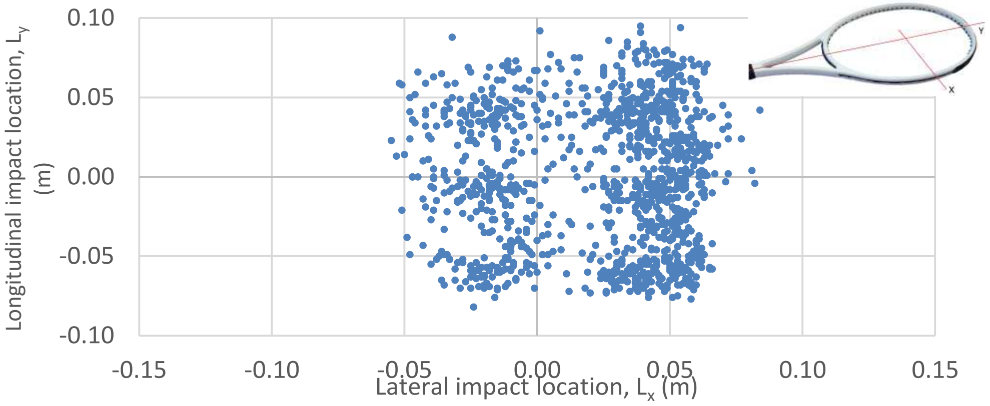

Figure 10.5 – A scatter graph showing the impact locations (lateral, L_x and longitudinal, L_y) for the training and validation dataset.

The scatter graph shows six broad clusters relating to the six nominal positions of the racket within the Impact Rig. The scatter within each cluster was associated with the inherent variability of the BOLA and the variability of positioning the racket before each test.

Ball launch velocity components:

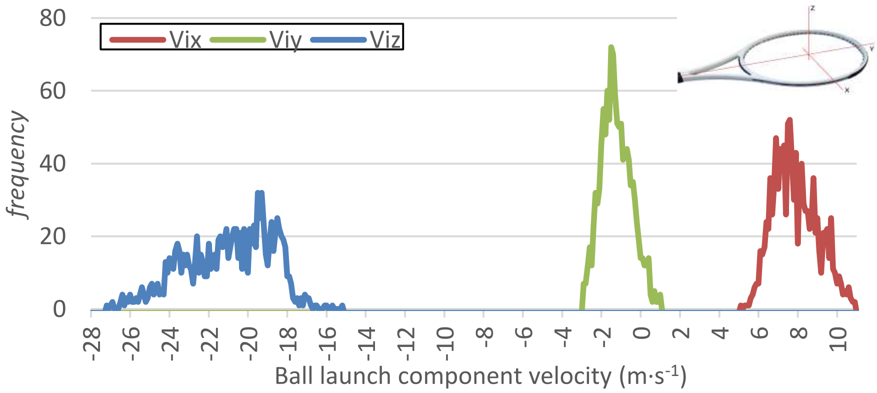

Figure 10.6 – A frequency chart showing the distributions of ball launch velocity components: lateral velocity, V_{ix} (red), longitudinal velocity, V_{iy} (green) and vertical velocity, V_{iz} (blue).

The frequency chart shown in figure 10.6 shows the vertical component of ball launch velocities, V_{iz} (blue line) were between -18 m·s^{-1} and -26 m·s^{-1}. The lateral component velocities, V_{ix} (red line) were between 5 m·s^{-1} and 11 m·s^{-1}, whilst the longitudinal velocities, V_{iy} (green line) were between -3 m·s^{-1} and 1 m·s^{-1}. The wider ranges of vertical and lateral components were an intentional outcome of the position and orientation of the BOLA relative to the racket. The inherent variability of the BOLA meant the four nominal launch velocities of the protocol were not clearly defined. This also caused the narrow spread of longitudinal component velocities. Given this narrow range, and its ascription to the inherent variability of ball launch, the longitudinal velocity data were excluded as an input parameter.

Ball launch spin rates:

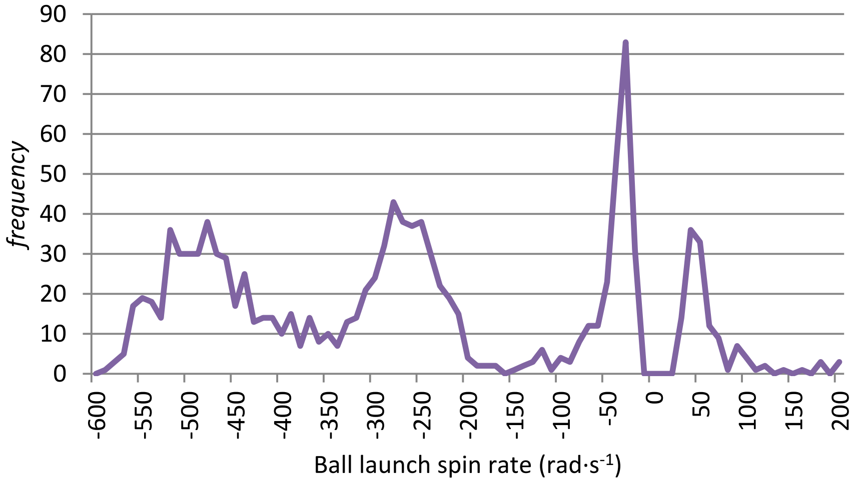

Figure 10.7 – A frequency chart showing the distributions of ball launch spin rates, S_i. The peaks correspond to the three nominal test spin rates.

The frequency chart shown in figure 10.7 shows a spread of data between -600 rad·s^{-1} and 200 rad·s^{-1}. Three regions are defined by the three nominal test values of the protocol. The largest peak (approximately -30 rad·s^{-1}) was due to a quirk of the *SpinTrack3D* algorithm resulting in a systematic error at spin rates close to 0 rad·s^{-1} (discussed in Chapter 8).

Ball launch spin axis components:

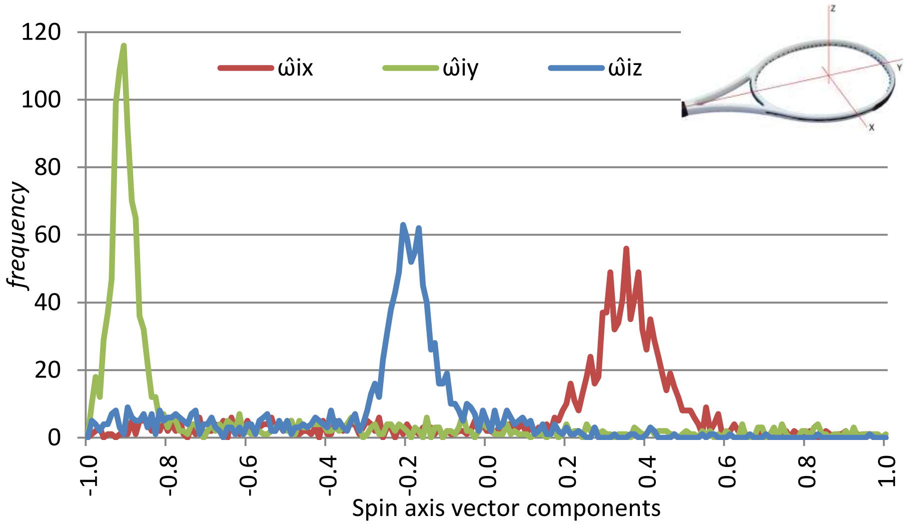

Figure 10.8 – A frequency chart showing the distributions of ball launch spin axis components: x-axis, $\hat{\omega}_{ix}$ (red), y-axis, $\hat{\omega}_{iy}$ (green) and z-axis, $\hat{\omega}_{iz}$ (blue).

The frequency chart shown in figure 10.8 shows a single, narrow peak for each component. The largest peak – for the y-axis component (green line) – was attributed to two of three nominal test values where spin was purposefully applied to the ball. The spin applied by the BOLA gave a spin axis closely, but not perfectly aligned to the longitudinal axis of the racket. This resulted in the peaks for the x- and z-axis components (red and blue lines). The spin axis measurements for the slow spinning impacts are represented by the random, low frequency noise across the entire width of the spin axis domain. This is further shown in figure 10.9, which also shows no dependency between the ball launch spin rate and lateral spin axis component. Similar data are shown for ball launch spin rate and the other two spin axis components.

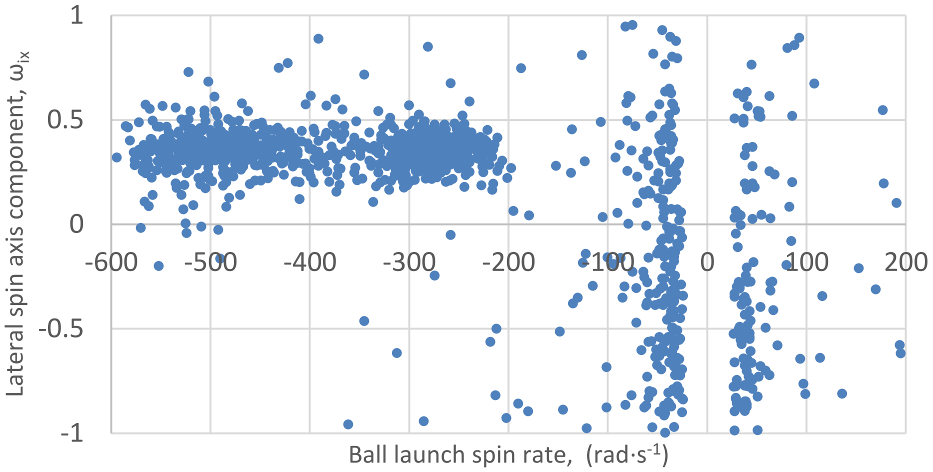

Figure 10.9 – The lateral spin axis component (ω_{i_x}) and spin rate of ball launch. The data shows no dependency between the variables. The spin axis component for low spin rate launches (<100 rad·s^{-1}) are randomly distributed between -1 and 1. The spin axis component for high spin rate launches (>200 rad·s^{-1}) are less random

An additional investigation showed the variability of spin axis within the 20 consecutive frames analysed for an individual impact. Figure 10.10 shows the rebound spin axis vectors for a single impact, over the 20 consecutive image pairs analysed.

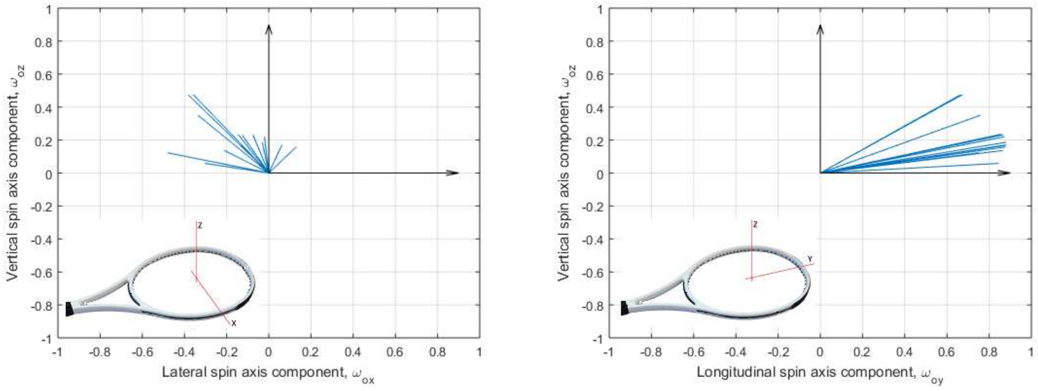

Figure 10.10 – The spin axis vectors for 20 image pairs of an rebound trajectory show spin axis variability. The left graph shows the lateral/vertical (x, z) spin axis components, the right graph shows the longitudinal/vertical (y, z) spin axis components.

The graphs show variability of the lateral (x-axis in figure 10.10 left) and vertical (y-axis in both figure 10.10) components of spin axis. This variability was hypothesised as representing spin precession, possibly caused by a non-uniform ball mass and moment of inertia. Spin precession has not been researched previously and represents an interesting route for further research. Given this information, and with the narrow range of the data, all spin axis data were excluded as inputs parameter for the models.

The longitudinal component of spin axis was still used to qualify spin direction, with spin rates given a positive or negative sign to indicate backspin or topspin, respectively (see chapter 8).

10.4.1 The reduced system domain

The datasets were reduced to six input parameters and three output parameters. The parameters of the new domain are shown in table 10.4.

Table 10.4 – The ball-to-racket impact system domain was reduced to six independent input parameters and three dependent output parameters.

Input parameters	Output parameters
Stringing tension	Rebound velocity components (v_{ox}, v_{oz})
Ball launch velocity components (v_{ix}, v_{iz})	Rebound spin rate, S_o
Ball launch spin rate, S_i	
Impact location components (L_x, L_y)	

10.5 Model training and validation

Multivariate fitting techniques allow complex systems to be modelled, offering two advantages. The predictive power of the model is improved, making the model increasingly useful for estimating more sophisticated scenarios. Relationships between parameters can be identified by varying individual input parameters to investigate the effect on an output parameter.

10.5.1 Multivariate fitting

Several multivariate fitting tools exist to model complex datasets and find correlations within the data (e.g. principal component analysis, neural networks, polynomial regression etc.). For this project, the MATLAB polynomial regression tool, *polyfitn* (Mathworks, 2008) was used to create multivariate polynomial models. Choppin (2008) used this tool with a comparable ball-racket impact dataset, comprising six input parameters and two output parameters.

The polynomial form of the ball-to-racket impact model is shown in equation 10.1. The equation uses the six independent input parameters: string tension (T), ball launch velocity components (V_{ix}, V_{iz}), ball launch spin rate (S_i), and impact location components, (L_x, L_y) to model each dependent output:

$$Output = \left(A \cdot T + B \cdot V_{ix} + C \cdot V_{iz} + D \cdot S_i + E \cdot L_x + \mathrm{F} \cdot L_y + G\right)^n \qquad 10.1$$

where n is the model order and A to G are the model term weightings. The *polyfitn* tool fits a model to the data by adjusting the term weightings to minimise model error in a least-squares sense. Expanding the equation for a given order gives the total number of terms and weightings. First through fourth order model terms are shown in table 10.5.

Table 10.5 – The model terms for the polynomial equation increased greatly as the model order increased. The number of model terms for first through fourth order models are shown.

Model order, n	1st	2nd	3rd	4th
Model terms	7	28	84	210

Choppin identified that as the model terms increased, so too did the data required to fit the model. For this reason, he concluded a lower order model would be more suitable for his dataset. Given the similarities to his dataset (i.e. the number of test parameters), first through third order models were investigated. The goal was to identify the best model order, to both fit the data and minimise predictive error.

10.5.2 Model training

Models were trained and validated for each output parameter using the '*n-fold and leave one out cross-validation'* method (Kohavi, 1995). For this, the training and validation dataset was randomised and split into 10 equal partitions, as shown in figure 10.11.

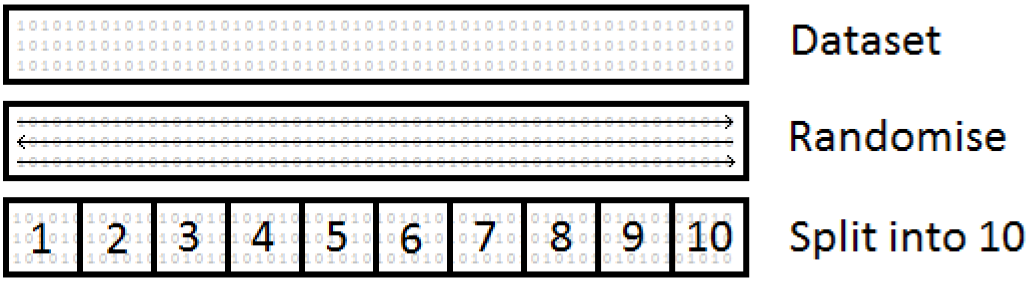

Figure 10.11 – The n-fold and leave one out cross-validation method (Kohavi, 1995) required the dataset to be randomised and split into 10 equal sections.

Models were trained using data from nine of the partitions. The remaining partition was isolated from training and used to validate each model. The process was repeated 10 times, isolating each partition in turn as shown in figure 10.12. For each output parameter, 10 first, second and third order models were trained – a total of 30 models per output parameters and 90 models in total.

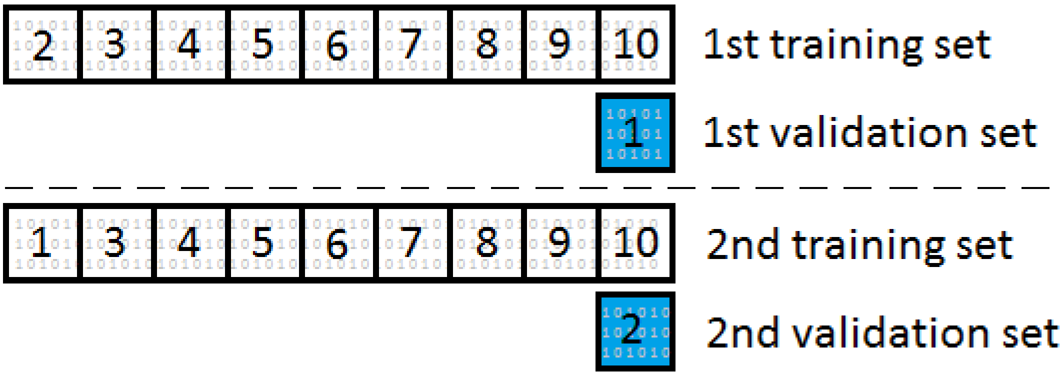

Figure 10.12 – Nine of the 10 data partitions were used to train the polynomial model. The tenth partition was isolated from training and used to validate each model. This was repeated 10 times by isolating each partition in turn and retraining the models.

10.5.3 Model validation

Two statistics were calculated to assess the performance of each model:

1. Model fit, R^2 was measured for each trained model. The mean R^2 value was calculated for each model order (e.g. the mean of the 10 1st order models).
2. Model estimation error was calculated as the sum of squared errors (SSE). SSE was calculated by comparing the predicted outcome of a trained model to the measured data of the isolated, validation partition. The mean and standard deviation of SSE were calculated for each model order.

Table 10.6 shows the mean R^2 values of first, second and third order models. The highest values for each output parameter are highlighted. The mean SSEs and standard deviations of SSE are shown in table 10.7. The lowest values for each output parameter are highlighted.

Table 10.6 – Mean R^2 values for 1st, 2nd and 3rd order models for the three output parameters. The highest values for each output parameter are highlighted in red.

	Model order		
	1st	2nd	3rd
Lateral rebound velocity, V_{ox}	0.89	0.93	0.94
Vertical rebound velocity, V_{oz}	0.79	0.98	0.98
Rebound spin rate, S_o	0.76	0.82	0.84

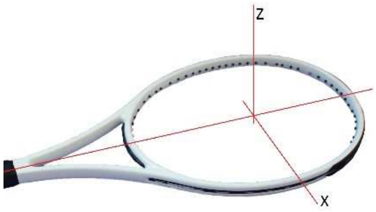

Table 10.7 – Mean and standard deviation of SSE for 1st, 2nd and 3rd order models. The lowest values for each output parameter are highlighted in red.

		Model order		
		1st	2nd	3rd
Lateral rebound velocity, V_{ox}	Mean SSE	49.3	32.6	28.5
	SD of SSE	10.0	7.4	7.1
Vertical rebound velocity, V_{oz}	Mean SSE	110.7	11.9	10.6
	SD of SSE	26.8	4.1	4.5
Rebound spin rate, S_o	Mean SSE	140163.1	109956.7	114471.5
	SD of SSE	14859.5	15925.3	23273.3

10.5.4 Model order selection

This section discusses the validation results and selects the best performing models:

Lateral rebound velocity (V_{ox}) models

The models showed increasing mean R^2 (0.89, 0.93 and 0.94 in table 10.6) and decreasing mean SSE (table 10.7) with model order. These show the higher order models better fit the data without over-fitting. The relatively consistent standard deviations of SSE (table 10.7) support this further. The third order model is the best performing. However, the second order model offers comparable performance, whilst being a simpler model (i.e. fewer model terms). Choppin (2008) made a similar observation, stating the simpler model was preferable. Therefore, the second order model was chosen.

Vertical rebound velocity (V_{oz}) models

The models showed increasing mean R^2 (0.79, 0.98 and 0.98 in table 10.6) and decreasing mean SSE (table 10.7) with model order. The changes in R^2 and SSE for the first and second order models suggests the former under-fit the data. As with the lateral rebound velocity models, the third order model was the best performing (joint highest R^2, lowest mean SSE). However, the second order model offered comparable results. Therefore, the second order model was chosen.

Rebound spin rate (S_o) model

The mean R^2 values increased with model order (0.76, 0.82 and 0.84 in table 10.6), showing improving model fit. The relatively low R^2 for the first order model suggests under-fitting. The mean SSE was lowest for the second order model, suggesting the third order model over-fit the training data. Further evidence supporting this is shown by the standard deviation of SSE, which was largest for the third order model. As such, the second order model was chosen.

10.5.5 Model order summary

The orders chosen for the dependent output parameter models are summarised in table 10.8:

Table 10.8 – The model orders chosen for the three dependent output parameter models.

Output parameter model	Polynomial model order
Lateral rebound velocity, v_{ox}	Second
Vertical rebound velocity, v_{oz}	Second
Rebound spin rate, s_o	Second

10.6 Model testing

The predictive errors of the models were calculated using the independent test dataset. The outputs of each model were compared to the measured outcomes for each set of measured input data. The mean errors and the root-mean-squared errors (RMSE) were calculated for each model and are shown in table 10.9.

Table 10.9 – The mean errors and the root-mean-squared errors of the lateral rebound velocity, vertical rebound velocity and rebound spin rate models for the test dataset (n = 1138).

	Output parameter model		
	Lateral rebound velocity, v_{ox} (m·s^{-1})	Vertical rebound velocity, v_{oz} (m·s^{-1})	Rebound spin rate, s_o (rad·s^{-1})
Mean error	0.40	-0.14	10.8
Root-mean-squared-error	0.75	0.49	27.6

The mean errors of each model show systematic differences between the model outputs and the test dataset. A positive value indicates an over-prediction. On average, the lateral rebound velocity and rebound spin rate models over-predicted the test data, whilst the vertical rebound velocity model under-predicted the test data. The RMSEs are measures of the variance between the models and test data and indicate the predictive power of the models.

10.6.1 Explaining variance

The predictive errors (RMSEs) of the velocity and spin models were partly explained by the inherent variability of the test objects – the ball and stringbed. These were quantified in the experiment described in Chapter 9. The standard deviations of rebound lateral and vertical rebound velocities, σ_{norm} and rebound spin rate, σ_{spin}, measured in that experiment are shown in tables 10.10 and 10.11, respectively.

Table 10.10 – The standard deviations of the normalised lateral rebound and vertical rebound velocities for repeated impacts at the geometric stringbed centre of a head-clamped racket (n = 277).

	Rebound velocity variabilities	
	Lateral (x-axis)	Vertical (z-axis)
σ_{norm} (m·s^{-1})	0.30	0.20

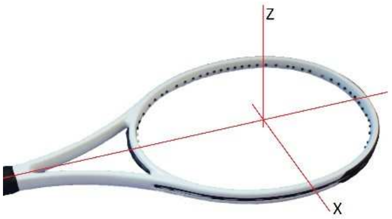

Table 10.11 – The standard deviation of rebound spin rate for repeated impacts at the geometric stringbed centre of a head-clamped racket (n=277).

	Rebound spin rate
σ_{spin} (rad·s^{-1})	8.6

The inherent variability of lateral rebound velocity (σ_{norm} = 0.30 m·s^{-1}) explains 40% of the variance measured in the test dataset (RMSE = 0.75 m·s^{-1}). The inherent variability of vertical rebound velocity (σ_{norm} = 0.20 m·s^{-1}) explains 41% of the variance measured in the test dataset (RMSE = 0.49 m·s^{-1}). The inherent variability of rebound spin (σ_{spin} = 8.6 rad·s^{-1}) explains 31% of the variance measured in the test dataset (RMSE = 27.6 rad·s^{-1}). These results show some additional mechanisms are causing the predictive errors of the model.

To further explore the variance in the test dataset, the predictive errors of each model were recalculated using a subset of the training dataset. The mean error and RMSE calculated from a random 10% of the training data are shown in table 10.12.

Table 10.12 – The mean errors and the root-mean-squared errors of the lateral rebound velocity, vertical rebound velocity and rebound spin rate models for a random 10% sample of the training and validation dataset.

	Output parameter model		
	Lateral rebound velocity, v_{ox} (m·s^{-1})	Vertical rebound velocity, v_{oz} (m·s^{-1})	Rebound spin rate, s_o (rad·s^{-1})
Mean error	-0.02	0.00	-3.4
Root-mean-squared error	0.45	0.26	28.9

This method is biased towards low mean errors, as the tested data was used to train the model. However, the measured RMSEs should be similar to those calculated previously, as the testing method to generate both datasets was repeated. The rebound spin rate model RMSEs were broadly similar (training data sub-sample RMSE = 28.9 rad·s^{-1}, test dataset RMSE = 27.6 rad·s^{-1}). The RMSEs for the lateral and vertical rebound velocity models were reduced (0.45 m·s^{-1} compared to 0.75 m·s^{-1} and 0.26 m·s^{-1} compared to 0.49 m·s^{-1}). These discrepancies, and the cause of the systematic errors between the models and test dataset, are explored further in the next section.

10.7. Model errors

To investigate the systematic errors of each model, error distributions were inspected. The discrepancies between the outputs of each model and measured outcomes for each set of measured input data for the test dataset were plotted. The error distributions are presented by the three stringing tensions (50 lbs, 60 lbs and 70 lbs) tested.

Lateral rebound velocity (V_{ox}) model errors

The error distributions for the lateral rebound velocity model are shown in figure 10.13.

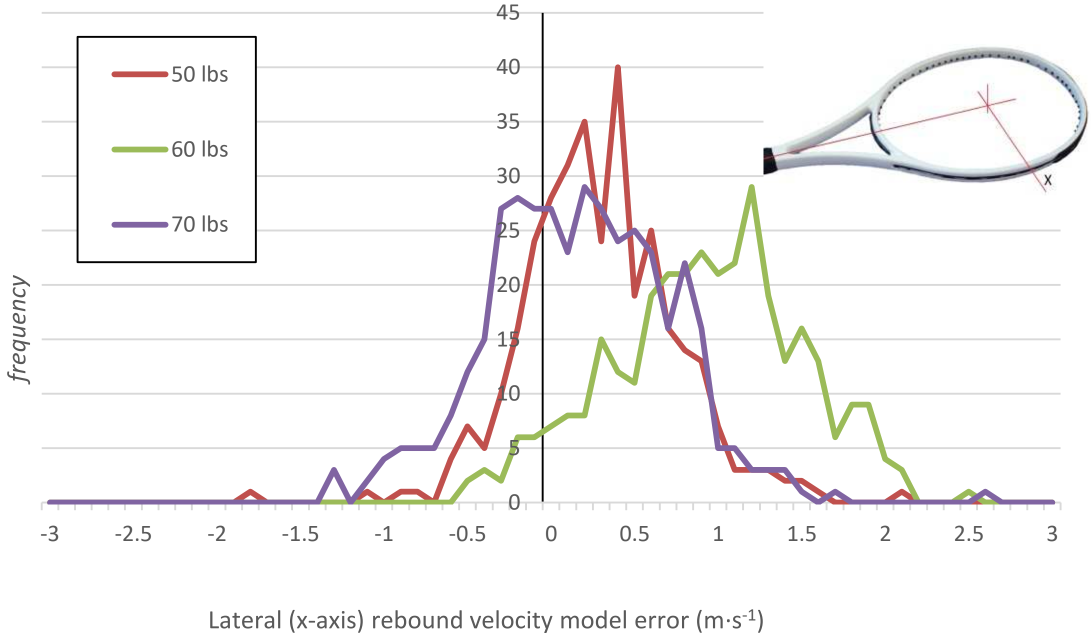

Figure 10.13 – A frequency chart of error distributions for the lateral (x-axis) rebound velocity model for the 50 lbs (red), 60 lbs (green) 70 lbs (purple) stringing tension data.

All three distributions show a positive systematic offset, with modal values above zero, giving the mean error for all data of 0.40 m·s^{-1} (table 10.9). The 60 lbs stringing tension test data (green line) shows a positive skew, with large modal value (approximately 1.3 m·s^{-1}), clearly offset from the other string tensions tested. This observation requires further investigation.

Vertical rebound velocity (V_{oz}) model errors

The error distributions for the vertical rebound velocity model are shown in figure 10.14.

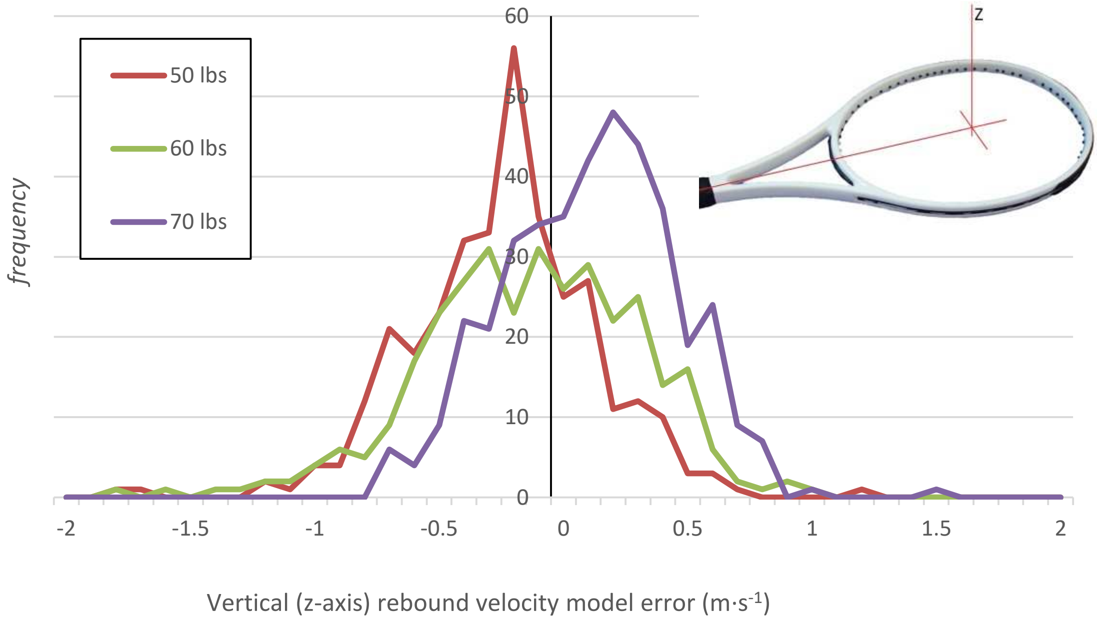

Figure 10.14 – A frequency chart of error distributions for the vertical (z-axis) component of rebound velocity model showing the 50 lbs (red), 60 lbs (green) 70 lbs (purple) stringing tension data.

The error distribution for the 60 lbs (green line) stringing tension data is neutral, with a modal value close to zero. The error distribution for the 50 lbs (red line) stringing tension test data shows a small negative systematic error, with a modal value of approximately -0.2 m·s^{-1}. The 70 lbs stringing tension test data (purple line) has a small positive systematic error, with a modal value of approximately 0.3 m·s^{-1}. These error distributions effectively cancel each other out, giving the mean error for all data of -0.14 m·s^{-1} (table 10.9).

Rebound spin rate (S_o) model errors

The error distributions for the rebound spin rate model are shown in figure 10.15.

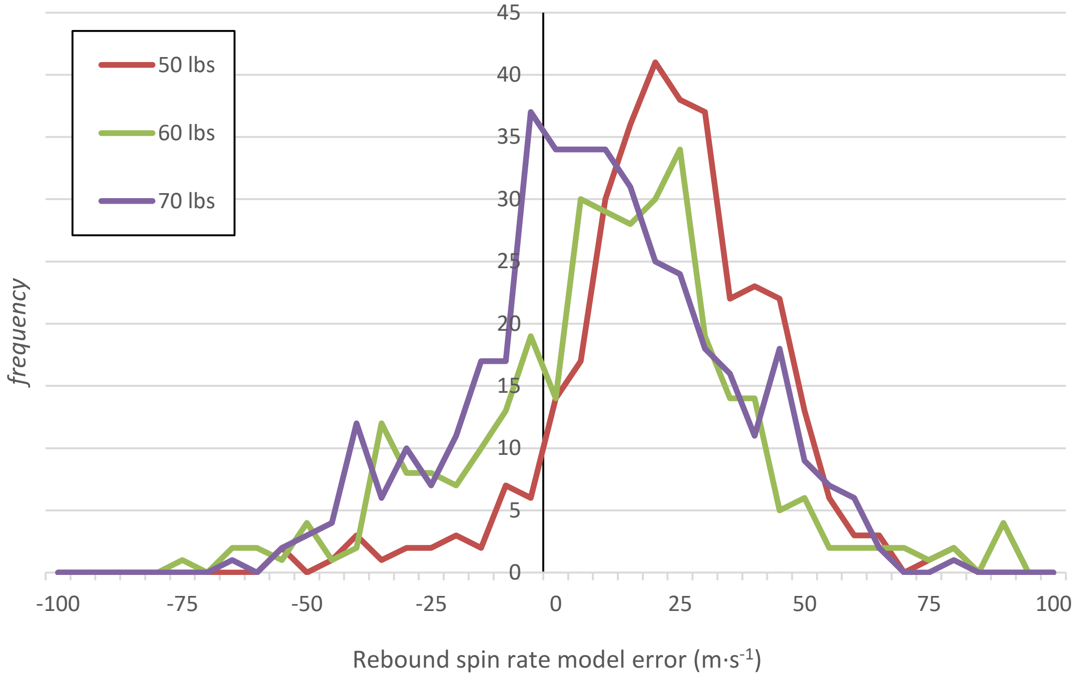

Figure 10.15 – A frequency chart of error distributions for the rebound spin rate model showing the 50 lbs (red), 60 lbs (green) 70 lbs (purple) stringing tension data.

All three distributions show a positive systematic offset, with modal values for the 50 lbs (red line) and 60 lbs (green line) stringing tension test data above zero. The modal values are approximately 20 rad·s^{-1} and 25 rad·s^{-1}, respectively. Although the modal error for the 70 lbs data is close to zero, the positive skew causes a mean error for all data of 10.8 rad·s^{-1} (table 10.9). These systematic errors require further investigation.

The distributions of errors for lateral rebound velocity and rebound spin rate model (figures 10.13 and 10.15) suggest some discrepancies between the two datasets. The mechanism causing these discrepancies is beyond the predictive power of the models. The mechanism could be measurement error present in either of the datasets. This is partially supported by the result of testing the models against a random sub-sample of the training and validation dataset. The mean errors resulting from this test, shown in table 10.12, are small. Discrepancies between the datasets are explored further in the next section.

10.7.1 Dataset discrepancies

The distributions of the ball launch spin rate data for the two datasets were examined. The repeated use of the testing protocol should have resulted in similar distributions. This is evident in the 50 lbs stringing tension data, shown in figure 10.16.

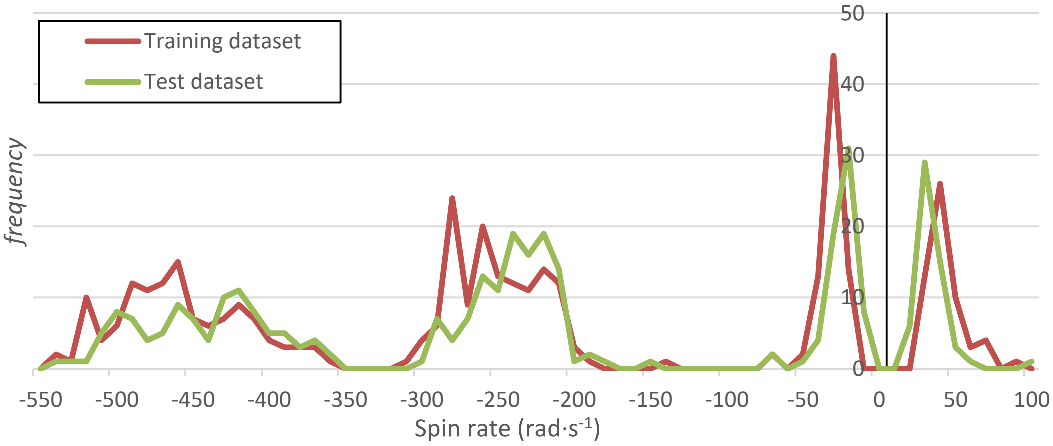

Figure 10.16 – A frequency chart showing the distribution of ball launch spin rates for the training (red) and test (green) datasets for the 50 lbs stringing tension tests.

The distributions of ball launch spin rates for the 60 lbs stringing tension tests are not similarly distributed, shown in figure 10.17.

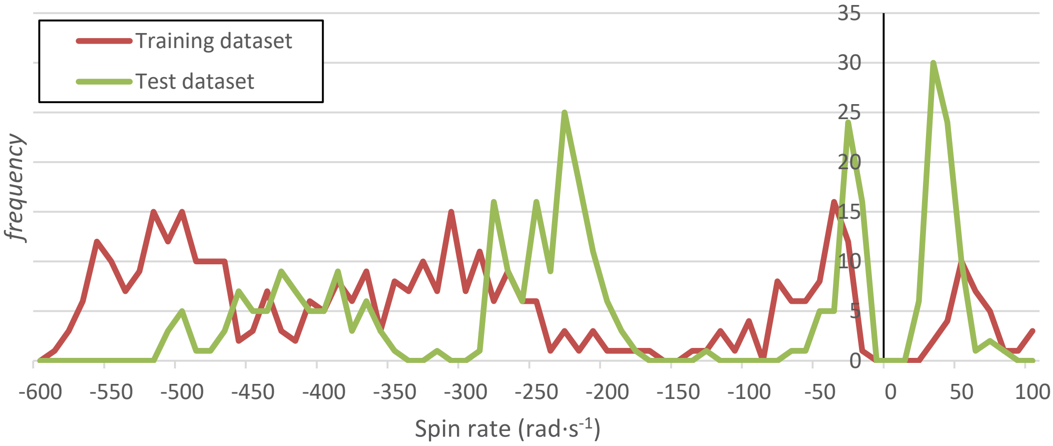

Figure 10.17 – A frequency chart showing the distribution of ball launch spin rates for the training (red) and test (green) datasets for rackets strung at 60 lbs stringing tension.

Below -150 rad·s^{-1} a discrepancy of approximately 100 rad·s^{-1} is evident. A discrepancy of approximately 30 rad·s^{-1} was observed in the 70 lbs stringing tension test data.

If the data are accurate, these discrepancies should not cause the systematic mean errors of the models. The models should be capable of interpolating the differences present in the test data. The relationships between individual input and output parameters were examined. Strong correlations were measured between ball launch spin rate and rebound spin rate ($R^2 = 0.7$) and ball launch spin rate and lateral rebound velocity ($R^2 = 0.8$). Figure 10.18 shows a scatter graph of ball launch spin rate plotted against rebound spin rates, for the 60 lbs stringing tension tests of the training and test datasets. The relationships between parameters for both datasets are shown by simple linear regression.

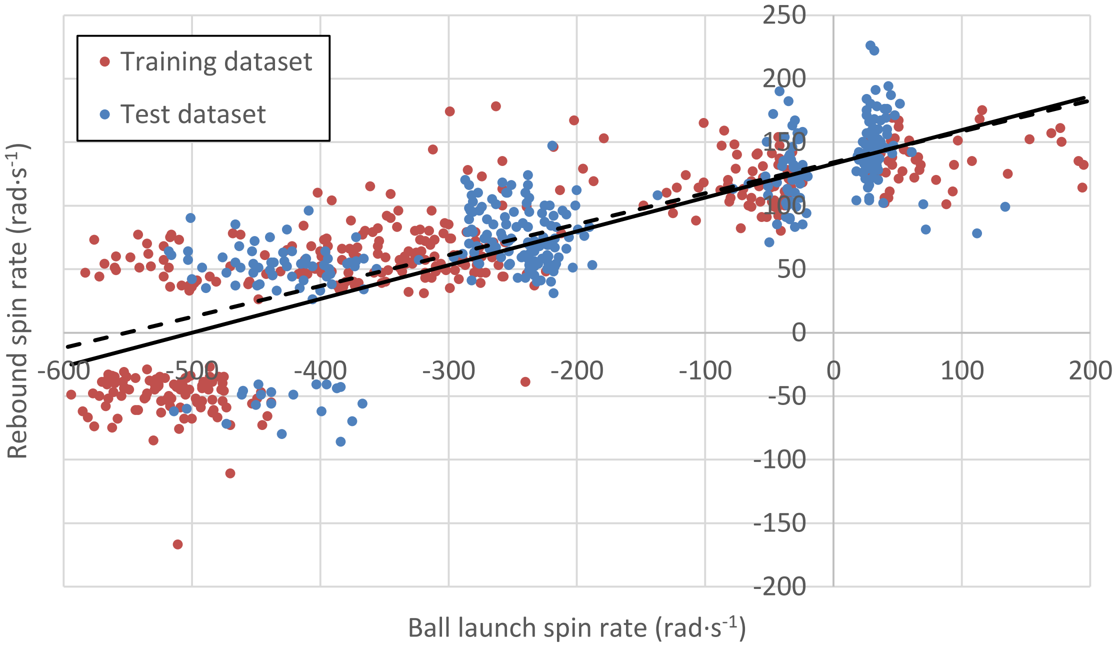

Figure 10.18 – A scatter graph showing ball launch spin rate plotted against rebound spin rate for the 60 lbs stringing tension tests from the training (red) and test datasets (blue). Simple linear regression show strong correlations between the parameters (solid line for training data, dashed line for test data).

The simple linear regression show direct relationships between the parameters. However, the regressions diverge as ball launch spin rate decreases. This is caused by lower spin rates (x-axis) for the test dataset (blue) at spin rates below -150 rad·s^{-1}, whilst the rebound spin rates (y-axis) appear similar in both datasets.

The same effect is more noticeable when ball launch spin rates are plotted against lateral rebound velocities for the 60 lbs stringing tensions data (figure 10.19). The relationships between parameters are shown by two simple linear regression.

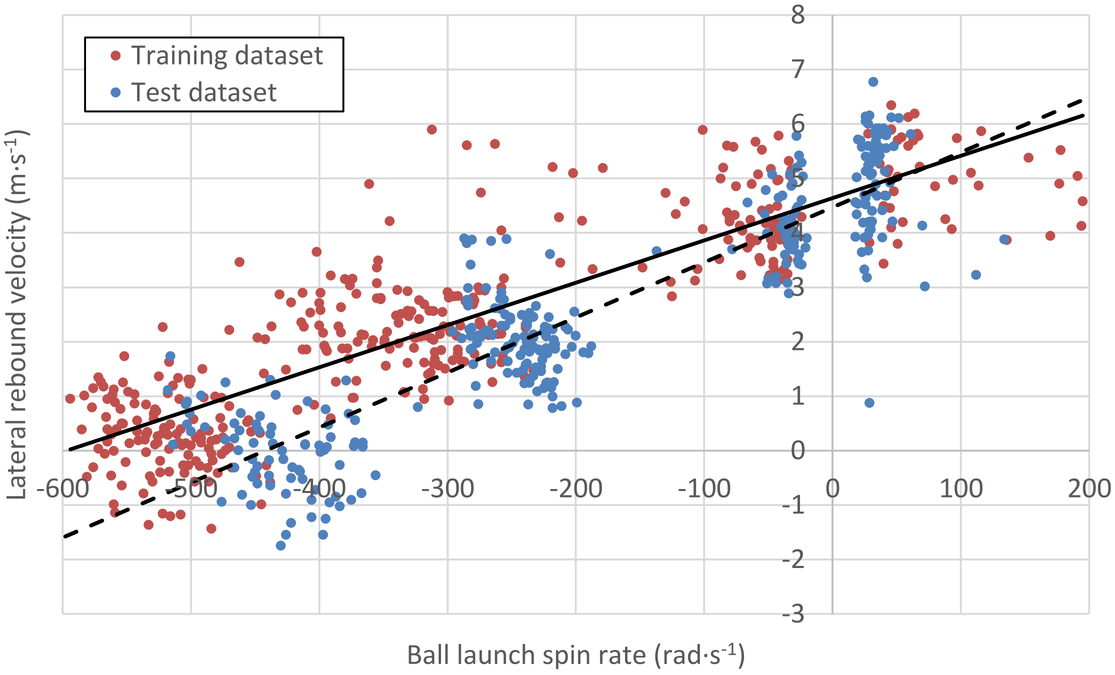

Figure 10.19 – A scatter graph showing ball launch spin rate plotted against lateral rebound velocity for the 60 lbs stringing tension tests from the training (red) and test datasets (blue). Simple linear regression show strong correlations between the parameters (solid line for training data, dashed line for test data).

A more pronounce divergence is noticeable, as spin rate decreases. The discrepancy in spin rates (x-axis) is apparent, whilst the velocity measurements (y-axis) appear similar.

The apparent shift in ball launch spin rate measurements between the datasets, is not accompanied by an equivalent shift in rebound spin rates or lateral rebound velocities. Given the strength of the correlations between these parameters, the evidence suggests issue with the accuracy of spin rate measurements. This could explain the systematic mean errors for the lateral rebound velocity and rebound spin rate models. The models were unable to interpolate the outputs for the erroneous ball launch spin data of the test dataset.

10.7.2 Spin rate measurement error

Visual inspection of the high-speed camera test images shows variable image brightness across each racket test. Specifically, the test images for the 60 lbs stringing tension test of the test dataset were considerably darker than the equivalent images from the training dataset tests. Examples images are shown figure 10.20.

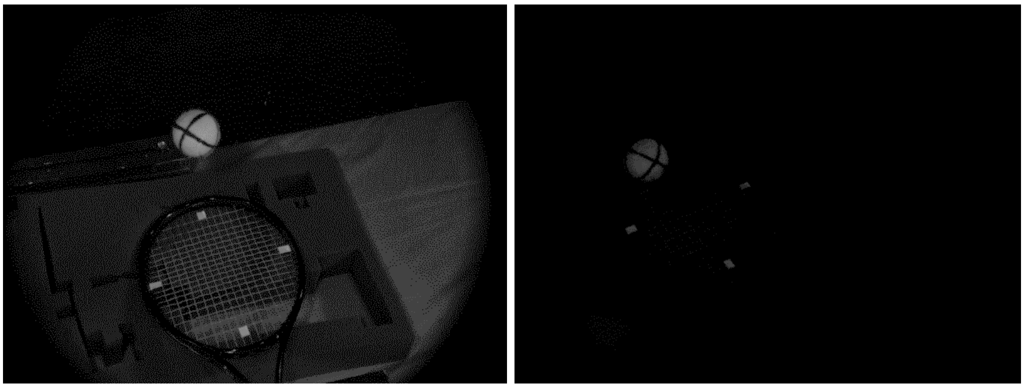

Figure 10.20 – Test images from the 60 lbs racket test of the training dataset (left) and the 60 lbs racket test of the test dataset (right).

The largest discrepancies in ball launch spin rate measurements were between the 60 lbs stringing tension tests. It was hypothesised that spin rate measurement accuracy was influenced by image brightness. Specifically, as image brightness decreased, spin rate measurements were increasingly over-measured.

To test this hypothesis, images from the *SpinTrack3D* algorithm assessment in chapter 8 were doctored to simulate the reduced brightness of the test images shown in figure 10.18. Two sets of images were used, to simulate zero-spin and high-spin scenarios. The image intensities were reduced to match the test images and spin rate measurements using the *SpinTrack3D* algorithm were compared. Examples of original ‘bright’ images and the artificially reduced ‘dark’ images are shown in figure 10.21.

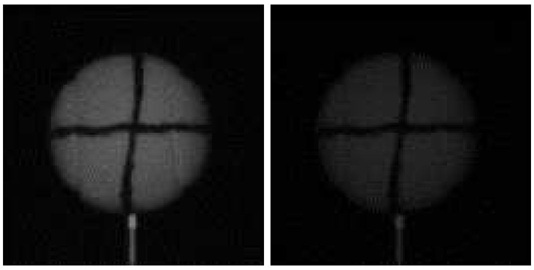

Figure 10.21 – The relationship between spin rate measurement accuracy and image brightness was assessed using test images to simulate zero-spin and high-spin scenarios. An example 'bright' image (left) and artificially 'dark' image (right) are shown.

The differences in spin rate measurements between the bright and dark images, simulating zero-spin and high-spin scenarios are shown in table 10.13.

Table 10.13 – The differences in spin rate measurement between bright and dark test images simulating zero-spin and high-spin scenarios.

	Zero-spin simulation	High-spin simulation
Difference in spin rate measurement (rad·s^{-1})	2.7	95.5

The result for the zero-spin simulation shows a small discrepancy between the bright and dark test images. The result for the high-spin simulation shows spin rate measurements were 95.5 rad·s^{-1} greater for the dark test images. These results agree with the discrepancies observed between the two datasets, where darker images corresponded with greater spin rate measurements. The cause of this error was the *SpinTrack3D* algorithm over-cropping the dark images, which reduced the radius of the ball. In the test images, the ball radius was 5 pixels smaller for the dark images. This reduction affected the method by which algorithm simulated rotations on hemispheres of the measured ball radius.

10.7.3 Effects of spin rate measurement error

The spin rate measurement error offers two options to improve the results of testing the models. The affected data can either be removed or corrected. Given the error affected a significant portion of the test dataset, removal would limit the results of model testing. Therefore, the erroneous data was corrected. For this, the mean image brightness for each test of the 60 lbs stringing tension test of the test dataset were calculated. A histogram of the average image brightness is shown in figure 10.22.

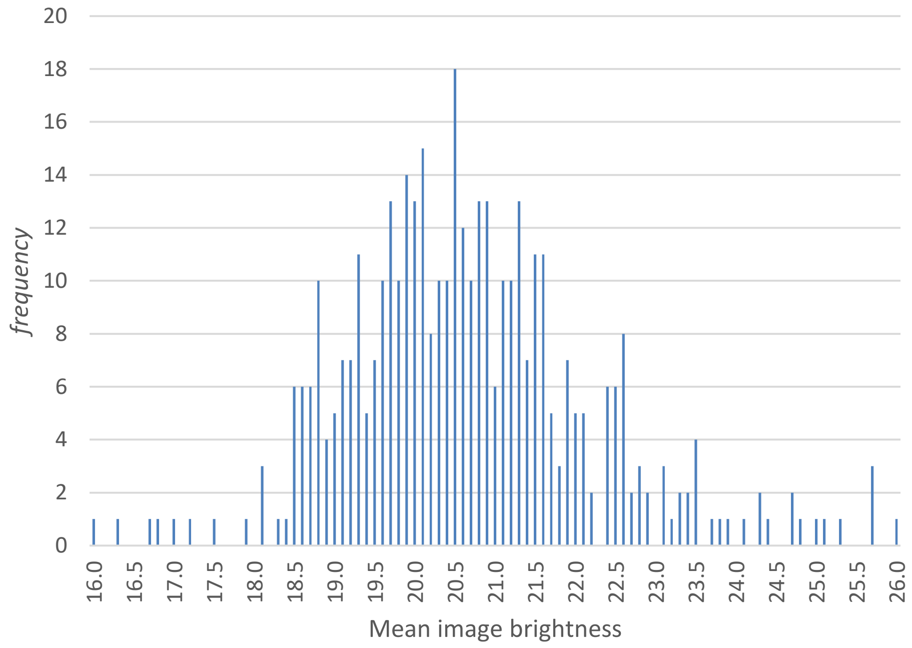

Figure 10.22 – A histogram showing the frequency of mean image brightness for the 60 lbs stringing tension impact tests of the test dataset (n=388).

The data shows the range of average image brightness were between 16.0 and 26.0. The experiment of section 10.7.2 was repeated to calculate the error in spin rate for image brightness over this range. As with the previous experiment, spin rate error was calculated for the zero-and high-spin simulations.

A spin rate error of 2.7 rad·s^{-1} was measured for the zero-spin simulation across the image brightness range. This was measured previously, and shown in table 10.13. Figure 10.23 shows the spin rate errors for the high-spin simulation.

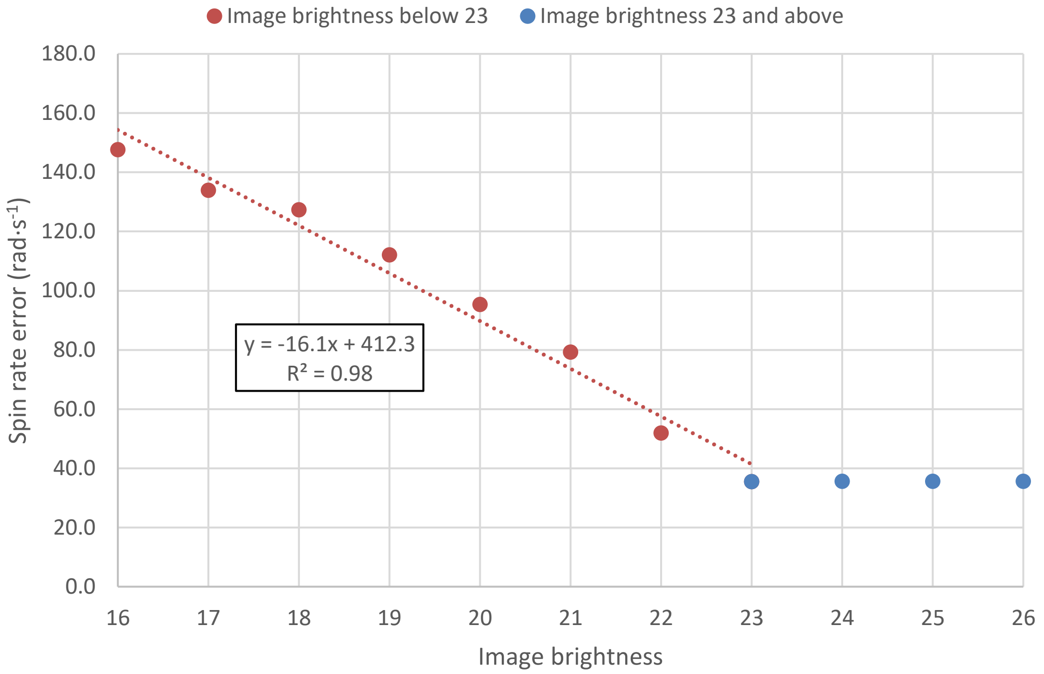

Figure 10.23 – Spin rate error plotted against image brightness for the high-spin simulation. The spin rate error for image brightness of 23 and above was a constant 35.5 rad·s^{-1} (blue). The spin rate error for image brightness below 23 were inversely proportional to image brightness (red). A linear regression has been plotted through these data to illustrate this relationship (red dashed line).

The spin rate error for image brightness between 23 and 26 was 35.5 rad·s^{-1}. The spin rate error increased as image brightness decreased below 23. A simple linear regression was plot through these data, showing an inversely proportional relationship.

A correction factor was applied to the original spin rate data for the test dataset. The correction factor was applied to balls with a spin rate less than -150 rad·s^{-1}. Spin rates above -150 rad·s^{-1} were deemed low spinning, for which the spin rate error was negligible (2.7 rad·s^{-1}) and therefore not requiring correction.

For tests with the higher spin rate and a mean image brightness of 23 or above, the inbound spin rate was increased by 35.5 rad·s^{-1}. For mean images brightness below 23, a spin rate correction was calculated from the simple linear regression model shown in figure 10.23 and the inbound spin rate increased appropriately.

Table 10.14 shows the mean errors and RMSEs for each model tested with the modified test dataset. The original mean errors and RMSEs are shown in parentheses.

Table 10.14 – The mean errors and the root-mean-squared errors of the rebound lateral component velocity model, rebound vertical component velocity model and rebound spin rate model for the test dataset with adjusted rebound spin rates for the 60 lbs stringing tension test data (n = 1138). Original mean and root-mean-squared errors are shown in parentheses.

	Output parameter model		
	Lateral rebound velocity, v_{ox} (m·s^{-1})	Vertical rebound velocity, v_{oz} (m·s^{-1})	Rebound spin rate, s_o (rad·s^{-1})
Mean error	0.33 (0.40)	-0.18 (-0.14)	8.4 (10.8)
Root-mean-squared error	0.57 (0.75)	0.48 (0.49)	30.5 (27.6)

The mean errors for the lateral rebound velocity and rebound spin rate model reduced as a result of correcting the ball launch spin rate data for the 60 lbs stringing tension test. The biggest change in RMSE was for the lateral rebound velocity model, which reduced by 0.18 m·s^{-1}. The RMSE for the rebound spin rate model increased by 2.9 rad·s^{-1}. The improvements in mean errors suggest the spin rate error was a real phenomenon. The RMSEs remained relatively large, but it is worth considering that the spin rate correction was applied to a subset data only. The small change in mean error for the vertical rebound velocity model (0.04 m·s^{-1}) suggests this output parameter is not strongly correlated with ball launch spin rate. This is further implied by the fact the RMSE for this model changed by only 0.1 m·s^{-1}.

Spin rate measurement error requires further research. The investigation into the error suggested it was isolated to ball launch spin rate measurements. It should be noted that this error would likely affect both ball launch and rebound spin data. Improvements beyond the application of a correction factor are required, as the assessment of the *SpinTrack3D* algorithm (chapter 8) showed measurement errors were present under controlled lighting conditions.

10.8 Model output confidence

The model were used to assess output confidence. The differences in outputs of several simulations were compared against the established uncertainties in ball velocity and spin rate measurements. To have confidence in the models calculations, the differences should be an order of magnitude greater than the measurement uncertainty. Ball velocity uncertainties were measured in Chapter 6 (V_{ox} and V_{oz} standard deviations in table 6.3) and spin rate uncertainty in Chapter 8 (standard deviation in section 8.6). The spin rate uncertainty was converted to rad·s^{-1}. The uncertainties are shown in table 10.15.

Table 10.15 – the uncertainties in measurement of the lateral and vertical components of rebound velocity and rebound spin rate.

	Uncertainty
V_{ox} (m·s^{-1})	0.0
V_{oz} (m·s^{-1})	0.1
Spin rate (rad·s^{-1})	1.3

The outputs of eight simulations were calculated and compared to the output of a control simulation. The inbound velocity, spin rate and impact location were adjusted in turn to assess the influence of each on the rebound velocity and spin rate. The inbound velocities, spin rates and impactions and the calculated outbound velocity and spin rate for each simulation are shown in table 10.16.

Table 10.16 – Rebound velocities and spin rates were calculated for nine simulations with changes in inbound velocity, spin rate and impact location. An initial 'Control' trajectory was defined from which inbound velocity, spin rate and impact location were adjusted (changes shown in black).

Simulation	Inbound velocity		Inbound spin rate (rad·s^{-1})	Impact location		Rebound velocity		Rebound spin rate (rad·s^{-1})
	V_{ix} (m·s^{-1})	V_{iz} (m·s^{-1})		X (mm)	Y (mm)	V_{ox} (m·s^{-1})	V_{oz} (m·s^{-1})	
Control	7.0	19.0	-200.0	0.0	0.0	2.6	7.9	56.2
1	5.0	14.0	-200.0	0.0	0.0	1.7	6.6	48.2
2	8.0	22.0	-200.0	0.0	0.0	3.2	8.9	69.2
3	7.0	19.0	0.0	0.0	0.0	4.1	8.1	107.4
4	7.0	19.0	-400.0	0.0	0.0	0.5	7.7	-25.6
5	7.0	19.0	-200.0	30.0	0.0	2.5	6.9	59.9
6	7.0	19.0	-200.0	60.0	0.0	2.5	4.5	67.2
7	7.0	19.0	-200.0	0.0	50.0	2.4	5.7	56.8
8	7.0	19.0	-200.0	0.0	-50.0	2.2	9.0	70.2

The differences in the lateral and vertical components of rebound velocity (V_{ox} and V_{oz}) and rebound spin rate for the eight simulations, compared to the control trajectory, are shown in table 10.17. The differences not an order of magnitude greater than the measurement uncertainties (table 10.15) are highlighted in red.

Table 10.17 – The differences in the lateral and vertical components of rebound velocity and rebound spin rate compare to the control simulation. Differences not an order of magnitude greater than measurement uncertainty are shown in red.

Simulation	V_{ox} (m·s^{-1})	V_{oz} (m·s^{-1})	Rebound spin rate (rad·s^{-1})
1	-0.9	-1.3	-8.0
2	0.6	1.0	13.0
3	1.5	0.2	51.2
4	-2.1	-0.2	-81.8
5	-0.1	-1.0	3.7
6	-0.1	-3.4	11.0
7	-0.2	-2.2	0.6
8	-0.4	1.1	14.0

The changes in the lateral component of rebound velocity were greater than the uncertainty in measurement. However, the uncertainty for this measure was 0.0 m·s^{-1} giving confidence in the data and therefore the simulation outputs.

The changes in the vertical component of rebound velocity for simulations three and four were not an order of magnitude greater than the uncertainty. Therefore, there is low confidence in the simulated outputs. However, these simulations measured differences in model outputs for changes inbound spin rate, which was previously shown to be correlation with lateral rebound velocity and rebound spin rate. Therefore, large changes in vertical rebound velocity were not expected.

Changes in rebound spin rate were not an order of magnitude greater than the measurement uncertainty for simulations one, five, six and seven. Therefore, there is less confidence in rebound spin rate for changes in inbound velocity and impact location. However, spin rate measurement error has already been highlighted, and this results only gives further cause to improve the measurement of spin rate.

10.9 Quantifying model errors with trajectory simulations

To give context to measured predictive errors of the three models, the effects of the model RMSEs on simulated ball trajectories were quantified using *TennisGUT* (Dignall et. al., 2004). Using the ball aerodynamics and ball-to-surface impact models of *TennisGUT*, the trajectories simulated the flight and bounce of a ball on a virtual tennis court.

10.9.1 Simulation method

To initiate a simulation, *TennisGUT* required initial conditions: ball launch velocity, ball launch angle (above horizontal) and ball launch spin rate. The start location of the trajectories was 1.5 m directly above the middle of the baseline on one side of the virtual court. The model RMSEs were used to adjust the initial conditions and calculate the deviations from a 'control' trajectory.

The control trajectory had the following initial conditions:

- Ball launch velocity: 30 m·s^{-1}
- Ball launch angle: 4°
- Ball launch spin rate: 2,500 rpm

Figure 10.24 shows the control trajectory, plotted onto a simple schematic of the virtual court, with the positions of baselines and the net also shown. The effects of the RMSEs on the control trajectory were quantified by the following three measures:

1. Trajectory apex height (point 1 in figure 10.24).
2. Bounce length (point 2 in figure 10.24)
3. Time to opposite baseline (point 3 in figure 10.24).

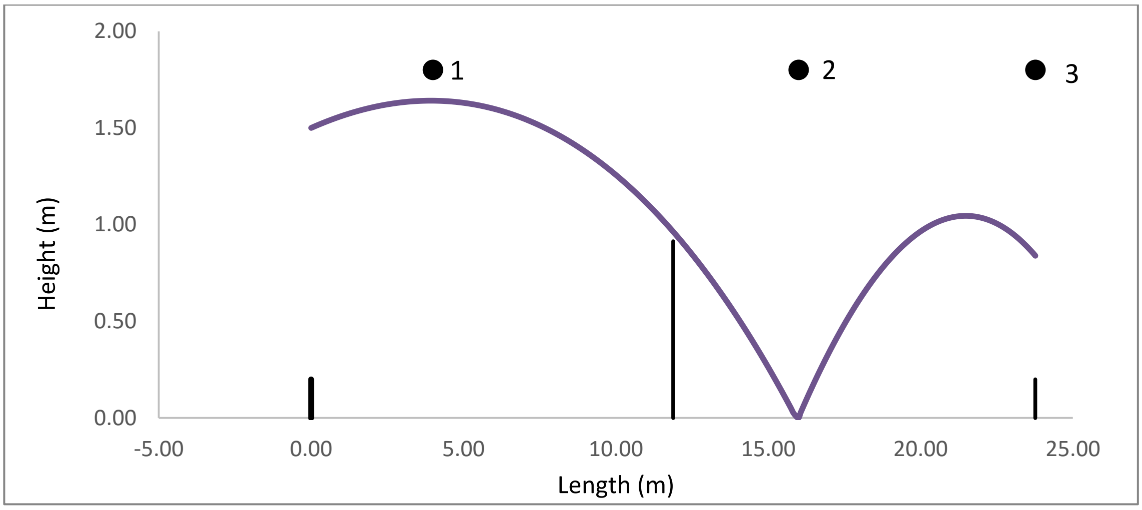

Figure 10.24 – Line plot showing the control trajectory modelled by *TennisGUT* to quantify the effects of model RMSEs. The measurements of apex height (1), bounce length (2) and time to baseline (3) for the simulations are shown. The positions of the baselines and net for a standard tennis court are indicated by the vertical lines.

10.9.2 Simulation results

The measurements for the control trajectory are shown in table 10.18.

Table 10.18 – The apex height, bounce length and time to baseline from *TennisGUT* simulations of the control trajectory.

	Apex height (m)	Bounce length (m)	Time to baseline (s)
Control trajectory	1.64	15.99	1.24

The RMSEs of each model were applied to the control trajectory in turn, to simulate the effects of adding and subtracting the errors. In total, six trajectories were simulated – two per RMSE. The trajectory measurements for the adjusted simulations are shown in tables 10.19 to 10.21. For each trajectory measurement, the absolute values and percentage change to the control trajectory are shown.

Table 10.19 – Apex heights, bounce lengths and times to baseline from *TennisGUT* simulations of the vertical rebound velocity model RMSE applied to the control trajectory. Absolute values and percentage change to the control trajectory are shown.

	Apex height (m)	Bounce length (m)	Time to baseline (s)
+ Vertical velocity model RMSE	1.64 (0.0%)	16.16 (1.0%)	1.22 (-1.5%)
- Vertical velocity model RMSE	1.64 (0.0%)	15.82 (-1.1%)	1.26 (1.8%)

Table 10.20 – Apex heights, bounce lengths and times to baseline from *TennisGUT* simulations of the lateral rebound velocity model RMSE applied to the control trajectory. Absolute values and percentage change to the control trajectory are shown.

	Apex height (m)	Bounce length (m)	Time to baseline (s)
+ Lateral velocity model RMSE	1.73 (5.5%)	17.01 (6.3%)	1.22 (-1.5%)
- Lateral velocity model RMSE	1.58 (-3.7%)	14.99 (-6.3%)	1.26 (1.8%)

Table 10.21 – Apex heights, bounce lengths and times to baseline from *TennisGUT* simulations of the rebound spin rate model RMSE applied to the control trajectory. Absolute values and percentage change to the control trajectory are shown.

	Apex height (m)	Bounce length (m)	Time to baseline (s)
+ Spin rate model RMSE	1.64 (0.0%)	15.74 (-1.6%)	1.24 (0.0%)
- Spin rate model RMSE	1.65 (0.6%)	16.57 (3.6%)	1.24 (0.0%)

10.9.3 Model error discussion

The changes in apex height and bounce length were greatest when the lateral rebound velocity model RMSE was applied to the control trajectory. The apex heights were 3.7% lower and 5.5% higher and bounce lengths 6.3% shorter and longer (table 10.20). The greatest change in time to baseline was measured with both the vertical rebound velocity and lateral rebound velocity model RMSEs were applied. The times to baseline were 1.5% quicker and 1.8% slower than the control trajectory (tables 10.19 and 10.20).

The RMSE of the lateral rebound velocity model resulted in a ±1.1° change to the ball launch angle of the control trajectory. This primarily influenced the vertical component of the simulated ball trajectory. Therefore, the changes in apex height and bounce length were relatively large, but an expected outcome. The vertical rebound velocity model RMSE changed the ball launch velocity of the control trajectory by ±0.5 $m \cdot s^{-1}$. Given the initial ball launch velocity was relatively large (30 $m \cdot s^{-1}$), the effects of these changes were modest. The effects of the rebound spin rate model RMSE were also relatively modest, given the initial spin rate of the control trajectory was also large (2,500 rpm).

These results suggest caution should be applied when interpreting the results of simulated ball trajectories using the velocity and spin rate models. The RMSEs were partially explained by the inherent variability of the ball and stringbed, which as real phenomenon, give some credence to the predictive errors. For example, 60% of the lateral rebound velocity model RMSE was due to inherent variability, and therefore accounts for 60% of the change in launch angle.

Explaining the remaining variance in the data should be a primary aim of further research. The first area to address is spin rate measurement error. Given the correlation with rebound spin rate and lateral rebound velocity, improvements to spin rate measurement should improve the predictive power of the models. Further to this, reintroducing the test parameters removed from the datasets may improve the predictive power of the models. For this, the test protocol should be modified to improve the range of these data. This should allow the models to better describe the system domain and ultimately improve the predictive powers.

10.10 Model applications

The purpose of the *TennisGUT* simulation software is to investigate the effects of changes in shot parameters, which would be difficult to measure experimentally. To demonstrate the possible applications of the new ball-racket impact models, several *TennisGUT* simulations were run to observe the effects of changes in the model parameters.

The first parameter investigated was stringbed stiffness. Three simulations were run with stringbed stiffness set to 50, 60 and 70 lbs. The rebound velocities, rebound angle, rebound spin, apex heights, bounce locations and times to baseline were measured. These are shown in table 10.22.

Table 10.22 – TennisGUT outputs using the new ball-racket impact models to simulate the effects of different stringbed stiffness.

	Stringbed stiffness		
	50 lbs	60 lbs	70 lbs
Rebound velocity (m·s^{-1})	30.0	29.9	29.8
Rebound angle (°)	4.0	4.3	5.4
Rebound spin (rad·s^{-1})	114.7	107.4	113.1
Apex height (m)	1.67	1.70	1.80
Bounce location (m)	17.66	18.02	19.04
Time to baseline (s)	1.22	1.22	1.20

The outputs from *TennisGUT* allow for the simulated trajectories to be visualised. The trajectories of the simulations are shown in figure 10.25.

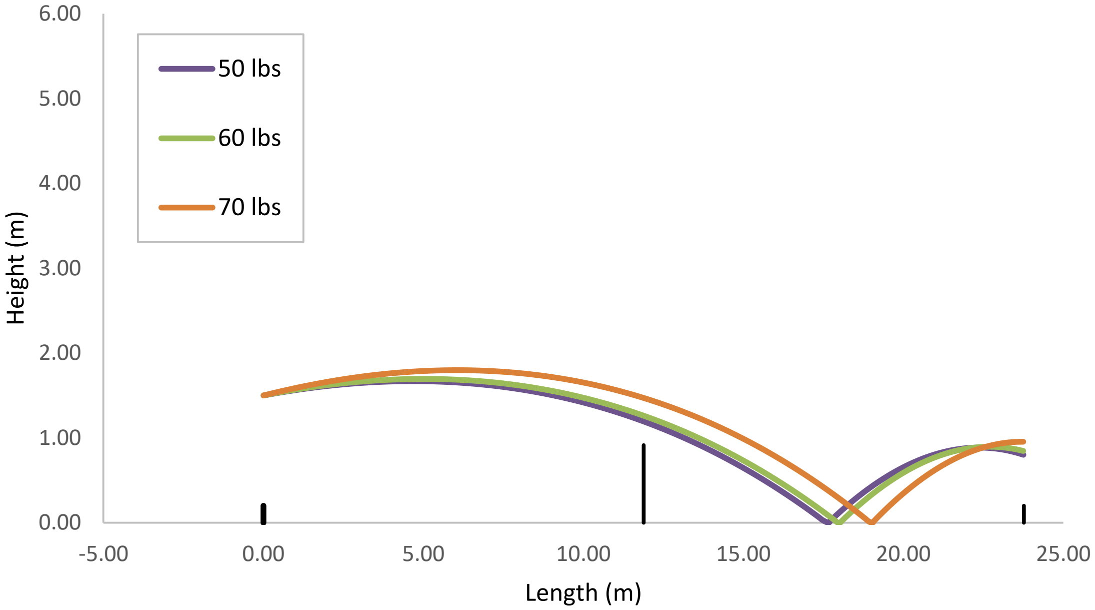

Figure 10.25 – TennisGUT trajectories using the new ball-racket impact models to simulate the effects of different stringbed stiffness. The positions of the baselines and net for a standard tennis court are indicated by the vertical lines.

The simulations show a decrease in rebound velocity as stringbed stiffness increases. This was expected, as the relationship between ball velocity and stringing tension is well researched (Brody et. al., 2002). Rebound angle increased with stringbed stiffness, causing increases in apex heights and bounce lengths. Rebound spin was lowest for the 60 lbs stringbed stiffness. Interestingly, the times to baseline were relatively static, with the ball reaching the opposite baseline 0.02 s quicker for the 70 lbs stringbed stiffness simulation. This may be counter intuitive, given this simulation had the slowest rebound velocity. However, the increase in bounce length decreased the distance between the bounce location and baseline. This reduced the bounce-baseline distance after the bounce, where the ball decelerates significantly.

The second parameter investigated was lateral offset in impact location. Three simulations were run with the lateral offset set to 0 mm (i.e. at the geometric stringbed centre), 30 mm and 60 mm offset. The outputs are shown in table 10.23.

Table 10.23 - TennisGUT outputs using the new ball-racket impact models to simulate the effects of different impact locations of increasing lateral offset.

	Impact location - lateral offset		
	No offset	30 mm	60 mm
Rebound velocity (m·s^{-1})	29.9	28.9	26.7
Rebound angle (°)	4.3	9.4	24.1
Rebound spin (rad·s^{-1})	107.4	108.0	112.1
Apex height (m)	1.70	2.31	5.38
Bounce location (m)	18.02	22.45	-
Time to baseline (s)	1.22	1.16	1.31

The simulation trajectories are shown in figure 10.26.

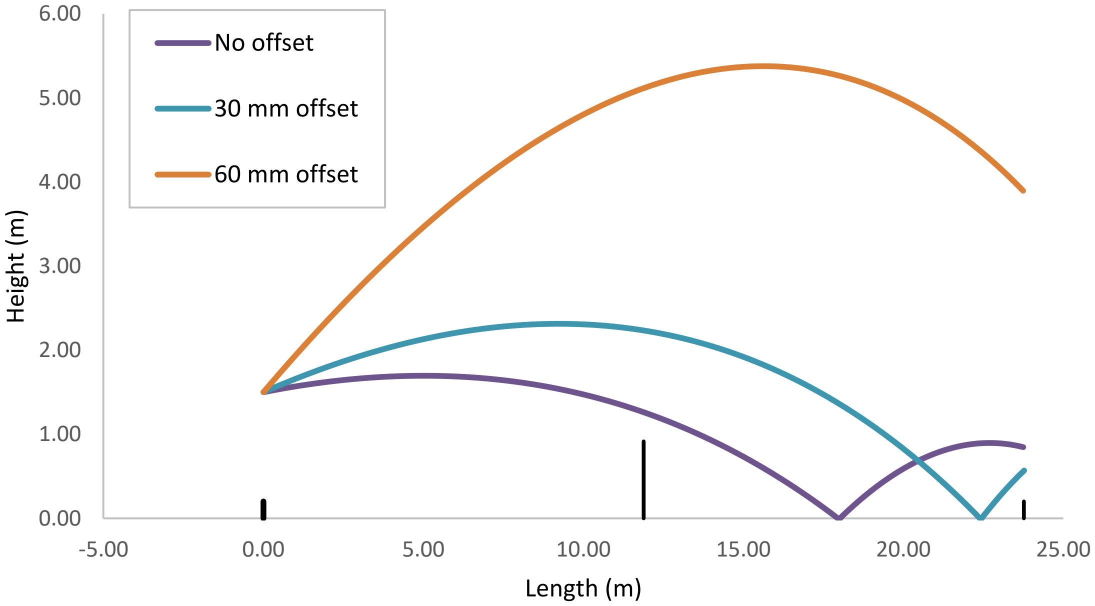

Figure 10.26 - TennisGUT trajectories using the new ball-racket impact models to simulate the effects of different impact locations of increasing lateral offset. The positions of the baselines and net for a standard tennis court are indicated by the vertical lines.

The simulations show a marked decrease in rebound velocity as lateral offset increased. This was accompanied by large increases in rebound angle, causing large increases in apex heights and bounce lengths. The increase in rebound angle for the 60 mm lateral offset meant the ball didn't bounce within the time constraints of the simulation. Interestingly, rebound spin increased with lateral offset. The mechanism of which is unknown, creating an interesting topic for future research. Despite the large decreases in rebound velocity, the times to baseline decreased with lateral offset. As with the first set of simulations, this was due to the bounce length increasing for the 30 mm offset, thereby reducing the remaining distance to cover to reach the baseline after the ball has decelerated during the surface impact. The 60 mm offset trajectory did not bounce, and therefore was not subject to the large deceleration associated with the surface impact.

10.11 Conclusions

This chapter presented the development of numerical models to describe the relationships between independent input parameters and dependent output parameters from impact testing using the Impact Rig. Impact data was collected using a testing protocol which defined a system domain initially described by 10 independent input parameters and seven dependent output parameters. The models were trained and validated and then tested with two independent datasets. These were collected using the same testing protocol.

Each dataset was subject to analysis failures and a process of data cleaning, which remove erroneous data. On average 14% of data were lost from the two datasets. The range of data for each input parameter of the training and validation dataset were reviewed. The range of four input parameters (longitudinal component of ball launch velocity, and the lateral, longitudinal and vertical components of ball launch spin axis) were deemed too narrow. These data, and the associated output parameters, were excluded from model training and testing. The remaining six input parameters were:

- Stringing tension.
- Ball launch components of ball velocity, in two-dimensions (lateral (x) and

vertical (z) axes).

- Ball launch spin rate.
- Impact location, in two-dimensions (lateral (x) and longitudinal (y) axes).

And three output parameters were:

- Rebound components of ball velocity, in two-dimensions (lateral (x) and vertical (z) axes).
- Rebound spin rate.

To model the complex dataset, multivariate polynomial regressions were created with a MATLAB multivariate fitting tool. The tool created parameterised models, for each output parameter, using the six input parameters as model terms. Each term was weighted to maximise model fit. First, second and third order models were trained and validated using the '*n-fold and leave one out cross-validation*' method. The models were assessed by fit (R^2) and estimation error (sum of squared errors). In all cases, the second order models were chosen.

The models were tested using the second, independent dataset. The mean errors and root-mean-squared errors (RMSEs) were calculated by comparing the model outputs for each set of measured input data against the measured output data. The mean errors of each model revealed systematic differences to the test data. The lateral rebound velocity and rebound spin rate models over-predicted the test data with mean errors of 0.40 $m \cdot s^{-1}$ and 10.8 $rad \cdot s^{-1}$, respectively. The vertical rebound velocity model under-predicted the test data, with a mean error of -0.14 $m \cdot s^{-1}$. RMSEs measured the variance in the test dataset, and were considered the predictive power of the models. The RMSEs for the lateral rebound velocity, vertical rebound velocity and rebound spin rate models were 0.75 $m \cdot s^{-1}$, 0.49 $m \cdot s^{-1}$ and 27.6 $rad \cdot s^{-1}$, respectively.

A discrepancy was discovered in the ball launch spin rate data between datasets. This was most noticeable for the 60 lbs string tension data. Spin rates from the test dataset below -150 $rad \cdot s^{-1}$ were approximately 100 $rad \cdot s^{-1}$ lower than the equivalent data in the training and validation dataset. Strong correlations were found between ball launch spin rate and rebound spin rate and lateral rebound velocity. Given the strength of these correlations, the lower ball launch spin rates should have been accompanied by offsets in rebound spin rates and rebound lateral velocities between dataset. However, no obvious differences between the datasets were observed for these parameters. If the offsets were present, the interpolative power of the models should have resulted in lower mean errors.

The spin rate measurement error was caused by darker high-speed camera images. This was proven by artificially reducing the image intensity of test images and measuring the change in spin rate measurements. No change in spin rate measurement was found with test images simulating zero-spin. For images simulating a high-spin scenario, a discrepancy of 95.5 rad·s^{-1} was measured for the darkened images. The cause of this error was due to the *SpinTrack3D* algorithm over-cropping the test images and under-measuring ball radius. To correct the erroneous data, the relationship between image brightness and spin rate error was established. Spin rate data measured from test images with brightness between 23 and 26 were corrected by 35.5 rad·s^{-1}. Spin rate error for test image brightness below 23 increased proportionally, with a simple linear regression describing the relationship. Spin rates for these test images were corrected using the model to establish the appropriate correction factor. The models were retested, resulting in lower mean errors for the lateral rebound velocity and spin rate models of 0.33 m·s^{-1} and 8.4 rad·s^{-1}, respectively. The RMSE for the lateral rebound velocity model decreased to 0.57 m·s^{-1}.

Confidence in the models was established by comparing the differences in several simulations to the established uncertainties of ball velocity and spin rate measurement. Eight simulations were compared to a control, with changes in inbound velocity, spin rate and impact location modelled in turn. The changes in the lateral and vertical components of rebound velocity were an order of magnitude greater than the measurement uncertainty, giving confidence to these simulations. Rebound spin rate for six of the eight simulations were not an order of magnitude greater than the measurement uncertainty. However, spin rate measurement errors had already been highlighted, with this result giving further cause to develop more accurate methods.

The predictive powers of the models were quantified using the tennis simulation software *TennisGUT*. Model RMSEs were used to vary a control trajectory. The changes in apex height, bounce length and time to opposite baseline were calculated. The vertical rebound velocity and spin rate model RMSEs caused less than 2% change in all three measures. The lateral rebound velocity model RMSE caused a 5.5% change in apex height and a 6.3% change in bounce length. The larger changes were attributed to the lateral rebound velocity model affecting the ball launch angle. Approximately 60% of the RMSE was explained by the inherent variability of the ball and stringbed. Therefore, the majority of the changes in apex height, bounce length and time to baseline were explained by the natural variability of the objects being modelled.

The models offer a significant improvement in the current simulation capabilities of *TennisGUT*. The input parameters of the models allow simulation of oblique impacts with impact locations offset from the longitudinal axis of the racket. The application of these new models were presented with several simulations modelling changes in stringbed stiffness and impact location lateral offset. Increases in stringbed stiffness and lateral offset were found to correlate with decreases in rebound ball velocity and increases in rebound angle. Interestingly, rebound spin rate was highest for the 60 lbs stringbed stiffness and 60 mm lateral offset simulations. The mechanisms causing these results is unknown, offering an interesting avenue for future research.

The new ball-racket impact model better represent realistic conditions, compared to the previous analytical model, allowing for more sophisticated simulations. However, prior to modifying *TennisGUT* to make use of the new models, further development of the research methods to generate the data and create the models should be carried out. Improving the accuracy of spin measurements using the *SpinTrack3D* algorithm should be a priority, with particular attention to the effects of image brightness on spin rate accuracy. Further to this, the testing protocol could be developed to expand the number of input and output parameters. This would allow for a greater complexity of shots to be simulated.

Chapter 11 - Conclusions

11.1 Introduction

The aim of this project was to create a statistical model of oblique, spinning, on-and off-axis tennis ball impacts with tennis rackets. To achieve this, the following objectives were set:

- To facilitate large scale data collection, an impact rig will need to be developed. The impact rig must replicate a range realistic shot conditions and allow measurement of ball velocity and spin and impact locations for each impact test.
- To collect impact test data, high-speed cameras will be used to film and analyse each impact. The analysis of the high-speed camera images must be automated, requiring the development and validation of automated image-processing algorithms. The automated algorithms must be capable of distinguishing between the inbound and outbound trajectories of the ball.
- The system domain of the ball-racket impact system must be defined with dimensions describing independent input variables (ball velocity, spin and impact location) and dependent output variables (ball velocity and spin). To populate the domain an impact testing protocol must be defined, which maps the domain adequately.
- To develop the statistical model, a two-step process of model training and validation and model testing will be used to establish the relationships between the independent input data and dependent output data. The predictive power of the model will be evaluated to establish the success of the model development.

The following chapter summarises the outcomes of the work. This summary is presented in the order in which the findings are reported, with proposed future developments.

11.2 Project summary

Literature Review (Chapter 2)

Chapter 2 reviewed relevant literature, in particular, the modelling of tennis. This gave compelling evidence for the need to continue developing the understanding of the mechanisms of tennis interactions. The research aim and objectives were established, with the need for novel research into the development of the equipment and methodologies to create statistical models of oblique, spinning, on- and off-axis ball impacts.

Experiment apparatus (Chapter 3)

Chapter 3 addressed the requirements of the first objective, in which a novel impact rig was developed. The rig was capable of launching balls over a range of realistic velocities and spin rates, at a range of impact locations making it suitable for data collection. The repeatability of ball launch was quantified, determining the need to develop methods to measure ball-racket impact test variables directly using high-speed videogrammetry.

Camera calibration (Chapter 4)

Chapter 4 partially addressed the second objective, in which high-speed videogrammetry was evaluated to use in filming impact testing using the Impact Rig. The digitisation and coordinate reconstruction of ball centroids was found to be an accurate method to measure ball velocities.

Racket parameter measurements (Chapter 5)

Chapter 5 partially addressed the second objective, with the development and validation of automated methods to measure the location of four reflective markers attached to the racket stringbed. The reflective markers were required to measure impact locations and transform the ball-racket impact test data to the local racket origin.

Ball tracking (Chapter 6)

Chapter 6 partially addressed the second objective, with the development and validation of automated methods to digitise ball centroids in the ball-racket impact test images. The validation compared the measurement of ball velocities using automated and manual digitisation. The comparison found good agreement between the two methods.

Impact location (Chapter 7)

Chapter 7 partially addressed the second objective, with the development and validation of a method to measure impact location from the digitised ball centroid and stringbed marker centroid data. A 1.5 mm discrepancy between impact locations measured using automated and manual digitisation data was found. This was justified using a rigid-body racket model, validating the automated measurements.

Spin measurement (Chapter 8)

Chapter 8 completed the requirements of the second objective, with the employment of an automated spin measurement method. The method was modified to account for the error due to camera perspective. The method was validated using an experimental set up. The validation found spin measurement error to have a similar magnitude to the error resulting from the resolution of the high-speed camera.

Data collection (Chapter 9)

Chapter 9 addressed the requirements of the third objective, in which a testing protocol was developed to populate the defined ball-racket impact system domain. The variabilities of ball launch and ball-string interactions were measured to assess the effects of repeated impact testing. This ensured data collection was not influenced by the inherent variabilities of, or systematic changes in, the ball and strings. The protocol required 432 impacts per racket tested, making data collection feasible.

Model development (Chapter 10)

Chapter 10 address the requirements of the final objective, in which statistical models describing oblique, spinning, on- and off-axis ball impacts onto a realistically supported racket were developed. The models were trained, validated and tested with two independent datasets. High confidence in the simulated ball rebound velocities was concluded, with model outputs an order of magnitude greater than the measurement uncertainty. Spin rate measurement error and uncertainty meant low confidence in the simulation of rebound spin rate. Model validation calculated the RMSEs of the models are measures of predictive error. These were 0.57 $m \cdot s^{-1}$ for the lateral rebound velocity model, 0.48 $m \cdot s^{-1}$ for the vertical rebound velocity model and 30.5 $rad \cdot s^{-1}$ for the rebound spin rate model. Experimental data variance was explained by the inherent variability of the ball and stringbed.

The final ball-racket impact models were combined with the existing ball aerodynamics and ball-surface impact models of *TennisGUT*. Several simulations were run using the new ball-racket model. These highlighted the power of the new model to simulate oblique, spinning, on-and off-axis tennis ball impacts and thereby fulfilling the aim of this project.

11.3 Project limitations

This section discusses the limitations of the project, whether through design or later discovery. The effects of these limitations with respect to the implemented processes, data collected and models developed are discussed.

The primary design criteria for the Impact Rig were the collection of large scale data and replicating real-play shot characteristics. Secondary to this were the considerations for analysis of the high-speed camera images, for example the use of lights to create uniform lighting within the test volume. However, the laboratory area was subject to ambient environmental conditions (e.g. sunlight, temperature etc.). Given the time required to collect the datasets, testing was conducted over several days, and therefore subject to variability in ambient conditions. A major finding of the influence of ambient lighting was described in Chapter 10, where darker high-speed camera images caused erroneous spin rate measurement. In retrospect, this variable could have been controlled for through greater consideration for the design of the test area, or by adjusting the camera and lens settings. Other environmental conditions would be harder to control for, but it cannot be assumed that changes in, for example temperature, would not influence the mechanisms of a ball-racket impact.

Other testing parameters that were assumed consistent throughout the project were ball and string properties. To limit the effect of inherent variability, a single ball brand and string were used. However, the measured inherent variabilities of the ball and string were a major cause of data variance. Effort to minimise test object variability could be undertaken. However, this would likely require a prohibitively large number of balls and could introduce an additional variable in the effects of testing balls and strings prior to impact testing.

The repetition of the test protocol to produce the two datasets to train, validate and test the models ultimately limited the assessment of the predictive power of the models. Ideally, the test datasets would have been collected using alternative nominal test values to assess the interpolative power of the model. This was not achievable for some test parameters, given the variability of the Impact Rig. However, stringing tension could have been varied to generate more widely spaced stringbed stiffness values between the two datasets.

The predictive power of the model was limited to the domain of the data collected. In part, this was by design. The testing protocol needed to efficiently map the defined dimensions of the ball-racket impact system, whilst producing useful data. However, for this, several system parameters were held constant (e.g. all racket geometric and physical properties) to create an achievable dataset target. The dimensionality of the collected data was further reduced after the datasets were scrutinised.

11.4 Future developments

The first steps to further develop the methods described within this project should be focused on improving spin measurements using *SpinTrack3D*. Alternative methods of reporting possible angles of rotation and spin axes between successive images should be investigated, as the current method of reporting the first highest scoring rotation is limited. One possible alternative is to report all assessed rotations and axes, with accompanying scores. This would allow for data interrogation and the potential for an improved methodology. The sensitivity of spin measurements to image brightness should also be prioritised. The research presented in this thesis found spin rate error below a mean image brightness of 26. However, there may be optimum values of image brightness. Overexposed images (i.e. overly bright images) may introduce an error not covered in the relevant investigations of this thesis. Ideally, established criteria for optimum spin measurement would greatly assist future data collection.

Further to this, research should be undertaken to investigate spin axis precession. This was noted as a possible phenomenon in the outbound spin axis measurements from impact testing. However, a focussed study, with considerations for the relationship between spin measurement accuracy and image resolution, could produce insight into this previously unreported observation.

The Impact Rig and analysis methods should be used to collect more impact data. The impact testing protocol used in this project limited the range of several test parameters. The testing protocol could be modified to increase the range of these parameters, thereby increasing the dimensionality of the system domain. The physical and geometric properties of the test equipment (i.e. the ball, racket and strings) were excluded as domain dimensions by using a single variant of each. Testing a range of equipment to expand the system domain dimensionality would increase the power of the models and the sophistication of the simulations. However, caution should be employed to ensure the impact testing and analysis describes each additional dimension appropriately. For example, including racket mass as a new domain dimension would require testing rackets over a range of masses. However, this would require control of all racket inertial properties (i.e. the mass moments of inertia) to avoid uncontrolled variables. Racket manufacture through rapid prototyping could facilitate this. Beyond this, testing could factor string and ball properties as additional parameters.

References

ABDEL-AZIZ, Y I and KARARA, H M (1971). Direct Linear Transformation from comparator coordinates into object space coordinates in close-range photogrammetry. *Proceedings of the Symposium on Close-Range Photogrammetry, 1-18.* USA: American Society of Photogrammetry.

ALLEN, Tom (2009). Finite Element Model of a Tennis Ball Impact with a Racket (Ph.D.). *The Centre for Sports Engineering Research,* Sheffield Hallam University.

ASHFIELD SPRINGS (2008). [online] http://www.ashfield-springs.com/

BABOLAT (2008). [online] http://www.babolat.co.uk/

BANWELL, Guy (2013). Impulsive Sound Quality of Tennis Rackets (Ph.D.). Loughborough University

BASHEER, I and HAJMEER, M (2000). Artificial neural networks: fundamentals, computing, design, and application. *Journal of Microbiological Methods 43, 3-31.*

BASSEMENT, M, GARNIER, C, LEPOUTRE, F-X and SAMPSON, M (2008). Kinematics and EMG analysis of expert pole vaulters lower limb during take off phase. *The Engineering of Sport 7,* **2**, 375-382. France: Springer-Verlag France.

BELONGIE, SERGE (2012). [online] Rodrigues' Rotation Formula. http://mathworld.wolfram.com/RodriguesRotationFormula.html

BISHOP, Christopher (1995). Neural Networks for Pattern Recognition. Oxford, Clarendon Press.

BRAY, K and KERWIN, D (2006). Modelling the ‘run-out’ Throw in Cricket. *The Engineering of Sport 6*, **2**, 161-166. USA: Springer.

BRODY, Howard (1979). Physics of the tennis racket. *American Journal of Physics,* **47** (6), 482-487.

BRODY, Howard (1984). That’s how the ball bounces. *Physics Teacher*, **22**, 494-497.

BRODY, Howard (1997). The Physics of Tennis. III. The ball-racket interaction. *American Journal of Physics,* **65** (10), 981-987.

BRODY, Howard, CROSS, Rod and LINDSEY, Crawford (2002). *The Physics and Technology of Tennis,* USA: Racquet Tech Publishing.

BOLA (2008). [online] http://www.bola.co.uk/

BOWERS GROUP (2008). [online] http://www.bowersgroup.co.uk/

CARRÈ, Matthew, HAAKE, Steve, ASAI, T and AKATSUKA, T (2002). The curve kick of a football. *The Engineering of Sport 4*, 315-321, UK: Blackwell Science Ltd.

CHADWICK, Steve and HAAKE, Steve, (2000). Methods to determine the aerodynamic forces acting on tennis balls in flight. *Tennis Science and Technology*. 127-134. UK: Blackwell Science.

CHECK2D (2012). [online] http://www.check2d.co.uk/

CHECK3D (2012). [online] http://www.check3d.co.uk/

CHOPPIN, Simon, WHYLD, N, GOODWILL, Simon and HAAKE, Steve (2005). 3D Impact Analysis in Tennis. *The Impact of Technology on Sport (Tokyo Institute of Technology)*, **1**, 373-378.

CHOPPIN, Simon, GOODWILL, Simon and HAAKE, Steve (2006). 3D Player Testing in Tennis. *The Engineering of Sport 6*, **1,** 385-390. USA: Springer.

CHOPPIN, Simon (2008). Modelling of tennis racket impacts using elite players (Ph.D.). *The Department of Mechanical Engineers,* University of Sheffield.

CORDINGLEY, Leon (2002). Advanced Modelling of Surface Impacts from Hollow Sports Balls (Ph.D.). Loughborough University

COTTEY, Robert (2002). The Modelling of Spin Generation with Particular Emphasis on Racket Ball Games (Ph.D.). Loughborough University

CROSS, Rod (1998). The sweet spot of a tennis racket. *Sports Engineering,* **1**, 63-78.

Cross, Rod (2000). Effects of friction between ball and strings in tennis. *Sports Engineering,* **3**, 85-97.

CROSS, Rod (2001). Stretch tests on strings. *Raquet Tech,* **9**, 12-19

CROSS, Rod (2005). Bounce of a spinning ball near normal incidence. American Journal of Physics, **73** (10), 914-920.

CROSS+MORSE (2008). [online] http://www.cross-morse.co.uk/

DAISH, C (1972). The physics of ball games. UK: English University Press.

DAVIES, Gareth (2005). Determination and Analysis of Dimensions of 'Feel' in Tennis Ball Impacts (Ph.D.). Loughborough University

DEZA, Elena, DEZA, Michel Marie (2009). Encyclopedia of Distances. UK: Springer Dordrecht Heidelberg London New York.

DIGNALL, Richard and HAAKE, Steve (2000). Analytical modelling of the impact of tennis balls on court surfaces. *Tennis Science and Technology*, 155-162. UK: Blackwell Science.

DIGNALL, Richard, GOODWILL, Simon and HAAKE, Simon (2004) *Tennis GUT – Modelling the game.* The Engineering of Sport 5, **2,** 382-388. USA: Central Plains Book Mfg.

DUNN, Marcus (2014) Video-based step measurement in sport and daily living (Ph.D.). *The Centre for Sports Engineering Research,* Sheffield Hallam University.

ELLIOTT, B, MARSH, T and BLANKSBY, B (1986). A three-dimensional cinematographic analysis of the tennis serve. International Journal of Sport Biomechanics, **2**, 260-271.

ELLIOT, B (1982). Tennis: the influence of grip tightness on reaction impulse and rebound velocity. *Medicine and Science in Sports and Exercise,* **14** (5), 348-352.

ELLIOTT, N (2015) Camera calibration and configuration for estimation of tennis racket position in 3D (Ph.D.). *The Centre for Sports Engineering Research,* Sheffield Hallam University.

GABINER, M, GROPPEL, J and CAMPBELL, K, (1983). Resultant tennis ball velocity as a function of off-centre impact and grip firmness. *Medicine and Science in Sports and Exercise,* **15** (6), 542-544.

GOODWILL, Simon (2002). The dynamics of tennis ball impacts on tennis rackets (Ph.D.). *The Department of Mechanical Engineers,* University of Sheffield.

GOODWILL, Simon and HAAKE, Steve (2002). Spring damper model of an impact between a tennis ball and racket. *Proceedings of the Institute of Mechanical Engineers*, **215** Part C, 1331-1341.

GOODWILL, Simon and HAAKE, Steve (2003). Modelling of an impact between a tennis ball and racket. *Tennis Science and Technology 2,* 79-86. UK: International Tennis Federation.

GOODWILL, Simon (2003). Progress Report – MYO Racket Performance. *Unpublished paper.*

GOODWILL, Simon, CHIN, S and HAAKE, Steve (2004). Aerodynamics of spinning and non-spinning tennis balls. *Journal of Wind Engineering and Industrial Aerodynamics,* **92** (11), 935-958.

GOODWILL, Simon, KIRK, Robert and HAAKE, Steve (2005). Experimental and finite element analysis of a tennis ball impact on a rigid surface. *Sports Engineering*, **8**, 145-158

GOODWILL, Simon, DOUGLAS, Jamie, MILLER, Stuart and HAAKE, Steve (2006). Measuring ball spin off a tennis racket. *The Engineering of Sport 6*, **1,** 379-384. USA: Springer.

GOODWILL, Simon (2009). Progress report – MYO racket performance. *Unpublished paper.*

GREENWAY, Thomas (2016). Tennis ball aerodynamics – A comparison of free flight and wind tunnel measurements (BSc Dissertation). *Wolfson School of Mechanical and Manufacturing Engineering*, Loughborough University.

GROPPEL, J. L., DILLMAN, C. J., and LARDNER, T. J. (1983). Derivation and validation of equations of motion to predict ball upon impact in tennis. *Journal of Sports Sciences,* **1** (2), 111-120.

HAAKE, Steve, CHADWICK, Steve, DIGNALL, Richard, GOODWILL, Simon and ROSE, Paul (2000). Engineering tennis – slowing the game down. *Sports Engineering*, **3** (2). 131-143

HAAKE, Steve, CARRÉ, Matthew and GOODWILL, Simon (2003). Modelling of oblique tennis ball impacts on tennis surfaces. *Tennis Science and Technology* 2, 133-137. UK: International Tennis Federation.

HAAKE, Steve, ALLEN, Tom, CHOPPIN, Simon and GOODWILL, Simon (2007). The evolution of the tennis racket and its effect on serve speed. *Tennis Science and Technology 3,* 257-271. UK: International Tennis Federation.

HAAKE, Steve, GOODWILL, Simon and CARRÈ, Matthew (2007). A new measure of roughness for defining the aerodynamic performance of sports balls. *Proceedings of the Institution of Mechanical Engineers, Part C: Journal of Mechanical Engineering Science,* **221**, 789-806

HAAKE, Steve, ALLEN, Tom, JONES, Alex, SPURR, James (2012). Effect of inter-string friction on tennis ball rebound. *Proceedings of the Institute of Mechanical Engineers, Part J: Journal of Engineering Tribology*, **226**, 626-635. SAGE.

HATZE, H (1976) Forces and duration of impact, and grip tightness during the tennis stroke. *Medicine and Science in Sports,* **8** (2), 88-95.

HAWK-EYE (2008). [online] http://www.hawkeyeinnovations.co.uk/

HOFMANN, M, GANTER, N, WITTE, K, EDELMANN-NUSSER, J and NOWOISKY, C (2006). Use of the Infrared Based Motion Capture System AS 200 in Sport Science. *The Engineering of Sport 6*, **2**, 45-50. USA: Springer.

ITF (2008a). [online] http://www.itftennis.com/officiating/

ITF (2008b). [online] http://www.itftennis.com/technical/

ITF (2008c). ITF Technical Commission meeting. *Unpublished paper.*

ITF (2012). ITF Technical Commission meeting. *Unpublished paper.*

ITF (2015). SPRite review. Internal meeting. *Unpublished paper.*

JAMES, David (2004). Understanding the playing performance of cricket pitches (Ph.D.). *The Department of Mechanical Engineers,* University of Sheffield.

KANDA, Y, NAGAO, H and NAROU, T (2002). Estimation of tennis racket power using three-dimensional finite element analysis. *The Engineering of Sport 4,* 207-214. Blackwell Science.

KELLEY, John (2011a). Measuring ball spin rates in match play tennis (Ph.D.). *The Centre for Sports Engineering Research,* Sheffield Hallam University.

KELLEY, John (2011b). Initial report on the sports ball spin analysis algorithm. *Unpublished paper: The Centre for Sports Engineering Research,* Sheffield Hallam University.

KIRK, Bob, CARRÈ, Matthew, HAAKE, Steve and MANSON, Graeme (2007). Modelling traction of studded footwear on sports surfaces using neural networks. *Tennis Science and Technology 3,* 403-408. UK: International Tennis Federation.

KOHAVI, Ron (1995). A study of Cross-Validation and Bootstrap for Accuracy Estimation and Model Selection. *International Joint Conference on Artificial Intelligence (IJCAI).*

KOTZE, Johan (2005). Tennis Racket Performance Studies and the Design of a Novel Test Machine (Ph.D.). Loughborough University.

LASERLINER (2010). [online] http://laser-liner.co.uk/

LEICA GEOSYSTEMS (2008). [online] http://leica-geosystems.com/

LIU-KING, Y (1983). Mechanical analysis of racket and ball during impact. *Medicine and Science in Sports and Exercise,* **15** (5), 388-392.

MAEDA, H and OKAUCHI, M (2002). The transmission of impact vibration from tennis racket to hand. *The Engineering of Sport 4*, 223-230. Blackwell Science.

MATHWORKS (2008). [online] http://www.mathworks.com/

MICROSOFT DEVELOPERS NETWORK (2012). [online] https://msdn.microsoft.com/

MILLER, Stuart (2006). Modern tennis rackets, balls, and surfaces. *British Journal of Sports Medicine*, **40** (5), 401–406.

MILLER, Stuart (2007). The role of ITF Science & Technical in evaluating and regulating tennis equipment. *Tennis Science and Technology 3,* 1-19. UK: International Tennis Federation.

MISSAVAGE, R and BAKER, J (1984). Theoretical Modelling of Grip Firmness During Ball-Racket Impact. *Research Quarterly for Exercise and Sport,* **55** (3), 254-260.

MITCHELL, Sean, JONES, Roy and KOTZE, Johan (2000). The influence of racket moment of inertia during the tennis serve: 3D analysis. *Tennis Science and Technology,* 395-400. UK: Blackwell Science.

MOORE & WRIGHT (2010). [online] http://www.bowersgroup.co.uk/

NEWTON (2010). [online] https://www.amazon.co.uk/

OEHLER RESEARCH (2007). [online] https://www.oehler-research.com/

PAPADOPOULOS, M and EMMANOUILIDOU, C (2000). Kinematic analysis of the service stroke in tennis. *Tennis Science and Technology,* 383-387. UK: Blackwell Science.

SIMI REALITY MOTION SYSTEMS GMBH (2008). [online] http://www.simi.com/en/contact/index.html/

SISSLER, Lise (2011). Advanced Modelling and Design of a Tennis Ball (Ph.D.). Loughborough University

SOLA (2008). [online] http://www.sola.us/

SPURR, James, GOODWILL, Simon, Kelley, John, HAAKE, Steve (2014). Measuring the inertial properties of a tennis racket. *The Engineering of Sport 10,* 569-574. UK: Elsevier Ltd.

STEELE, Carolyn (2006). Tennis Ball Degradation (Ph.D.). Loughborough University

STROBL, Klaus, SEPP, Wolfgang, FUCHS, Stefan, PAREDES, Cristian and ARBTER, Klaus (2007). [online] Camera Calibration Toolbox for Matlab http://www.vision.caltech.edu/bouguetj/calib_doc/

SYLVAC (2008). [online] https://www.sylvac.ch/

TAMAKI, Toru, TAKAHIKO, S and YAMAMOTO, M (2004). Measuring ball spin by image registration. *The 10th Korea-Japan Joint Workshop on Frontiers of Computer Vision*, 269-274.

TARNOWSKI, K (2004). Analysis of tennis impacts on a realistically supported racket (MEng Dissertation). *Department of Mechanical Engineering*, University of Sheffield.

WANG, L, WU, C, SU, F, LO, K and WU, H (2000). Kinematic of trunk and upper extremity in tennis flat service. *Tennis Science and Technology,* 395-400. UK: Blackwell Science

WANG, L, WU, C, and SU, F (2002). Three-dimensional kinematics of the upper extremity in tennis volley. *The Engineering of Sport 4*, 725-729. Blackwell Science

WATANABE, T, IKEGAMI, Y and MIYASHITA, M (1979). Tennis: the effects of grip firmness on ball velocity after impact. *Medicine and Science in Sports,* **11** (4), 359-361.

ZHANG, Z (1999). Flexible camera calibration by viewing a plane from unknown orientations. *International Conference on Computer, Vision*Corfu, Greece. 666-6